UNIVERSIDAD COMPLUTENSE DE MADRID
FACULTAD DE CIENCIAS FÍSICAS
DEPARTAMENTO DE FÍSICA ATÓMICA, MOLECULAR Y NUCLEAR

TESIS DOCTORAL

Analysis of the first underground run and background studies of the Argon Dark Matter experiment

Análisis de la primera toma de datos subterránea y estudios de fondo del experimento Argon Dark Matter

MEMORIA PARA OPTAR AL GRADO DE DOCTORA

PRESENTADA POR

Bárbara-Rosario Montes Núñez

DIRECTORES

Luciano Romero Barajas
Roberto Santorelli

Madrid, 2017

Centro de Investigaciones Energéticas, Medioambientales y Tecnológicas

Departamento de Física Atómica, Molecular y Nuclear
Facultad de Ciencias Físicas, Universidad Complutense de Madrid

* * *

Analysis of the first underground run and background studies of the Argon Dark Matter experiment

Análisis de la primera toma de datos subterránea y estudios de fondo del experimento Argon Dark Matter

Ph. D. Thesis submitted by
Bárbara-Rosario Montes Núñez
for the degree of Doctor of Physics

Supervised by:
Dr. Luciano Romero Barajas
Dr. Roberto Santorelli

Madrid, April of 2016

Contents

Summary

Dark Matter is a collisionless and non-luminous kind of matter, whose existence is inferred through its gravitational effects at the galactic, cluster and large scales in the Universe. From the analysis of the PLANCK latest data, Dark Matter accounts for the 26.6% of the composition of the energy density of the Universe, while ordinary matter only represents 4.9% [1]. Revealing the nature of Dark Matter has become one of the most challenging problems in modern physics. A possible explanation comes from particle physics in the form of Weakly Interacting Massive Particles (WIMPs), a particularly interesting class of new particle that can naturally account for the measured abundance of Dark Matter.

WIMPs would be produced thermally in the early Universe and, since they interact only weakly, their annihilation rate would become insignificant as the Universe expands, thus freezing out with a relic abundance. Supersymmetry, an extension of the Standard Model of particle physics, foresees interesting possible WIMP candidates in the form of the Lightest Supersymmetric Particle (LSP), which is neutral, stable and massive.

A great experimental effort has been undertaken in the last years to detect Dark Matter in underground and space-based detectors or produce it in accelerators. This Thesis is focused on the analysis of the first underground run and background studies of the Argon Dark Matter (ArDM) experiment, which aims to detect WIMPs via the nuclear recoils produced by their elastic scattering off argon nuclei. The detector is a ton-scale double-phase (liquid-gas) TPC, which is currently installed at the Canfranc Underground Laboratory (LSC) under the Pyrenees in Spain and it is the first ton-scale argon detector for Dark Matter to take data underground.

The ArDM experiment with a first design foreseeing the charge readout already addressed, on surface at CERN in 2009, the possibility to detect independently ionisation and scintillation signals thanks to the double-phase TPC technology. However, different technical problems have caused the delay of the construction and the start of operation of the ArDM detector. The LSC facility was completed and inaugurated in 2006, however, one year later, signs of rock instabilities started to appear and the laboratory was closed. The new underground hall A was not completed until 2010 and other infrastructures, like the mechanical workshop, have been available only after January 2011. At the same time, ArDM is the first big size detector

operative at LSC, so the experiment helped to prepare and improve the laboratory safety rules for underground operations. In addition, ArDM went through a redesign of the charge readout system, replacing the Large Electron Multiplier (LEM), whose technology was not mature enough for Dark Matter detection, by another array of photomultiplier tubes (PMTs), using the same technology than for the light readout.

The above mentioned technical problems have unequivocally influenced the natural development of the experiment and consequently have also affected the research activities related to this PhD thesis. Even though the first Dark Matter run is foreseen on 2016, the data analysis presented in this Thesis allowed to carry out an extensive investigation of the background and of the detector performances and to measure for the first time the rejection power capability at ton-scale, thus allowing to assess the potential of the experiment.

Since ArDM is a small collaboration led by two research groups, the ETH of Zurich and CIEMAT of Madrid, with the support of CERN and LSC, I could participate in many different aspects of the experiment. Although these circumstances have resulted in a very extensive thesis work, I obtained a valuable experience and wide knowledge on both hardware and software aspects related to ArDM. I have been personally involved in the ArDM detector installation underground, which took place at LSC in February 2013, after an initial successful commissioning phase on surface at CERN and a first underground phase, which included the installation of the supporting platform, the electronics and control system at LSC. In addition, I have actively participated in hardware shifts, being the responsible person of the experiment in the laboratory several times.

Furthermore, I had the opportunity to attend some interesting international conferences and meetings, presenting my personal contributions to the ArDM project. Particularly, I have contributed to carry out the analysis of the first underground data taken in single phase (both gas and liquid), which includes: evaluation of the detector's light yield with ^{57}Co and ^{83}Kr sources, detection of the radioactive contamination in natural argon and study of the background produced by the detector materials. I participated in the analysis of the material screening measurements, which evaluate the presence of radioactive isotopes coming from the natural ^{238}U and ^{232}Th decay chains in the detector components. In particular, I calculated the flux and the energy spectra of the neutrons coming from these internal sources, which, combined with the Monte Carlo simulation of the event interaction in ArDM, provides the number of expected neutrons coming from each material composing the detector.

One of the most relevant results of the Thesis regards the discrimination of the electron recoils produced by the ^{39}Ar contamination. I studied the distribution of events in the nuclear recoil and electron recoil bands, assessing for the first time, at the ton scale, the background rejection power through the pulse shape analysis of the scintillation light. The result is not only relevant for ArDM but also for other noble liquid experiments working in the Dark Matter field. Additionally, taking into account the results concerning the neutron and gamma background, I developed a dedicated theoretical study to predict the expected ArDM sensitivity. The results show the possibility for ArDM to set the most competitive Dark Matter limit in the world with an argon detector within a few weeks of data taking.

A great effort was dedicated to the study of the external neutron background, mainly coming from the laboratory rocks and materials, by developing a setup to measure the environmental neutron flux in the laboratory hall in which ArDM is installed. A liquid scintillator detector was characterised at CIEMAT, optimising the setup, and installed at LSC next to ArDM in November 2014, initiating several months of data taking, which also preceded a challenging period of data analysis.

Finally, I developed specific tools to study the dynamic of the positive charge in liquid argon, excluding the possibility that the ions have a significant impact in the underground operation of a Dark Matter detector. At the same time, the study proves some potential concern for the future giant argon neutrino detectors.

This Thesis has been financed by the Ministry of Economy and Competitiveness through the FPA2012-30811 support. Several papers including the main results from the analysis presented in this Thesis are under preparation [2]. In addition, results regarding the event position reconstruction have been accepted for publication in HAIS (LNAI 9648) 2016.

Resumen

La Materia Oscura es un tipo de materia no luminosa y sin colisiones cuya existencia es inferida a través de sus efectos gravitacionales en la escala galáctica, de cúmulos de galaxias y a grandes escalas en el Universo. De acuerdo con el análisis de los datos más recientes de PLANCK, la Materia Oscura da cuenta del 26,6% de la composición de la densidad de energía del Universo, mientras que la materia ordinaria sólo representa un 4,9% [1]. Revelar la naturaleza de la Materia Oscura se ha convertido en uno de los problemas más desafiantes de la física moderna. Una posible explicación proviene de la física de partículas en la forma de Partículas Masivas Débilmente Interactuantes (WIMPs), una nueva clase de partícula especialmente interesante que puede dar cuenta de forma natural de la abundancia medida de Materia Oscura.

Los WIMPs se producirían térmicamente en el Universo primitivo y, puesto que sólo interaccionan débilmente, su tasa de aniquilación se convertiría en insignificante conforme el Universo se expande, permaneciendo así con una abundancia determinada. Supersimetría, una extensión del Modelo Estándar de partículas, proporciona candidatos a WIMPs en forma de la Partícula Supersimétrica Más Ligera (LSP), que es neutra, estable y masiva.

Un gran esfuerzo experimental ha sido realizado en los últimos años para detectar Materia Oscura con detectores subterráneos o espaciales o para producirla en aceleradores. Esta Tesis está centrada en el análisis de la primera toma de datos subterránea y estudios de fondo del experimento Argon Dark Matter (ArDM), cuyo objetivo es detectar WIMPs a través de los retrocesos nucleares producidos por su dispersión elástica por núcleos de argón. El detector, actualmente instalado en el Laboratorio Subterráneo de Canfranc (LSC) bajo los Pirineos en España, es una TPC de doble fase (líquido-gas) de una tonelada y es el primer detector de Materia Oscura basado en argón de la escala de la tonelada en tomar datos en un laboratorio subterráneo.

El experimento ArDM con un primer diseño que ya preveía la detección de carga, en superficie en el CERN (2009), abordaba la posibilidad de detectar independientemente las señales de ionización y centelleo gracias a la tecnología de TPC de doble fase. Sin embargo, diferentes problemas técnicos han causado el retraso de la construcción y el inicio de la operación del detector ArDM. Las instalaciones del LSC se

completaron e inauguraron en 2006, sin embargo, signos de inestabilidad en la roca empezaron a aparecer y el laboratorio fue clausurado. El nuevo hall A subterráneo no fue completado hasta 2010 y otras infraestructuras, como el taller mecánico, sólo están disponibles desde enero de 2011. Al mismo tiempo, ArDM es el primer detector de gran tamaño en operar en el LSC, por lo que el experimento ha ayudado a preparar y mejorar las medidas de seguridad del laboratorio para operaciones subterráneas. En suma, ArDM sufrió un rediseño del sistema de medida de carga, reemplazando el Gran Multiplicador de Carga (LEM), cuya tecnología no estaba lo suficientemente desarrollada para la detección de Materia Oscura, por otra matriz de fotomultiplicadores (PMTs), usando la misma tecnología que para la detección de luz.

Las dificultades técnicas mencionadas anteriormente han influenciado de manera inequívoca en el desarrollo natural del experimento y, en consecuencia, han afectado también a las actividades de investigación relacionadas con la presente Tesis Doctoral. A pesar de que la primera toma de datos de Materia Oscura está prevista para 2016, el análisis presentado en esta Tesis ha permitido realizar una extensa investigación del fondo y del funcionamiento del detector y ha posibilitado medir por primera vez el poder de discriminación a la escala de la tonelada, haciendo posible, por tanto, evaluar el potencial del experimento.

Puesto que la colaboración ArDM está formada por dos grupos de investigación, uno perteneciente al ETH de Zurich y el otro procedente del CIEMAT, con el apoyo del CERN y del LSC, he contribuido en numerosos aspectos diferentes del experimento. Aunque estas circunstancias han resultado en un extenso trabajo de tesis, he obtenido una valiosa experiencia y un amplio conocimiento en aspectos de hardware y software relacionados con ArDM. He estado personalmente involucrada en la instalación subterránea de ArDM, que tuvo lugar en el LSC en febrero de 2013, después de una primera y exitosa fase de medidas en superficie en el CERN y una primera fase subterránea, que incluyó la instalación de la base de soporte, la electrónica y el sistema de control en el LSC. En suma, he participado activamente en la operación del hardware y la toma de datos, siendo la persona responsable del experimento en el laboratorio en varias ocasiones.

Además, he tenido la oportunidad de asistir a conferencias y reuniones internacionales, en las que he presentado mi aportación personal al proyecto ArDM. En particular, he contribuido al análisis de la primera toma de datos subterránea en fase pura (gaseosa y líquida), que incluye: evaluación de la luz producida en el detector mediante calibración con ^{57}Co y ^{83}Kr, detección de contaminación radioactiva en argón natural y estudio del fondo producido por los materiales del detector. He participado en el análisis de las medidas de emisión de los materiales, que evalúan la presencia de isótopos radioactivos procedentes de las cadenas de desintegración del ^{238}U y ^{232}Th en los componentes del detector. En concreto, he realizado los cálculos de flujo y del espectro de energía de los neutrones procedentes de estas fuentes internas, los cuales, combinados con la simulación Monte Carlo de la interacción de partículas en ArDM, proporcionan el número de neutrones esperados de cada material que compone el detector.

Uno de los resultados más relevantes de la Tesis está relacionado con la discriminación de los retrocesos electrónicos producidos por la contaminación de ^{39}Ar. He estudiado la distribución de sucesos en las bandas de retroceso nuclear y retroceso electrónico, evaluando por primera vez, a la escala de la tonelada, el poder de discriminación de fondo a través del análisis de la forma de pulso de la luz de centelleo. El resultado no sólo es relevante para ArDM, sino también para otros experimentos de gases nobles que trabajen en el campo de la Materia Oscura. Además, considerando los resultados referidos al fondo de neutrones y fondo gamma, he desarrollado un estudio teórico para predecir la sensibilidad esperada para ArDM. Los resultados muestran la posibilidad de que ArDM pueda establecer el límite de Materia Oscura más competitivo del mundo para un detector basado en argón tras unas pocas semanas de toma de datos.

Un gran esfuerzo se ha dedicado al estudio del fondo de neutrones externo, que procede principalmente de las rocas y materiales del laboratorio, mediante el desarrollo de un sistema para medir el flujo ambiental de neutrones en el hall en el que ArDM está instalado. Un detector de centelleo líquido fue caracterizado en el CIEMAT, optimizando el sistema de toma de datos, e instalado en el LSC en las proximidades de ArDM en noviembre de 2014, iniciando varios meses de toma de datos, que precedieron un exigente período de análisis.

Finalmente, he desarrollado herramientas específicas para estudiar la dinámica de cargas positivas en argón líquido, excluyendo la posibilidad de que los iones tengan un impacto significativo en la operación subterránea de un detector de Materia Oscura. Al mismo tiempo, el estudio prueba la existencia de una potencial preocupación por los detectores gigantes de neutrinos que operarán con argón en el futuro.

Esta Tesis ha sido financiada por el Ministerio de Economía y Competitividad a través de la ayuda FPA2012-30811. Varios artículos que incluyen los resultados más relevantes del análisis presentado en la Tesis están en preparacin [2]. Además, resultados relacionados con la reconstrucción de la posición han sido aceptados para publicación en HAIS (LNAI 9648) 2016.

Introduction

An overwhelming amount of astrophysical and cosmological observations at different scales have led us to conclude that our Universe is dominated by two main components whose nature still remains unknown. The first one is a new, collisionless and non-luminous type of matter, called Dark Matter, whose interactions with ordinary matter are mainly through the gravitational force. The second one is a uniformly distributed component called Dark Energy, which is responsible for the accelerated expansion of the Universe. According to the latest PLANCK satellite data, Dark Matter and Dark Energy components are required to account for ~95% of the content of our Universe, while ordinary matter only represents ~5% [1].

Although there are different possible explanations for the origin of the Dark Matter component, a very attractive hypothesis comes from particle physics in the form of thermal relic particles produced during the Big Bang that naturally freeze-out with the right abundance and that are present now in the halo surrounding the galaxies. In that scenario, the Supersymmetric extension of the Standard Model of particle physics provides an ideal WIMP candidate in the form of the Lightest Supersymmetric Particle (LSP) and a theoretical framework to compute its properties and possible detection rates.

In the last years, a great experimental effort has been undertaken in the Dark Matter field, pushing the development of a great variety of techniques. WIMPs can potentially be detected by three complementary methods. They may be produced at accelerators, such as the Large Hadron Collider. Relic WIMPs may be detected indirectly when they clump in massive astrophysical objects, increasing the probability of annihilation, such that it is possible to detect the production of high-energy gammas and neutrinos in the Sun or Earth. Finally, relic WIMPs may be also detected directly when they scatter off target nuclei in terrestrial detectors, producing low energy nuclear recoils, typically in the 1-100 keV range.

Among direct detection experiments, the ones based on noble liquids are currently leading the hunt for Dark Matter. Noble liquids are dense and homogeneous which makes them excellent media for building massive Dark Matter detectors up to the ton scale and beyond, allowing to detect low interaction rates. Furthermore, they are bright scintillators with high ionisation yields, making possible the full 3D reconstruction of the interaction position if operated in time projection chamber

(TPC) mode. Finally, noble gases are quite safe and affordable targets since they are inert, not flammable and they are also available in large amounts as by-products of the industry. Among them, argon is the most affordable choice, showing a powerful discrimination against background, that configures it as an ideal detection medium for nuclear recoils.

One of the currently operating experiments based on liquid argon is the Argon Dark Matter (ArDM) experiment, a ton-scale double-phase (liquid-gas) argon TPC, which is currently installed at the Canfranc Underground Laboratory (LSC) under the Pyrenees in Spain, being the first ton-scale argon Dark Matter detector to take data underground. ArDM started underground operation with data taking in warm gas argon in 2013. The detector is now going through an upgrade in order to prepare it for the second underground run, that will be devoted to Dark Matter search.

Since ArDM is a small collaboration led by two research groups, the ETH of Zurich and CIEMAT of Madrid, with the support of CERN and LSC, my work spanned consequently over all the operational aspects of the detector, which include sharing the responsibility during the commissioning phase, doing on-site shifts. This global aspect of the work within ArDM is reflected in the extension of the Thesis, which is oriented to the data analysis and it has been possible given the previous work carried out by other ArDM members, who performed the first test on surface and prepared the detector for underground operation. I personally collaborated with L. Epprecht, A. Gendotti from the ETH of Zurich, whose work was essential for the detector design and construction, and with M. de Prado from CIEMAT, who also had an important contribution on hardware aspects. During the data analysis, I mainly cooperated with K. Nguyen and K. Nikolics, also from the ETH, who were part of the software group.

The Thesis begins with the description of the main evidences of the existence of Dark Matter and possible particle candidates. Different experimental approaches for WIMP detection and a review of the latest experimental results and future prospects in the Dark Matter field are also described in Chapter 1. The following Chapter is devoted to direct detection techniques, specially the ones based on noble liquids, including a theoretical study of the experimental sensitivity. The ArDM experiment is presented in Chapter 3, while background contributions and discrimination techniques are introduced in Chapter 4. Results from the analysis of data taken with ArDM in pure gas phase and liquid phase are discussed in Chapters 5 and 6 respectively. The Thesis ends with the results obtained from neutron measurements in Chapter 7 and a study of the ions drift in liquid argon detectors in Chapter 8.

Chapter 1

Dark Matter

Nowadays, there are compelling evidences that provide a solid scenario for the existence of a cold, collisionless and non-luminous new type of matter, called Dark Matter, which mainly interacts gravitationally with ordinary matter. In this first Chapter we will introduce the different astrophysical and cosmological evidences of Dark Matter and the Dark Matter particle candidates arising form several theoretical models. Finally, the great variety of experimental techniques that have been developed in the last decades to detect, in a direct or indirect way, or produce in accelerators these Dark Matter particles are also presented in this Chapter.

According to the currently accepted cosmological model, which is based on General Relativity and describes mathematically the origin, evolution and the status of the Universe, Dark Matter and Dark Energy constitute the main components of the energy density of the Universe. One of the basic elements of any cosmological model is the metric, which contains the information regarding the space-time symmetries and is written as [3]

$$\mathrm{d}s^2 = g_{\mu\nu}\mathrm{d}x^\mu \mathrm{d}x^\nu, \tag{1.1}$$

where $g_{\mu\nu}$ is the metric tensor and μ, ν=0,1,2,3. Assuming a homogeneous and isotropic Universe, $g_{00} = 1$ and $g_{0i} = 0$ with $i = 1, 2, 3$. In a comoving reference system, a reference frame in which an observer is at rest with respect to the Universe in expansion, the space-time metric can be expressed as follows:

$$\mathrm{d}s^2 = \mathrm{d}t^2 - a^2(t)\left(\frac{\mathrm{d}r^2}{1-kr^2} + r^2(\mathrm{d}\theta^2 + \sin^2\theta \mathrm{d}\phi^2)\right). \tag{1.2}$$

This is the so-called Freeman-Lemaître-Robertson-Walker metric, where k is a constant that can be 0 or take positive or negative values and accounts for the curvatures of the spatial sections, defined as the hypersurfaces of constant time. The scale factor, $a(t)$, which takes into account the expansion of the Universe, relates the physical distance, d, with the comoving distance, Δx, in the form $d = a(t)\Delta x$.

Another crucial ingredient of the cosmological model is given by the Einstein equations, which are written as follows:

$$R_{\mu\nu} - \frac{1}{2} g_{\mu\nu} R = 8\pi G T_{\mu\nu}, \tag{1.3}$$

where $R_{\mu\nu}$ is the Ricci tensor, R is the Ricci scalar, and $T_{\mu\nu}$ is the energy-momentum tensor that includes the contributions from baryonic matter, electromagnetic radiation, neutrinos, Dark Matter and Dark Energy. The latter is usually assumed to be in the form of a cosmological constant, Λ. The positive vacuum Dark Energy density resulting from a cosmological constant implies a negative pressure, which will drive an accelerated expansion of the Universe, as it has been observed.

The so-called Friedmann equation is obtained from the "00" component of Equation 1.3, resulting:

$$\frac{\dot{a}^2}{a^2} = \frac{8\pi G}{3}\rho_t - \frac{k}{a^2}. \tag{1.4}$$

In Equation 1.4, ρ_t is the total average energy density of the Universe and $H = \dot{a}(t)/a(t)$ is the Hubble parameter representing the expansion of the Universe, which, calculated in a particular time, t_0, is called Hubble constant, $H_0 = \dot{a}(t_0)/a(t_0)$. Evaluating Equation 1.4 in $t = t_0$ and dividing by H_0^2, we get:

$$1 = \frac{8\pi G}{3H_0^2}\rho_0 + \frac{8\pi G}{3H_0^2}\rho_\Lambda - \frac{k}{a_0^2 H_0^2}, \tag{1.5}$$

which is usually expressed as

$$1 = \Omega_m + \Omega_\Lambda + \Omega_K, \tag{1.6}$$

where Ω_m is the fraction of matter contributing to the energy density of the Universe, Ω_Λ is the Dark Energy contribution and Ω_K is the curvature contribution.

According to latest large scale and Cosmic Microwave Background measurements, the current accepted cosmological model, ΛCDM, describes our Universe with $\Omega_m = 0.315$, $\Omega_\Lambda = 0.685$ and $|\Omega_K| < 0.005$, meaning that the spatial sections are essentially flat. Ω_m includes the contribution from both ordinary matter, $\Omega_b = 0.049$, and Dark Matter, $\Omega_c = 0.266$, which represents a crucial component to explain the observed energy density of the Universe. The main observational evidences of the presence of this Dark Matter component will be presented in the next Section.

1.1 Evidences of Dark Matter

An extensive amount of cosmological and astrophysical observations at many different scales support the presence of Dark Matter in the Universe. Since Dark

Matter neither emits nor absorbs light or any other electromagnetic radiation, these evidences, that will be reviewed throughout the present Section, are related to the gravitational interaction of Dark Matter with ordinary matter at the galactic, cluster and large scales in the Universe.

1.1.1 Rotational curves of galaxies

In individual galaxies the presence of Dark Matter has been convincingly established through the use of Kepler's third law. For a circular orbit, considering Newtonian physics, the gravitational force is equal to the centripetal acceleration due to the curved trajectory described by the body:

$$m\frac{v^2}{r} = \frac{GMm}{r^2} \rightarrow v = \sqrt{\frac{GM}{r}} \propto r^{-\frac{1}{2}}. \tag{1.7}$$

This expression allows us to determine the rotation curve, $v(r)$, at a given radial distance from the galactic centre. According to the previous formula and considering M approximately constant, we expect a decrease of the rotational velocity for a larger radius at the expected rate of $v \propto r^{-1/2}$, and this is, in fact, what is observed in the Solar System. However, observations of galaxies show that the velocity remains constant for stars that are far from the centre of the galaxy, which implies that the mass contained in the galaxy has to grow with the radius, $M(r) \propto r$. At the same time, there is no luminous matter component to account for this increase.

According to surface photometry, the luminosity density, also known as surface brightness, of most spiral galaxies is essentially given by [4]:

$$I(R) = I_0 \mathrm{e}^{-R/a}. \tag{1.8}$$

where I_0 is the central surface brightness (intensity scale) and a is the characteristic size of the disk (length scale), which typically takes values in the range 1-5 kiloparsecs (kpc), where 1 kpc=3262 light-years. For example, the Milky Way has a scale length $a = 3.5$ kpc and a central surface brightness (in blue light) of $I_0 = 140\ L_\odot/\mathrm{pc}^2$. Then, a typical value of the "disk mass-to-light ratio", which illustrates how many solar masses of stars there are for each solar luminosity of brightness, is assumed to be in the range 0.5-2.0 $\mathrm{M}_\odot/\mathrm{L}_\odot$, so that the mass in the disk and its contribution to the velocity curve can be calculated.

In Figure 1.1 we present the rotational velocity curves, measured by the Doppler shift of the 21 cm emission line from neutral hydrogen (HI), for two different galaxies as a function of their distance from the galactic centre. The contribution coming from the luminous component is not enough to fit the data. However, the velocity curve behaviour can be explained by assuming the presence of a Dark Matter component in the halo of the galaxy in both cases. The photometric data and the

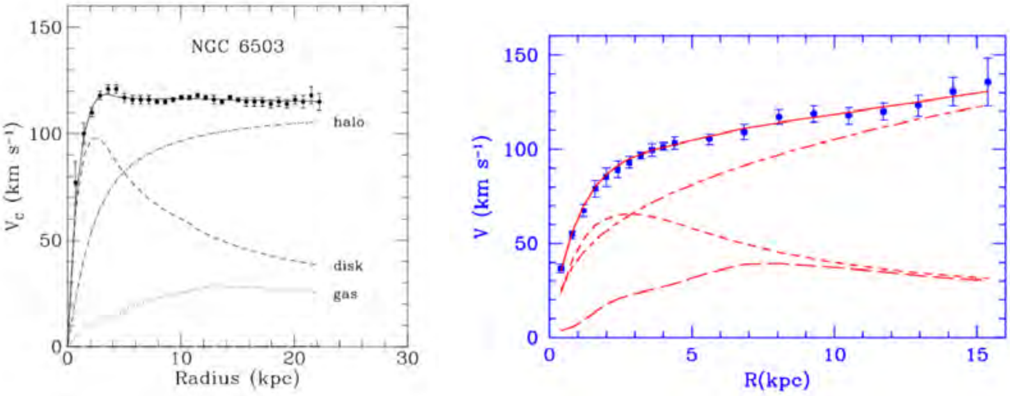

Figure 1.1: Measured velocity curves (points) for dwarf spiral galaxy NGC 6503 (left) [5] and M33 spiral galaxy (also known as NGC 598) (right) [6]. The best three-parameter fit model to the data points is represented as a solid curve. The contribution of the individual components is also shown: the dashed curve corresponds to the visible component in the disk, the dotted curve accounts for the gas and the dashed-dotted curve represents the dark halo.

measured neutral hydrogen distribution, which is used as a tracer of the distribution of the observable mass, are thus combined with isothermal dark-halo models in a least-squares fit to the observed velocity curves. In the fitting dark-halo models, a spherical halo is assumed with a density distribution given by [5]:

$$\rho(r) = \rho_0 \left[1 + {\frac{r}{r_c}}^{2} \right]^{-1} . \tag{1.9}$$

These fits have in most cases three parameters: the mass-to-light ratio of the visible component, M/L, the central halo density, ρ_0, and the halo core radius, r_c. The observed velocity curve is then fitted via a non-linear squares routine, allowing the two halo parameters and M/L for the visible matter to vary. This procedure, based on the dark-halo model, perfectly fits the measured velocity curves, as it is shown in the plots of Figure 1.1, thus pointing out the necessity of a Dark Matter component in the galactic halo to explain the data.

Velocity curves as the ones shown in Figure 1.1 have been compiled for more than 1000 spiral galaxies. The results indicate that the "galactic mass-to-light ratio" is $M/L = (10 - 20)M_\odot/L_\odot$ in spiral galaxies and in ellipticals, while this ratio can increase to $M/L = (200 - 600)M_\odot/L_\odot$ in dwarf galaxies [7]. Even considering astronomical objects that cannot be observed directly because they do not emit light, such as brown stars, neutron stars and black holes, there is not enough mass to explain the observed rotational curves, thus the existence of a Dark Matter component in the halo of the galaxy is required to explain the data at the galactic scale.

Assuming that the velocity curve is flat in the midplane, the data imply a local Dark Matter density of $\rho_W = 0.3 \pm 0.1$ GeV $\cdot$ cm^{-3} [8], which is fully consistent with other estimations of this quantity carried out with different techniques.

Another possible method to constrain the local density of Dark Matter is based on determining the dependence of the gravitational potential on distance above the midplane of the galactic disk ("height"), from measuring the kinematics of stars. The contributions from ordinary matter and Dark Matter can be thus disentangled by measuring the gravitational potential out to larger "heights". In particular, at "heights" of several times the disk thickness, the dark halo and the disk contributions to the potential have a different "vertical" dependence. Since most of the disk mass lies below ~ 1.5 kpc, above this "height" the disk contribution to the integrated surface density, $\Sigma(Z) \equiv \int_{-Z}^{Z} \rho(z)\mathrm{d}z$, is roughly constant with "height", while the disk potential varies as $\Phi(Z) \propto |Z|$. Regarding the Dark Matter component in the halo, we have $\Sigma(Z) \propto |Z|$ and $\Phi(Z) \propto Z^2$. Thus, any measured increase in the surface density at $|Z| > 2$ kpc must be due to the dark halo.

1.1.2 Mass of galaxy clusters

First measurements of velocities of galaxies in the Coma cluster (performed by Zwicky in 1933 and confirmed by Rubin in 1970) revealed much larger values than the ones predicted by the virial theorem, meaning that the cluster would be gravitationally bound only if its total mass exceeded the mass of the luminous matter contained in its component galaxies.

Galaxy clusters are composed by groups of galaxies gravitationally bounded. If the system is in equilibrium, there is a relationship between the mean velocity of galaxies and the mass of the cluster given by the virial theorem, which is expressed as a relationship between the average kinetic energy, $< T >$, of a system and its average potential energy, $< V >$, as follows

$$< T >= -\frac{1}{2}\sum_{i=1}^{N} < F_i \cdot r_i >, \tag{1.10}$$

where F_i represents the force applied to the particle i, which is located in position r_i. If the force between two particles of the system is produced by a potential energy $V(r) \propto r^n$, which is proportional to a certain power of the distance between both particles, r, the virial theorem is written as

$$2 < T >= n < V > . \tag{1.11}$$

In particular, considering a gravitational potential, $V(r) \propto r^{-1} \rightarrow n = -1$, we get:

$$< T > +\frac{1}{2} < V >= 0, \tag{1.12}$$

where $T \simeq 3M < v_r^2 > /2$ is the kinetic energy, with $< v_r^2 >^{1/2}$ the velocity dispersion, and $V \simeq -GM^2/R$ is the potential energy of a cluster of mass M and radius R. The radius can be estimated from a model of the cluster density profile. One typically obtains from this type of analysis values of order [9]:

$$M \simeq 10^{15} h^{-1} M_{\odot} \tag{1.13}$$

where $h = H_0/100$ kms^{-1}Mpc^{-1} is the present Hubble parameter, which is, according to latest PLANCK results, $H_0 = 67.64 \pm 0.48$ [10]. This result, which corresponds to a mass to light ratio that can be as large as $M/L \simeq 300 M_{\odot}/L_{\odot}$, reveals that the total mass required to explain the dynamics of the galaxy clusters is much higher than the sum of the mass of their luminous components, thus the presence of a Dark Matter component becomes necessary to explain the dynamics of galaxy clusters.

1.1.3 Gravitational lensing

It is possible that the light coming from distant galaxies that are placed behind galaxy clusters is bended by their intense gravitational fields, simulating the effect of a lens. Corrections have to be introduced since gravitational lensing distorts the size of the observed objects and frequently generates multiple images, as it is shown in Figure 1.2. These pictures illustrate how gravitational lensing by foreground clusters of galaxies influences the appearance of far more distant background galaxies, whose brightness is being amplified by the effects of foreground intense gravitational fields.

Thanks to the gravitational lensing effect, it is possible to obtain detailed maps of the matter distribution in galaxy clusters, such as the Bullet cluster, shown in Figure 1.3, which was formed by collision of two large clusters of galaxies that took place 150 million years ago and constitutes one of the strongest evidences for the existence of Dark Matter.

During the collision of the two clusters, the hot gas from each of them, represented in pink colour in Figure 1.3, suffers a dragging force which reduces its velocity when it passes through the gas from the other cluster. As a result, hot gas remains close to the centre after the collision. In a clear contrast with this behaviour, Dark Matter, depicted in blue, which only interacts gravitationally, is not affected or slowed down by the collision, thus the luminous centre of the galaxy is different than the centre of mass.

In addition, if the interactions of Dark Matter particles are frequent but exchange little momentum, Dark Matter will be decelerated by an additional drag force. On the contrary, if the interactions are rare but exchange a lot of momentum, Dark Matter will tend to be scattered away and lost. The observation of the lack of deceleration of Dark Matter in the Bullet cluster collision constrained its self-interaction cross section to $\sigma_{DM}/m < 1.25$ cm^2/g (68% C.L.) for long-ranged forces. Using

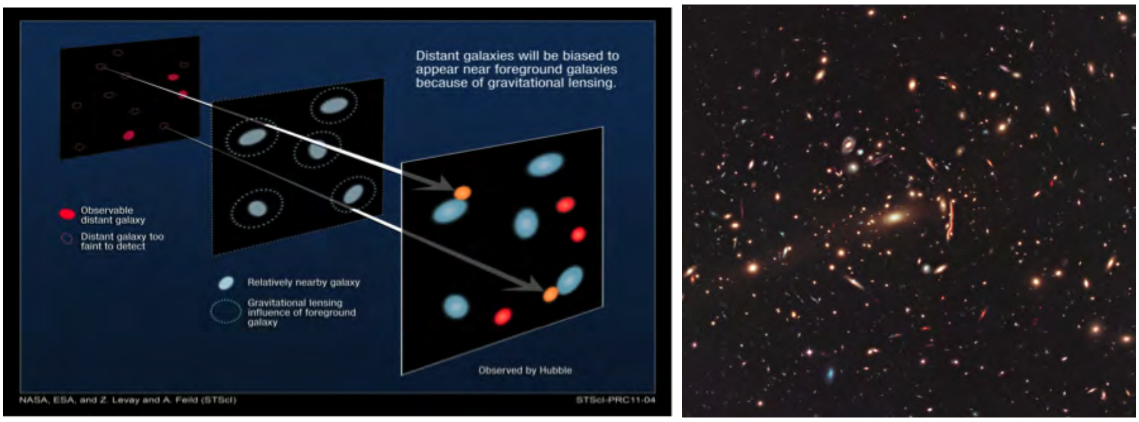

Figure 1.2: (Left) Diagram illustrating the effect of gravitational lensing, including changes in the brightness of distant objects and the appearance of multiple images [11]. (Right) Image taken by the Hubble Space Telescope showing the gravitational lensing caused by Dark Matter distribution in the MACS 1206 cluster of galaxies, which lies 4 billion light-years from Earth. The distorted shapes in the cluster are distant galaxies from which the light is bent by the gravitational pull of Dark Matter within the cluster of galaxies [12].

the Chandra and Hubble Space Telescopes, 72 galaxy collisions have been observed and combining these measurements statistically, the existence of Dark Matter has been detected at 7.6σ significance, establishing a limit for the self-interaction cross section of $\sigma_{DM}/m < 0.47$ cm^2/g (95% C.L.) [14].

1.1.4 Cosmic Microwave Background

The Cosmic Microwave Background (CMB) radiation, whose existence was predicted by George Gamow and his collaborators in 1948 [15] and discovered by Arno Penzias and Robert Wilson in 1965 [16], is an isotropic radiation produced after the Big Bang, when the temperature dropped enough to allow electrons and protons forming hydrogen atoms and making the Universe transparent to radiation.

After many decades of research with satellites (COBE, WMAP and more recently PLANCK), this radiation is known to be quite homogeneous, following with extraordinary precision the spectrum of a black body corresponding to a temperature of $T = 2.726$ K. Despite its general homogeneity, some fluctuations in temperature at the 10^{-5} level (that means fluctuations in density were small when temperature fluctuations were originated) have been observed, as shown in Figure 1.4. These fluctuations, which have been measured by PLANCK satellite, were originated during the inflationary period of the Universe expansion and are very sensitive to the parameters of the cosmological model, thus they provide essential information about

Figure 1.3: Bullet cluster. The image is composed by an optical picture and another one in X-ray taken by Chandra telescope. Contributions from hot gas depicted in pink are clearly separated from the Dark Matter component depicted in blue [13].

the first instants of the Universe and its evolution.

PLANCK satellite has been specifically designed to measure temperature and polarisation anisotropies of the CMB, being capable to produce high resolution (down to 5') maps of these anisotropies, with μK sensitivity per resolution element, over the entire sky. The wide frequency coverage of PLANCK (30-857 GHz) has been chosen to provide accurate discrimination of Galactic emission, which is particularly important for polarisation, and to study galaxy clusters and extragalactic point sources [17].

The observed temperature anisotropies are usually expressed in terms of spherical harmonics as follows [18]:

$$\frac{\delta T}{T}(\theta, \phi) = \sum_{l=2}^{+\infty} \sum_{m=-l}^{+l} a_{lm} Y_{lm}(\theta, \phi), \tag{1.14}$$

where $Y_{lm}(\theta, \phi)$ are the spherical harmonics. The variance of a_{lm}, C_l, is given by

$$C_l \equiv < |a_{lm}|^2 > \equiv \frac{1}{2l+1} \sum_{m=-l}^{l} |a_{lm}|^2. \tag{1.15}$$

Assuming that the temperature fluctuations are Gaussian, the whole information contained in the CMB can be summarised into the power spectrum, essentially giving the behaviour of C_l as a function of l. In Figure 1.5, $D_l = l(l+1)C_l/2\pi$ is plotted as a function of the multipole, l.

The detailed analysis of the CMB anisotropies provides a valuable test of cosmological models and puts stringent constraints on cosmological parameters. Their

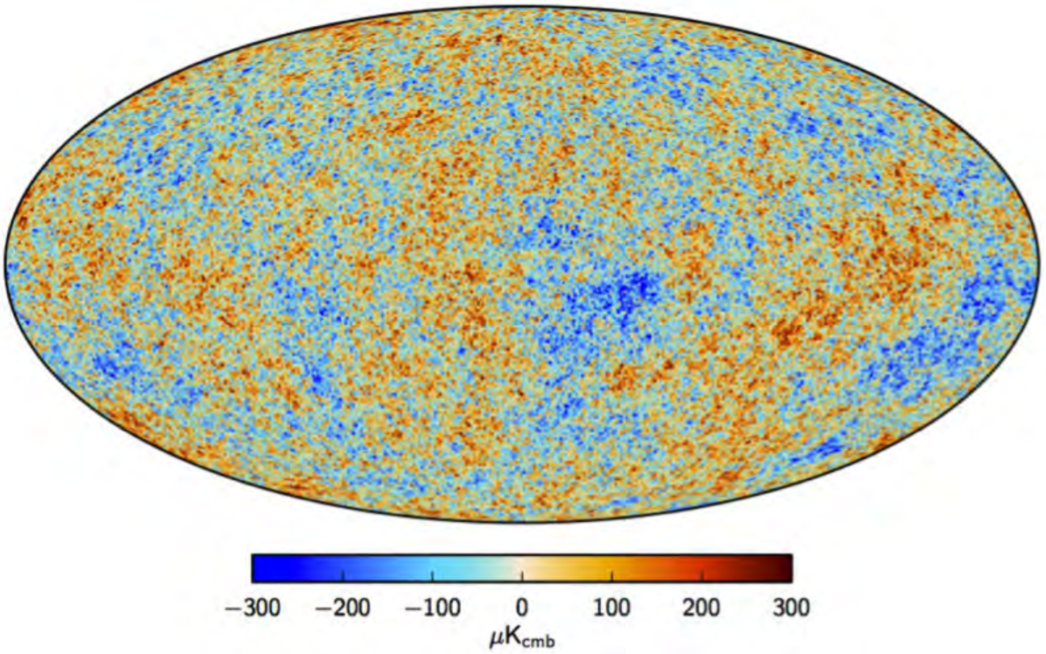

Figure 1.4: CMB map showing temperature fluctuations measured by PLANCK satellite [1].

structure is principally determined by the Baryon Acoustic Oscillations (BAO), which arise because of a tension in the photon-baryon plasma in the early Universe. The BAO are originated as a result of the conflict between the pressure of the photons, which tends to erase anisotropies, and the gravitational attraction of the baryons, which makes them tend to collapse to form dense haloes. These two effects compete to create acoustic oscillations, which generate the characteristic peak structure of the CMB.

The peaks of the CMB anisotropies correspond, roughly, to resonances in which the photons decouple when a particular mode is at its peak amplitude. The angular scale of the first peak determines the curvature of the Universe. The second peak determines the reduced baryon density, while the third peak can be used to get information about the Dark Matter density. In order to extract information from CMB anisotropy maps, a cosmological model with a fixed number of parameters (usually 6 or 7) is assumed. The best-fit parameters are determined from the peak of the N-dimensional likelihood surface. From the analysis of the PLANCK latest data, the composition of the energy density of the Universe, which is given by Equation 1.6, is as follows [10]:

$$\Omega_m = 0.315, \quad \Omega_b = 0.049, \quad \Omega_c = 0.266, \quad \Omega_\Lambda = 0.685, \tag{1.16}$$

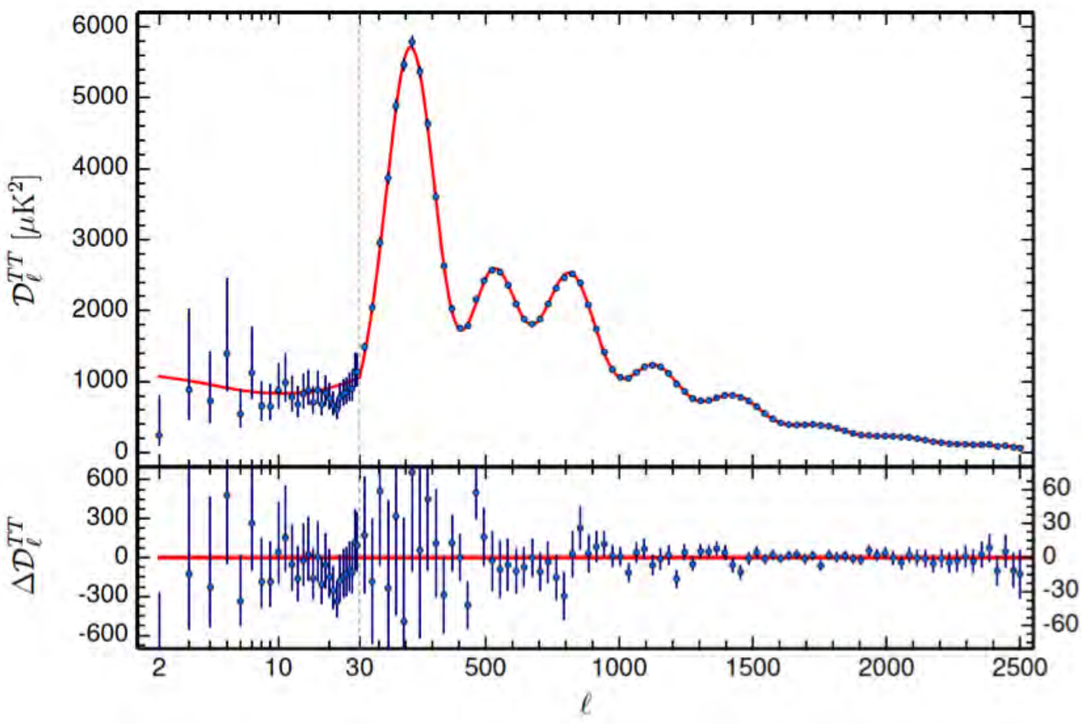

Figure 1.5: CMB temperature power spectrum measured by PLANCK [1].

where Ω_m is the matter component, which includes the contribution from both ordinary matter, Ω_b, and Dark Matter, Ω_c, and Ω_Λ is the Dark Energy component. This composition is usually summarised in a chart as the one presented in Figure 1.6, showing that $\sim$ 95 % of the energy density of the Universe is dominated by both Dark Energy and Dark Matter.

1.1.5 Big Bang nucleosynthesis

The CMB results have to be compared with the values obtained from Big Bang nucleosynthesis (BBN), which predicts the abundances of the light elements, such as deuterium (D), helium (^{3}He, ^{4}He) and lithium (^{7}Li), in the early Universe. These elements were synthesised at the end of the first three minutes of the existence of the Universe and their abundances vary within nine orders of magnitude, from He-4/H ~ 0.08 down to ^{7}Li/H $\sim 10^{-10}$.

The synthesis of the light elements is sensitive to physical conditions in the early radiation-dominated era of the Universe, in which weak interactions were in thermal equilibrium. We can define the interaction rate, the number of collisions per unit of

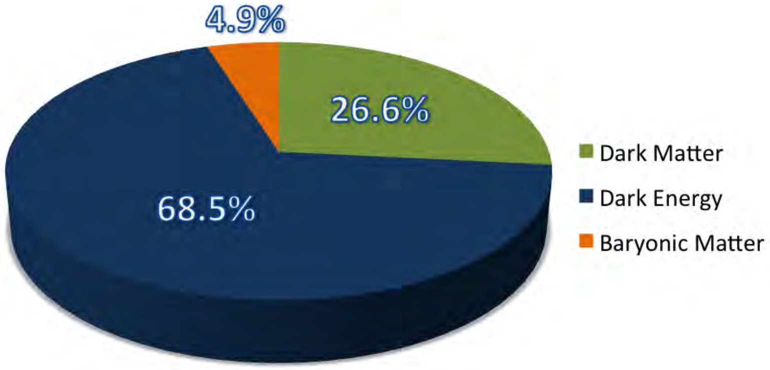

Figure 1.6: Current composition of the Universe from latest PLANCK satellite data [10].

time, as follows [19]:

$$\Gamma_A = n_{eq} < \sigma_A v > \simeq G_F^2 T^5, \tag{1.17}$$

where $n_{eq} \propto T^3$ is the particle density in equilibrium, G_F is the Fermi constant, $G_F \simeq (300 \text{ GeV})^{-2}$, and $< \sigma_A v >$ is the volume that a particle traverses per unit of time. The variation of particle density with time is expressed as

$$\frac{\mathrm{d}n}{\mathrm{d}t} = -3Hn - < \sigma_A v > (n^2 - n_{eq}^2) \tag{1.18}$$

Both the particle interaction rate, $\Gamma_A(T)$, and the expansion rate of the Universe, $H(T)$, depend on the temperature, T. If $\Gamma_A(T) >> H(T)$, particles are coupled to radiation, since the interaction rate is fast enough to maintain thermal equilibrium, so $n = n_{eq}$. However, if $\Gamma_A(T) << H(T)$, which means that the Universe expansion rate is higher than the particle interaction rate, particles are decoupled and n $\propto a^{-3}$, with a the scale factor. Therefore, the departure from chemical equilibrium (freeze-out) is achieved when

$$\Gamma_A(T) \simeq H(T). \tag{1.19}$$

Protons and neutrons were in equilibrium in the early Universe through the reaction:

$$\nu_e + n \to p + e^-, \tag{1.20}$$

fixing the ratio of the neutron and proton number densities to be

$$\frac{n}{p}_{eq} = e^{-Q/T}, \tag{1.21}$$

where Q is given by the neutron-proton mass difference, $Q{=}m_n{-}m_p{=}1.293$ MeV.

According to Equation 1.19 and obtaining $H(T)$ from Friedmann equation (Equation 1.4), the decoupling of protons and neutrons occurred for

$$G_F^2 T_D^5 \simeq \sqrt{\frac{8\pi G}{3} g_*} T_D^2, \tag{1.22}$$

where g_* accounts for the number of relativistic particle species determining the energy density in radiation. Consequently, at temperatures lower than $T_D \sim$0.8 MeV, corresponding to an age of $t \sim 1$ s, the neutron-proton inter-conversion rate per nucleon fell faster than the Hubble expansion rate, leading to the freeze-out. The neutron fraction at this time, $n/p = e^{-Q/T} \simeq 1/6$, is thus sensitive to every known physical interaction, since Q is determined by both strong and electromagnetic interactions while T_D depends on the weak as well as gravitational interactions.

After freeze-out, the neutrons were free to β-decay, so the neutron fraction dropped to $n/p \simeq 1/7$ by the time nuclear reactions began. The rates of these reactions depend on the density of baryons, which is usually expressed normalised to the black body photon density as $\eta \equiv n_b/n_\gamma$. The starting reaction $n+p \rightarrow D+\gamma$ makes D atoms. At that time, $t \sim 1$ s, photodissociation of D is rapid because of the high entropy (low η) and this prevents significant abundances of nuclei until, at $t \sim 100$ s, the temperature has dropped to 0.1 MeV, well below the binding energies of the light nuclei. About 20% of free neutrons decay prior to being incorporated into nuclei. The ^{4}He abundance is then given approximately by assuming that all remaining neutrons are incorporated into ^{4}He [20].

In Figure 1.7 we show the calculated elemental abundances of deuterium (D), helium (^{3}He and ^{4}He, with an abundance represented by Y) and lithium (^{7}Li) as a function of $\eta_{10} = \eta \cdot 10^{10}$. The spread in the curves corresponds to the 2σ uncertainties in nuclear cross sections, as estimated by Monte Carlo methods, while the boxes show the observationally inferred primordial abundances with their associated uncertainties.

While the ranges spanned by the boxes in Figure 1.7 do not all overlap, they are all within a factor ~ 2 of each other. However, there is a discrepancy in the lithium abundance, which corresponds to values that are inconsistent with that of the D/H abundance as well as with the less constraining ^{4}He abundance, giving raise to the so-called "lithium problem". This problem could simply reflect the difficulty in determining the primordial lithium abundance or could hint at a more fundamental omission in the theory. If we exclude the lithium constraint, because its inferred abundance may suffer from systematic uncertainties, then D/H and ^{4}He are in agreement and the concordant range is essentially [21]

$$5.7 \leq \eta_{10} \leq 6.7 \text{ (95\%C.L.)}. \tag{1.23}$$

Despite the lithium problem, considering only well-established microphysics we can extrapolate from $t \sim 1$ s to predict current light element abundances spanning 9

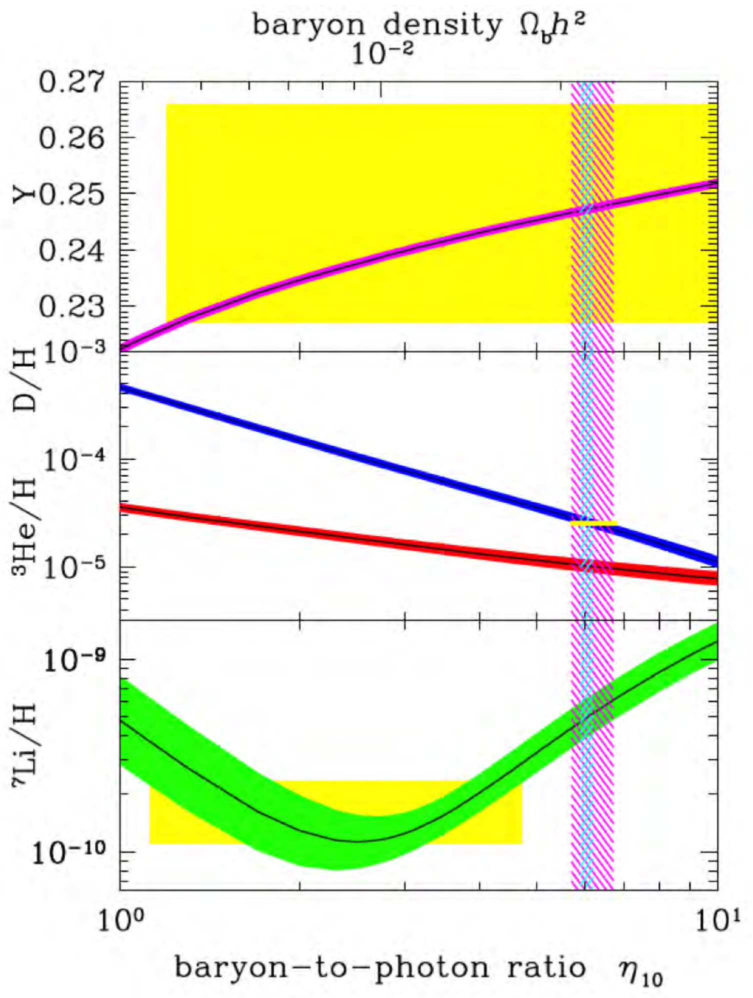

Figure 1.7: The abundances of D, ^{3}He, ^{4}He (Y) and ^{7}Li as predicted by the standard model of BBN (bands show the 95% C.L. range). Boxes indicate the observed light element abundances. The narrow vertical band indicates the CMB measurement of the cosmic baryon density, while the wider band indicates the BBN concordance range (both at 95% C.L. range) [21].

orders of magnitude, in approximate agreement with observation, which represents a major success for the standard cosmology. This concordance provides a measurement of the baryon content:

$$0.046 \leq \Omega_b \leq 0.055 \ (95\%\text{C.L.}). \tag{1.24}$$

In conclusion, the CMB result of the baryon density given in Equation 1.16 is remarkably consistent with the BBN range quoted in Equation 1.24, which constitutes an extremely relevant result that plays a key role in our understanding of the matter budget of the Universe. The first conclusions that can be extracted from this result are the following ones:

1. Since $\Omega_b = 0.049$, baryons represent only $\sim 5\%$ of the Universe energy density.
2. The mass-to-light ratio has been measured to be $M/L = (10-20)M_\odot/L_\odot$ in spiral and elliptical galaxies, while this ratio can increase to $M/L = (200 - 600)M_\odot/L_\odot$ in dwarf galaxies, meaning that most matter in galaxies is optically dark.
3. Given that $\Omega_m = 0.315$, which implies $\Omega_m >> \Omega_b$, we infer that there is much more matter composing the energy density of the universe than the one that simply comes from baryonic matter.

The strong evidences that we have reviewed so far lead us to conclude that most matter in the Universe is not only dark, but also non-baryonic, constituting the so-called Dark Matter.

1.2 Dark Matter candidates

As it has been presented in previous Section, the total amount of baryonic Dark Matter can be inferred from BBN and observations of the CMB. Since the stellar objects that constitute the baryonic contribution to Dark Matter, called MACHOs (Massive Astrophysical Compact Halo Objects), including brown dwarfs, stellar remnants, supermassive and primordial black holes cannot account for the observations, a new kind of non-baryonic elementary particle is considered to be the dominant contribution to the observed Dark Matter.

Let us suppose that this new elementary particle is a stable and neutral weakly interacting massive particle (WIMP), χ, produced during the Big Bang and currently present in the halo surrounding the galaxy. For temperatures of the Universe greater than the particle mass, $T >> m_\chi$, the number density of these particles at equilibrium is $n_\chi \propto T^3$. In this epoch, WIMPs are abundant and rapidly convert into lighter particles and vice versa: $\chi\bar{\chi} \to l\bar{l}$, where $l\bar{l}$ represent quark-antiquark and lepton-antilepton pairs and even gauge or Higgs bosons as well if m_χ is high enough. However, as the Universe evolves, its temperature decreases and after it drops below m_χ, $T << m_\chi$, the equilibrium abundance is exponentially suppressed, $n_\chi \propto e^{-mw/T}$ and the rate for WIMP annihilation, $\Gamma =< \sigma v > n_\chi^2$ with $< \sigma v >$ the thermally average total cross section for annihilation of $\chi\bar{\chi}$ into lighter particles times relative velocity v, drops below the expansion rate of the Universe, $\Gamma \simeq H$. At this point, WIMPs cease to annihilate efficiently, falling out of equilibrium, and naturally freeze-out, remaining a relic cosmological abundance. In Figure 1.8 we show numerical solutions to the Boltzmann equation which determines the WIMP

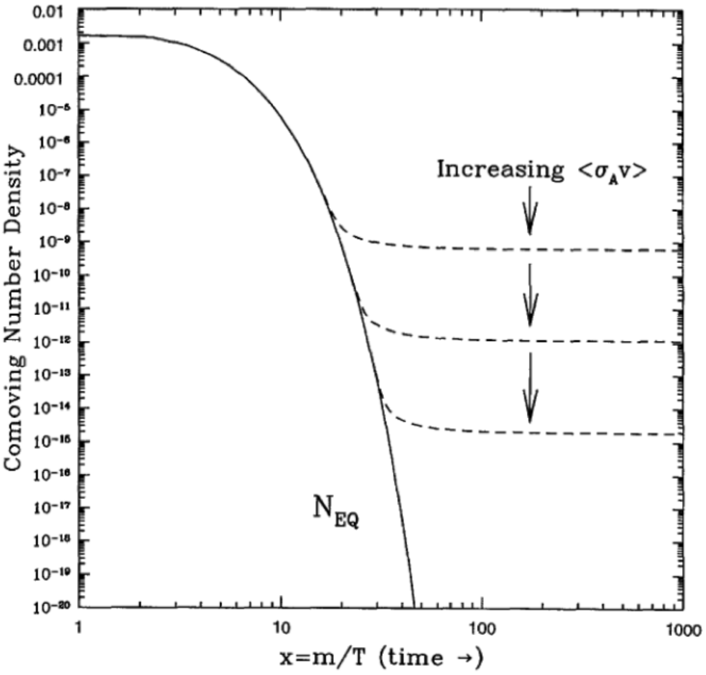

Figure 1.8: Comoving number density of WIMPs in the early Universe. The dashed curves represent the current abundance and the solid curve corresponds to the equilibrium abundance [19].

abundance. The abundances per comoving volume are plotted as a function of $\chi = m_\chi/T$, with the solid line corresponding to the equilibrium abundance while the dashed lines represent current abundances, showing that as the annihilation cross section increases, the WIMPs stay in equilibrium for a longer time and the relic abundance becomes smaller.

An approximate solution to the Boltzmann equation yields the following estimation for the current cosmological abundance of the WIMPs [22]:

$$\Omega_\chi h^2 = \frac{m_\chi n_\chi}{\rho_c} \simeq \frac{3\times 10^{-27}\mathrm{cm}^3\mathrm{s}^{-1}}{<\sigma_A v>} \tag{1.25}$$

with h the Hubble constant in units of 100 km s^{-1} Mpc^{-1} and $\rho_c \simeq 10^{-5}h^2$ GeV cm^{-3} the current critical density, which is the necessary density for the curvature of the Universe to be zero. The result is a first approximation, independent of the WIMP mass, and it is inversely proportional to its annihilation cross section.

If a new stable massive particle with electroweak interactions exists, then its annihilation cross section can be estimated to be:

$$\sigma_{EW} \simeq \frac{\alpha^2}{m_{EW}^2}, \tag{1.26}$$

where $\alpha \simeq O(0.01)$ and $m_{EW} \simeq O(100 \text{ GeV})$. Therefore, in Equation 1.25, $< \sigma_A v > \sim 10^{-25}\text{cm}^3\text{s}^{-1}$, which is remarkably close to the value required to account for the Dark Matter in the Universe. The coincidence with the electroweak cross section suggests that if a new stable massive particle with electroweak interactions exists, then it is a natural Dark Matter candidate.

A major classification of non-baryonic Dark Matter candidates is based on its temperature at the time of galaxy formation [23], so that we can first divide candidates into three types:

1. Hot dark matter (HDM): weakly interacting particles that decoupled from radiation being relativistic. Among the already existing particles, neutrinos would constitute HDM, but they are not massive and abundant enough to account for the main component of Dark Matter.
2. Cold Dark Matter (CDM): weakly interacting particles that were non relativistic at the epoch of galaxy formation, and thus were able to collapse effectively under gravity because of their negligible pressure. Some examples of CDM are neutralinos and axions.
3. Warm Dark Matter (WDM) constitutes an intermediate case between the previous ones. WDM was semi-relativistic at the time of galaxy formation and one of the main examples of WDM is the keV-mass sterile neutrino.

Both the composition and abundance of Dark Matter have influence in the Universe Large Scale Structure (LSS) formation. It is possible to study the growing of fluctuations analytically when these ones are small; but, as they grow in amplitude, it becomes necessary the use computer simulations, as the ones performed by The Center for Cosmological Physics (University of Chicago) [24], whose results are shown in Figure 1.9. In this simulation, cluster formation and growing filaments of LSS are shown for a model that includes CDM and Dark Energy (DE). The considered region in space includes 43 millions of parsecs (140 millions of light years) from redshift, z, equal to 30 to current time ($z = 0$). In the initial time ($z \simeq 30$), shown in Figure 1.9 (top-left), when the age of the Universe was lower than 1% of the current one, the initial fluctuations were small, thus the matter distribution was uniform. However, as time goes by, those fluctuations grow, resulting in a great richness of structures, among which we distinguish galaxies forming filaments that become more and more defined with time, as shown in Figure 1.9.

Therefore, CDM particles, which were non relativistic when they decoupled from radiation in the early Universe, are favoured by observations since they allowed small groups of matter join to form larger structures (bottom to top structure formation). On the contrary, HDM, which would be relativistic at the beginning of structure formation, would have prevented the formation of high density regions (galaxies) due to the free-streaming and only large structures may be formed at early epochs. In this case, the structure formation would be hierarchical from top to bottom,

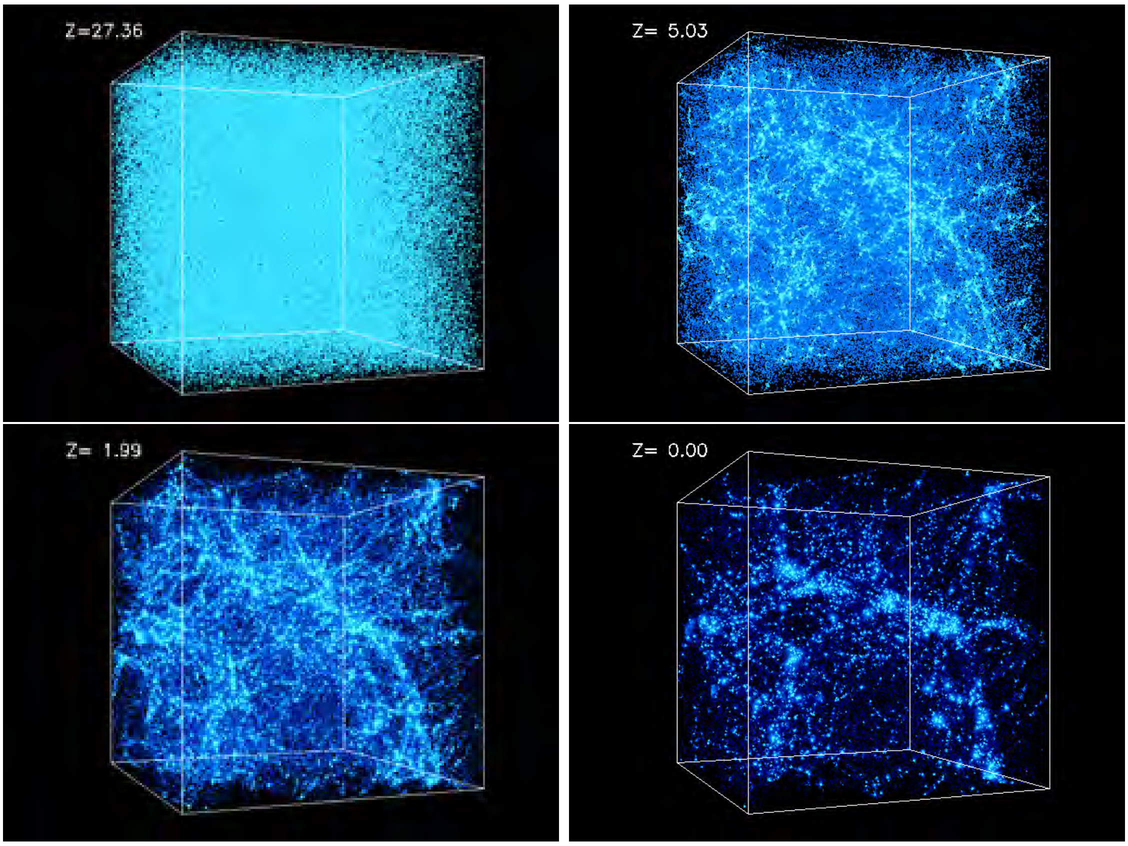

Figure 1.9: Simulation of the evolution of LSS of the universe from $z \simeq 30$ to current time ($z = 0$), showing the growth of fluctuations and the formation of filament structure with decreasing z [24].

since large structures lead to smaller ones by fragmentation, which is extremely disfavoured by observations.

Despite the fact that the so-called Standard Model (SM) of particles does not provide any suitable candidates for Dark Matter, a wide array of non-baryonic particle candidates arising naturally in theoretical extensions of the SM have been discussed in the literature, and most of them are currently being searched with a great variety of experimental strategies. In order to distinguish among the different candidates, we can establish some requirements, based on the already presented astrophysical and cosmological observations, that a particle has to fulfil to be a suitable Dark Matter candidate:

1. It has to be stable enough in order to be present in the actual Universe.
2. It has to be CDM in order to explain the current hierarchical LSS of the Universe.
3. It has to be optically dark. Dark Matter does not emit light, thus a good

particle candidate should be electrically neutral and interact weakly with ordinary matter. An important consequence of these properties is that Dark Matter cannot cool down by radiating photons.

4. It must be massive enough to account for the measured Ω_m.

In general, particles satisfying the previous constraints are known as WIMPs (Weakly Interacting Massive Particles). Throughout the following sections we will briefly review some of the most studied Dark Matter candidates and we will analyse whether or not they satisfy the requirements exposed above.

1.2.1 Neutrinos

Neutrinos, which are present in nature in three known flavours (the electron neutrino ν_e, the muon neutrino ν_μ and the tau neutrino ν_τ), are particles that interact weakly with other types of matter, a requirement for a good Dark Matter candidate. Due to the observation of neutrino flavour oscillations, we know that neutrinos do have a mass since the probability of conversion from one flavour to another one oscillates in time with a frequency proportional to difference of squares of neutrino masses.

The neutrino was a favoured particle Dark Matter candidate in the period starting in the end of the 1970s, with the advantage of being known to exist. However, there are restrictive observational limits from cosmology on the value allowed for the sum of the neutrino masses. In particular, from recent PLANCK satellite results $\sum_i m_{\nu i} < 0.23$ eV [10], which gives a contribution to the Dark Matter density of:

$$\Omega_\nu < 0.005. \tag{1.27}$$

Since this result is much lower than the Dark Matter density reported previously, $\Omega_c = 0.266$, light neutrinos cannot be the main contribution to Dark Matter. Besides, neutrinos would be hot Dark Matter, while a good candidate should fulfil the requirements of cold Dark Matter.

Although the properties of the three known types of neutrino are not quite right for Dark Matter, a hypothetical fourth type, called the sterile neutrino, which would interact even more weakly than the other three types, could be, in principle, a suitable Dark Matter candidate. Sterile Neutrinos, which were proposed as WDM candidates by Dodelson and Widrow in 1993, are spin-1/2 SU(2)-singlet particles similar to standard SU(2)-doublet (active) neutrinos, but much heavier and they interact only gravitationally with ordinary matter, apart from a small mixing with ordinary neutrinos. If, like the known flavours, the sterile neutrino also exists as a mixture of different masses, it would lead to mixing of neutrinos from known flavours to the sterile flavour, thus giving proof of its existence in the form of disappearance of neutrinos of known flavours.

Reactor and short-baseline neutrino oscillation experiments have suggested the possible existence of one or two sterile neutrinos with mass splittings relative to the active flavours of the order of $\Delta m^2 \sim 1\mathrm{eV}^2$ and fairly large mixing parameters. In the early Universe, flavour oscillations would bring these sterile states into thermal equilibrium before neutrino decoupling at T $\sim$ 1 MeV, thus increasing the relativistic energy density in the form [25]:

$$\rho_r = \frac{\pi^2}{15} T_\gamma^4 \quad 1 + (3.046 + \Delta N_{eff})\frac{7}{8} \quad \frac{4}{11} \quad ^{4/3} \quad , \tag{1.28}$$

where T_γ is the CMB temperature and $N_{eff} \equiv (3.046 + \Delta N_{eff})$ is the effective number of relativistic neutrino degrees of freedom, with $\Delta N_{eff} = 1$ for each additional species, considering thermalisation in the early Universe. The presence of a non-zero ΔN_{eff} due to sterile neutrinos would modify the cosmic expansion rate and affect the BBN of light elements, the CMB anisotropies and the formation of LSS. However, according to latest PLANCK results [10], the combined constraints in the single massive sterile model are

$$N_{eff} < 3.7, \quad m_{\nu,sterile}^{eff} < 0.38 \text{ eV}. \tag{1.29}$$

which implies that $N_{eff} = 4$ is excluded at 99% of confidence level (C.L.), thus showing no evidence for a deviation from the base ΛCDM cosmological model.

1.2.2 Axions

Another hypothesis for a Dark Matter candidate comes from axions, with the advantage of having been proposed to solve a problem completely unrelated to Dark Matter. They were introduced in the 1970s by Peccei and Quinn to solve the so-called CP violation problem in Quantum Chromodynamics (QCD) by introducing a global symmetry, $U(1)_{PQ}$, which is spontaneously broken. The Goldstone boson of this broken global symmetry is the axion, however it gets a non-zero mass from the QCD anomaly, which can be interpreted as a mixing of the axion field with the π and η mesons.

The phenomenology of the axion is determined by the scale of symmetry breaking, f_a. In particular, the mass is given by [26]

$$m_a = 0.62 \text{ eV}\frac{10^7 \text{ GeV}}{f_a}. \tag{1.30}$$

The two main mechanisms for non-thermal axion production are vacuum alignment and emission from cosmic strings. In the vacuum alignment mechanism, a potential is generated for the axion field at the chiral symmetry breaking; and the axion field, which can in principle be at any point in this potential, starts moving towards the minimum of the potential and then oscillates around it. From the Quantum Mechanics point of view, the field oscillations correspond to the generation of axion particles. In the other main non-thermal mechanism for axion production, axions are emitted in the decay of cosmic strings. In both cases, axions are produced with small momentum, << keV, and thus they are CDM [23].

The experimentally important coupling to two photons is due to the effective Lagrangian term:

$$\mathcal{L}_{a\gamma\gamma} = g_{a\gamma\gamma}(\vec{E} \cdot \vec{B})a. \tag{1.31}$$

where $g_{a\gamma\gamma} = g_\gamma \alpha_{EM}/\pi f_a$ is the axion-photon coupling strength, with g_γ a model-dependent parameter of order unity, $\vec{E}$ is the electric field, $\vec{B}$ is the magnetic field and a is the axion field. The coupling in Equation 1.31 implies that resonant conversion between a galactic axion and two photons may take place in the presence of a strong magnetic field, thus searches for axions as galactic Dark Matter rely on the coupling of axions to photons. An incoming galactic axion passing through the magnetic field of a resonant cavity can convert into photons with enhanced probability when an electromagnetic resonance in the cavity is tuned to correspond to the frequency of the photons produced. Therefore, Dark Matter axions would be detected as an excess power at this frequency [27]:

$$P = \frac{2\pi\hbar^2 g_{a\gamma\gamma}^2 \rho_{DM}}{m_\alpha^2 c} f_\gamma \frac{1}{\mu_0} B^2 V_{nlm} Q, \tag{1.32}$$

where m_a denotes the axion mass, f_γ the frequency of the converted photon and ρ_{DM} the Dark Matter density in the local halo. The enhancement in the expected axion power due to its conversion in a resonant cavity is expressed in terms of the quality factor of the cavity, Q. The effective volume of the cavity for coupling to a given resonant mode, V_{nlm}, is given by:

$$V_{nlm} = \frac{\left(\int \mathrm{d}^3\vec{x}\vec{E}(\vec{x}) \cdot \vec{B}(\vec{x})\right)^2}{B^2 \int \mathrm{d}^3\vec{x}|\vec{E}|^2(\vec{x})}, \tag{1.33}$$

with $\vec{B}(\vec{x})$ the static magnetic field and $\vec{E}$ the electric field of a normal resonant mode denoted by integers n, l, m. Physically, the size of a closed resonator must decrease in order to achieve higher resonant frequencies, decreasing consequently both the volume and Q of the resonator and limiting the sensitivity of experiments based on this architecture.

This procedure has been recently used by different experiments, such as ADMX, to constraint the mass window where axions can be relevant contributors to Dark Matter. The mass range in which axions are suitable candidates for Dark Matter has been gradually more and more constrained, by this type of laboratory searches, stellar cooling and supernova dynamics, to very light masses in the range $\mu\text{eV} \leq m \leq 0.01$ eV [28]. However, axions still remain undetected.

1.2.3 SUSY candidates

Amongst the many Dark Matter candidates proposed, WIMPs occupy a special place, as they arise naturally from well motivated extensions of the SM of particle physics, achieving the currently observed relic abundance in the Universe, as it has been presented previously in this Section.

Although the SM of high-energy physics provides a successful description of presently known phenomena, the huge ratio between the Planck mass and the electroweak (EW) scale, $M_P/M_{EW} \sim 10^{16}$, represents a powerful hint for physics beyond the SM, because of the so-called hierarchy problem. The electrically neutral part of the Standard Model Higgs field is a complex scalar H with a classical potential [29]

$$V = m_H^2|H|^2 + \lambda|H|^2. \tag{1.34}$$

The SM requires a non-vanishing vacuum expectation value (VEV) for H at the minimum of the potential, which will occur if $\lambda > 0$ and $m_H^2 < 0$, resulting in $< H >= \sqrt{-m_H^2/2\lambda}$. Then, m_H^2 will suffer from enormous quantum corrections from the virtual effects of all particles that couple to the Higgs field.

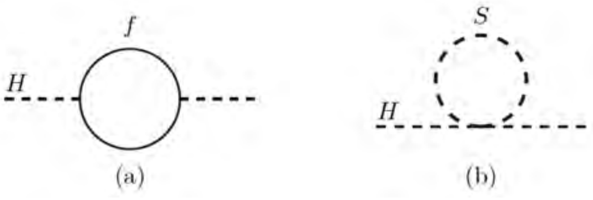

Figure 1.10: One-loop corrections to m_H^2 due to (a) a Dirac fermion, f, and (b) a scalar, S [29].

Let us consider as an example that we have a correction to m_H^2 due to a Dirac fermion of mass m_f, then the Higgs field couples to f with a term in the Lagrangian $-\lambda H\bar{f}f$. Thus, considering the Feynman diagram from Figure 1.10(a), it yields to a correction

$$\Delta m_H^2 = -\frac{|\lambda_f|^2}{8\pi^2}\Lambda_{UV}^2 + ... \tag{1.35}$$

where Λ_{UV} is an ultraviolet momentum cut-off used to regulate the integral and f can be any of the leptons or quarks of the SM (with a factor 3 accounting for the colour in the case of the quarks). The largest correction comes from the top quark, with $\lambda_f \simeq 1$. Due to the fact that Λ_{UV} is of the order of M_P, there is a quantum correction to m_H^2 which is 30 orders of magnitude larger than the experimental m_H^2. Consequently, since all quarks, leptons and EW gauge bosons $(Z^0, W^{\pm})$ acquire masses from their interaction with the Higgs boson, the entire mass spectrum of the SM is sensitive to the cut-off given by Λ_{UV}.

Furthermore, there are contributions similar to the one written on Equation 1.35 coming from any arbitrarily heavy particles that might exist. As an example, let us suppose there exists a heavy complex scalar particle S with mass m_S that couples to the Higgs with a Lagrangian term $-\lambda|H|^2|S|^2$. Then, the correction to m_H^2 given by the Feyman diagram depicted in Figure 1.10(b) would be

$$\Delta m_H^2 = \frac{\lambda_S}{16\pi^2}[\Lambda_{UV}^2 - 2m_S^2 \mathrm{ln}(\Lambda_{UV}/m_S) + ...]. \tag{1.36}$$

Expression 1.36 shows that m_H^2 is sensitive to the heaviest particles that H couples to. Even if there is no direct coupling between the SM Higgs and the particle S, the effects of M_S on the SM do not decouple and make difficult to understand the fact that m_H^2 is so small, specially if m_S is very large.

Assuming that the Higgs boson is a fundamental particle, a cancellation is thus needed between the contributions to m_H^2 in the form of a symmetry. The comparison of Equations 1.35 and 1.36 strongly suggests that the required symmetry relates bosons and fermions because of the relative minus sign that differences fermion and boson loop contributions to m_H^2. In the case of having two complex scalars with $\lambda_S = |\lambda_f|^2$ for each SM quark and lepton, the contributions of the diagrams shown in Figure 1.10(a) and (b) will cancel. Therefore, if this type of symmetry relating fermions and bosons, called Supersymmetry (SUSY), exists, the cancellation of the mentioned terms is not only possible but also unavoidable. For this reason, SUSY is one of the most studied extensions of the SM; and it also provides several suitable Dark Matter candidates.

The generators of SUSY, Q_α, are fermionic operators and, consequently, they transform bosons into fermions. As a result, for each bosonic state of non-zero energy, there is a fermionic state with the same energy and vice versa.

$$\begin{aligned} Q_\alpha|\mathrm{boson}\rangle &= |\mathrm{fermion}\rangle, \\ Q_\alpha|\mathrm{fermion}\rangle &= |\mathrm{boson}\rangle. \end{aligned} \tag{1.37}$$

Therefore, this theory postulates that each SM particle has a superpartner (sparticle), with R-parity= 1 for standard particles and R-parity= -1 for SUSY particles, where R-parity is a symmetry that forbids couplings which do not conserve baryon and lepton numbers. R-parity can be defined as [30]:

$$R = (-1)^{3B+L+2s} \tag{1.38}$$

where B, L, and s are the baryon number, lepton number, and spin respectively. The additive conservation of the quantum numbers B, L, and s means that R-parity must be conserved multiplicatively, which implies different relevant consequences, namely:

1. The collisions of conventional particles must always produce supersymmetric particles in pairs.
2. Heavier supersymmetric particles can decay only into lighter supersymmetric particles.
3. The lightest $R = -1$ state or lightest supersymmetric particle (LSP), must be stable, because it has not allowed decay mode, and can only disappear via pair annihilation.

This fact converts SUSY in an extremely interesting theory from the astrophysical and cosmological points of view, as the LSP naturally becomes a viable Dark Matter candidate.

The LSP candidate that is most often considered is the lightest neutralino. According to the Minimal Supersymmetric Standard Model (MSSM), which contains the smallest possible field content necessary to give rise to all the fields of the SM, there are four neutralinos, each of them being a linear combination of several $R = -1$ neutral fermions. These fermions are the superpartners of the B and W_3 gauge bosons, which are called bino and wino, and two higgsinos (H_1^0 and H_2^0), the supersymmetric partners of the neutral components of the two Higgs doublets, leading to the following linear combination of fields:

$$\chi = N_{11}\tilde{B} + N_{12}\tilde{W}_3 + N_{13}\tilde{H}_1^0 + N_{14}\tilde{H}_2^0. \tag{1.39}$$

This particle fulfils all the conditions for being an appropriate Dark Matter candidate. Its mass can range from about 50 GeV to a few TeV; and its interaction cross sections with ordinary matter and with itself are such that it can account for all the Dark Matter in the Universe while remaining consistent with all known experiments.

1.3 Dark Matter detection

In order to determine the nature of Dark Matter and discriminate among the large number of candidates and models, a great experimental effort is currently being undertaken. Essentially, there are two different approaches to detect Dark Matter: direct detection and indirect detection. In direct detection experiments, the detection of WIMPs from the galactic halo is made via elastic scattering off ordinary target nuclei. Direct detection experiments, such as Argon Dark Matter (ArDM), usually operate underground in order to be able to distinguish a possible signal due to WIMP particles from the overwhelming background contribution. Differently from direct search experiments, indirect WIMP search is based on the detection of the Dark Matter annihilation or decay in gamma rays or in cosmic rays (detection of antimatter). In addition, WIMPs could be also produced at high energy colliders, such as the Large Hadron Collider (LHC), which has restarted operations recently, and it is expected to find, or to severely constrain, the most studied extensions of the SM, including SUSY.

In the present Section the indirect and direct detection techniques and the principles of different Dark Matter search strategies will be described in detail. In the same framework, the latest and most relevant results in each field will be presented, together with future experimental prospects.

1.3.1 Indirect detection experiments

Indirect detection consists of the search for the WIMP-pair annihilation products, such as gamma rays, positrons, antiprotons, antinuclei and neutrinos [31]. These particles can be detected by space-based detectors (PAMELA, Fermi-LAT, AMS), Cherenkov telescopes (MAGIC, H.E.S.S.) or by neutrino experiments, located underground (Super-Kamiokande), underwater (ANTARES) or under-ice (IceCube).

The Dark Matter annihilation rate scales as n_W^2 because the process requires two WIMPs, thus it would be enhanced in regions where WIMPs can be slowed down and accumulate due to gravitational capture, such as the centre of the Sun, the centre of galaxies, galactic halos or dwarf galaxies. Furthermore, due to the cold nature of Dark Matter, the available energy in the annihilation process is essentially the WIMP rest mass. Therefore, we can search indirectly for Dark Matter by looking for an excess of photons, anti-matter or neutrinos in astrophysical data at energies between 1 GeV and 10 TeV. However, obtaining clear evidence for Dark Matter from astrophysical observations has proven to be a difficult task, since there are different possible explanations for this kind of excesses, such as pulsar emission or cosmic rays interacting with giant molecular clouds [18]. At the same time, the detection of an excess in the positron fraction, $e^+/(e^+ + e^-)$, can constitute a quite clear evidence for Dark Matter since it has a unique signature, with a complete different behaviour than the one expected from ordinary cosmic ray collisions, which result in the positron fraction decreasing steadily with energy.

PAMELA [32], one of the satellites studying cosmic rays has recently published results on measurements of the positron energy spectrum, in the energy range between 500 MeV and few hundred GeV, and the positron fraction [33]. These measurements have revealed a positron excess over the predictions, which suggests that a source of high energy positrons exists. This rise has been confirmed by other experiments, such as Fermi-LAT and AMS. Fermi-LAT has measured the positron and electron spectra separately between 20 and 200 GeV, using a novel separation technique which exploits the charge dependent displacement of the Earth shadow due to the geomagnetic field [34]. The results are consistent with the increase in the positron fraction reported by PAMELA [35].

Latest precision measurements by AMS of the primary cosmic-ray electron flux in the range 0.5 to 700 GeV and the positron flux in the range 0.5 to 500 GeV were presented in [36]. As it is shown in Figure 1.11 (left), the rate of change between 20 and 200 GeV of the positron flux is much higher than that for electrons, which constitutes an important proof that the excess seen in the positron fraction is due to a relative excess of high-energy positrons, and not to the loss of high-energy electrons. These results can be compared with the ones obtained by different experiments by plotting the combined flux of electrons plus positrons as presented in Figure 1.11 (right), showing a clear improvement in the precision, which reduces the errors, for the whole measurement range.

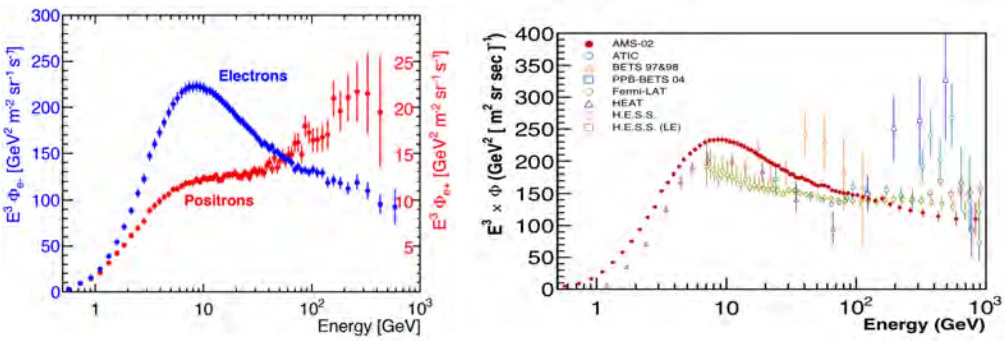

Figure 1.11: (Left) Difference between the electron flux (blue dots, left scale) and the positron flux (red dots, right scale) from AMS. (Right) Combined flux of electrons plus positrons measured by AMS together with the results from earlier experiments [37].

The distribution of the electron and positron in the energy range of 0.5 to 500 GeV shows a well-measured increase of positrons from 8 GeV with no preferred incoming direction in space. The energy at which the positron fraction ceases to increase has been measured to be 275 ± 32 GeV [38]. This slight decrease after the cut-off energy could indicate that the excess of positrons is the signature of Dark Matter particles of mass on the order of 1 TeV annihilating into pairs of electrons and positrons.

Cherenkov telescopes, such as MAGIC, H.E.S.S. or VERITAS, detect showers of secondary particles produced by the interaction of incident high energy gamma rays high up in the atmosphere. The images obtained with the telescopes show the track of the air shower, which points back to the astrophysical object where the incident gamma ray was originated. The intensity of the image is related to the energy of the gamma ray and its shape can be used to reject unwanted background, such as showers induced by cosmic ray particles.

The latest result from MAGIC constitutes one of the most stringent current constraints to the annihilation cross section obtained from observations of satellite galaxies, for masses above few hundred GeV. In particular, the strongest limit (95%

C.L.) corresponds to a ∼500 GeV Dark Matter particle annihilating into $\tau^+\tau^-$ with $< \sigma_{ann} v >= 1.2 \times 10^{-24}$ cm$^3 \cdot$ s^{-1} [39].

During the last years, another Cherenkov telescope, H.E.S.S., has observed five dwarf galaxies for more than 140 hours in total, searching for TeV gamma-ray emission from annihilation of Dark Matter particles. In the absence of a signal, H.E.S.S. put new constraints on the annihilation cross section of WIMPs, achieving the best constraint at 1-2 TeV WIMP masses with a cross section upper bound of $< \sigma_{ann} v >= 3.9 \times 10^{-24}$ cm$^3 \cdot$ s^{-1} at 95% C.L [40].

Another strategy consists of the observation of high energetic neutrinos produced by annihilation of WIMPs in the nuclear reactions in the centre of the Sun. Since neutrinos coming from the Sun have energies that are typically in the MeV range, the observation of 10^2 - 10^4 GeV neutrinos would require an explanation in terms of new physics, which could be provided by the process of capture and annihilation of Dark Matter particles in the Sun. Following this approach, Super-Kamiokande, a large water Cherenkov detector ($5 \cdot 10^4$ tons of ultra pure water) installed underground in Japan, has set one of the best current upper limits on WIMP annihilation cross sections after $\sim$ 3903 days of data taking without any significant excess over the expected atmospheric-neutrino background. The limit on the spin-dependent WIMP-proton cross section for WIMP masses below 200 GeV was set to 1.49×10^{-39} cm^2 at 10 GeV for the $\chi\chi \rightarrow b\bar{b}$ annihilation channel and to 1.31×10^{-40} cm^2 for $\chi\chi \rightarrow \tau^+\tau^-$ [41]. Furthermore, some fraction of WIMP candidates with spin-independent coupling in the few-GeV mass range were ruled out.

IceCube, the largest neutrino detector in the world, encompassing a cubic kilometre of ice at the South Pole, has recently used a multipole expansion technique to analyse a high-purity muon neutrino sample from the Northern Hemisphere. The result on Dark Matter self-annihilation cross section limits is $< \sigma_{ann} v >= 1.9 \times 10^{-23}$ cm$^3 \cdot$ s^{-1} for a Dark Matter particle mass from 700 GeV to 1 TeV and direct annihilation into $\nu\bar{\nu}$ [42].

1.3.2 Accelerators

Accelerators constitute a different approach to the Dark Matter issue. The significant difference from the detection processes and experiments described in the previous section lies in the fact that WIMPs would not be detected but produced as decay products in particle collisions. Since WIMPs are electrically neutral and can have only weak interactions, the commonly-expected signature of Dark Matter particle production at colliders is transverse missing energy, E_T^{miss}, carried away by undetected WIMPs. Therefore, events with an energetic jet and large missing transverse momentum in the final state, usually referred as monojet-like events, constitute a clean and distinctive signature in searches for new physics beyond the SM, such as SUSY, at colliders.

The interaction of WIMPs with SM particles is described, using an effective field theory (EFT) approach, as a contact interaction mediated by a single new heavy particle or particles with mass too large to be produced directly at current accelerators. As it is shown in Figure 1.12 (a), a pair of WIMPs is produced by a contact interaction associated with a jet from a initial state radiation of a gluon. It is assumed here that the DM particle is either a Dirac fermion or a scalar χ, taking into account that the only difference for Majorana fermions is that certain interactions are not allowed and that the cross sections for the allowed interactions are larger by a factor of four. The interaction operators describe different bilinear quark couplings to WIMPs, $q\bar{q} \to \chi\bar{\chi}$, or coupling to gluons, $gg \to \chi\bar{\chi}$, thus Dirac fermions and scalars fall into several categories with characteristic E_T^{miss} spectral shapes. Within this framework, interactions between SM and DM particles are described by only two parameters: the suppression scale $M_\star$ and the DM particle mass m_χ. Apart from the EFT operators, the pair production of WIMPs is also investigated within a simplified model, shown in Figure 1.12 (b), where a pair of WIMPs couples to a pair of quarks explicitly via a new mediator particle, a vector boson Z' [43].

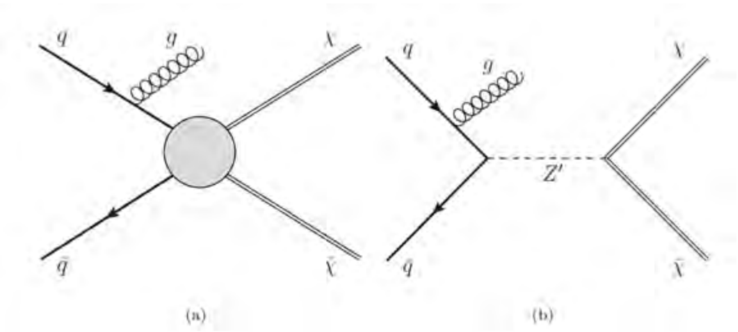

Figure 1.12: Feynman diagrams for the production of WIMP pairs, $\chi\bar{\chi}$, associated with a jet from initial-state radiation of a gluon, g in the case of: (a) a contact interaction described with effective operators and (b) a simplified model with a Z' vector boson as mediator [43].

One of the biggest and most important present accelerators, the LHC, built at CERN, the particle physics research centre near Geneva (Switzerland), has been designed to extend the frontiers of particle physics with its unprecedented high energy and luminosity. In fact, the high interaction rates, particle multiplicities and energies, as well as the requirements for precision measurements achieved by LHC have set new standards for the design of particle detectors. Inside LHC, bunches of up to $\sim 10^{11}$ protons (p) collide 40 million times per second to provide 13 TeV proton-proton collisions at a design luminosity of 10^{34} cm^{-2}s^{-1}. In addition, LHC collides heavy ions (A), in particular lead nuclei, at 5.5 TeV per nucleon pair. Two general purpose detectors from LHC, ATLAS (A Toroidal LHC ApparatuS) [44] and CMS (Compact Muon Solenoid) [45], which have been built for probing $p-p$ and $A-A$ collisions, include the search for Dark Matter as one of the highest priorities in their scientific program.

ATLAS results of a search for new phenomena in final states with an energetic jet and large missing transverse momentum have been recently published. The search uses 20.3 fb^{-1} of $\sqrt{s} = 8$ TeV data collected in 2012 with the ATLAS detector, requiring at least one jet with $p_T > 120$ GeV and no leptons for the event selection. Nine signal regions are considered with increasing missing transverse momentum requirements between $E_T^{\text{miss}} > 150$ GeV and $E_T^{\text{miss}} > 700$ GeV, achieving a good agreement between the number of events in data and SM expectations [43].

Latest CMS results have been also presented from a search for new physics in final states containing a photon and missing transverse momentum. The data correspond to an integrated luminosity of 19.6 fb^{-1} collected in $p-p$ collisions at $\sqrt{s} = 8$ TeV, with no observed deviation from the SM predictions for the final states [46].

In spite of the fact that the cited measurements performed at LHC have put some constraints on theoretical parameters, they have not provided any hint about Dark Matter nature due to the lack of signals. However, LHC, which restarted operation in April 2015 after a major upgrading procedure, is currently running at 13 TeV in the centre of mass. It is expected that this new run will allow to test the existence of new particles at the TeV scale, where, according to predictions of different theories, signs of new physics should appear. In fact, there are large portions of the Supersymmetric parameter space within the reach of the LHC, and, if it exists, there are chances to discover it within next years. However, even if SUSY is discovered, and the mass spectrum of new particles is determined with good accuracy, reconstructing the relic density of the neutralino will be challenging. In this sense, particle astrophysics experiments can provide complementary information on the nature of Dark Matter and direct detection searches could represent an effective method to reduce degeneracies in the parameter space of new theories, when reasonable assumptions are made on the distribution of Dark Matter particles in the Milky Way.

1.3.3 Direct detection experiments

In direct Dark Matter searches, the detection of WIMPs from the galactic halo is made via elastic scattering off ordinary target nuclei. Since WIMPs do not interact electromagnetically, it is expected that they will recoil elastically on the nuclei, giving rise to nuclear recoils. On the contrary, betas and gammas, one of the main sources of background, will interact with the electrons of the target atoms, producing the so-called electron recoils.

The kinematics of the WIMP-nucleus elastic scattering process depend on the initial WIMP incident energy, the mass of the WIMP, the mass of the target nucleus and the scattering angle. Considering that the WIMP velocity is about 220 km/s, the expected recoil energy is very low, of the order of some tens of keV, which makes its detection particularly challenging. In addition, the interaction cross section of WIMPs with nucleons is expected to lie between $\sigma = 10^{-6}$ pb and $\sigma = 10^{-12}$ pb, meaning that these events are extremely rare, which implies that specific requirements are necessary in direct detection searches. Firstly, experiments must have a large mass and a low energy threshold to be sensitive to wide cross section and mass ranges, being able, at the same time, to distinguish a positive signal from background. For this reason, direct detection experiments need to operate in ultra low background conditions that are fulfilled in underground facilities/laboratories, where rock shields detectors from the confounding effects of cosmic rays arriving on Earth's surface. Finally, in order to identify the signals due to Dark Matter particles with respect to background events, an event by event discrimination is also required.

In direct detection, there are three different ways to record the energy of the recoiling nucleus in the target medium: scintillation (photons are produced in the target medium), ionisation, when the target nucleus releases charge along the recoil track, and heat, generated by phonons or lattice vibrations. Differently from the first generation of direct Dark Matter searching experiments, which detected just one of these signals, the new generation is able to detect at least two signals at the same time (like ionisation and scintillation or ionisation and phonon) in order to ensure particle identification and to carry out background discrimination.

Another experimental signature for WIMPs is the annual modulation in the differential WIMP event rate, which is the consequence of the orbit of the Earth around the Sun. The speed of the Earth with respect to the galactic rest frame is a superposition of the motion of Earth around the Sun and the rotation of the Sun around the galactic centre. This speed is maximum in the summer when the component of the orbital velocity vector of the Earth in the direction of solar motion is the largest and minimum in winter, thus the differential WIMP rate presents an annual modulation. This effect can be used to search for Dark Matter [47].

Finally, there is a recently developed technique for direct Dark Matter detection which aims to detect the direction of the recoil from a WIMP-nucleon interaction in the detector medium. A detector located at 45^{o} latitude on Earth will see the Dark Matter wind oscillate in direction over the course of a day. Since the use of a low pressure gas as a target microscopically extends the particle tracks, background rejection then comes from measuring the direction, or head-to-tail effect, of a particle as it passes through the target. If the particle comes from the direction of the WIMP wind, it is identified as Dark Matter candidate, while if it comes from any other direction, it is identified as background [48].

Among the main target materials that have been or are being used in different direct detection experiments we should stress: crystals (DAMA/LIBRA, ANAIS, CDMS, EDELWEISS, CRESST, CoGeNT), liquid noble elements (DEAP, XMASS, ArDM, DarkSide, LUX, XENON100, WARP) and bubble chambers (PICASSO, SIMPLE, COUPP). In the present document we are not going to review all these experiments in detail; instead of that, we will describe their general principles of operation as well as the current status and future prospects of direct Dark Matter searches.

Crystal detectors

One of the most widely extended experimental techniques for direct Dark Matter searches is the use of inorganic crystal scintillators, such as NaI(Tl), CsI(Tl) and CaF_2(Eu).

As it has been mentioned previously, in direct detection it is necessary that the target constitutes an active detector that can measure small energy depositions of few tens of keV due to nuclear recoils, thus crystal scintillators made of target elements that have large cross sections for WIMP interactions are preferred. Some alkali halide crystals with a small concentration of impurity atoms as an activator, such as NaI(Tl) and CsI(Tl), are the most luminescent among the scintillators currently available in large quantities, with the advantage of well established techniques to grow large-sized high-quality crystals of these types. In experiments such as DAMA/LIBRA, NaI crystals, placed inside a sealed copper box flushed with highly pure nitrogen, are used to measure the scintillation signal. In order to reduce the natural environmental background, the copper box is surrounded by a low background multi-ton shield [49].

Another scintillating target material is $CaWO_4$, which is used in CRESST experiment. In this crystal a particle interaction produces mainly heat in the form of phonons. To achieve the milliKelvin temperatures necessary to detect the low energies involved, the detector is mounted in a dilution refrigerator, which can reach temperatures below 10 mK. In the second phase of this experiment, CRESST II, a system based on simultaneous detection of light and heat has been installed, adding to the phonon/heat detector a small calorimeter working as light detector [50].

Ge or Si crystals, such as the ones composing CDMS, also provide two different sets of information about interactions with incident particles: ionisation and phonon signals. On one surface of the detectors, charge-collection plates are installed in order to record the amount of electrical charge displaced within the body of the detector by the incident particle. On the opposite detector surface we find an array of tiny superconducting transition edge sensors (TES), consisting of micro strips of tungsten coupled to aluminium fins, which collect phonon energy from the crystal [51].

Due to the fact that nuclear recoils generate only one-third as much ionisation as electron recoils of equivalent energy, the ratio of charge and phonon signals depends on the class of particle interaction, thus the rejection of background events in these detectors is performed by discriminating between electron and nuclear recoils on an event-by-event basis. Further discrimination against surface electron recoils (which may reduce charge collection) is achieved using the detailed shape of the phonon pulse.

Liquid noble detectors

Liquid noble detectors based on argon or xenon can be designed to operate in single-phase (liquid) or double-phase (liquid-gas). In single-phase detectors, the experimental strategy is based on the use of the self-shielding of the liquid in order to achieve an effectively background-free inner volume. This technique, together with pulse shape discrimination (in the case of argon), constitutes the background rejection strategy in this type of experiments. The light generated by the interaction of WIMPs with target nuclei is detected by an array of photomultipliers (PMTs) installed on the inner detector surface, which allow event position reconstruction from the observed light pattern. Single-phase detectors have the advantage of being much more simple than double-phase ones since there is no need for high-voltage and cathode/anode-grid systems due to the lack of electron drift [52].

An example of single-phase noble liquid detector is XMASS, which aims to directly detect Dark Matter using ~ 1 ton of liquid xenon (LXe) at about -100 °C. It was installed underground in the Kamioka Observatory (Japan) inside a 800-ton water tank in order to reduce radioactive backgrounds. The installation was completed in 2010 and, after the commissioning run, the detector started to take data in 2013. The XMASS collaboration plans to extend the project to a 20-ton multi-purpose detector which will cover not only Dark Matter but also neutrino physics [53].

DEAP-3600 is another single-phase Dark Matter particle search experiment, but it is based on liquid argon (LAr) instead of LXe. The detector, installed 2 km underground in the SNOLAB laboratory in Sudbury, Ontario (Canada), consists of a large spherical volume of LAr (3600 kg of active mass) contained in a transparent acrylic vessel, which is viewed by 255 PMTs. After completing the construction of DEAP-3600 detector, which is prepared for a data taking period of three years, commissioning started in 2014 and first physics data are expected in early 2016. There are also plans for the construction of a future multi-ton experiment, DEAP-50T [54].

In double-phase (liquid-gas) noble detectors, which rely on the time projection chamber (TPC) technique, both ionisation and scintillation signals are detected simultaneously. When a Dark Matter particle interacts within the active volume of the detector, it produces the recoil of a nucleus, which generates electrons and photons from the ionisation and excitation of the surrounding atoms. These photons, which constitute the primary scintillation component (S1), are detected by two arrays of PMTs, one placed in the bottom of the detector, in the liquid phase, and the other one located in the top part of it, in the gas phase. The array immersed in liquid collects most of the S1 component, which is partially reflected at the liquid-gas interface.

The generated electrons are drifted in liquid under the influence of an external electric field and then extracted into gas phase by a stronger field that allows surpassing the liquid-gas potential barrier. The electrons increase their energy thanks to the high electric field applied in gas phase and interact with argon atoms, generating proportional electroluminescence scintillation (component S2), which is mainly detected by the top PMT array. The possibility of detecting both scintillation and ionisation signals provides a powerful tool for particle identification and background discrimination, since the ratio of these two signals is different for nuclear recoils, generated by WIMP or neutron interactions, than for electronic recoils, produced by electrons and gammas. In addition, argon provides pulse shape discrimination thanks to the great difference between the decay times of the two excited states (singlet and triplet), that will be reviewed in more detail within the following Chapters of this document.

Furthermore, thanks to the TPC technique, position reconstruction of the interaction is possible in double-phase noble liquid detectors. Since electron diffusion in liquid nobles is very low, the proportional scintillation photons carry the $x-y$ position information of the interaction, while the z coordinate can be obtained from the drift time measurement of the TPC, allowing a 3D position reconstruction of the interaction. Some examples of double-phase detectors are ArDM, DarkSide, LUX and XENON100.

The present Thesis is based on the results of the ArDM experiment, which is currently under commissioning at the Canfranc Underground Laboratory (LSC). With a ton-scale LAr target for direct WIMP searches, it will be operated as a double-phase TPC with imaging and calorimetric capabilities [55]. The light detection is currently performed by two arrays of 12 borosilicate glass PMTs each, that will be replaced by silicon PMTs in order to reduce internal background contribution and to improve light collection efficiency at the same time. After commissioning, the ArDM detector is expected to start physics run in 2016. The ArDM TPC and experimental setup will be described in detail in Chapter 3.

DarkSide-50, an experiment for direct Dark Matter search, is operating in the underground Laboratori Nazionali del Gran Sasso (LNGS). The detector is a LAr-TPC with a (46.4 ± 0.7) kg active mass, operated inside a 30-ton organic liquid scintillator neutron veto, which is at the same time installed at the centre of a 1 kton water Cherenkov veto for the residual flux of cosmic rays. DarkSide-50 has the current most sensitive Dark Matter search performed with an argon target [56].

The XENON100 Dark Matter experiment is a LXe-TPC designed to search for

WIMP nuclear recoils. The active target of XENON100, which is installed underground at LNGS, contains 62 kg of LXe enclosed in a cylinder that reflects scintillation light and separates it from the outer LXe volume, that works as an active veto of 99 kg, both instrumented with PMTs operating inside the liquid or in xenon gas. The LXe target and veto are contained in a low-radioactivity stainless steel vessel, embedded in a passive radiation shield [57].

The Large Underground Xenon (LUX) experiment is a 370 kg (250 kg) total (active) mass LXe-TPC installed in a water Cherenkov shield at the Sanford Underground Research Facility (SURF) in Lead, South Dakota (USA). The TPC, which is 47 cm in diameter and 48 cm in height, has two arrays of 61 PMTs, one in the liquid and one in the gas region, to detect the S1 and S2 scintillation signals [58]. As it will be explained in the following Sections, LUX has set the best current limit on the spin-independent WIMP-nucleon cross section.

Bubble chambers

An alternative to the already reviewed direct detection experiments is provided by bubble chambers, which are based on superheated fluids. When a particle interacts in a chamber filled with a superheated fluid in a metastable state, an expanding bubble is formed if it deposits energy above a threshold in a small enough radius, while smaller or more diffuse energy depositions result in a bubble that immediately collapses.

In these detectors, instead of relying on discrimination between electron and nuclear recoils to distinguish background events from Dark Matter signals, accurate temperature and pressure operating conditions are chosen in order to become blind to electron recoils. The discrimination against α particles, which can deposit enough energy to form bubbles, is performed making use of acoustic signals. Additional advantages of these detectors include excellent spin-dependent WIMP-nucleon cross section sensitivity and the ability to operate with interchangeable target liquids. One of the drawbacks of this technology is the lack of an energy measurement on a per event basis. Consequently, in order to produce an energy spectrum, these detectors perform threshold scans by varying the operational temperature and pressure. Some examples of detectors using superheated fluids are SIMPLE, PICASSO and COUPP.

SIMPLE experiment operates in the Laboratoire Souterrain à Bas Bruit de Rustrel (LSBB) in Southern France with 0.2 kg active volume of superheated C_2ClF_5 droplets in a gel matrix. The dominant backgrounds are α particles from environmental radon together with neutrons created via U and Th initiated (α,n) reactions in the detector materials. Next phase of SIMPLE will operate a target volume of 1-2 kg, using $C_3F_8CF_3Br$ in addition to the mentioned C_2ClF_5 [59].

PICASSO, operating at SNOLAB, has 32 detector modules and 2.7 kg of the target material C_4F_{10}. This experiment promoted the use of acoustic sensors to reject background α particles, allowing them to achieve good sensitivity to spin-dependent WIMP interactions [60].

COUPP contains 4 kg of superheated fluid (CF_3I) in a single bubble chamber. In this experiment, bubbles are recorded by cameras and the acoustic signal of the nucleated bubbles for α rejection is also recorded. Recording images allows COUPP to have an excellent position reconstruction and identification of multiple scattering background events. Next phase of the experiment will use a 60 kg chamber, also filled with CF_3I [61].

Furthermore, COUPP and PICASSO groups have agreed to collaborate in a single project: a half ton-scale experiment named PICO. This collaboration is currently operating two detectors: a 37 kg bubble chamber filled with the target material CF_3I and a 3 kg chamber filled with C_3F_8 [62]. In addition, a much larger version of the experiment with 500 kg of active mass is in development. It is expected that this joint project will have significant sensitivity to WIMPs over a broad mass range for both spin-dependent and spin-independent scattering contributions.

1.3.4 Exclusion plots

The already described different type of experiments compete to achieve the highest sensitivity and thus establish the lowest possible limit to the WIMP-nucleon cross section. Figure 1.13 illustrates the sensitivity of current and upcoming direct detection experiments in the WIMP-nucleon cross section (cm^2) versus WIMP mass (GeV/c^2) plane. In order to be able to compare results coming from different experiments, the cross section is defined as the probability of a WIMP scattering off a target nucleon (instead of nucleus), which corresponds to a scalar (or spin-independent) coupling. This spin-independent contribution to the cross section dominates over the interaction with the spin of the nucleon, given by an axial (or spin-dependent) coupling. The difference between spin-independent and spin-dependent couplings will be treated in detail in Section 2.1.6.

As it is shown in the plot of Figure 1.13, there is a huge uncertainty (several orders of magnitude) in both WIMP mass and WIMP-nucleon cross section. The characteristic shape of the different curves is determined by the kinematics of the WIMP-nucleon scattering. In particular, the minimum of the curve corresponds approximately to the mass of the target material, which plays a significant role for high values of the WIMP mass; while, for lower WIMP mass values, the most relevant parameter is the energy threshold that can be achieved by the detector. This fact determines the type of experiments dominating the different regions of the WIMP mass range, with small crystal detectors specialised for low WIMP masses and huge liquid noble detectors mainly studying the high WIMP mass range.

Different experiments try to make a discovery and point out the particular cross section-mass region where WIMPs can be found. However, if a experiment cannot

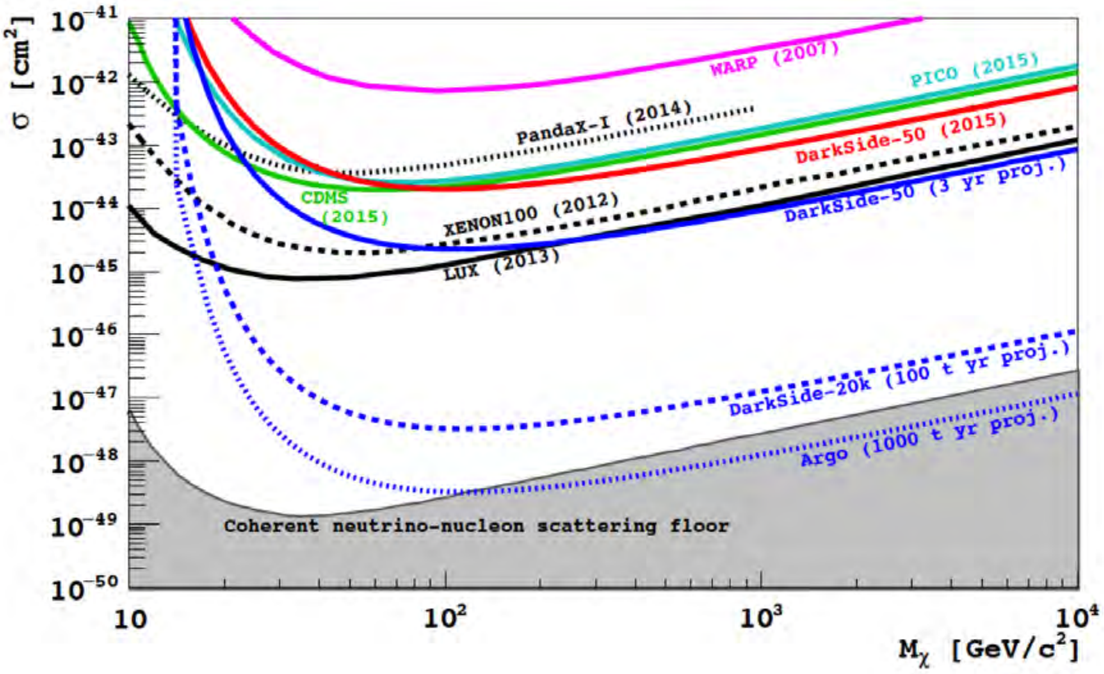

Figure 1.13: Summary of results from direct Dark Matter search experiments in the WIMP-nucleon spin-independent cross section - WIMP mass plane [63, 64]. The current experimental limits are represented together with projected sensitivities for future experiments (DarkSide-20k and Argo) that are expected to operate in the direct detection field over the next years. The grey shaded region is an approximate band in which coherent scattering of solar, atmospheric and supernova neutrinos with nuclei will begin to limit the sensitivity of direct detection experiments.

claim a discovery, exclusion curves can be set, as shown in the plot of Figure 1.13, meaning that above each curve this particular experiment has rejected the existence of WIMPs in that region at a certain confidence level. In this sense, pushing down the achievable limits by becoming more and more sensitive represents a major milestone that requires a great experimental effort. In general, experiments based on noble gases are currently leading direct Dark Matter detection. XENON100 has been the experiment having the most sensitive results in the last years until LUX experiment published their latest results, which improved the sensitivity in a factor 2-5 with respect to already published XENON100 results. As it will be presented in detail in the following Section, dedicated to the current direct Dark Matter search status, there were some claims of detecting WIMP signals from DAMA and later from CoGeNT and CRESST, that were not favoured by theory and not only remained unconfirmed by the other experiments, but also became excluded by many of them. In particular, thanks to the achieved increasing sensitivity and according to the latest results, the existence of low mass WIMPs in this region has been rejected.

A big portion of the parameter space where theoretical models lie will be probed by ton-scale experiments that are currently starting operation or are expected to start operations soon. However, it is worth recalling that neutrinos coherent interactions provide an irreducible background for these searches, therefore limiting the capability to probe very low scattering cross sections.

1.3.5 Direct searches status

During the last few years, the progress made in direct Dark Matter searches has been remarkable, pushing down the sensitivity of direct detection experiments by more than 3 orders of magnitude. Despite the extraordinary technological progress, however, the nature of Dark Matter has not been identified yet.

Some possible positive Dark Matter signals have been suggested during the past years. The first claim came from the DAMA/NaI experiment, located in the Laboratori Nazionali de Gran Sasso (LNGS), Italy, at a depth of approximately 3500 meters water equivalent (mwe). This experiment, with 100 kg array of highly radiopure scintillating NaI(Tl) crystals operated from 1996 to 2002. Data collected by DAMA during two yearly cycles (statistics of 38475 kg×day) were analysed in terms of WIMP annual modulation signature due to the Earth motion around the Sun. The cumulative analysis of all the available data at that time (statistics of 57986 kg×day) favoured the possible presence of a WIMP with $M_W = (52^{+10}_{-8})$ GeV and $\sigma = (7.2^{+0.4}_{-0.9}) \cdot 10^{-6}$ pb at 4 σ C.L., considering standard astrophysical assumptions [65].

The DAMA claim of detecting the annual modulation of the WIMP signal has been widely criticised, since these results are incompatible with results from other experiments. However, the tension in the field increased after the confirmation of the result by the DAMA/LIBRA experiment, an upgrade to an array of 250 kg scintillating NaI crystals which began operation in 2003, on several years and high statistical significance. The cumulative exposure with results previously released by DAMA/NaI and by DAMA/LIBRA already represented 1.17 ton × yr in 2010, corresponding to 13 annual cycles. The data possibly confirmed the model independent evidence of the presence of Dark Matter particles in the galactic halo on the basis of the Dark Matter annual modulation signature (8.9 σ for the cumulative exposure) [66]. Recently, DAMA/LIBRA has released the summary of results obtained with the total cumulative exposure of 1.33 ton × yr, corresponding to 14 annual cycles, that give evidence of Dark Matter annual modulation at 9.3 σ C.L, as shown in Figure 1.14. The modulation amplitude of the single hit events in the (2-6) keV energy interval is (0.0112 ± 0.0012) cpd/kg/keV, the measured phase is (144 ± 7) days and the measured period corresponds to (0.998 ± 0.002) yr; values in agreement with those expected for Dark Matter particles [67].

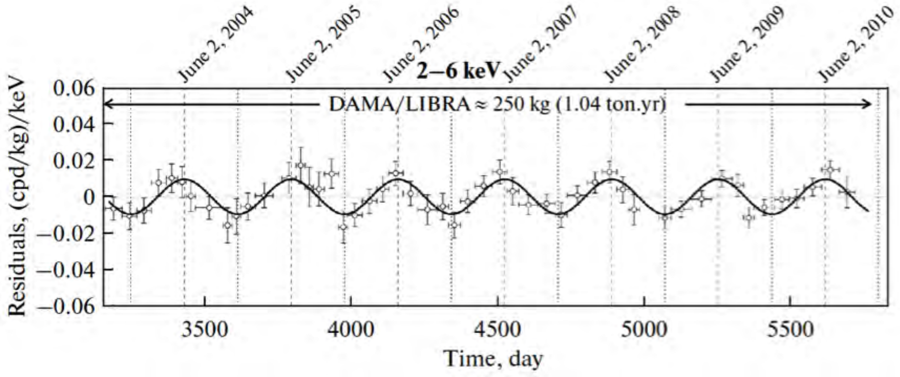

Figure 1.14: Experimental residual rate of the single-hit scintillation events measured by DAMA/LIBRA in the (2-6) keV energy interval as a function of the time. The experimental errors are represented in the data points by vertical bars and the associated time bin width is represented by horizontal bars. The superimposed curves are the cosinusoidal functions that behave as $A\cos\omega(t-t_0)$ with a period $T = 2\pi/\omega = 1$yr, a phase $t_0 = 152.5$ day (June 2nd) and modulation amplitudes, A, equal to the central values obtained by best fit on data points. The dashed vertical lines correspond to the expected maximum for the DM signal (June 2nd), while the dotted vertical lines correspond to the minimum [67].

An independent possible evidence of annual modulation came from CoGeNT experiment, which began collecting data at the Soudan Underground Laboratory in Minnesota (USA) in December 2009. This experiment uses a p-type point-contact germanium detector of mass 440 g, which acts as an ionisation spectrometer, cooled to liquid nitrogen temperatures to detect Dark Matter particles. It collected data from December 4, 2010 to March 6, 2011 when data collection stopped due to a fire in the mine. After data collection resumed again in July 2011, fifteen months of cumulative data were examined for indications of an annual modulation, with statistical significance of 2.8 σ, concluding that available data supported the presence of a modulated component of unknown origin, compatible with a galactic halo composed of light-mass WIMPs [68].

More recent results for 3.4 years of operation show that the previously reported modulation persists, but with a lower statistical significance of 2.2 σ, concentrated in a region of the energy spectrum populated by an exponential excess of unknown origin. Its phase and period agree with phenomenological expectations, but its amplitude is a factor 4-7 larger than predicted for a standard WIMP galactic halo. The possibility of a non-Maxwellian local halo velocity distribution is considered as a plausible explanation of this discrepancy [69]. This interpretation of the results, in the line of DAMA/LIBRA, is in tension with results coming from many other experiments.

Some possible alternative explanations for DAMA/LIBRA and other positive results have been proposed. An alternative source of modulation has been proposed in the form of neutrons, which may be released from material surrounding the detector by a combination of solar neutrinos and atmospheric muons. Despite the fact that the phase of the muon modulation lags 30 days behind the data, adding the modulated neutrino component shifts the phase of the combined signal forward. In addition, it is estimated that neutrinos and muons need 1000 m^3 of scattering material in order to generate enough neutrons to constitute the signal. Considering currently available data, the proposed model gives as good fit to data as Dark Matter does [70]. Additional experimental data supporting these alternatives will be required in order to discriminate among the different possible explanations to the detected annual modulated signal and to lighten the tension in this field.

An illustrative case of the difficulties associated to confirm these evidences comes from CRESST. CRESST-II, consisting of eight $CaWO_4$ crystals instrumented to readout phonon energy and scintillation, completed 730 kg×day of data taking in 2011. In the data analysis, 67 events were found in the acceptance region where a WIMP signal in the form of low energy nuclear recoils would be expected. They concluded, using a maximum likelihood analysis, that background sources alone are not sufficient to explain the data at a significance larger than 4 σ; and they pointed out that the addition of a signal due to scattering of relatively light WIMPs could account for this discrepancy [71]. However, there are more recent results collected in 2013 with an exposure of 29.35 kg×days. A low-threshold analysis of a these data coming from a single upgraded detector module, sets a limit on spin-independent WIMP-nucleon scattering in a region of parameter space for WIMP masses below 3 $\mathrm{GeV/c^2}$, previously not covered in direct detection searches. In this analysis, the possible excess over background discussed previously is not confirmed. Finally,

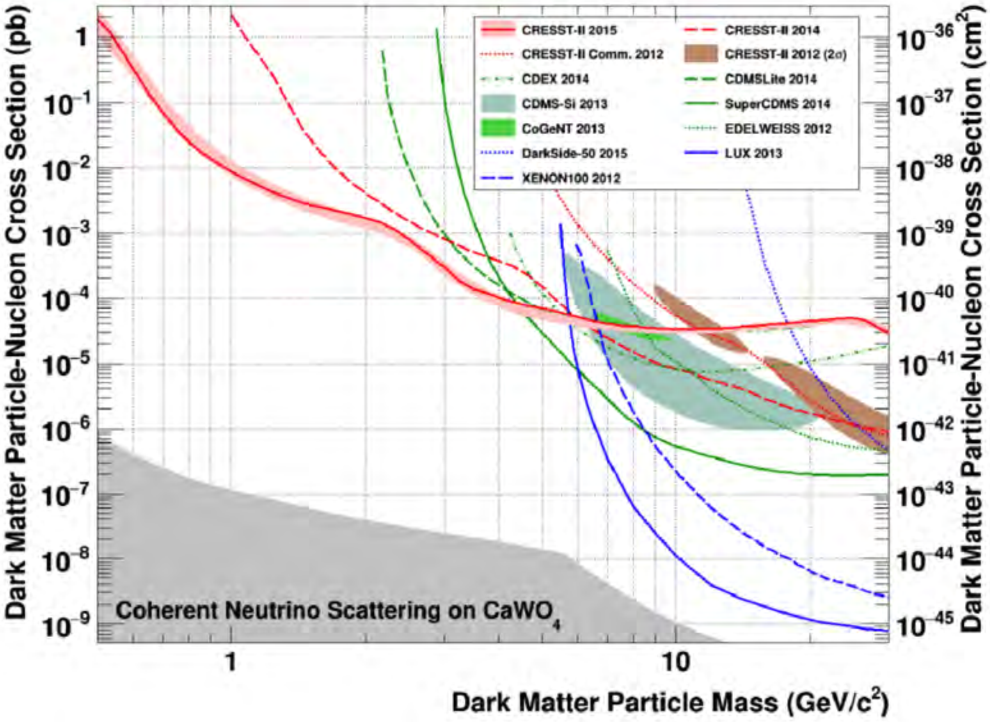

Figure 1.15: Parameter space for elastic spin-independent Dark Matter nucleon scattering. Latest exclusion limit from CRESST-II is drawn in solid red together with the expected sensitivity (1σ C.L.) from the data-driven background-only model (light red band). The remaining red lines correspond to previous CRESST-II limits. For comparison, exclusion limits (90% C.L.) of the liquid noble gas experiments are depicted in blue. In the grey area, coherent neutrino nucleus scattering, dominantly from solar neutrinos, will be an irreducible background for a $CaWO_4$-based Dark Matter search experiment [72].

latest results from data of a single detector module corresponding to 52 kg×day have been used to calculate an upper limit with 90% C.L. on the elastic spin-independent interaction cross section of Dark Matter particles with nucleons, as shown in the plot of Figure 1.15. With an energy threshold for nuclear recoils of 307 eV, CRESST-II substantially enhances the sensitivity for light Dark Matter, demonstrating that the energy threshold is the key parameter in the search for low mass Dark Matter particles [72].

There are many other different experimental results in clear tension with the conclusions that have just been presented, as shown in Figure 1.16. Among them we introduce the cases of CDMS end EDELWEISS.

The CDMS II experiment operated in the Soudan Underground Laboratory from

June 2006 until March 2009. It consisted of 19 Ge and 11 Si detectors that were instrumented to readout the phonon and ionisation energy of an event, thus discrimination between electron and nuclear recoils comes from the ratio of ionisation to phonon energy. Data taken between October 2006 and September 2008 using eight germanium detectors were reanalysed with a low 2 keV recoil energy threshold, providing strong constraints for WIMP masses below 9 GeV/c^2 and excluding parameter space associated with possible low-mass WIMP signals from the DAMA/LIBRA and CoGeNT experiments [73]. In 2013 new results from CDMS II were published revealing three WIMP-candidate events for an exposure equivalent to 23.4 kg $\times$ day, a recoil energy range of 7-100 keV and a WIMP mass of mass 10 GeV/c^2. The probability that the known backgrounds would produce three or more events in the signal region was evaluated to be 5.4% [74].

The EDELWEISS-II experiment took data in the Laboratoire Souterrain de Moudan (LSM), which is located between Italy and France, using ten 400 g ionisation-heat bolometers. These bolometers are Ge crystals instrumented by electrodes and with a small ultra-sensitive rectangular thermometer glued on the lateral side of the crystal. In [75] they report on a search for low-energy ($E < 20$ keV) WIMP-induced nuclear recoils using data collected in 2009-2010 from four Ge detectors. The data indicate no evidence for nuclear recoils that could be attributed to WIMP elastic scattering after an exposure of 113 kg$\times$day. The detection of one event in the WIMP search region results in a 90% C.L. limit of $1.0 \cdot 10^{-5}$ pb on the spin-independent WIMP-nucleon scattering cross section, which excludes great part of the parameter space associated with previous findings reported by CoGeNT, DAMA and CRESST experiments. EDELWEISS-III, with 40 detectors of 800 g with improved performances, is now starting data taking. Several improvements have been made over EDELWEISS-II including a lower detector threshold and higher resolution, paying also special attention to reduce backgrounds (through additional shielding and improved radiopurity in detector components).

Finally, noble liquid detectors, such as XENON100 and LUX, which are currently dominating the field of direct Dark Matter searches, also obtain results that are in clear disagreement with the claims from annual modulation analysis.

After 13 months of data taking during 2011 and 2012, the XENON100 collaboration published their results of 224.6 live days$\times$34 kg exposure, reporting no evidence for Dark Matter interactions. The two candidate events observed in the pre-defined nuclear recoil energy range of 6.6 - 30.5 keV$_{\mathrm{nr}}$ are consistent with the background expectation. From the profile likelihood analysis, the limit on the spin-independent WIMP-nucleon scattering cross section was set for WIMP masses above 8 GeV/c^2, with a minimum of $2 \cdot 10^{-45}$ cm^2 at a 55 GeV/c^2 WIMP mass and 90% C.L. [76] as presented in the plot shown in Figure 1.17 (left).

The LUX experiment, which was cooled and filled in February 2013, has seen no events consistent with Dark Matter in 110 days of data taking. In particular, the

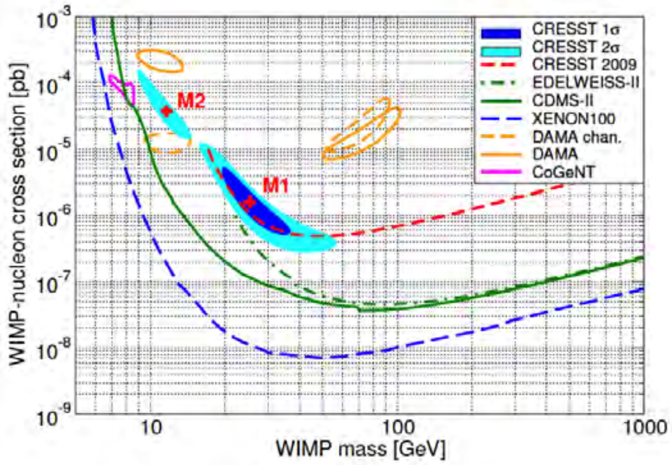

Figure 1.16: WIMP-nucleon cross section represented as function of WIMP mass. Exclusion limits from CDMS-II, EDELWEISS-II and XENON100 in clear disagreement with the 90% confidence regions favoured by CoGeNT and DAMA/LIBRA and the 1 σ and 2 σ CRESST contours are shown together with a exclusion limit previously obtained in an earlier run [75].

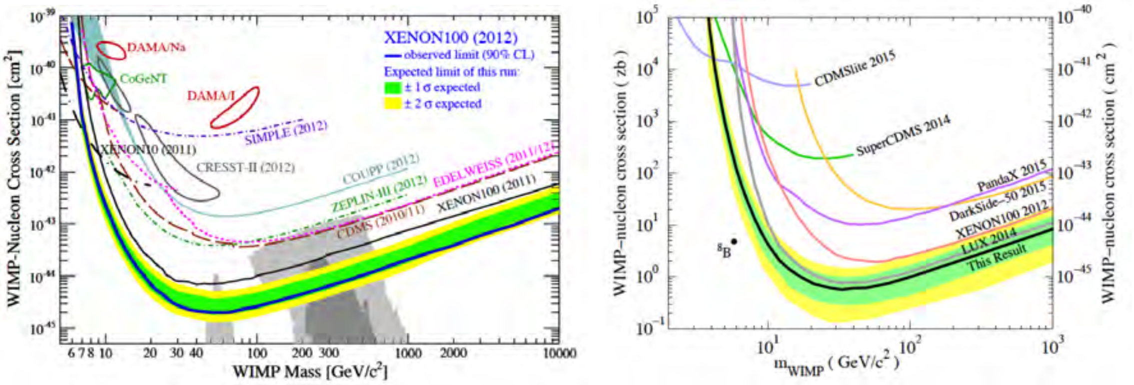

Figure 1.17: (Left) Result on spin-independent WIMP-nucleon scattering cross section from XENON100. The expected sensitivity is shown by the green-yellow band ($1\sigma - 2\sigma$) and the resulting exclusion limit (90% C.L.) in blue, together with other exclusion limits and detection claims coming from different experiments. The shadowed regions in grey represent theoretical predictions from SUSY minimal models [76]. (Right) LUX exclusion limits of $7.6 \cdot 10^{-46}$cm^2 and $6 \cdot 10^{-46}$cm^2 at a WIMP mass of 33 GeV/c^2 depicted in grey and black respectively, which improve previous XENON100 results and represent the current most sensitive WIMP-nucleon cross section limits [77, 78].

LUX collaboration has reported the results of the first WIMP search dataset, taken during the period April-August 2013, presenting the analysis of 85.3 live×days of data with 160 events detected in the 118 kg fiducial volume. A profile likelihood analysis technique shows LUX data to be consistent with background levels of radioactivity from the materials making up the experiment. This result allows to set a 90% C.L. on spin-independent WIMP-nucleon elastic scattering with a minimum upper limit on the cross section of $7.6 \cdot 10^{-46}$ cm^2 at a WIMP mass of 33 GeV/c^2 [77]. Improved WIMP scattering limits from the LUX experiment, including $1.4{\cdot}10^4$ kg×days of search exposure, have been recently released [78]. Under standard Dark Matter halo assumptions and in the mass range above 4 GeV/c^2, these new results give the most stringent direct limits on the spin-independent WIMP-nucleon cross section. The 90% C.L. upper limit has a minimum of 0.6 zb ($6 \cdot 10^{-46}$ cm^2) at 33 GeV/c^2 WIMP mass, a bit lower than their previous one, as it is shown in the plot of Figure 1.17 (right).

Given the current situation in direct Dark Matter searches, the detection of Dark Matter particles in several experiments, with a different target material, would actually provide a strong support to a discovery claim, allowing a precise determination of the WIMP mass and providing an effective way to discriminate among WIMP candidates.

1.3.6 Prospects and future direct detection experiments

There is a promising future in direct Dark Matter searches due to the remarkable development of the different techniques to detect and identify the nature of Dark Matter particles. During next years, many projects will compete to build and operate the so-called ultimate WIMP detectors, capable of probing spin-independent interactions down to the incredibly low cross section of 10^{-48} cm^2, before the irreducible neutrino coherent scattering background becomes a real limitation to the achievable sensitivity. In case of a discovery in the near future, these experiments will be able to constrain WIMP properties such as its mass, scattering cross section and possibly spin. If there is a positive Dark Matter signal and thanks to the input from LHC and from indirect searches, direct detection experiments will also allow to determine the local density and to constrain the local structure of our Dark Matter halo [79]. Some of the experiments that will be leading this challenge are SuperCDMS, XENON1T, LUX, ArDM and DarkSide.

The following phase of the CDMS experiment, SuperCDMS, employs detectors with high sensitivity to the ionisation and phonon signals that result from a WIMP-nucleus collision. The detectors, known as iZIP (interleaved Z-sensitive Ionisation Phonon), feature state-of-the-art superconducting thin films deposited on 600 g Ge crystals to accurately detect WIMP collisions. SuperCDMS, which is installed at the Soudan Underground Laboratory and operates a total detector mass of ∼10 kg, has already reported a first search for WIMPs. An exposure of 577 kg×day has been analysed for WIMPs with $M_W < 30$ GeV/c^2, observing 11 events in the signal region. A physically motivated background model generally agrees with the data and this analysis strongly disfavours a WIMP-nucleon scattering interpretation of the excess reported by CoGeNT, which also uses a germanium target. An upper limit on the spin-independent WIMP-nucleon cross section of 1.2×10^{-42}cm^2 at 8 GeV/c^2 has been set, which is, once again, in tension with WIMP interpretations of recent experiments and probes new parameter space for WIMP-nucleon scattering for $M_W < 6$ GeV/c^2 [80].

The next phase of the XENON program will be a detector at the ton-scale, XENON1T, based on 2.2 tons of LXe viewed by low radioactivity PMTs and housed in a water Cherenkov muon veto at LNGS. It is expected to start operation in early 2016 with an experimental aim of probing WIMP interaction cross sections of the order of $\sigma_{\rm SI} \sim 2 \times 10^{-47}$ cm^2 within 2 years of operation. If the original goal is achieved, XENON1T will provide the sensitivity to probe a particularly favourable region of electroweak physics on a timescale compatible with complementary ground and satellite based indirect searches and with accelerator Dark Matter searches at LHC. In fact, for a $\sigma_{\rm SI} \sim 10^{-45}$ cm^2 and 100 GeV/c^2 WIMP mass, XENON1T could detect ∼100 events in this exposure, providing statistics for placing significant constraints on the WIMP mass [81].

After DarkSide-50, already installed and taking data at LNGS, a LAr-TPC with an active (fiducial) mass of 23 (20) tons, has been proposed for the next phase of the experiment. DarkSide-20k will be a detector with ultra-low background levels, the ability to measure its backgrounds in situ, and sensitivity to WIMP-nucleon interactions with cross section of 9×10^{-48}cm^2 for WIMPs of 1 TeV/c^2 mass, achieved in a background-free exposure of 100 ton×year, accumulated in a run of 5 years. In this sense, DarkSide-20k could become the most powerful Dark Matter experiment searching for high mass Dark Matter to start data taking by 2020 [82]. DarkSide-20k will be followed after five years at LNGS by Argo, a 300-ton Dark Matter detector also capable of performing a set of very high precision measurements of several solar neutrino sources.

As it has been mentioned previously, LUX released its first Dark Matter search results in 2014 and the publication of their latest results, which have been released very recently, is expected within 2016. In the meantime, some additional background studies have been recently published, showing that the expected background rate from the model for the 85.3 day WIMP search is $(2.6 \pm 0.2_{\rm stat} \pm 0.4_{\rm sys}) \times 10^{-3}$events keV$_{\rm ee}^{-1}$kg^{-1}day^{-1} in a 118 kg fiducial volume. The observed background rate of $(3.6 \pm 0.4_{\rm stat}) \times 10^{-3}$events keV$_{\rm ee}^{-1}$kg^{-1}day^{-1} is therefore consistent with model predictions [83]. Furthermore, a collaboration with ZEPLIN experiment has been established to construct a 7-ton LXe detector called LUX-ZEPLIN (LZ). The experiment, which will be located in the Sanford Underground Facility, will have an active LXe cylindrical volume of 1.5 m in diameter and height and a TPC with 488 PMTs, placed above and below the LXe volume. The central part of this volume will be surrounded by a thin instrumented region of LXe, an outer detector of gadolinium-loaded liquid scintillator and a layer of ultrapure water, to identify and reduce false signals. A 3-year run of the LZ experiment is projected to achieve a sensitivity close to fundamental limits from the cosmic ray neutrino background [84]. The underground installation of the LZ detector has been programmed to begin in July 2018 and the commissioning phase is expected to start in February 2019.

Chapter 2

Direct detection techniques and noble liquids

In direct detection experiments, the search of WIMPs from the galactic halo is made via elastic scattering off an ordinary target nucleus. When an incident WIMP scatters off a target nucleus, this nucleus recoils with an energy that is proportional to the incident WIMP energy and depends on the WIMP and the nucleus masses and also on the scattering angle. As we have already discussed in the previous Chapter, the scattering is non relativistic since WIMPs are Cold Dark Matter. Considering M_W the mass of the WIMP and E_0 its initial kinetic energy, $E_0 = \frac{1}{2} M_W v_0^2$, a nucleus of mass M_N will recoil at a scattering angle θ, as shown in the scheme of Figure 2.1, with an energy E_R which is given by [85]:

$$E_R = E_0 r \frac{(1 - cos\theta)}{2}, \tag{2.1}$$

where r a kinematic factor related to the reduced mass of the WIMP-nucleus system, $\mu = M_W M_N/(M_W + M_N)$, and defined as:

$$r \equiv \frac{4\mu^2}{M_W M_N} = \frac{4 M_W M_N}{(M_N + M_W)^2}. \tag{2.2}$$

We can estimate the typical recoil energies considering parameters of our galactic halo, namely galactic velocities of the order of $10^{-3}c$ and an estimated range for the WIMP mass of $M_W = 10-1000$ GeV/c^2. Taking into account these values, typically, the recoil energies would be in the range 1 - 100 keV. For this reason, detectors with keV thresholds are required in direct WIMP searches. Those low energetic recoil nuclei are extremely difficult to detect and discriminate against backgrounds, thus making the WIMP direct search very challenging.

The differential energy spectrum of these nuclear recoils, which depends on the WIMP kinetic energy distribution, is featureless and exponentially decreasing in the

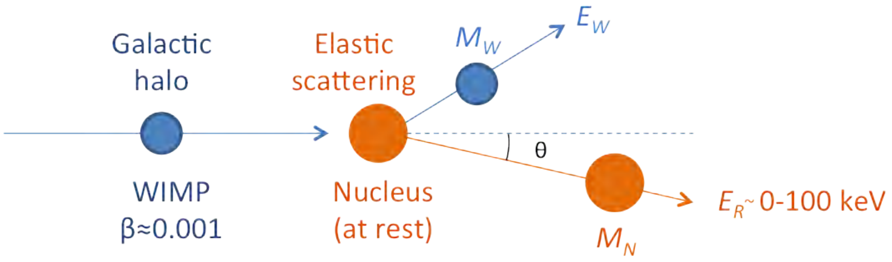

Figure 2.1: Scheme showing an incident WIMP that scatters off a target nucleus. The recoil energy, E_R, depends on the incident WIMP energy, E_0, on the WIMP and nucleus masses, M_W and M_N, and also on the scattering angle, θ. The typical recoil energies are in the range 1-100 keV.

approximated form:

$$\frac{\mathrm{d}R}{\mathrm{d}E_R} = \frac{R_0}{E_0 r} \exp \quad -\frac{E_R}{E_0 r} \quad , \tag{2.3}$$

where R is the event rate per unit mass and R_0 is the total event rate, which includes the dependence on the WIMP density.

2.1 Theoretical sensitivity study

In order to study the expected ArDM sensitivity, we can develop a full analytical computation of the differential WIMP recoil energy spectrum, which gives fundamental information about both the WIMP-nucleus cross section and the WIMP mass. Corrections given by the nuclear form factor (to correct for momentum transfer q, corresponding to a wavelength h/q comparable to the nuclear radius), the annual modulation of the signal due to the Earth's motion around the Sun and the finite galactic escape velocity have to be included to obtain a complete formula of the WIMP-nucleon cross section as a function of the WIMP mass. This mathematical expression, which allows to compare results coming from different experiments and target mediums, will be used to evaluate ArDM sensitivity, after including the expected neutron background from screening measurements.

2.1.1 Analytical calculation of the total event rate

In direct Dark Matter searches, the interaction rate of WIMPs with ordinary matter will depend on the WIMP density, ρ_W, and the WIMP velocity distribution, $f(v, v_E)$. The standard halo model, conventionally used in sensitivity calculations, assumes a spherical halo in which the WIMPs are trapped in the gravitational field at thermal equilibrium. Therefore, the full phase-space distribution function for an isothermal halo composed of particles of mass M_W takes the form of a Boltzmann distribution with the gravitational potential, $\phi(\vec{x})$,

$$f(\vec{r},\vec{v},\vec{v}_E) \propto e^{-\frac{M_W(\vec{v}_E+\vec{v})^2/2+M_W\phi(\vec{r})}{k_B T}}, \tag{2.4}$$

where $\vec{v}$ is the WIMP velocity respect to the Earth, $\vec{v}_E$ is the total velocity of the Earth with respect to the centre of the galaxy (taking into account the speed of the Sun) and with $k_B T$ given by the WIMP kinetic energy.

In the standard halo model, the spherical symmetry of the Dark Matter halo is assumed, thus the thermal velocity distribution of the WIMPs is isotropic and presents the following Maxwellian form:

$$f(\vec{v},\vec{v}_E) = e^{-(\vec{v}+\vec{v}_E)^2/v_0^2}, \tag{2.5}$$

where $v_0 \sim 230$ km/s is the rotational velocity of the Solar System around the galactic centre.

In order to calculate the differential event rate, we consider the density of WIMP particles dn with velocity v contained in the volume swept per unit time, as shown in the scheme of Figure 2.2.

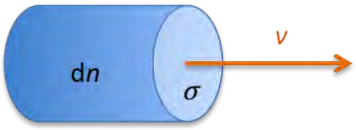

Figure 2.2: The volume σv swept per unit time contains dn WIMP particles with velocity v.

The differential event rate per unit mass on a certain target of atomic mass A is defined as follows [85]:

$$\mathrm{d}R = \frac{N_0}{A}\sigma_N v \mathrm{d}n, \tag{2.6}$$

where N_0 is the Avogadro number, A is the atomic number of the target nucleus, σ_N is the WIMP-nucleus cross section, v is the particle velocity and dn is the differential particle density, defined as:

$$\mathrm{d}n = \frac{n_0}{k} f(\vec{v},\vec{v}_E)\mathrm{d}^3v. \tag{2.7}$$

In Equation 2.7, $\mathrm{d}^3v = v^2\mathrm{d}\phi\,\mathrm{d}\theta\,\mathrm{d}v$ is the volume element in spherical coordinates, n_0 is the mean WIMP particle density, defined as $n_0 = \rho_W/M_W$, with

$\rho_W \sim 0.3$ GeV/cm^3 is the WIMP density [8], M_W is the WIMP mass and k is a normalisation constant such that:

$$\int_0^{v_{esc}} \mathrm{d}n \equiv n_0, \tag{2.8}$$

with $v_{esc} \sim 600$ km/s the local escape velocity from the galaxy, thus:

$$k = \int f(\vec{v}, \vec{v}_E)\mathrm{d}^3v = \int_0^{2\pi} \mathrm{d}\phi \int_{-1}^{1} \cos\theta \mathrm{d}\theta \int_0^{v_{esc}} f(\vec{v}, \vec{v}_E)v^2\mathrm{d}v. \tag{2.9}$$

Considering the zero momentum transfer approximation, which assumes that the momentum transfer is such that the wavelength h/q is large compared to the nuclear radius and implies $\sigma_N = \sigma_{0N} =$ constant, the total event rate, R, is obtained by integration of Equation 2.6 over the WIMP velocity distribution, using Equations 2.5 and 2.7:

$$R = \frac{N_0}{A}\sigma_{0N} \int_0^{v_{esc}} v\mathrm{d}n = \frac{N_0}{A}\sigma_{0N}n_0 \int_0^{v_{esc}} \frac{1}{k} v e^{-(v+v_E)^2/v_0^2}\mathrm{d}^3v. \tag{2.10}$$

Therefore, from Equation 2.10, we can define R_0 as the event rate per unit mass for $v_E = 0$ and the limit of infinite galactic escape velocity, $v_{esc} = \infty$,

$$R_0 = \frac{N_0}{A}\sigma_{0N}n_0 \int_0^{\infty} \frac{1}{k_0} v e^{-v^2/v_0^2}\mathrm{d}^3v, \tag{2.11}$$

where k_0 is calculated from Equation 2.9 as follows:

$$\begin{aligned} k_0 &= \int_0^{2\pi} \mathrm{d}\phi \int_{-1}^{1} \mathrm{d}(\cos\theta) \int_0^{\infty} e^{-\frac{v^2}{v_0^2}} v^2\mathrm{d}v = 4\pi \int_0^{\infty} e^{-\frac{v^2}{v_0^2}} v^2\mathrm{d}v \\ &= 4\pi \left[\left(\frac{-v_0^2}{2} \quad v e^{-\frac{v^2}{v_0^2}} \right|_0^{\infty} - \int_0^{\infty} \frac{-v_0^2}{2} \quad e^{-\frac{v^2}{v_0^2}}\mathrm{d}v \right] \\ &= 2\pi v_0^2 \int_0^{\infty} e^{-\frac{v^2}{v_0^2}}\mathrm{d}v = \pi v_0^2 \quad \sqrt{\frac{\pi}{1/v_0^2}} = (\sqrt{\pi}v_0)^3. \end{aligned} \tag{2.12}$$

If we substitute Equation 2.12 in Equation 2.11 and recall that we are considering an isotropic velocity distribution, which implies that $\mathrm{d}^3v \rightarrow 4\pi v^2\mathrm{d}v$, we get:

$$\begin{aligned} R_0 &= \frac{4\pi}{(\sqrt{\pi}v_0)^3}\frac{N_0}{A}\frac{\rho_W}{M_W}\sigma_{0N} \int_0^{\infty} v^3 e^{-v^2/v_0^2}\mathrm{d}v \\ &= \frac{4}{\sqrt{\pi}v_0^3}\frac{N_0}{A}\frac{\rho_W}{M_W}\sigma_{0N} \left[\left(\frac{-v_0^2}{2} \quad v^2 e^{-\frac{v^2}{v_0^2}} \right|_0^{\infty} - \int_0^{\infty} \frac{-v_0^2}{2} \quad 2v e^{-\frac{v^2}{v_0^2}}\mathrm{d}v \right] \\ &= \frac{4}{\sqrt{\pi}v_0^3}\frac{N_0}{A}\frac{\rho_W}{M_W}\sigma_{0N}v_0^2 \quad \frac{-v_0^2}{2} \quad e^{-\frac{v^2}{v_0^2}} \Big|_0^{\infty} = \frac{4}{\sqrt{\pi}v_0^3}\frac{N_0}{A}\frac{\rho_W}{M_W}\sigma_{0N}\frac{v_0^4}{2}. \end{aligned} \tag{2.13}$$

The final expression for R_0 is written as follows:

$$R_0 = \frac{2}{\sqrt{\pi}}\frac{N_0}{A}\frac{\rho_W}{M_W}\sigma_{0N}v_0. \tag{2.14}$$

In order to compare the results from several experiments using different targets, it is convenient to express Equation 2.14 as a function of the WIMP-nucleon cross section, σ_{0n}, which is related to the WIMP-nucleus cross section, σ_{0N}, by [86]:

$$\sigma_{0N} = \frac{\mu_N^2}{\mu_n^2}A^2\sigma_{0n} \leftrightarrow \sigma_{0n} = \frac{1}{A^2}\frac{\mu_n^2}{\mu_N^2}\sigma_{0N}. \tag{2.15}$$

Therefore, the total event rate per unit mass, R_0, as a function of the WIMP-nucleon cross section is obtained by substituting Equation 2.15 in Equation 2.14, resulting:

$$R_0 = \frac{2}{\sqrt{\pi}}\frac{N_0}{A}\frac{\rho_W}{M_W}\quad\frac{\mu_N}{\mu_n}A\quad^{2}\sigma_{0n}. \tag{2.16}$$

2.1.2 Form factor correction

Equation 2.16 has been calculated in zero momentum transfer approximation, which assumes that the momentum transfer is such that the wavelength h/q is large compared to the nuclear radius. In case this approximation is no longer valid, we have to introduce a form factor, $F(qr_n)$, which depends on both the momentum transfer and the effective nuclear radius, thus the scattering cross section behaves as

$$\sigma(qr_n) = \sigma_0 F^2(qr_n), \tag{2.17}$$

where σ_0 is the cross section in the zero momentum transfer approximation. Separating the formula into two terms, σ_0 containing the dependence on the specific interaction and $F(qr_n)$ accounting for the momentum transfer, allows comparing results from different experiments.

In the present study we will consider the distribution proposed by Helm, which gives very similar results to the ones obtained from the Fermi distribution, but provides an analytic form factor expression:

$$F(qr_n) = 3\frac{j_1(qr_n)}{qr_n}\exp^{-\frac{(qs)^2}{2}}, \tag{2.18}$$

where $j_1(qr_n)$ is the corresponding Bessel function and s accounts for the nuclear skin thickness, $s \simeq 0.9$ fm.

$$j_1(qr_n) = \frac{\sin(qr_n) - qr_n\cos(qr_n)}{(qr_n)^2}. \tag{2.19}$$

The Helm form factor was introduced as a modification of the form factor for a uniform sphere multiplied by a Gaussian to account for the soft edge of the nucleus. The parameters r_n and s are chosen to match numerical integration of Two-Parameter Fermi (Woods-Saxon) or other parametric models of nuclear density.

The momentum transfer, q, is expressed as a function of the atomic number of the target material, A, and the recoil energy, E_R, defined previously in the present Chapter.

$$q(\mathrm{MeVc^{-1}}) = [2 \times 0.932(\mathrm{GeVc^{-2}}) A E_R(\mathrm{keV})]^{1/2}. \tag{2.20}$$

The effective nuclear radius has the following formula:

$$r_n^2 = c^2 + \frac{7}{3}\pi^2 a^2 - 5s^2, \tag{2.21}$$

where $c \simeq 1.23A^{1/3} - 0.60$ fm and $a \simeq 0.52$ fm. Considering units of $= 1$ (we divide Equation 2.20 by $= 197.3$ MeV·fm), qr_n is a dimensionless quantity.

Taking into account previous expressions, the form factor correction is plotted in Figure 2.3 as a function of the nucleus recoil energy, E_R, for different elements, such as Xe, Ar, Ge and Na, which are typically used as targets in WIMP direct detection experiments. This plot clearly illustrates the limitation of large A materials, which show a remarkable influence of the form factor correction, specially for high E_R values.

2.1.3 Velocity corrections

In order to obtain the differential recoil energy spectrum (E_R), we need to integrate over the whole range of incident energies. For an isotropic scattering, the recoil energy is uniformly distributed between 0 and Er, with E the initial kinetic energy of the WIMP, $E = 1/2M_W v^2$, which means that the contribution to the differential rate for a given initial WIMP kinetic energy is written as follows:

$$\frac{\mathrm{d}R}{\mathrm{d}E_R}(E_R) = {}_{E_{min}}^{E_{max}} \frac{\mathrm{d}R(E)}{Er}, \tag{2.22}$$

where $\mathrm{d}R$ is the differential rate expressed in Equation 2.6, with r given by Equation 2.2. The maximum initial WIMP energy may be infinity in a first approximation or, more accurately, be based upon the Galactic escape velocity, v_{esc}, thus $E_{max} = M_W v_{esc}^2/2$, while the minimum initial WIMP kinetic energy to cause a recoil of E_R, which corresponds to the case of head-on scattering $(\theta = \pi)$, gives $E_{min} = E_R/r$.

The differential rate per unit mass can be expressed as function of the total event rate, R_0, taking into account Equations 2.6, 2.7 and 2.12,

$$\mathrm{d}R \;=\; \frac{N_0}{A} n_0 \sigma_N \frac{v}{k} f(v, v_E) \mathrm{d}^3 v = \frac{\sqrt{\pi} R_0}{2v_0} \frac{k_0}{(\sqrt{\pi} v_0)^3} \frac{v}{k} f(\vec{v}, \vec{v}_E) \mathrm{d}^3 v, \tag{2.23}$$

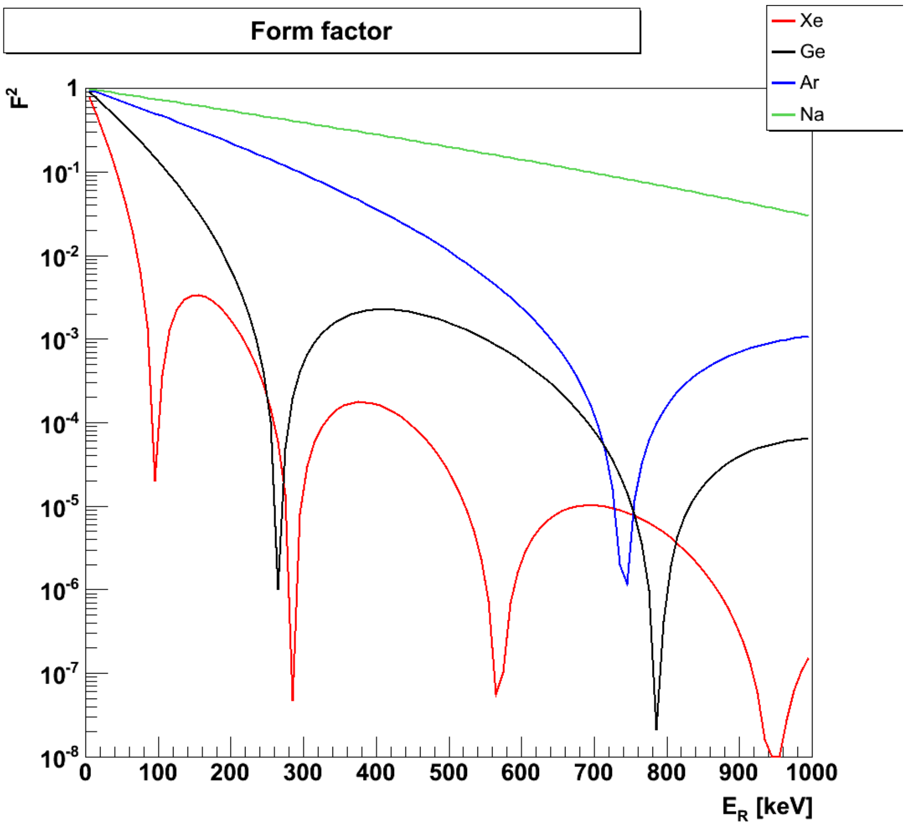

Figure 2.3: Form factor correction plotted as a function of the nucleus recoil energy, E_R, for different target materials.

which gives

$$\mathrm{d}R = R_0 \frac{k_0}{k} \frac{1}{2\pi v_0^4} v f(\vec{v}, \vec{v}_E) \mathrm{d}^3 v. \tag{2.24}$$

Now we write Equation 2.22 as a function of v and substitute Equation 2.24:

$$\frac{\mathrm{d}R}{\mathrm{d}E_R} = \int_{v_{min}}^{v_{max}} \frac{\mathrm{d}R(v)}{1/2 M_W v^2 r} \frac{1/2 M_W v_0^2}{E_0} = \frac{R_0}{E_0 r} \frac{k_0}{k} \frac{1}{2\pi v_0^4} \int_{v_{min}}^{v_{max}} \frac{v_0^2}{v^2} v f(\vec{v}, \vec{v}_E) \mathrm{d}^3 v. \tag{2.25}$$

Finally, we get the expression for the differential rate of WIMP scattering on Earth, which is given by:

$$\frac{\mathrm{d}R}{\mathrm{d}E_R} = \frac{R_0}{E_0 r} \frac{k_0}{k} \frac{1}{2\pi v_0^2} \int_{v_{min}}^{v_{max}} \frac{1}{v} f(\vec{v}, \vec{v}_E) \mathrm{d}^3 v, \tag{2.26}$$

where $v_{min} = \sqrt{\frac{2E_{min}}{M_W}} = \sqrt{\frac{2E_R}{M_W r}} = \sqrt{\frac{E_R}{E_0 r}} v_0$, with E_0 the most probable incident kinetic energy of the WIMP, $E_0 = \frac{1}{2} M_W v_0^2$.

From Equation 2.26, using Equation 2.5, and considering, as a first approximation, $v_{max} = v_{esc} = \infty$ for the local galactic escape velocity, we obtain:

$$\frac{\mathrm{d}R(v_E,\infty)}{\mathrm{d}E_R} = \frac{R_0}{E_0 r}\frac{\sqrt{\pi}}{4}\frac{v_0}{v_E} \quad \mathrm{erf} \quad \frac{v_{min}+v_E}{v_0} \quad - \mathrm{erf} \quad \frac{v_{min}-v_E}{v_0} \quad , \tag{2.27}$$

where erf $\frac{v_{min}+v_E}{v_0} \; = \frac{2}{\sqrt{\pi}}\int_0^{(v_{min}+v_E)/v_0} \mathrm{e}^{-t^2}\mathrm{d}t$ is the error function. Equation 2.27 is usually approximated, for practical purposes, by introducing two fitting constants in the form:

$$\frac{\mathrm{d}R(v_E,\infty)}{\mathrm{d}E_R} = c_1 \frac{R_0}{E_0 r} e^{-c_2 E_R/E_0 r}, \tag{2.28}$$

with the following average values for the fitting constants: $c_1 = 0.751$ and $c_2 = 0.561$.

If we consider v_{esc} finite, from Equation 2.26 we have

$$\frac{\mathrm{d}R(v_E,v_{esc})}{\mathrm{d}E_R} = \frac{k_0}{k_1} \quad \frac{\mathrm{d}R(v_E,\infty)}{\mathrm{d}E_R} - \frac{R_0}{E_0 r}\exp^{-v_{esc}^2/v_0^2} \quad , \tag{2.29}$$

with k_0 from Equation 2.12. In a similar way we calculate:

$$\begin{aligned} k_1 &= \underset{0}{\overset{2\pi}{}} \mathrm{d}\phi \underset{-1}{\overset{1}{}} \mathrm{d}(\cos\theta) \underset{0}{\overset{v_{esc}}{}} \exp^{-\frac{v^2}{v_0^2}} v^2 \mathrm{d}v \\ &= 4\pi \quad v_{esc} \frac{-v_0^2}{2} \exp^{-\frac{v_{esc}^2}{v_0^2}} - \underset{0}{\overset{v_{esc}}{}} \frac{-v_0^2}{2} \exp^{-\frac{v^2}{v_0^2}} \mathrm{d}v \\ &= 2\pi v_0^2 \quad -v_{esc}\exp^{-\frac{v_{esc}^2}{v_0^2}} + \underset{0}{\overset{v_{esc}}{}} \exp^{-\frac{v^2}{v_0^2}} \mathrm{d}v \quad . \end{aligned}$$

Since erf $\frac{v_{esc}}{v_0} \; = \frac{2}{\sqrt{\pi}}\int_0^{v_{esc}/v_0} \mathrm{e}^{-t^2}\mathrm{d}t$, we finally obtain:

$$k_1 = 2\pi v_0^2 \quad \frac{\sqrt{\pi}}{2}\mathrm{erf} \quad \frac{v_{esc}}{v_0} \quad - v_{esc}\exp^{-\frac{v_{esc}^2}{v_0^2}} \quad . \tag{2.30}$$

Making use of the previous Equations 2.12 and 2.30, k_0 and k_1 are related as follows

$$\frac{k_0}{k_1} = \quad \mathrm{erf} \quad \frac{v_{esc}}{v_0} \quad - \frac{2}{\sqrt{\pi}}\frac{v_{esc}}{v_0}\exp^{-\frac{v_{esc}^2}{v_0^2}} \quad {}^{-1} \quad . \tag{2.31}$$

Finally, taking into account Equations 2.27 and 2.29, we have:

$$\frac{\mathrm{d}R(v_E,v_{esc})}{\mathrm{d}E_R} = \frac{k_0}{k_1}\frac{R_0}{E_0 r} \quad \frac{\sqrt{\pi}}{4}\frac{v_0}{v_E} \quad \mathrm{erf} \quad \frac{v_{min}+v_E}{v_0} \quad - \mathrm{erf} \quad \frac{v_{min}-v_E}{v_0} \quad - \exp^{-v_{esc}^2/v_0^2} \quad , \tag{2.32}$$

where $v_0 = 230$ km/s and $v_{esc} = 600$ km/s. In this last expression, the Earth velocity has to be determined by considering its different components, including the Earth orbit around the Sun, which causes an interesting annual modulation effect of the signal and has to be determined in order to calculate the expected differential spectrum.

2.1.4 Annual modulation effect

The Earth velocity in the galactic frame, $\vec{v}_E$, can be divided into three contributions: the rotational velocity of the galactic disk, $\vec{v}_d$, the velocity of the Sun with respect to the disk, measured by the relative motion with respect to nearby stars, $\vec{v}_S$, and finally the motion of the Earth with respect to the Sun, $\vec{v}_{ES}$:

$$\vec{v}_E = \vec{v}_d + \vec{v}_S + \vec{v}_{ES}. \tag{2.33}$$

The dominant contribution in Equation 2.33 comes from the tangential velocity of the Sun around the galactic centre, 230 km/s, while the Earth moves around the Sun in an almost circular orbit with a speed of approximately 30 km/s. Since this last contribution is an order of magnitude smaller than the one of the Sun, it is usually neglected in most of the studies. However, it gives rise to a very interesting seasonal effect in the WIMP flux detected on Earth.

As it is shown in the scheme of Figure 2.4, the direction vector of the Earth plane orbit around the Sun is tilted 60° with respect to the Sun propagation direction. As a result, the Earth velocity component in the direction of the rotation of the galaxy disk, $v_{ES} \cdot \cos(60^\circ) = 15$ km/s, is alternatively added and subtracted to the velocity of the Sun relative to the WIMP flux, thus giving an annual modulation effect of the WIMP signal. The variation of v_E during the year due to the rotation of the Earth around the Sun is therefore given by [87]:

$$v_E(t)[\text{km/s}] = 232 + 15\cos \quad 2\pi\frac{t-152.5}{365.25} \quad , \tag{2.34}$$

where t is measured in days, with 00:00 January 1 corresponding to $t = 0$. Due to the sinusoidal variation in v_E, there is a small modulation of the order of 7% in the recoil energy spectrum on an annual basis, with an enhancement of the average kinetic energy of the WIMP flux measured on Earth on 1^{st} of June and a decrease of it on 1^{st} of December, providing a relevant experimental signature of the presence of Dark Matter in the galactic halo.

As discussed in Chapter 1, Section 1.3.5, the DAMA/LIBRA-phase 1 and the former DAMA/NaI data (cumulative exposure 1.33 ton×yr, corresponding to 14 annual cycles) have given evidence of 9.3 σ C.L. for the presence of Dark Matter (DM) particles in the galactic halo, on the basis of the exploited model independent

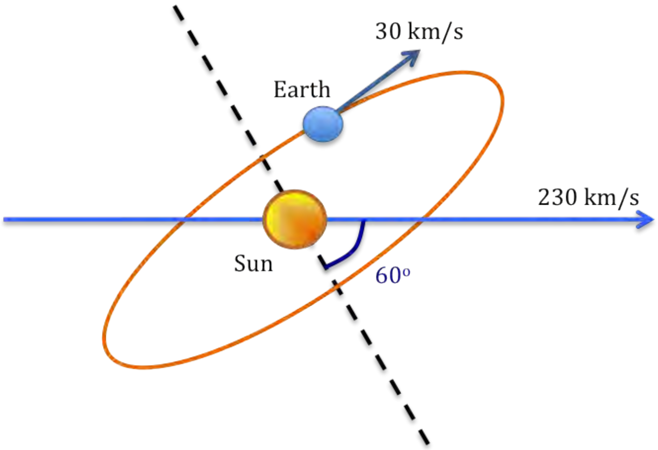

Figure 2.4: Drawing of the system formed by the Sun and the Earth, showing the tilt of the orbit plane with respect to the galaxy plane. Both the velocity of the Earth in its orbit around the Sun, 30 km/s, and the velocity of the Sun around the galactic centre, 230 km/s, are depicted. The composition of velocities gives rise to the so-called annual modulation effect.

DM annual modulation signature by using highly radiopure NaI(Tl) target. The modulation amplitude of the single hit events in the (2-6) keV energy interval is: (0.0112±0.0012) cpd/kg/keV; the measured phase is (144±7) days and the measured period is (0.998±0.002) yr [67]. These values are, in principle, in agreement with those expected for DM particles.

2.1.5 Calculation of the differential energy spectrum and WIMP-nucleon cross section

Once we have developed the full theoretical calculation of the recoil energy spectrum, we can evaluate the effect of the different corrections as well as the dependence of the spectrum on the WIMP mass. In order to do that, we substitute Equations 2.16 (taking into account Equations 2.17) and 2.31 in Equation 2.32. Then, we find:

$$\begin{aligned}\frac{\mathrm{d}R(v_E, v_{esc})}{\mathrm{d}E_R} &= \frac{2}{\sqrt{\pi}}\frac{N_0}{A}\frac{\rho_W}{M_W} \quad \frac{\mu_N}{\mu_n}A \quad ^{2} \sigma_n \quad \mathrm{erf} \quad \frac{v_{esc}}{v_0} \quad - \frac{2}{\sqrt{\pi}}\frac{v_{esc}}{v_0}\exp^{-\frac{v_{esc}^2}{v_0^2}} \quad ^{-1} \quad \frac{1}{E_0 r} \\ &\cdot \quad \frac{\sqrt{\pi}}{4}\frac{v_0}{v_E} \quad \mathrm{erf} \quad \frac{v_{min}+v_E}{v_0} \quad - \mathrm{erf} \quad \frac{v_{min}-v_E}{v_0} \quad - \exp^{-\frac{v_{esc}^2}{v_0^2}} \quad F^2(qr_n),\end{aligned} \tag{2.35}$$

whose dependence on E_R comes from $v_{min} = \sqrt{\frac{E_R}{E_0 r}} v_0$ and q in the form factor, $F^2(qr_n)$. However, as we already mentioned in Section 2.1.3, the Equation 2.35 is usually approximated by the exponentially falling form written in Equation 2.28. The difference between both expressions of the differential recoil spectrum is evaluated in the plot shown in Figure 2.5, where we have plotted the differential event rate for argon target, expressed in events keV^{-1}kg^{-1}day^{-1}, with respect to the recoil energy for a fixed value of the WIMP-nucleon cross section, $\sigma_n = 10^{-45}$ cm^2. As it is shown in this plot, there is a clear difference between the exact and the approximated formulas, plotted in red and blue colours respectively for the case of $M_W = 100$ GeV, that starts to be relevant for $E_R \simeq 30$ keV and increases with E_R. Since the form factor has been taken into account in both cases, this difference essentially comes from the consideration of a finite galactic escape velocity and also from the annual modulation effect.

The result from Equation 2.35 has been compared with the publicly available DM online tools [88], which have been developed by the Tübingen University and are represented by stars in the plot of Figure 2.5. From this comparison, we can conclude that, after introducing all velocity corrections, the form factor contribution and the annual modulation effect, the agreement between the calculated formula and the results form the DM online tools is excellent, thus validating our theoretical calculation.

Another evidence is the dependence of the differential recoil spectrum with the WIMP mass. In particular, there is a fast decrease of the energy spectrum with increasing recoil energy, which is more evident for very light WIMPs. As a consequence, low energy thresholds, $E_{th} < O(10$ keV$)$, will be required, particularly for low WIMP mass searches, $M_W < O(10$ GeV$)$ [89].

Finally, we would like to obtain the WIMP-nucleon cross section as a function of the WIMP mass. In direct detection experiments, such as ArDM, in case of lack of a Dark Matter positive signal, the data may yield to a limit on the cross section from the total number of events detected in a finite energy range. In these cases, we need to isolate σ_n from Equation 2.35 and consider the integrated rate over a recoil energy range $E_R = E_1$ to $E_R = E_2$ defined by the lower and upper energy threshold values. Since it is not possible to integrate Equation 2.35 analytically with respect to E_R, we do it numerically for a full range of different M_W values, so we obtain σ_n as follows

$$\sigma_n = \frac{R(v_E, v_{esc})}{\text{integral}}, \tag{2.36}$$

where $R(v_E, v_{esc})$, expressed in units of events keV^{-1}kg^{-1}day^{-1}, is directly given by the experimental exposure. As an example, the effect of three different energy threshold ranges has been evaluated by plotting the WIMP-nucleon cross section with respect to the WIMP mass for an experimental exposure of 5000 kg×day, as

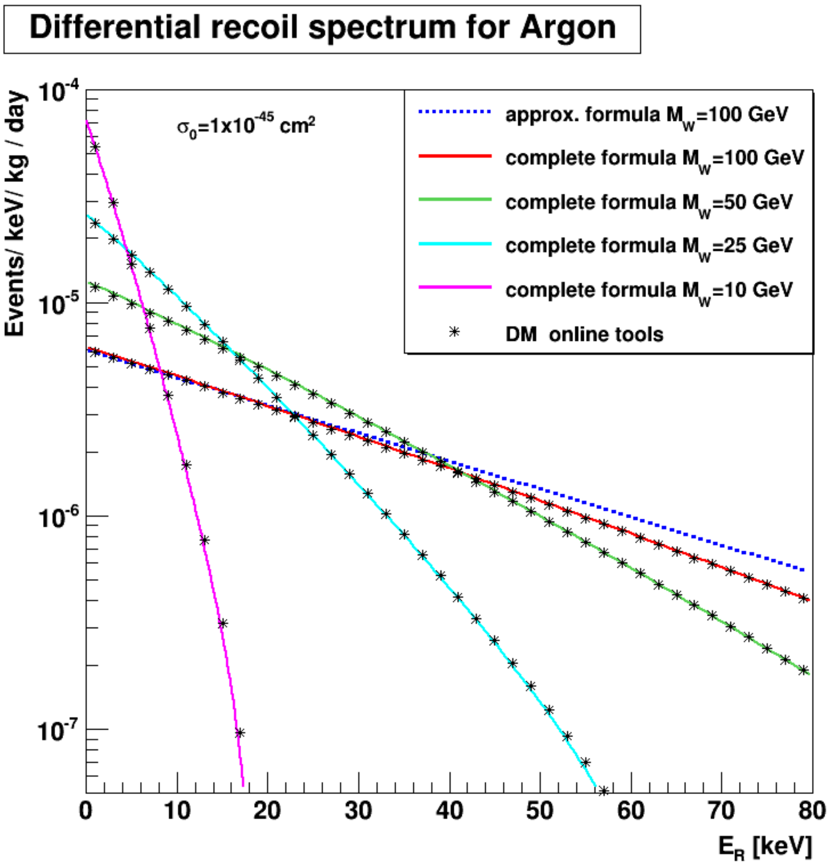

Figure 2.5: Differential recoil spectrum of argon as a function of the recoil energy, E_R, for an experimental exposure of 5000 kg×day and no background. The approximated (dashed line) and complete formulas (solid lines) are compared with the predictions from the DM Online Tools (stars) for different values of the WIMP mass, M_W. The complete formula (Equation 2.35) includes the nuclear form factor corrections, the annual modulation of the signal and the finite galactic escape velocity, which results in an excellent agreement with the DM Online Tools.

shown in the plot of Figure 2.6. This type of plot plays an extremely relevant role to evaluate the sensitivity of a Dark Matter experiment based on its experimental parameters and the assumed halo model. Once again, the obtained results have been compared with the DM online tools, achieving a perfect agreement among each other.

According to the results, the influence of the lower energy threshold in the evaluation of the expected experimental sensitivity is remarkable. This lower threshold effect was expected from the approximately exponentially form of the differential

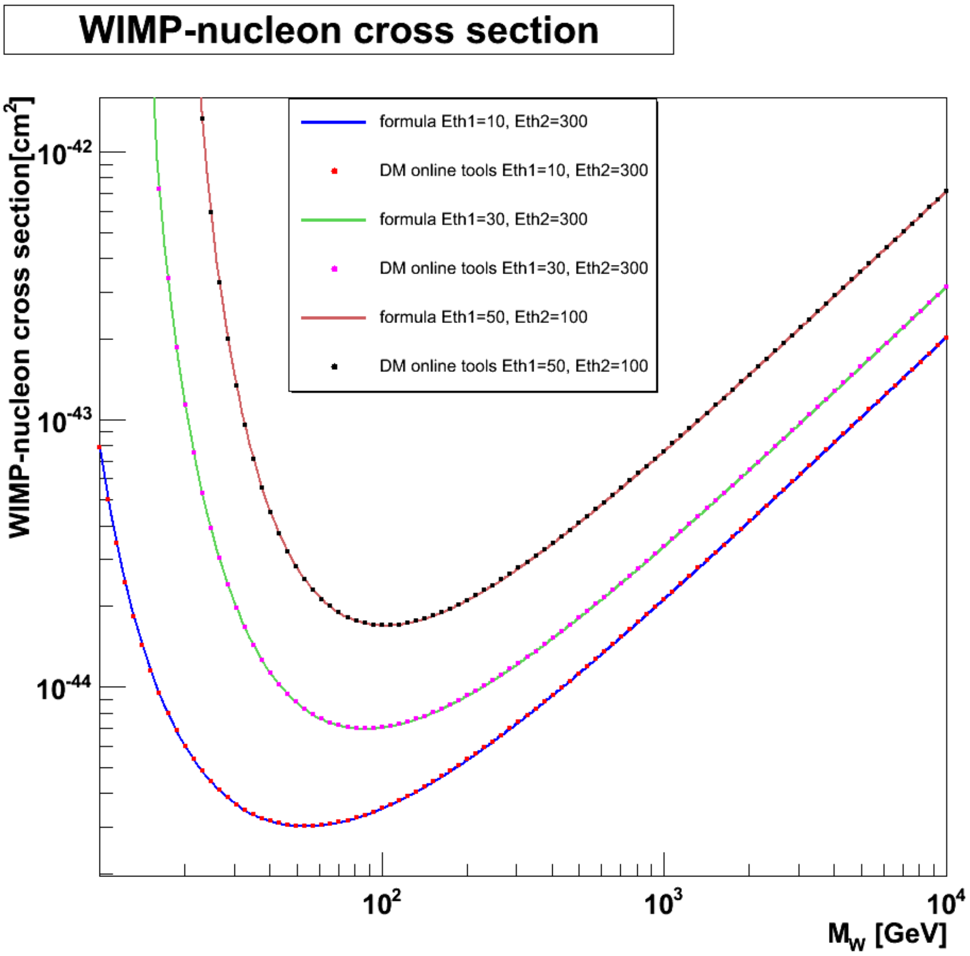

Figure 2.6: Cross section for different energy thresholds values and considering an exposure of 5000 kg×day. The analytically computed curves including all corrections introduced in the present section (solid lines) are in perfect agreement with the predictions obtained from the DM Online Tools (dotted lines).

spectrum, which requires, as explained before, low energy thresholds in order to be sensitive to low WIMP masses. Despite the fact that there has been a general concern in Dark Matter direct detection experiments for lowering this threshold, recent experimental results have constrained substantially the low WIMP mass region, pointing to the importance of reaching a good sensitivity in the high M_W region. In this sense, argon can play a decisive role in direct Dark Matter searches in the upcoming years.

2.1.6 Spin-independent and spin-dependent interactions

The elastic scattering of a WIMP off a nucleus can occur via spin-dependent or spin-independent channels since the contribution of several nucleons to the scattering cross section will not always be added coherently. In the spin-dependent case, only the unpaired nucleon will have a remarkable contribution to the interaction, while in the spin-independent case all the contributions of the different nucleons are added, so that they give rise to a scale factor. Consequently, the cross section expression will vary depending on the type of interaction. In general, we will write the differential cross section as [90]:

$$\frac{\mathrm{d}\sigma}{\mathrm{d}|\vec{q}|^2} = G_F^2 \frac{C}{v^2} F^2(|\vec{q}|) = \frac{\sigma_0}{4\mu^2 v^2} F^2(|\vec{q}|), \tag{2.37}$$

where $|\vec{q}|$ is the absolute value of the linear momentum transfer, v is the WIMP velocity relative to the target, G_F is the Fermi coupling constant, C is a dimensionless number that carries all the information of the considered particle physics model, $F(|\vec{q}|)$ is the form factor normalised so that $F(0) = 1$ and σ_0 is the cross section in the zero momentum transfer approximation, which is obtained as follows:

$$\sigma_0 = \int_0^{4\mu^2 v^2} \frac{\mathrm{d}\sigma(q=0)}{\mathrm{d}|\vec{q}|^2} = 4G_F^2 \mu^2 C. \tag{2.38}$$

For the spin-dependent (SD) case:

$$C_{spin} = (8/\pi)\Lambda^2 J(J+1), \tag{2.39}$$

$$\sigma_{0spin} = (32/\pi) G_F^2 \mu^2 \Lambda^2 J(J+1), \tag{2.40}$$

where J is the total angular momentum of the nucleus and Λ, which is obtained from detailed nuclear calculations, indicates the spin content of neutrons and protons inside the nucleus. The SD cross section occurs through the axial vector coupling to the spin content of the nucleus, so there is a $J(J+1)$ enhancement. This contribution to the cross section is only present in nuclei with an odd number of nucleons, since the spin of the all paired nucleons are anti-aligned and cancel among each other.

For the spin-independent (SI) case:

$$C_{scalar} = (1/\pi G_F^2)[Zf_p + (A-Z)f_n]^2, \tag{2.41}$$

$$\sigma_{0scalar} = (4\mu^2/\pi)[Zf_p + (A-Z)f_n]^2, \tag{2.42}$$

where f_p and f_n represent the WIMP couplings to nucleons. Considering that $f_n \simeq f_p$, $C_{scalar} \propto A^2 \propto m_N^2$. This means that for a heavy nuclear target, the coherent scattering increases the cross section by the square of the atomic number, A.

For this reason, in principle target materials with high atomic number are preferred in direct searches.

The difference between spin-independent and spin-dependent interactions provides an important cross check in the case of a positive Dark Matter signal. As an example, there are two different Xe isotopes with odd atomic number of nucleons (^{129}Xe, ^{131}Xe) while Ar has none, thus in Ar argon only spin-independent interaction can be observed.

2.2 Noble liquids for Dark Matter detection

One of the most promising detector technologies in direct Dark Matter searches is based on noble liquids [52], specifically because:

1. Liquefied noble gases do not attach electrons and can be easily purified, making possible to build stable detectors up to the ton scale and beyond with high purity levels. Electron mobilities are high for the heavier noble gases, which allows long drift distances (>1m).
2. They are bright scintillators, with light yields comparable to that of NaI (∼40 photons/keV).
3. Moreover, if the detector is operated as a TPC, the small diffusion coefficient allows a good resolution of the position reconstruction.
4. Discrimination between nuclear and electron recoils can be achieved thanks to the differences in the ionisation to scintillation ratio and, in some cases, also to pulse shape discrimination.
5. These liquids are dense and homogeneous ($\sim 1-3$ g/cm^3), as reported in Table 2.1, which makes them excellent media for building massive and compact Dark Matter detectors, allowing to explore low cross section values.
6. Additionally, noble liquids are affordable targets since they are available in large amounts as by-products of the industry and, in particular, argon is the third most abundant gas in the atmosphere (9340 ppm), following nitrogen and oxygen.
7. Finally, noble gases are inert, not flammable, and very good dielectrics, which convert them in quite safe targets.

However, due to their low boiling points ($\sim$ 100 K), cryogenic operation is required in detectors based on LXe, LAr or LNe, having the advantage that Xe and Ar can be liquefied using liquid nitrogen (boiling point 77.36 K).

Among noble liquids, LXe and LAr are excellent scintillators in response to particle interaction, with very high light yields of 46 γ/keV and 40 γ/keV respectively; while LNe only has a light yield of 7 γ/keV. For this reason, mainly LAr and LXe are considered to be employed in current and near future experiments, while LNe

Parameter	**Xenon**	**Argon**	**Neon**
Atomic number	54	18	10
Atomic mass	131.3	40.0	20.2
Liquid density [g/cm^3]	2.94	1.40	1.21
Boiling point [K]	165.0	87.3	27.1
Scintillation [γ/keV]	46	40	7
Scintillation wavelength [nm]	178	128	78
Ionisation [e$^-$/keV]	64	42	46
Energy to generate a ion pair [eV]	15.6	23.6	–
Fraction in the Earth atmosphere [ppm]	0.09	9340	18.2
Price	$$$$	$	$$

Table 2.1: Comparison of some physical properties of noble liquids that are relevant for Dark Matter detection [91].

has only been suggested as a medium for low-energy neutrino detection. However, LNe could potentially be employed in the future search for WIMPs [92], as it has been considered for example in the miniCLEAN experiment [93].

The particle interaction in noble liquids not only produces the emission of the scintillation light, but also releases ionisation electrons, which can remain free and be drifted over long distances ($D > 1$ m) due to the fact that they are not attached by noble liquids, thus allowing fiducial volume cuts and 3D interaction positions reconstruction in a time projection chamber (TPC), a detector that not only provides 3-dimensional information on points along a track but also information on energy loss that can be used for particle identification. As it will be explained in detail in Section 2.2.1, the simultaneous detection of ionisation and scintillation signals allows to identify the primary particle interacting in the liquid, since the ratio of the two signals depends on the deposited energy along the particle track, providing a powerful background discrimination method.

An important difference between LAr and LXe is related to the scintillation wavelength, which is 178 nm in LXe, while it is shorter in LAr (128 nm). Although most PMT photocathodes have high sensitivity down to the UV region, this radiation tends to be absorbed by the window material of the PMT, with an intensity that depends on the UV transmittance of each material, as it is shown in the plot of Figure 2.7. The most common material for PMT windows, the borosilicate glass, does not transmit UV radiation shorter than 300 nm. Other window materials, such as sapphire and synthetic silica have lower UV transmittance limits, in particular, 150 and 160 nm respectively, allowing to detect LXe scintillation light, but not the one coming from LAr. Finally, the MgF_2 crystal is superior in transmitting UV radiation (above 115 nm), but it has the disadvantage of deliquescence [94]. For this reason, the scintillation light emitted in LXe can be observed with commercially available PMTs; while for LAr the inner detector surfaces and the PMT windows must be coated with a wavelength shifter, such as tetra phenyl butadiene (TPB), which shifts the wavelength of the light to about 420 nm. One must ensure an optimal efficiency of the wavelength shifter, and its long-term stability in a cold, LAr environment.

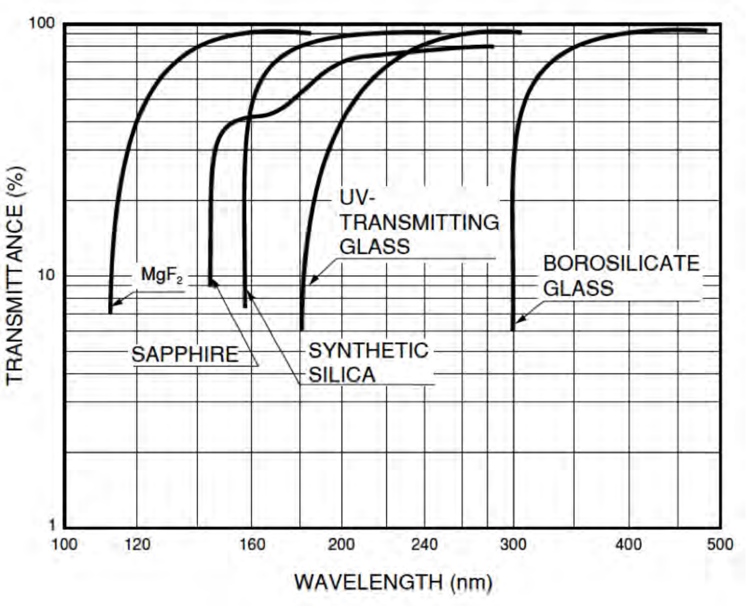

Figure 2.7: Spectral transmittance of PMT window materials [94].

Another crucial difference between LAr and LXe, which is due to the kinematics of the recoiling process, is illustrated in the plot shown in Figure 2.8. In this plot, we present the expected event rate per keV per kg of target and per day, obtained from Equation 2.28 as a function of the recoil energy, E_R in keV, for different target materials and considering a WIMP-nucleon cross section of 10^{-43} cm^2 (10^{-7} pb) and a WIMP mass of 1 TeV. As it is observed in the plot, the expected nuclear recoil energy spectra are featureless exponentials, as we introduced previously in this Chapter, with an event rate which is less sensitive to the threshold on the recoil energy in Ar than it is for Xe. This is due to the different contributions of the form factor, which have a remarkable influence in the recoil spectrum for targets with higher atomic number, A. In particular, since the Xe nucleus is larger than the Ar one, coherence is lost for large momentum transfers, leading to a form factor suppression of the rate at high E_R, as it is shown in the plot of Figure 2.8. A low detector threshold is therefore mandatory for LXe, while LAr presents a higher interaction rate for high values of E_R.

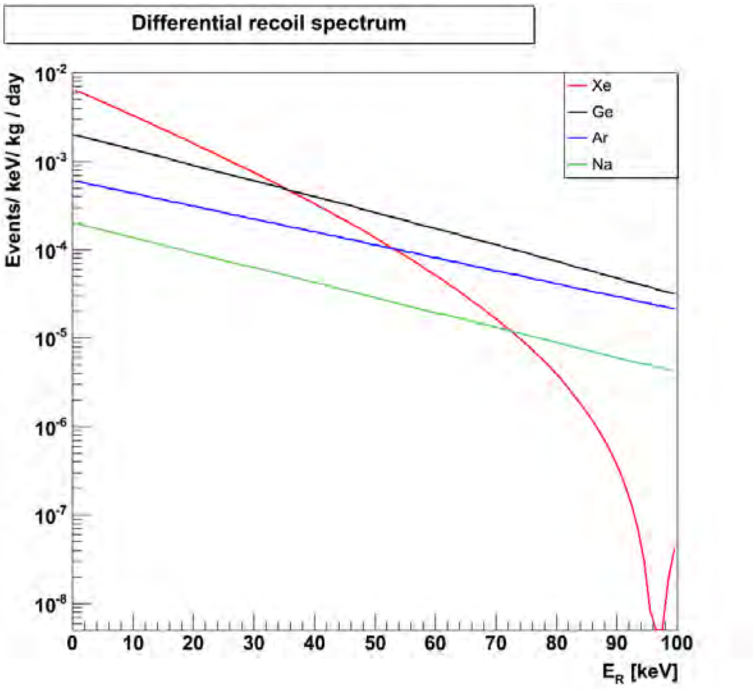

Figure 2.8: Differential recoil spectrum for different targets (Xe, Ge, Ar and Na) considering a WIMP-nucleon cross section of 10^{-43} cm^2 (10^{-7} pb) and a WIMP mass of 1 TeV. The event rate per keV per kg of target and per day is plotted versus the recoil energy of the nucleus in keV, showing that the event rate for argon is less sensitive to the energy threshold than it is for xenon.

2.2.1 Liquid Argon for Dark Matter Detection

Although, at first sight, some properties make LXe a very attractive candidate target for direct Dark Matter detection, due to its higher density, higher scintillation and ionisation yields and longer scintillation wavelength, there are several features that convert LAr in the most competitive choice for very large detectors. Firstly, high purity argon is commercially available in large quantities at low costs, due to its high natural abundance in the Earth atmosphere (9340 ppm), while the Xe fraction in the atmosphere is pretty low (0.09 ppm). For this reason, a multiton-scale detector with LAr is the most affordable and competitive option. However, argon-based Dark Matter experiments, must confront the presence of the intrinsic ^{39}Ar background. The radioactive ^{39}Ar, which is a beta emitter with an endpoint energy of 565 keV and half-life of 269 yr, is present in natural Ar with an activity of 1.01±0.02(stat)±0.08(syst) Bq/kg in commercial argon derived from the atmosphere [95]. Although the ^{39}Ar isotopic abundance of 8×10^{-16} [96] appears to be small, the background due to ^{39}Ar decay electrons in a large scale detector using atmospheric argon can represent a relevant contribution to the total background. As an example, the ^{39}Ar decay rate in 1 ton of atmospheric argon is $\sim 3 \times 10^{10}$ in one year. The strategy to face this problem of internal radioactivity is the use of depleted Ar, which is free of ^{39}Ar since it is extracted from underground wells.

In argon, there are two different background discrimination methods to distinguish between electron recoils and nuclear recoils: charge to light ratio and pulse shape discrimination. In a LAr-TPC the relative amount between the produced and extracted electrons depends strongly on the charge track ion pair density (besides the drift field). In a high density track, recombination is enhanced. Therefore, the light signal (S1) is enhanced with respect to the charge signal (S2). Consequently, the ratio between the two amplitudes of the primary and secondary scintillation signals, S1 and S2, change for different interaction types and it can be used for discriminating the nuclear recoil from the electron recoil interactions.

Additionally, argon provides another powerful discrimination tool against background: the pulse shape discrimination. The scintillation light emitted in LAr corresponds to radiative decays from the molecular Ar_2^* singlet and triplet excited states ($^1\Sigma_u^+$ and $^3\Sigma_u^+$) to the ground state ($^1\Sigma_g^+$), consisting of two independent argon atoms, Ar. The emission spectrum is peaked around 128 nm in the vacuum ultraviolet (VUV) region, with a full width at half-maximum of this peak of about 8 nm [97]. These two transitions have very different lifetimes due to the fact that singlet transition, $^1\Sigma_u^+ \rightarrow ^1\Sigma_g^+$, is strongly allowed with decay time $\tau_1 = 5$ ns while triplet transition, $^3\Sigma_u^+ \rightarrow ^1\Sigma_g^+$, is only allowed by spin-orbit coupling, leading to a decay time of $\tau_3 = 1.6\ \mu$s [98]. Therefore, scintillation in argon has two components: fast and slow, originated from the singlet and triplet decays respectively, that can be separated thanks to the significant difference in their lifetimes.

The population ratio of the two Ar excited molecular states, $r = p(^1\Sigma_u^+)/p(^3\Sigma_u^+)$, depends strongly on the ionisation density of the track, which is directly determined by the incident particle, meaning that light particles, such as electrons and gammas will lead to a ratio of $r \simeq 1/2$, while heavier particles, including neutrons, α particles and fission fragments, will show $r \simeq 4/5$ [98]. Consequently, the pulse shape will be different depending on the type of interacting particle, which constitutes an important tool for particle identification and eventually background discrimination in argon. ArDM results on discrimination will be presented in Chapter 4, Section 4.3.

Given the large separation in time of the two decay components (ns and μs), this technique is particularly effective for LAr; while it is less effective in LXe, since both scintillation components are of the order of ns [99]. Furthermore, since the total rejection power against background is obtained as the combined discrimination coming from the two described techniques, LXe detectors, with their low PSD rejection power, cannot be easily scaled up reaching large background free exposures. For this reason, the favourite option for a multi-ton noble liquid detector that is expected to achieve the limit given by the neutrino coherent scattering is based on the LAr technique.

Finally, the experimental technology based on LAr is well proved with a wide experience in handling massive cryogenic LAr detectors provided by, for example, the ICARUS neutrino experiment. The ICARUS-T600 detector with 760 tons of LAr (∼500 tons of sensitive mass), is the largest LAr-TPC ever constructed representing the state of the art for this detection technology and demonstrating the viability of the cryogenic operation and the high voltage system for the drift of the charge in long-term operation of multiton-scale LAr detectors [100]. This LAr-TPC technology is common to other present and future neutrino experiments, such as the Long-Baseline Neutrino Experiment (LBNE), which, with a 34-kton fiducial mass (50-kton) LAr-TPC, is expected to be fully constructed and ready for operations in 2022 [101].

2.2.2 Light and charge production mechanisms in argon

Charged particles crossing a target argon medium lose energy mainly by interacting with the electrons of the argon atoms. Collisions of the particles with the electrons lead to excitation and, if the transferred energy is large enough, to ionisation of the atoms [102]. In contrast to photons and charged particles, neutrons and WIMPs interact mainly with the nuclei of the medium. All these particles produce excited atoms Ar^* and ions Ar^+ in LAr, which results in the emission of scintillation light and ionisation electrons.

The emission of scintillation light in the LAr bulk is due to two mechanisms: the excited Ar^* luminescence and the recombination Ar^+ luminescence. The excited argon atoms, Ar^*, form excimers with other argon atoms, Ar_2^*, in a short time scale ($\sim 10^{-12}$s). These excimers subsequently decay into two argon atoms in the ground state, emitting a scintillation photon with energy hν [103]:

$$\begin{aligned}\mathrm{Ar}^* + \mathrm{Ar} &\rightarrow \mathrm{Ar}_2^*, & (2.43)\\ \mathrm{Ar}_2^* &\rightarrow 2\mathrm{Ar} + \mathrm{h}\nu. & (2.44)\end{aligned}$$

Since the energy of the emitted scintillation photons, 9.8 eV, is lower than the required energy to excite an argon atom to its first excited state, it cannot be reabsorbed and propagates within the detector, thus argon is transparent to its own scintillation light.

The argon ions, Ar^+, collide with Ar atoms and lead to the formation of an ionised argon molecule, Ar_2^+, in a short time scale. Eventually, they recombine with a free electron and form a highly excited argon atom, Ar^{**}, and an argon atom in the ground state. Finally, the Ar^{**} de-excites in a non-radiative process to Ar^{*} [105]:

$$\begin{aligned} \mathrm{Ar}^{+} + \mathrm{Ar} &\rightarrow \mathrm{Ar}_2^{+}, && (2.45)\\ \mathrm{Ar}_2^{+} + \mathrm{e}^{-} &\rightarrow \mathrm{Ar}^{**} + \mathrm{Ar}, && (2.46)\\ \mathrm{Ar}^{**} &\rightarrow \mathrm{Ar}^{*} + \mathrm{heat}. && (2.47) \end{aligned}$$

Then, Ar^{*} leads to scintillation emission by the excited luminescence process as explained before.

The required average energy to produce one scintillation photon in liquid argon, W_γ, is calculated dividing the deposited energy, E, by the total number of scintillation photons produced, N_γ, that is the sum of photons produced by excitation, N_{ex}, and the ones produced by ionisation N_i [106]:

$$W_\gamma = \frac{E}{N_\gamma} = \frac{E}{N_i + N_{ex}} = \frac{E}{N_i(1 + N_{ex}/N_i)}. \tag{2.48}$$

It is necessary to take into account that in argon $N_{ex}/N_i = 0.19 - 0.21$ and that the average energy required to produce an electron-ion pair in LAr, called W-value, is $W = E/N_i = 23.6$ eV, thus [107]

$$W_\gamma = \frac{W}{1 + N_{ex}/N_i} = 19.5 \text{ eV}. \tag{2.49}$$

In the case of particles with high linear energy transfer (LET), such as non-relativistic proton, alpha particles or fission fragments, the measured values for W_γ differ from the value calculated above. This is due to the fact that the excitation density is very high, thus the free excited argon atoms can diffuse and collide before forming excimers, given rise to a quenching effect in LAr [104]:

$$\mathrm{Ar}^{*} + \mathrm{Ar}^{*} \rightarrow \mathrm{Ar} + \mathrm{Ar}^{+} + \mathrm{e}^{-}, \tag{2.50}$$

The electrons emitted in this scintillation quenching process carry away the excess energy in the form of kinetic energy and spend it before recombining with parent ions.

Apart from the scintillation light, charge is also produced by ionisation of argon atoms, leading to electron-ion pair formation. In order to evaluate the conversion efficiency of the absorbed energy into measurable number of electron-ion pairs, the W-value is expressed as follows [108]:

$$W = E_i + E_{ex} N_{ex}/N_i + \epsilon. \tag{2.51}$$

where, E_i is the average energy loss per ionisation collision, E_{ex} is the average energy loss per excitation, N_{ex} is the number of excited atoms produced and N_i is the number of electron-ion pairs produced. Finally, is the average kinetic energy of the ionisation electrons with energy below the lowest excitation level of argon. For noble gases, the ratio W/I_{gas}, with I_{gas} the ionisation potential of the atom, is about 1.7, meaning that ∼40% of the absorbed energy is converted into free charge. In liquid phase, the ratio is close to 1.6, thus ∼60% of the absorbed energy is converted into ionisation electrons [102].

In the absence of an electric field, all electrons and ions released by absorbed radiation eventually recombine and generate a flash of UV light. The recombination process is usually described assuming that a dense plasma of positive and negative ions is formed along tracks of ionising particles. According to this theoretical model [109], both the electrons and the ions are described by the same spatial distribution function. This theory of columnar recombination, which provides good agreement with experimental data, predicts the dependence of the free ion yield on the electric field in the form of

$$Q = \frac{Q_0}{1 + K/E}, \tag{2.52}$$

where Q_0 is the total charge and K is the recombination coefficient. Since the recombination rates are so high in detectors filled with noble liquids, a strong field, applied in a time projection chamber, is required to reduce the charge loss due to recombination and to drift the electrons towards the charge readout plane of the detector.

The experimental data acquired from ionisation chambers filled with dense noble gases and irradiated with relativistic electrons prove the effectiveness of an electric field (∼1 kV/cm) to increase the percentage of charge collected, Q, as it is shown in the plot of Figure 2.9, in which the percentage of charge collected increases significantly with the applied drift field. In addition, the data show that there is a saturation effect of the collected charge expressed as function of the drift strength, achieving ∼80% of total charge collected for a drift field of ∼1.7 kV/cm [110].

2.2.3 Time projection chambers and electroluminescence in argon

Argon Time Projection Chambers (Ar-TPCs) consist of a detection volume filled with gas and/or liquid in an electric field with a position-sensitive charge readout and often also with a light collection system. The ion/electron pairs generated in LAr can partly recombine, producing light, or can be separated through a drift field in an Ar-TPC, thus migrating to the anode and cathode respectively. In a typical Ar-TPC, photon sensors, such as PMTs, are present to detect the scintillation photons, while a constant field drifts the electrons to the charge readout. Charge measurement can be done through the induction or the collection of the electrons on

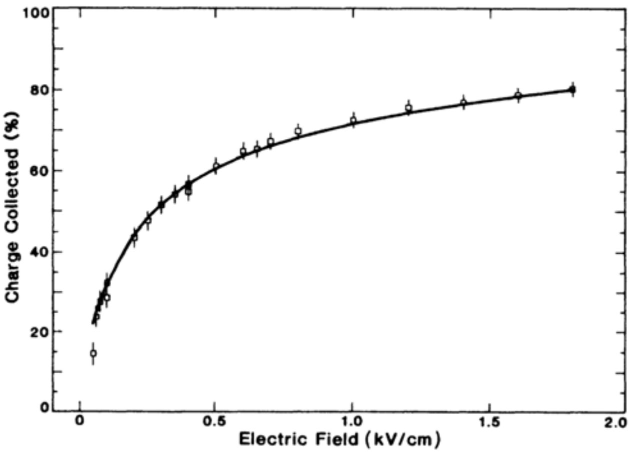

Figure 2.9: Fit to the charge collected in LAr as a function of the drift electric field (kV/cm) [110].

thin wires placed directly in liquid or, in case of a double phase liquid-vapour detector, through the extraction of the electrons from the liquid and their multiplication in the gas region placed above the sensitive volume. Since WIMP interactions are typically of the order of tens of keV and the ionisation yield in LAr is $42\,\mathrm{e}^-/\mathrm{keV}$, the charge amplification becomes necessary to detect the ionisation electrons. Additionally, the advantage of having a double-phase detection technique lies on the fact that both scintillation light and ionisation charge can be measured with the same device, providing a particle identification tool and a powerful discrimination method between nuclear recoils and electron recoils, produced by background events.

A typical double-phase Ar-TPC like ArDM is schematically represented on Figure 2.10. The argon excimers decay radiatively, emitting 128nm VUV primary scintillation light (S1) [111]. Since S1 cannot be reabsorbed by neutral argon atoms (because the energy of the single atomic excited state is too high), it propagates within the detector. In this case, the light detection is performed by two arrays of PMTs placed on the top and bottom parts of the detector, as it is shown in Figure 2.10. Both the inner surface of the detector and the PMTs are covered by a wavelength shifter that converts the VUV light into ~420 nm, allowing its detection.

The electrons produced by the interaction in liquid that do not recombine are drifted towards the interface liquid-gas by a uniform electric field, E_l, typically of the order of ~1kV/cm, perpendicular to the readout plane. The fraction of the ionisation charge that is detectable, R, depends on the applied electric field and also on the local ionisation density, since electrons not only recombine with the parent ions, but also with other ions produced within the charged particle track. Therefore,

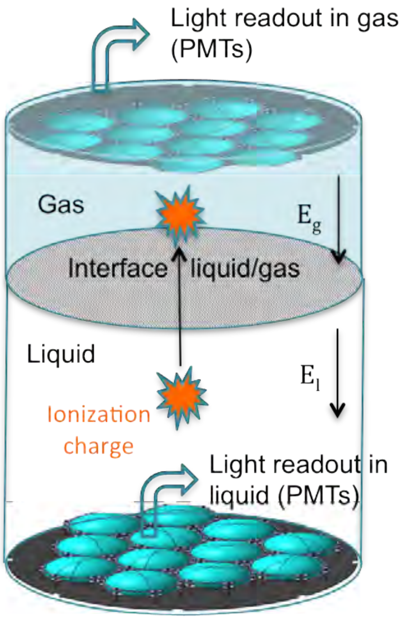

Figure 2.10: Scheme of the ionisation charge production and light detection in a TPC.

R is expressed by the modified Birk´s equation [112]:

$$R = \frac{A}{1 + \frac{k}{\varepsilon}\frac{\mathrm{d}E}{\mathrm{d}x}}. \tag{2.53}$$

where $A = 0.800 \pm 0.003$ and $k = 0.0486 \pm 0.0006$ (kV/cm)(g/cm^2)/MeV are obtained from the fit to the 3-ton ICARUS data [113], ε is the electric field strength and $\mathrm{d}E/\mathrm{d}x$ is the average energy loss per unit of path length, also called stopping power, which is proportional to the ionisation density. This approximation is valid and provides an accurate description for recombination in the range $0.1 < \varepsilon < 1.0$ kV/cm and $1.5 < \mathrm{d}E/\mathrm{d}x < 30$ MeV/(g/cm^2).

The detectable fraction of ionisation charge also depends on the impurities present in LAr since, some of them, such as N_2, O_2 and CO_2, capture the ionisation electrons and prevent them from being drifted [114]. Due to the interaction with impurities, the number of free electrons decreases with time following an exponential form:

$$N_e(t) = N_e^0 e^{-t/\tau_e}, \tag{2.54}$$

where τ_e is the lifetime of drifting electrons, which decreases with the concentration of impurities, and N_e^0 is the initial number of electrons that do not recombine. Since each impurity has a particular attachment rate coefficient that depends on the cross section, which is dependent on the electric field strength, argon purity is usually expressed as a function of oxygen equivalent concentration, $[O_2]_{eq}$. Therefore, assuming that all the argon impurity contamination is due to oxygen, the electron lifetime is estimated to be [115]:

$$\tau_e(\mu s) \simeq \frac{300}{[O_2]_{eq}(\text{ppb})}. \tag{2.55}$$

The drift speed of the electrons towards the gas phase can be expressed as a linear function with the temperature as follows [116]:

$$v_d(T,\varepsilon) = (P_1(T-T_0)+1) \quad P_3\varepsilon\ln \quad 1+\frac{P_4}{\varepsilon} \quad + P_5\varepsilon^{P_6} \quad + P_2(T-T_0). \tag{2.56}$$

This polynomial function that evidences the increase of the drift velocity with the electric field strength, has been obtained after measuring the drift speed, $v_d(T,E)$, for different electric field and temperature values contained in the ranges $0.5 \leq |E(\text{kV/cm})| \leq 12.6$ and $87 \leq T(K) \leq 94$ as it is shown in the plot of Figure 2.11. The obtained parameters after a fit to the data are written in Table 2.2.

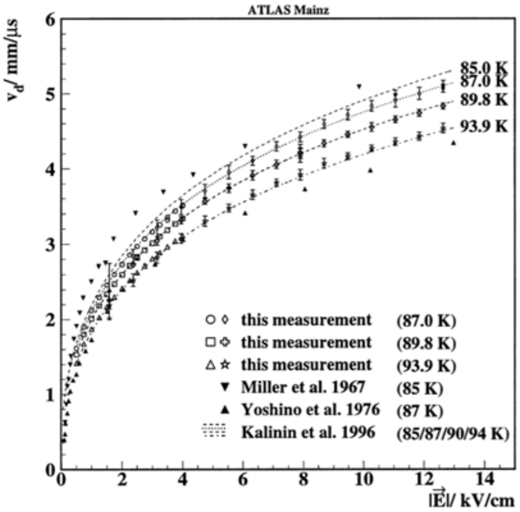

Figure 2.11: Drift velocity, v_d measured as a function of the electric field, $|E|$, in different temperature ranges. Results are compared with previous measurements [116].

Once the electrons reach the interface liquid-gas, it is necessary to overcome a potential barrier to extract them into the gas phase, which is experimentally lowered by applying a collinear electric field in gas, E_g (∼4 kV/cm). After the electrons

Parameter	**Value**
P_1	-0.01481 ± 0.00095 K^{-1}
P_2	-0.0075 ± 0.0028 K^{-1}
P_3	0.141 ± 0.023 KV/cm^{-1}
P_4	12.4 ± 2.7 KV/cm
P_5	1.627 ± 0.078 KV/cm^{P_6}
P_6	0.317 ± 0.021
T_0	90.371 K (Fixed)

Table 2.2: Result of the global fit of parameterisation written in Equation 2.56 to the total set of data points from two different drift sections [116].

are extracted into the gas phase, they acquire energy thanks to the electric field applied in gas and interact with argon atoms, leading to the emission of secondary electroluminescence scintillation light when the produced excimers relax to the state Ar_2^*, that decays to the ground state emitting a VUV photon [117]:

$$\mathrm{Ar}_2^* \;\rightarrow\; 2\mathrm{Ar} + \mathrm{h}\nu. \tag{2.57}$$

If the field is adjusted so that the energy of drifting electrons is between the excitation and ionisation thresholds, which depend on the density of the argon gas, the number of generated photons in the gas phase will be proportional to the drift length in gas and also to the strength of the electric field. These thresholds are usually expressed as reduced quantities, dividing by the number density of the argon gas, n, so that the reduced secondary scintillation yield is defined as the number of photons produced per electron and per path length divided by n [118]:

$$\frac{Y}{n} = 0.081\frac{\varepsilon}{n} - 0.190, \tag{2.58}$$

where Y/n is given in units of 10^{-17} photons electron^{-1}cm^{2}atom^{-1} and ε/n is given in units of 10^{-17} Vcm^{2}atom^{-1}. Considering a drift field in gas argon of 3 kV/cm, an electron produces of the order of 80 photons per cm of drift path.

The produced secondary photons (S2 signal) are mainly detected by the top PMT array as a delayed coincidence relative to the primary scintillation (S1 signal). Since the number of secondary scintillation photons produced in gas is proportional to the number of extracted electrons, the detection of the ionisation charge is made through the detection of the proportional scintillation light.

Due to the fact that both S1 and S2 are detected and diffusion in LAr is quite low, which preserves the position interaction in the drift, the LAr-TPC allows 3D position reconstruction. The xy interaction coordinates can be reconstructed by using the light pattern of the top PMT array, while the z coordinate is reconstructed taking into account the drift velocity and the delay in S2 with respect to S1 signal.

Chapter 3

The ArDM experiment

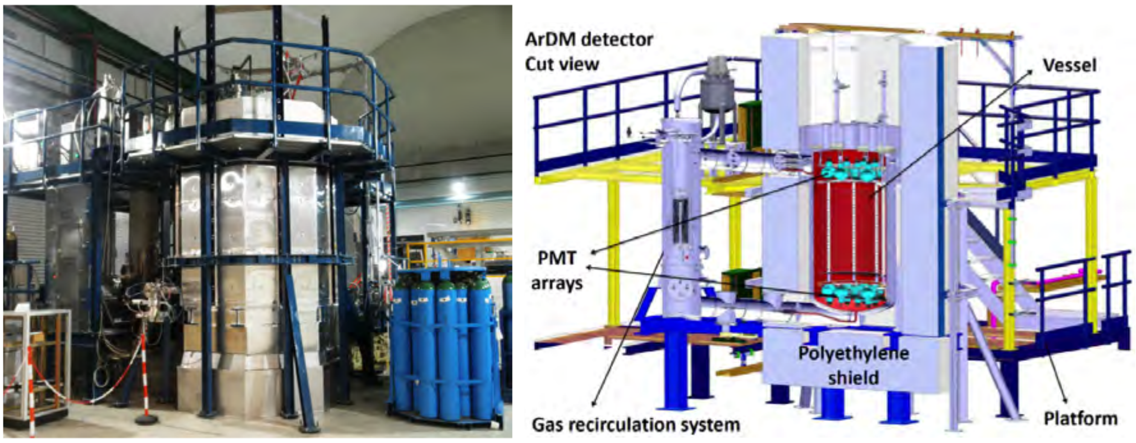

Figure 3.1: (Left) ArDM detector installed underground in hall A of LSC. (Right) Schematic drawing of the main ArDM detector parts, specifying the location of the detector vessel with the PMT arrays, the gas recirculation system and the polyethylene neutron shield.

ArDM is a collaboration led by two research groups, the ETH of Zurich and CIEMAT of Madrid, with the support of CERN and LSC. The ArDM experiment, which is installed and currently operating in the Canfranc Underground Laboratory (LSC) in Spain, as shown in Figure 3.1 (left), is a ton-scale double-phase liquid-gas argon TPC, whose aim is to measure signals from WIMPs [119]. The elastic scattering of WIMPs from argon nuclei could be measurable by observing free electrons from ionisation and photons from scintillation, which are produced by the recoiling nucleus interacting with neighbouring atoms, being the typical kinetic energy of these recoils in the range of 1-100 keV. As it has been explained previously, the advantage of having a double-phase detection technique lies on the fact that both scintillation light and ionisation charge can be measured at the same time, providing a particle identification tool and a powerful discrimination method between nuclear recoils and electron recoils.

The experimental setup, schematically presented in Figure 3.1 (right), consists of a cylindrical dewar (vessel) with 80 cm diameter sensitive volume and a 112 cm maximal drift length, which is delimited by a reflector covered with a wavelength shifter. About 850 kg of ultra-clean liquid argon, which is used as target material, are contained in the sensitive volume. The scintillation and ionisation signals are detected by two arrays of 12 Hamamatsu photomultiplier tubes (PMTs), one immersed in liquid argon and the other one in gas, placed in the bottom and top parts of the detector respectively. The setup is completed with purification and recirculation systems, a cryogenic system composed by vacuum insulation and three cryocoolers to control temperature and a polyethylene neutron shield.

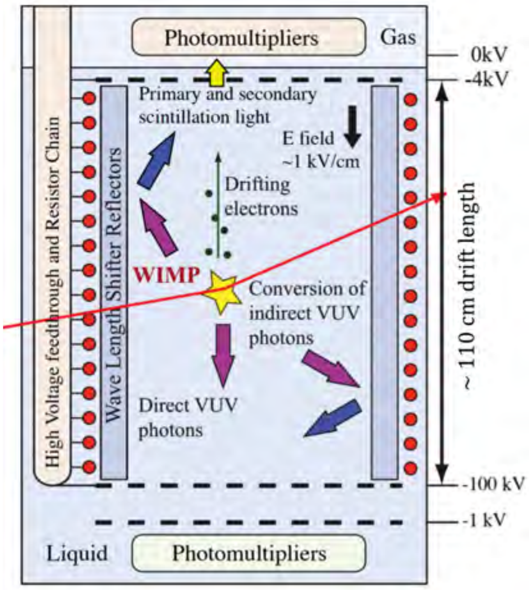

Figure 3.2: Schematic description of light production and detection in the ArDM LAr-TPC [111].

The detection process in the ArDM Ar-TPC is schematically represented on Figure 3.2. The primary VUV (128 nm) scintillation light (S1) is emitted when the argon excimers, produced by particle interaction in the liquid bulk, de-excite. This scintillation light is converted to the optimal detection wavelength (~420 nm) thanks to a wavelength shifter that covers the inner surfaces of the detector, including lateral reflector and PMTs. The re-emitted light can reach the bottom or the top of the detector, where it is detected by the two arrays of PMTs. The electrons produced by the interaction in liquid are drifted towards the interface liquid-gas by a uniform electric field of the order of 1 kV/cm, perpendicular to the readout plane. These electrons are extracted and accelerated from the liquid into the gas phase applying an electric field of 4 kV/cm, thus producing secondary electroluminescence scintillation light in gas (S2), proportional to the charge extracted in liquid.

3.1 Cryostat, vacuum and cooling systems

ArDM is composed by a complete vacuum insulated cryogenic system consisting of a double-volume cryostat with high vacuum tightness (better than 10^{-6} mbar), containing ∼2 t of LAr, gas/liquid argon purification and cooling systems.

The cryostat is composed by a cylindrical stainless steel dewar vessel with a inner diameter of 1 m and 2 m of total height, which is made of four walls designed to shield the main volume from outside heat entering the vessel. There are two LAr circuits: the main one contains ultra-clean LAr and the second one is a cooling shield that stabilises the temperature of the first circuit. The two internal walls of the dewar vessel contain LAr, forming a cooling bath of 15 mm thickness, which provides thermal stability to the main volume inside; and in between the two external walls there is a vacuum region, which isolates the system from environmental temperature. The main detector volume of 1.7 m^3 contains $\sim$ 1.4 m^3 of ultra-pure LAr for double-phase operation, that is kept free of impurities by establishing a slight over pressure (∼50 mbar over atmosphere pressure), which prevents these impurities coming from possible existing minimal leaks to reach the LAr volume.

The vacuum insulation of the ArDM cryostat is divided into two separate volumes with identical instrumentation: the first one surrounding the detector vessel and the other one dedicated to the purification and cooling systems, as it is shown in the scheme presented on Figure 3.3. Having two parallel vacuum systems allows substituting one of them by the other one in case of failure, which ensures the safety of the setup. The lateral and bottom parts of the detector vessel have been insulated by covering them with highly reflecting super insulation foils to minimise heat input due to radiation effect and the pressure is constantly kept lower than 10^{-4} mbar. In order to monitor the pressure and the vacuum level, both volumes are equipped with independent pressure sensors for the range between 0.1-1 bar and a vacuum gauges for lower values. The vacuum volume is separated from the pumping system, consisting of a turbo molecular pump and a backing oil pump, by a pneumatic gate valve. A third vacuum system is used to clean the LAr volume before filling.

The top part of the detector vessel, which is the only part that is not cooled or vacuum insulated with an active mechanism, is closed with a 40-mm-thick stainless steel top flange with feedthroughs for different connexions, a vacuum valve and several temperature and pressure sensors. In order to reduce the heat input from the top flange, a passive insulator has been installed on top of it, currently polystyrene

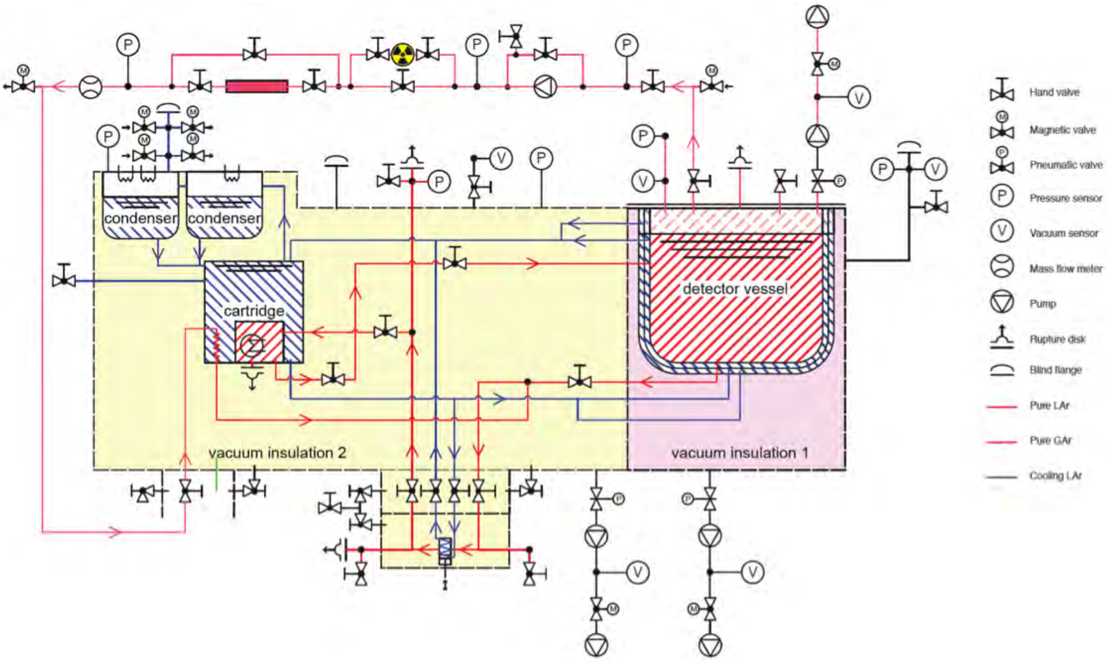

Figure 3.3: Instrumentation diagram of the ArDM experiment.

in the form of bags filled with small 5 mm diameter balls forming a layer of about 40 cm in thickness.

Due to the 87 K boiling point of argon, the system needs to be constantly cooled to compensate the heat input, maintaining at the same time stable temperature and pressure conditions. For this reason, a dedicated cooling system consisting of three 300-W Gifford-MacMahon cryocoolers has been installed and operates on the cooling bath by re-condensing the boil-off argon gas. Thus, the LAr contained in the main volume is cooled via heat conduction through the vessel inner wall, which connects it thermally to the cooling bath. The cryocoolers are maintained at full power and the control of the cooling power is done by three electrical heaters located in the cryocooler heads. In an emergency due to a loss of cooling power during an extended period of time, the required high stability of temperature and pressure conditions inside the main volume is obtained thanks to the large mass of liquid and to the possibility of evaporating LAr from the bath.

3.2 Drift cage, extraction grids and high voltage system

The active LAr target volume is contained entirely inside a cylindrical optically closed surface, which is delimited by the top and bottom PMT arrays and the drift cage, whose inactive surface is entirely covered by the main side reflectors. These reflectors, which will be described in detail in the next Section, have been designed to ensure that incident light will be reflected and converted to optimal wavelength for its detection by the PMT arrays.

Figure 3.4 (left) shows a schematic drawing of the ArDM detector, where both PMT arrays are represented together with the drift cage, which is composed by 27 ring-shaped stainless steel electrodes (field shapers) of 4 mm diameter and 1 mm wall thickness set to linearly decreasing potentials from bottom (near the cathode) to top thanks to a resistor chain, creating a uniform drift electric field of the order of $\sim$ 1 kV/cm. The drift cage is cylindrical with 112 cm in height, 80 cm in diameter and a vertical flat section in one side, aiming to hold the high voltage system. The active volume of about 540 L, which corresponds to 750 kg of LAr, is delimited on the top part by two extraction grids, set near to ground potential, and by the cathode on the bottom part, with a maximum potential of 100 kV.

The two horizontal extraction grids, the bottom one placed in liquid and the top one placed in gas phase, are separated 10 mm and have independent hanging systems. The vertical position of the grids can be adjusted so that the LAr surface remains in the centre. In order to create an electric field strong enough to extract the ionisation electrons generated in liquid into the gas phase, the required voltage difference between top and bottom extraction grids is of the order of 4 kV.

The cathode, which is installed on the bottom part of the detector, above the bottom PMT array, consists of 0.5-mm-thick wires regularly spaced in 20 mm intervals and stretched over a ring-shaped frame in two orthogonal directions. The rigidity of the field cage structure is ensured by assembling the cathode and the field shapers to seven polyethylene (PE) pillars, which are vertically distributed with constant distance of 40 mm between one and the other, as shown in Figure 3.4 (left).

The high-voltage (HV) system has been specifically designed for the ArDM experiment, following a model previously used by ICARUS. This system, which has been successfully tested to sustain HVs higher than 150 kV, consists of a 1.4-m-long coaxial conductor made of a thin stainless steel tube with ultra-high molecular weight polyethylene (UHMW PE) as insulator. It is connected to the cathode with a spring receptacle that can tolerate slight thermal contractions of the detector structure and to an external 100-kV/1-mA power supply from Heinzinger electronic GmbH.

In Figure 3.4 (right) the totally mounted field cage is shown, hanging from the

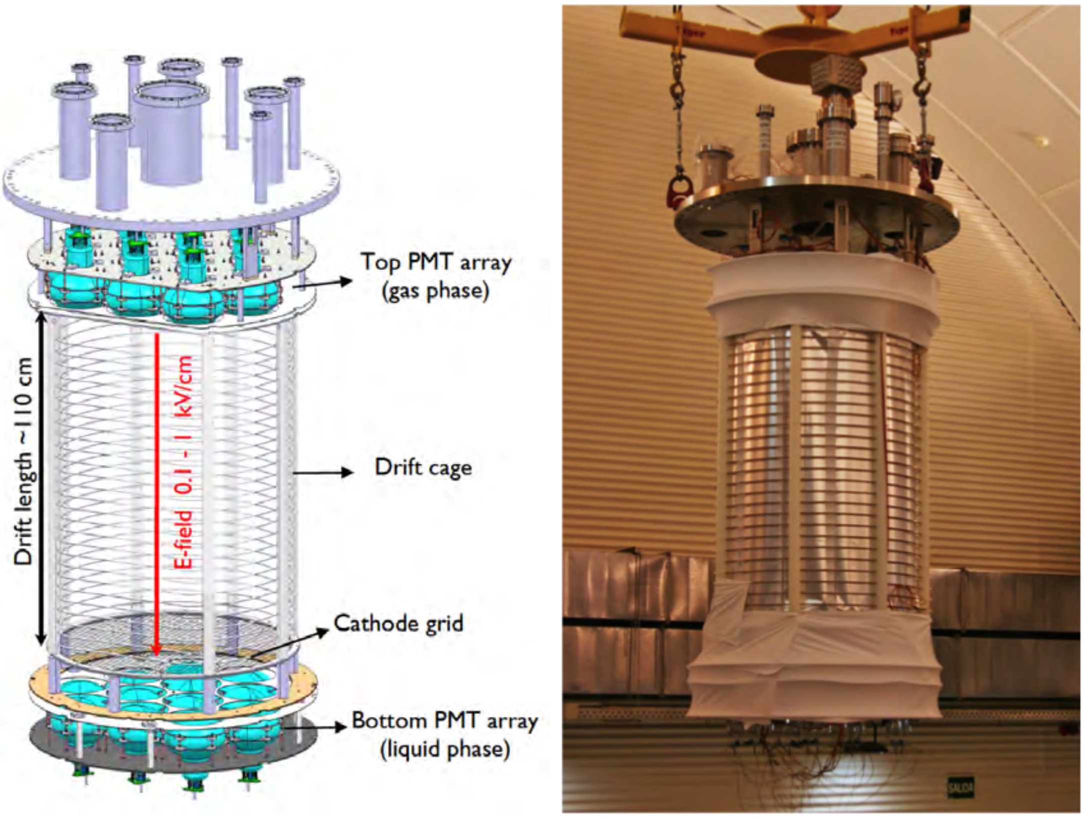

Figure 3.4: (Left) Schematic drawing of the ArDM field cage, showing also the position of the PMT arrays and the cathode grid. (Right) ArDM TPC hanging from the crane during installation, with the field cage covered by the reflectors.

top flange by the laboratory crane during the underground installation. The main reflectors are clearly distinguishable covering the lateral surface of the field cage.

3.3 Reflectors

There are three different type of reflectors installed inside the ArDM detector: the main reflectors, installed in the sides of the drift cage, the top/bottom main reflectors, perpendicular to the previous ones, and the top/bottom side reflectors.

The main reflectors, covering the whole lateral area of the drift cage, are made of 200×1080 mm^2 Tetratex foils (TTX), which have been coated with tetraphenyl butadiene (TPB), an organic wavelength shifter (WLS). The TPB converts vacuum ultraviolet (VUV) argon scintillation light peaked around 128 nm into blue visible wavelength ($\sim$ 420 nm), making possible the light detection on the PMTs, installed on top and bottom parts of the detector. TTX shows an important advantage with respect to standard Polytetrafluoroethylene (PTFE), commonly known as teflon, since TPB molecules attach better to this material due to the non smooth surface. In order to provide the necessary mechanical rigidity, a multi-layer plastic film reflector, Vikuiti$^{\mathrm{TM}}$ ESR (Enhanced Specular Reflector) from 3M$^{®}$ was sewed on the back side of the TTX.

An extensive study of different WLS was performed by the ArDM collaboration in order to select the best possible option for the coating of several detector components. Among the available WLS, organic WLS were selected for their fast response, due to the radiative recombination process of electron/hole pairs at the benzene rings present in their chemical structure. This fast response is required for recording the waveform of the fast scintillation component ($\sim$ns) without distorting it and ensures the possibility of using pulse shape discrimination methods. Some of the considered WLS are p-Terphenyl, POPOP, PPO and bis-MSB, but the one that showed the best light yield to convert argon scintillation light for its optimal detection on the PMTs was TPB. Furthermore, TPB coatings show a good adherence for long periods of time, high resistance to mechanical abrasion and can be removed if necessary by using toluene, chloroform ($CHCl_3$) or other organic solvents. Finally, the TPB coatings have been tested in high vacuum conditions for an extended period of time without any evidence of aging.

The deposition process of TPB on the inner surface of the main reflector is based on vacuum evaporation, which showed to be the most efficient method for TPB deposition among the tested ones [120], ensuring a precise thickness of the deposition layer of the order of 1 mg/cm^2. This process was performed by using the evaporator developed for ArDM at CERN, schematically represented on Figure 3.5 (left), which consists in two parts: a horizontal tube with pumping connection on its closed end and an access flange with several crucibles, which are electrically nested

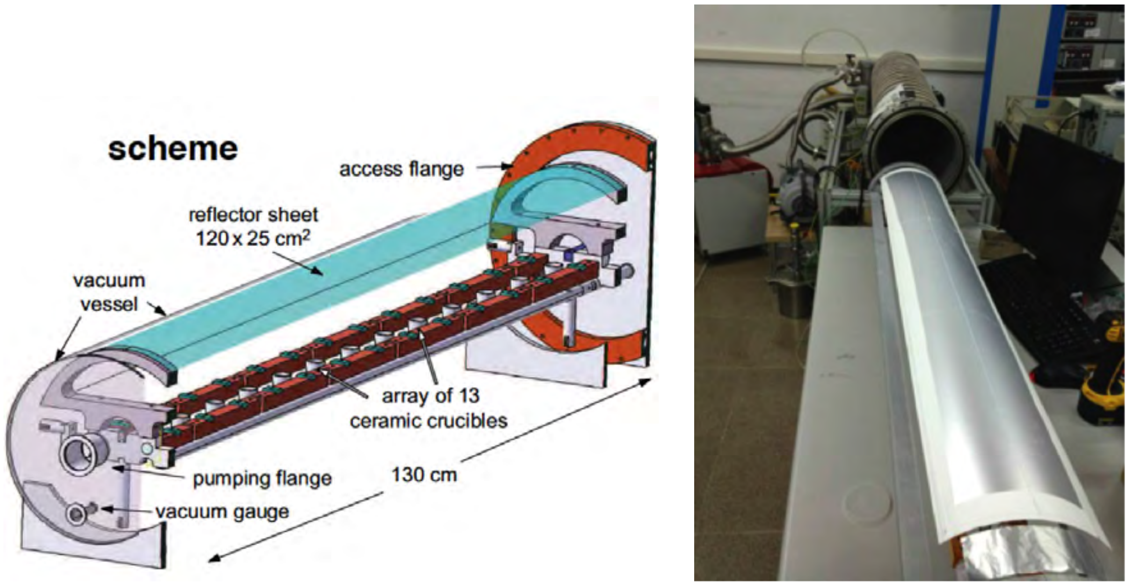

Figure 3.5: (Left) Drawing of the TPB evaporator showing the position of the reflector sheet with respect to the crucibles and the other evaporator components. (Right) One reflector foil prepared for being introduced in the TPB evaporator.

with resistors. The substrate to be coated is introduced in the vacuum chamber as shown in Figure 3.5 (right) and kept at a fixed distance above the crucibles thanks to a support of 100 μm wires placed in crescent arrangement. After filling the crucibles with TPB powder, evaporator pumping with a turbo molecular pump starts until it reaches 10^{-5} mbar, then the heating current in the crucibles is switched on and left running for several hours to heat up the crucibles to approximately 200 °C, so the TPB evaporates, it diffuses approximately isotropically and forms a thin deposition layer over the surface of the reflector. The total amount of TPB deposited on 20 reflector foils (including several spares) has been calculated to be 43 g, while 104 g of TPB where introduced in the crucibles, with the resulting efficiency of 42% in this coating process.

The top/bottom reflectors, which cover the area around the PMT windows, are made of a 1-mm-thick PTFE and were cut with water jet in a shape of a disc with 12 circular holes (200 mm in diameter) to insert the PMT windows of each array. These reflectors were coated with TPB using a different method than the one explained above. The change in the coating method is due to the fact that for a very large surface, vacuum evaporation is not convenient because it requires an evaporation facility involving a vacuum system, which is large enough to host the substrate. The coating technique used for the top/bottom reflectors, called dipping method, consists of immersing the substrate in a TPB solution, take it out and leave it to be dried so that the TPB can form a thin layer after the solvent has evaporated completely.

The third type of reflectors, the top/bottom side ones, are uncoated TTX foils, wrapping around the space between the other two type of reflectors previously described. Since the PMT plane is larger than the top/bottom face of the drift cage, the top/bottom side reflectors have a slightly conical shape, which has been kept uncoated in order to avoid the conversion of the scintillation light when it is produced outside of the active volume.

Over the total inner surface, approximately 14% is covered by the PMT windows and 85% by the reflectors. Among the reflectors, 80% of the surface is coated with TPB, without taking solid angle into account.

3.4 Light readout system: PMT arrays

The ArDM detector readout is composed by 24 low radioactivity 8” cryogenic PMTs aiming to measure the scintillation light [121], that are distributed in two independent arrays of 12 PMTs each, one immersed in LAr on the bottom part of the detector and the other one placed on top, above the drift cage in the argon gas phase. In each array, the 12 PMTs are attached to a common stainless steel base support plate in triangular symmetry positions, achieving a mirror symmetric configuration for the two arrays, as it is shown in Figure 3.6 (left). Each PMT is held individually with two stainless steel rings and small polyethylene (PE) clamps, as it can be seen in Figure 3.6 (left). This configuration optimises both the symmetry in light collection and the packing of the PMTs at the same time and ensures the PMT glass safety against thermal contraction due to cryogenic temperatures.

The PMTs, manufactured by Hamamatsu R5912-02MOD-LRI, are made of radiopure borosilicate glass and detect visible light by bialkali photocathode with platinum underlay, which preserves electrical conductivity at cryogenic temperatures. Their 14 dynode stages ensure the possibility to reach a gain of 1×10^9 at typical operation high voltages of 1700 V. In order to achieve the gain of 5×10^7, corresponding to a single photoelectron peak pulse height of 20 mV and 4 pC of collected charge, the adjustment of the operation high voltage for the 24 PMTs is performed in the relatively low range of 976-1333 V, which avoids electric discharges in cold argon gas phase.

Since these PMTs are designed to detect visible light, it is necessary to coat their windows with TPB, as it was also done with the reflectors. However, the coating method requires a specific optimisation to avoid the reduction of the light detection efficiency, considering that part of the incident light has already been converted into visible wavelength by the main side reflectors. This PMT coating process, which lasts about a day per PMT, was performed by the Thin Film & Glass CERN group by using an evaporation chamber with a stainless steel crucible set in a configuration

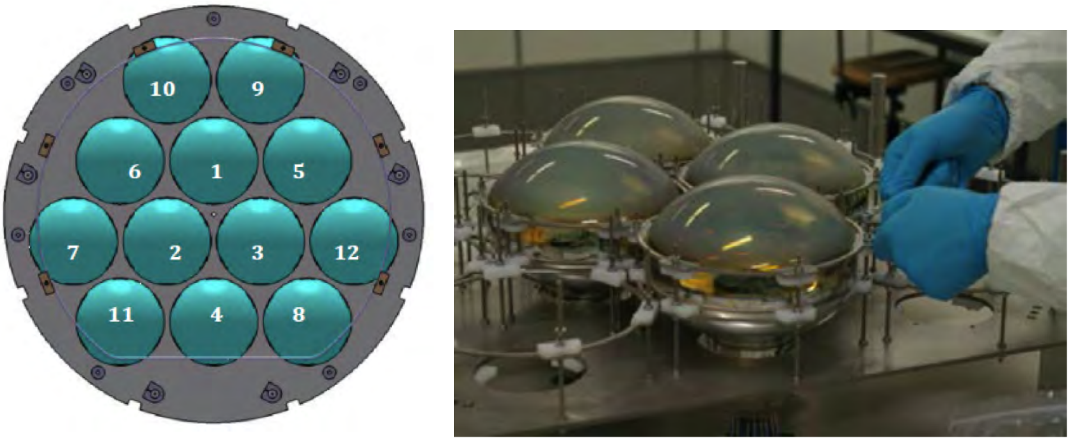

Figure 3.6: (Left) Diagram illustrating PMTs attached to a stainless steel support plate, showing the triangular distribution in one array. (Right) Installation of the PMTs in one array. Each PMT is held individually with two stainless steel rings and small polyethylene clamps.

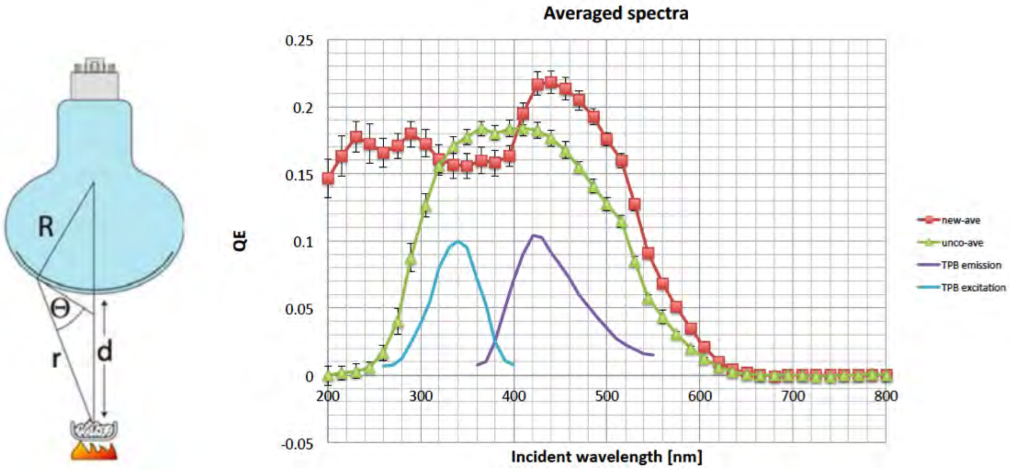

Figure 3.7: (Left) Scheme of the evaporation setup used for the TPB coating process of the PMTs. (Right) Measured quantum efficiency (QE) spectra for each individual PMT before and after coating. The QE enhancement in the region below 300 nm ensures the effectiveness of the coating process.

as the one shown schematically in Figure 3.7 (left), where $d = 250$ mm is the distance from the centre of the photocathode to the crucible. The thickness of the resulting deposited layer depends on the angle following the expression:

$$T(\Theta) = T_0 \frac{d^2}{r^2} \cdot sin\Theta, \tag{3.1}$$

where T_0 is the thickness at the centre ($\Theta = 90^o$) and d is the already mentioned distance from the centre of the photocathode to the crucible. The distances r and $R = 131$ mm and the angle Θ are the ones defined in Figure 3.7 (left). Since previous ArDM collaboration studies had shown that the maximum conversion efficiency is reached at a deposition of 0.05 mg/cm^2 and stays constant at larger thicknesses, a value of $T_0 = 0.2$ mg/cm^2 was chosen.

The quality of the resulting coating was evaluated by measuring the quantum efficiency (QE) spectra for each individual PMT before and after coating. The QE curve measured before coating (averaged over the bottom PMTs), which is represented by triangles in the plot shown in Figure 3.7, is clearly lower than the one obtained after coating, represented by squares, in the region below 300 nm, which ensures the effectiveness of the coating process. The apparent decrease in the range 300-415 nm after coating can be explained for a lack of symmetry and possible internal reflections in the used setup.

3.5 Argon purification and recirculation systems

As it has been introduced in previous Sections, impurities such as N_2, CO_2 and O_2 can reabsorb VUV light and attach electrons, affecting the detection of scintillation light and the drift of the charge. Consequently, achieving a high purity of the liquid argon is an essential requirement for the detector operation and, for this reason, the ArDM cryogenic system is equipped with a purification cartridge located outside the detector vessel. This cartridge, which is filled with copper powder to filter the oxygen out of argon, is connected to the detector vessel by two stainless steel tubes as illustrated in Figure 3.8. In order to filter the argon, it is necessary to establish a constant recirculation of the LAr from the detector vessel to the purification cartridge and back, which is performed by the action of a membrane pump.

Complementary to this system, there are also external gas purification and recirculation systems. These systems consist of a double diaphragm pump, a high flow gas purification cartridge, a flow meter and the recirculation line, made of stainless steel pipes of 40 mm in diameter. The cold gas from the top of the detector is warmed up by heaters on its way to the pump and pushed through the cartridge. The purified gas is then re-condensed and sent back to the bottom of the vessel. The control of the temperature and pressure is performed in three different points of the recirculation line: before the pump, between the pump and the cartridge, and after the cartridge.

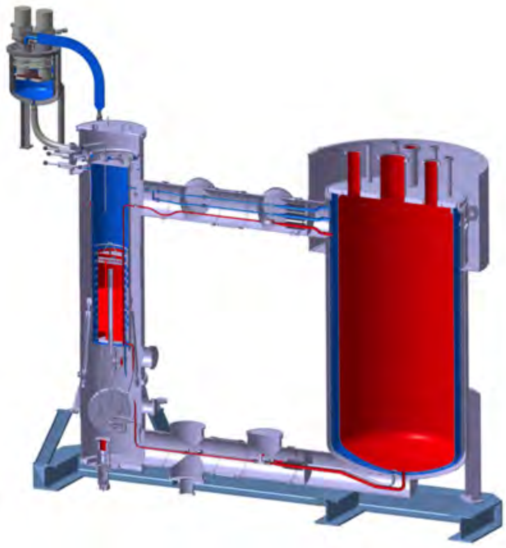

Figure 3.8: Drawing of the recirculation and purifications systems of ArDM, showing the detector vessel on the right part and the purification cartridge and the condenser on the left part. The pure LAr circuit is marked in red.

3.6 Polyethylene neutron shield and calibration systems

Neutrons coming from environmental sources are one of the most problematic background contributions in direct Dark Matter detection experiments, thus it requires dedicated systems for its reduction. In ArDM, a neutron shield consisting of a polyethylene wall of half a meter thickness, that completely surrounds the detector, has been installed. The shield, whose conceptual design is drawn in Figure 3.9 (left), has an octagonal prism shape with a height of 4.47 m, 1 m on the side and a base inscribed in a circle of 2.6 m of diameter. This shield, with a total weight of 17 tons, is divided in three parts: a lateral body, made out of 12 tons of polyethylene, and the top and bottom covers (2.5 tons each), being the top one removable to make possible the access to the top part of the detector. Each ring composing the lateral body is formed by individual pieces as the ones shown in Figure 3.9 (centre). To provide quick access to the top flange of the detector, a removable column that can be easily separated in one block by the laboratory crane has been installed as shown in Figure 3.9 (right). The design of the shield ensures that the minimum thickness of polyethylene for neutrons to traverse is 50 cm, reducing the rate of neutrons hitting the detector vessel from about $1.2 \cdot 10^4$ neutrons per hour without shield to 0.7 neutrons per day. Only 12% of these neutrons ($\sim$0.08 neutrons/day), have an energy

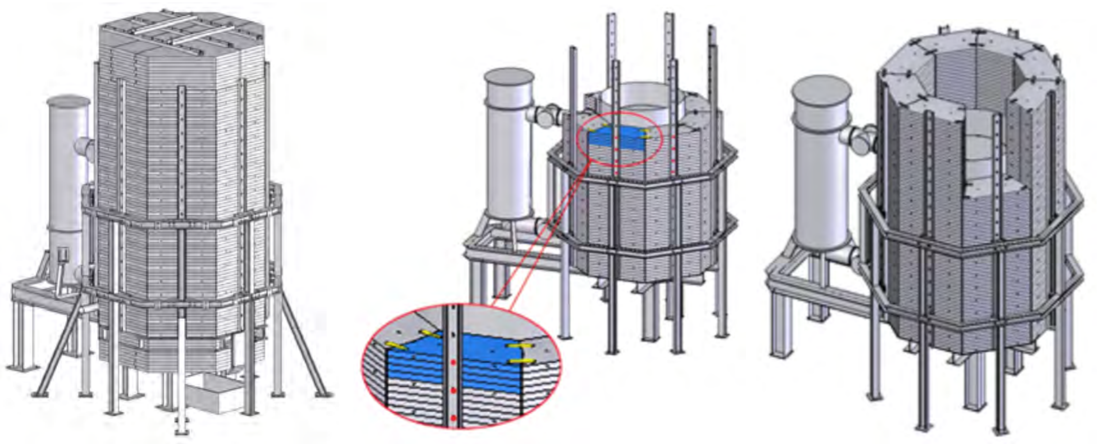

Figure 3.9: (Left) Scheme of the total polyethylene neutron shield including lateral part and top/bottom covers. (Centre) Drawing of the polyethylene shield partially mounted, showing an individual piece of one ring in blue. (Right) Detail of the removable column of the polyethylene shield, installed to provide quick access to the top flange of the detector.

above 100 keV and thus are able to produce nuclear recoils that can be detected with ArDM.

Due to the high amount of polyethylene composing this shield and in order to ensure the safety of the experiment and the laboratory against fire, several protection requirements were fulfilled. The fire protection of the shield external lateral surface was completed in several phases. The first step was to cover the external surfaces of the shield with fire retardant paint. To finalise the process, the whole lateral surface was covered by two protective layers made of different materials: thermal isolation sheet with mineral wool and 1-mm-thick aluminium layer. Finally, the junctions between different layers were sealed with aluminium foil, which would distribute the heat over the whole surface in case of external fire [122]. Figure 3.10 shows the lateral polyethylene shield before and after installing the fire protection.

The shield has a drawer on its side, which is placed at half of its height and it is made of the hole left by a removable polyethylene brick, as shown in the picture of 3.11 (Left). This drawer, which has been designed at CIEMAT, can be slid out and in from outside to introduce external neutron or gamma sources for calibration. The source can be attached to a specifically designed supporting system, including a drilled lead brick for collimated gamma calibration, shown in the picture of Figure 3.11 (Centre). This lead brick is introduced in the drawer with the help of a stainless steel bar, which is screwed to the polyethylene supporting part of the system, as shown in Figure 3.11 (Right).

In addition, two guiding pipes made of corrugated plastic have been installed

Figure 3.10: (Left) Lateral view of ArDM experiment showing the neutron shield already painted with fire retardant paint and before installing the outer fire protection layers. (Right) Lateral view of ArDM experiment showing the neutron shield with the outer fire protection already installed. The entire lateral surface is covered by two protection layers: an inner mineral wool thermal isolation sheet and the external aluminium layer.

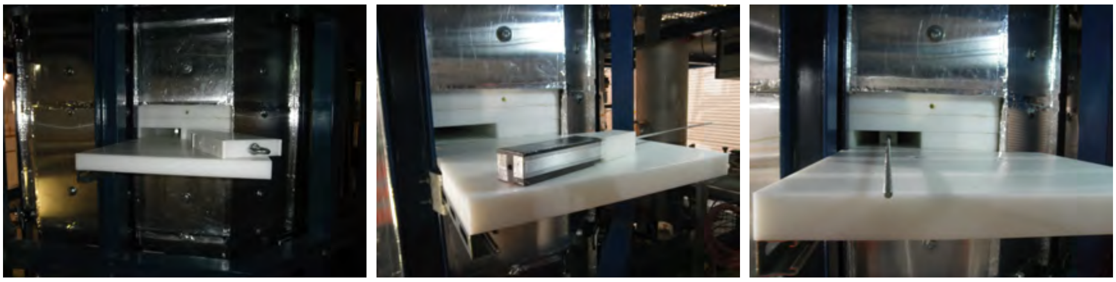

Figure 3.11: (Left) Calibration drawer formed by the hole left by a removable brick on the side of the polyethylene shield at roughly half of its height. (Centre) Drilled lead brick and supporting system for collimated calibration runs. (Right) Calibration setup introduced inside the polyethylene drawer during data taking.

inside the polyethylene shield structure, as shown in the scheme of Figure 3.12 (left). One of them is straight and vertical along the lateral face of the vessel, allowing gamma calibration at different z positions of the source, and the other one is circular around the vessel at about the middle of the height, which makes possible to take calibration data at different $x - y$ positions for the same z position of the gamma source.

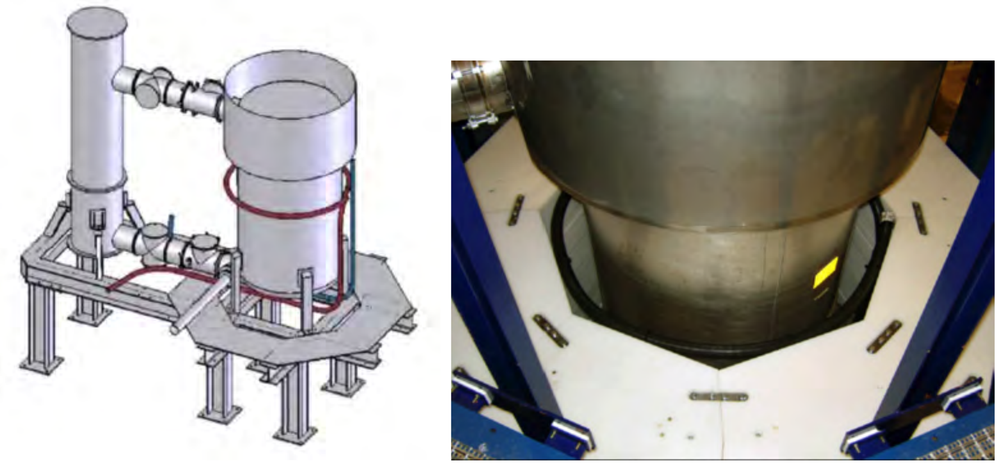

Figure 3.12: (Left) Scheme of the calibration pipes: the vertical one, depicted in blue and designed for gamma calibration at different z positions, and the one surrounding the detector vessel, intended for different $x - y$ position calibrations and drawn in dark red. (Right) Circular calibration pipe made of black corrugated plastic and installed inside the polyethylene lateral neutron shield at about the middle in height of the active volume.

3.7 Data acquisition and control systems

The data acquisition system (DAQ) of ArDM is composed by four electronic modules of 250-MHz 12-bit FADC (flash analog-to-digital converter) CAEN V1720 digitisers. A waveform of each PMT channel is recorded with 250-MHz sampling rate and a time window of 4 or 8 μs, resulting in 1024 or 2048 samples per event per PMT channel respectively. For 12-bit ADC the buffer size thus amounts to 2 or 4 kB/event/ch, respectively. This DAQ system has been tested up to the 2 kHz trigger rate, which is the one expected for LAr runs, by using a pulse generator. Each of the four digitiser boards recording signals from six PMTs is connected to the DAQ PC, containing two processors of eight cores each, via an optical link, with a expected limit of 80 MB/s in data rate ($\sim$ 320 MB/s with four optical links). After reading data to the digitisers, a dedicated software writes the data to hard disks with 86 TB of total storage space. The entire DAQ system is illustrated in Figure 3.13.

The DAQ can be controlled remotely and the data processing is fully automatised with the output being directly accessible via a data quality monitoring website. In

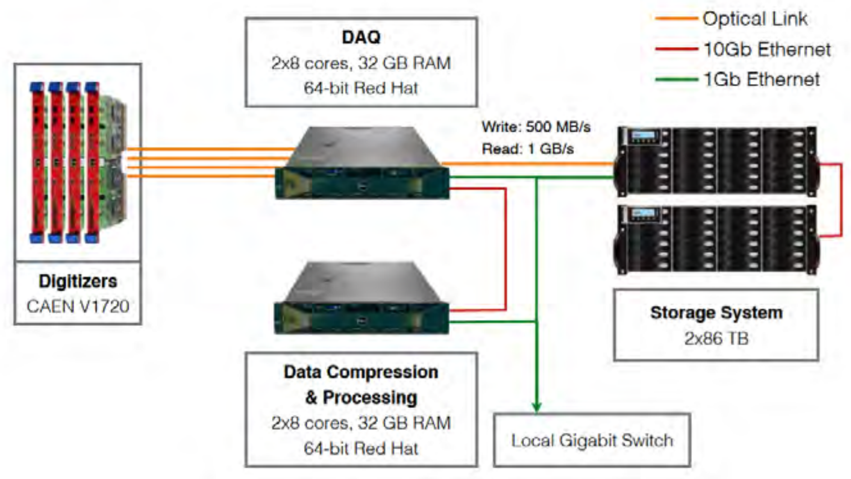

Figure 3.13: Scheme of the ArDM DAQ system including digitisers, DAQ PC, data processing and compression systems and storage. The type of connections between different units are also specified.

order to cope with the high data acquisition rate ($\sim$ 200 MB/s) expected for LAr runs, real-time data processing becomes essential and, consequently, an automatic process chain has been developed. Each run typically contains $\sim$90k events, which corresponds to an average trigger rate of $\sim$ 25 Hz in warm gas, $\sim$ 40 Hz in cold gas, $\sim$ 1.86 kHz in liquid with the neutron shied opened and $\sim$ 1.35 kHz in liquid with the neutron shield closed. The DAQ reads data from the four digitisers and writes a raw data file. At the same time, an index file that reconstructs full events out of four sub-events (each containing six PMTs) and is required for data processing is also generated.

A pseudo-online data processing software (LRAnalysis) has been developed to find hits from the raw waveform of each PMT and write the event information and the first-level analysis variables into a ROOT TTree, on which higher level physics analyses are performed. At the end of each run, an automatic monitoring software generates several representative histograms, as the ones shown in Figure 3.14. These histograms include the component ratio, calculated as the ratio of the fast scintillation component respect to total scintillation light, the hit map, which shows the number of photoelectrons per event detected by each PMT, the peak time distribution, in which we distinguish the peak of the fast scintillation component and the contribution of the slow component, and the top to total ratio (TTR), obtained as the light detected by the top PMT array divided by the total light detected by both PMT arrays. The software stores these histograms together with time evolution graphs of relevant variables, such as the trigger rate, as pictures, which can be

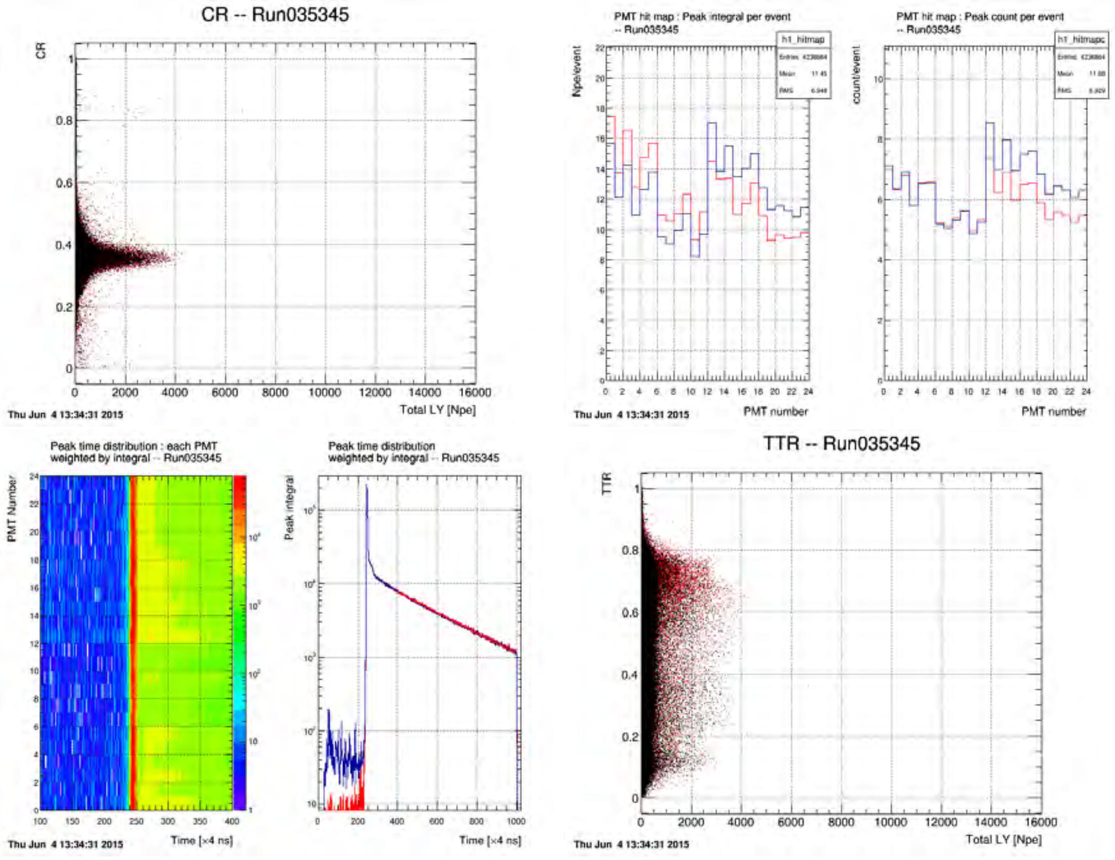

Figure 3.14: Examples of monitoring histograms stored on the ArDM web site.

easily checked and monitored in a dedicated web site.

Both the DAQ and the run status are also monitored on the ArDM web site by using a colour code that immediately informs of the current status, as shown in Figure 3.15. In case of problems, this colour code allows distinguishing among data acquisition, index creation, data processing or compression problems in a very fast and efficient way. However, if DAQ keeps sending errors for more than 900 s, SMS alarm is sent to relevant people on shift, to software/hardware experts and to the physics coordinator.

run id	Start Time	End Time	Run step status done in progress none	Type	Nb events with 1/2/3/4 subevents Percentages Good Bof Bad	Subevents Nb	Rate(Hz)	Time Range (uSec)	Remarks	Actions
35352 (430)	2015-06-04 13:56:29	run in progress...	daq index analyze compress	data	0-0-0-0 0.0- 0.0- 0.0- 0.0 (%)	0	0	0		Valid remarks run:35352
35351 (429)	2015-06-04 13:53:25	2015-06-04 13:54:29	daq index analyze compress	data	1-3-2-84647 0.0- 0.0- 0.0-100.0 (%)	338603	1323	4		Valid remarks run:35351
35350 (428)	2015-06-04 13:50:16	2015-06-04 13:51:24	daq index analyze compress	data	1-0-2-89110 0.0- 0.0- 0.0-100.0 (%)	356451	1310	4		Valid remarks run:35350
35349 (427)	2015-06-04 13:47:07	2015-06-04 13:48:15	daq index analyze compress	data	0-4-1-90875 0.0- 0.0- 0.0-100.0 (%)	363517	1336	4		Valid remarks run:35349

Figure 3.15: DAQ and the run status monitored on the ArDM web site by using a colour code, making possible a fast and efficient response in case of problems.

Thanks to the full detector control system based on PLC (Programmable Logic Controller), the entire experiment operates automatically and can be remotely controlled over the internet. The data acquisition system as well as the data processing taking place locally at LSC can be controlled remotely. When specific interventions are necessary at LSC, local shifters connect to experts of different subsystems sitting in the Control Centre at CERN via a videoconference system and the ArDM members on the different sites do operations together coherently, communicating closely to each other. Since the middle of January 2015, the experiment has been automatically operating for a long period and it has been maintained only by an engineer from the Collaboration, permanently on location and with immediate access to the laboratory, and by remote shifters.

3.8 First measurements at CERN

Before moving the ArDM 1-ton detector to an underground environment, a successful campaign of cryogenic LAr operation took place on surface at CERN [121]. Firstly, a several-month-long ultra-high vacuum evacuation of the main detector vessel, which removed outgassing from detector surfaces and materials, certified leak-tightness and finally resulted in a residual pressure $<< 10^{-5}$ mbar in the full volume encompassing the detector and the purification circuit. After this period, four weeks engineering run of ArDM-1t with a preliminary version of the light readout took place for the first time on surface at CERN in spring 2009. This first run was preceded by a careful assessment of the cryogenic requirements and the related safety issues.

During this first run, a reduced temporary set of 7 PMTs with various TPB covering treatments was installed to test the efficiency for the direct light detection by taking calibration data with different radioactive sources. The PMT array and support structure that were used during this period are shown in Figure 3.16 (left). In Figure 3.16 (right) the lateral foils covered with TPB are shown under UV illumination before insertion into the cryostat.

These measurements indicated a slightly better performance (at the 10% level) from evaporating a thin layer of TPB on the PMT entrance windows instead of coating them with a thin TPB-Paraloid layer. In addition, the first process could also be done with better uniformity [120].

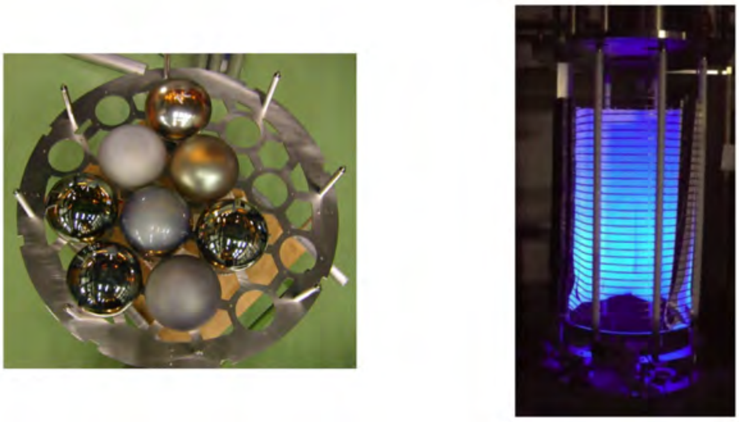

Figure 3.16: (Left) Top view of the temporary 7 PMT array used for the first measurements in liquid argon. (Right) TPB covered lateral TTX foils within the drift field shaper ring electrodes, illuminated with UV light.

The measurements to evaluate the detector light yield of low energy events were performed with an external 20 kBq ^{22}Na gamma source at zero electric field. This source delivers positrons (annihilating into two 511 keV gamma particles) and monochromatic 1275 keV gammas. The light yield produced by one of the 51 keV gamma particles was measured by triggering with a 4” NaI(Tl) scintillation crystal on the second 511 keV gamma emitted in the opposite direction, and on the 1275 keV gamma. The coincidence of at least 2 PMT signals within typically 10-1000 ns was used as the event trigger. The time digitised waveforms were analysed offline to identify charge clusters coming from groups of photons or from single photons. The individual charge clusters were then added in an optimised time window of 4500 ns located around the peak found with maximum amplitude, to obtain integrated pulse heights.

In order to compare with the experimental results, a full Monte Carlo (MC) simulation of the ArDM detector was developed [123]. The code, based on GEANT4 [124], included tracking of all particles through a detailed detector geometry description and had in addition a full simulation of the light propagation and detection in ArDM (isotropic emission of the primary scintillation light, VUV propagation, wavelength shifting, surface optical properties, reflections, and PMT response). The ^{22}Na external source was taken into account by simulating a 511 keV gamma particles emitted in a cone covering the NaI solid angle.

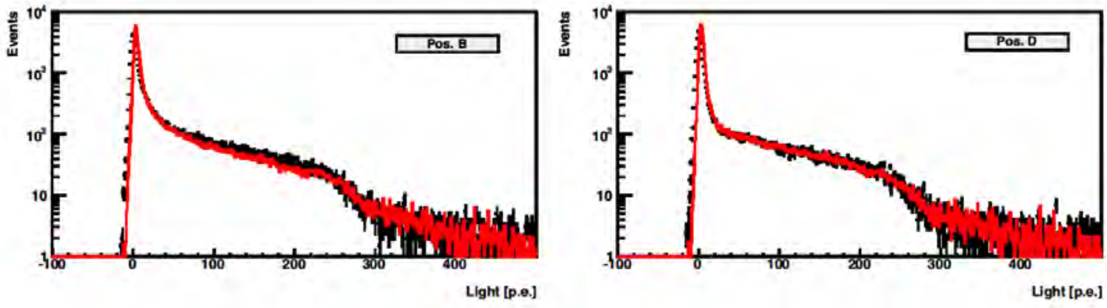

Figure 3.17: Light detection in the ArDM detector for 511 keV gamma particles, in photoelectrons (p.e.) at two different positions (in height) of the ^{22}Na source. The measurements, shown as black points with error bars, are compared to MC simulated data, plotted in red, showing an overall good agreement between both of them.

Figure 3.17 (left) and (right) show the spectrum of light detected in p.e. for two different positions (in height) of the ^{22}Na source absolutely normalised to the MC (black points with error bars) compared to the calculated light distribution from MC simulation, shown in red. An overall good agreement is found between the calculated and measured distributions, with discrepancies of less than 10% in the light yield. The drops in the spectra around 200-300 p.e. correspond to full absorption of the 511 keV photon in the fiducial volume. No clear full energy peak is visible due to the fact that most of the 511 keV photons undergo multiple interactions and are not fully absorbed. Since MC simulation reproduces successfully our data, the absolute light yield per unit energy for electron recoils can be estimated from it. With a preliminary and incomplete set of 7 PMTs, the light yield at zero electric field is found to be between 0.3-0.5 p.e./keV$_{ee}$ depending on the position within the detector volume, confirming the expectations based on smaller detector setups [121]. Results on background discrimination obtained from these data will be presented in Section 4.3.

3.9 The Canfranc Underground Laboratory

Due to the expected low rate of WIMP interactions, it is necessary to reduce the overwhelming contribution of backgrounds, specially the ones derived from cosmic rays, by operating the experiment in underground facilities, which are usually located under mountains or in mines, providing a natural shielding against muons. The ArDM experiment is installed in the Canfranc Underground Laboratory (LSC), which is located under the Spanish Pyrenees and was built between an old railway tunnel, that is currently disused, and the newly built Somport road tunnel, connecting Spain with France, as it is shown in Figure 3.18.

Figure 3.18: LSC installations located between an old railway tunnel and the Somport road tunnel. Hall A in which ArDM experiment is installed is depicted in green.

The facility was completed and inaugurated in 2006. However, one year later signs of rock instabilities started to appear and the laboratory was closed. A complete revision of the original project was performed by the Zaragoza University and the rock support structures necessary to guarantee the safety of the personnel and of the properties were installed. In order to increase safety margin, a dedicated structure of optical fibres continuously monitors rock stability. The new laboratory is run by a Consortium between the Spanish Ministerio de Economía y Competitividad, the Government of Aragon and the University of Zaragoza. The underground facilities were completed and delivered by the University of Zaragoza to the Consortium on 30 June 2010.

The experimental activities are supported by a dedicated building at Canfranc Estación village with mechanical workshop, specialised laboratories, offices for the LSC personnel and users, headquarters, conference, exhibition and meeting rooms, available since January 2011. Seven experiments have been approved (ANAIS, ROSEBUD and ArDM on Dark Matter, BiPo, NEXT and SuperK-GD on neutrinos and GEODYN on geodynamics) and more are under discussion (such as CUNA on nuclear astrophysics). These projects involve about 200 scientific users from 15 countries.

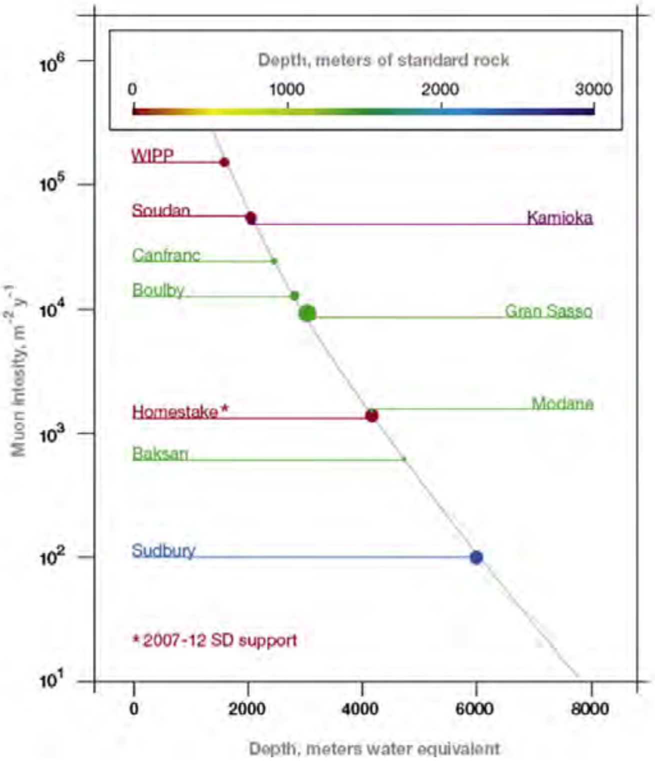

Figure 3.19: Muon intensity plotted versus depth in meters water equivalent for different underground laboratories.

The underground facility, with a total surface of 1560 m^2 and a total volume of 10500 m^3, contains two experimental halls: a big one of 15 × 40 m^2 (hall A), in which ArDM experiment is installed, and a smaller one of 10 × 15 m^2, a clean room and a workshop [125]. The laboratory depth is 850 m under Mount Tobazo. In order to compare among different underground installations, the laboratory depth is usually measured in meters water equivalent unit (m.w.e.), which allows determining the depth without any dependence on the type of rocks placed surrounding the laboratories. In particular, the depth expressed in m.w.e. provides a standard measurement of cosmic ray attenuation in underground laboratories. As an example, a laboratory at a depth of 1000 m.w.e is shielded from cosmic rays equivalent to a laboratory built 1000 m below the surface of a body of water. In addition to m.w.e., underground laboratory depth can also be measured in meters of standard rock, which is defined to have mass number A = 22, atomic number Z = 11, and density 2.65 g/cm^3. The muon intensity at LSC versus depth (2450 m.w.e.) is compared to other underground facilities in the plot of Figure 3.19. According to this plot, LSC is a middle-depth laboratory, with a muon flux of $\sim 2-4\times 10^{-3}$ m^{-2}s^{-1} [125].

3.10 Installation at LSC

The first phase of ArDM installation at LSC took place during 10 days in February 2012. The ArDM supporting structure, detector vessel, cryogenic hardware, slow control system and other detector parts were professionally packed and boxed at CERN laboratory before transporting to LSC (Figure 3.20, top left). The transport was made by lorry, arriving in Canfranc on the 30$^{\text{st}}$ of January (Figure 3.20, top right). The first step of the installation process consisted of the mounting of the supporting structure. This metallic structure, which was specifically designed to hold the detector vessel and all cryogenic systems, is made of two platforms connected by a set of stairs. Before mounting the detector vessel, a load test was performed to ensure the stability of the whole structure. With the help of the laboratory personnel, ∼32 tons of lead were mounted on the platform, which allowed to evaluate the distribution of the weight (Figure 3.20, middle left). After checking that the main deformation came from the rubber spacers between concrete ground and platform, the full structure was stabilised.

Once the main structure was properly prepared, the detector vessel was installed in it, together with the cryogenic hardware (Figure 3.20, middle right). The cryogenic part included cryocoolers, vacuum insulation pumps, the condenser for liquifying pure gas argon and the gas purification system. This last one contains a membrane pump, a purification cartridge and several sensors for measuring pressure, temperature and the gas flow. The cooling of the condenser is done with three cryocoolers, used for cooling the argon bath around the detector volume. Finally, the PLC slow control system, commissioned at CERN, was moved in one box ($4\times 1\times 2.5$ m^3) (Figure 3.20, bottom left). From the PLC, signal cables are connected to two distributor boxes placed close to the detector and from there they are distributed to the sensors, while the power cables are separated and go directly to the pumps (Figure 3.20, bottom right) and heaters. This PLC system allows monitoring the vacuum operations remotely.

The first phase of the lateral neutron shield installation at LSC was performed

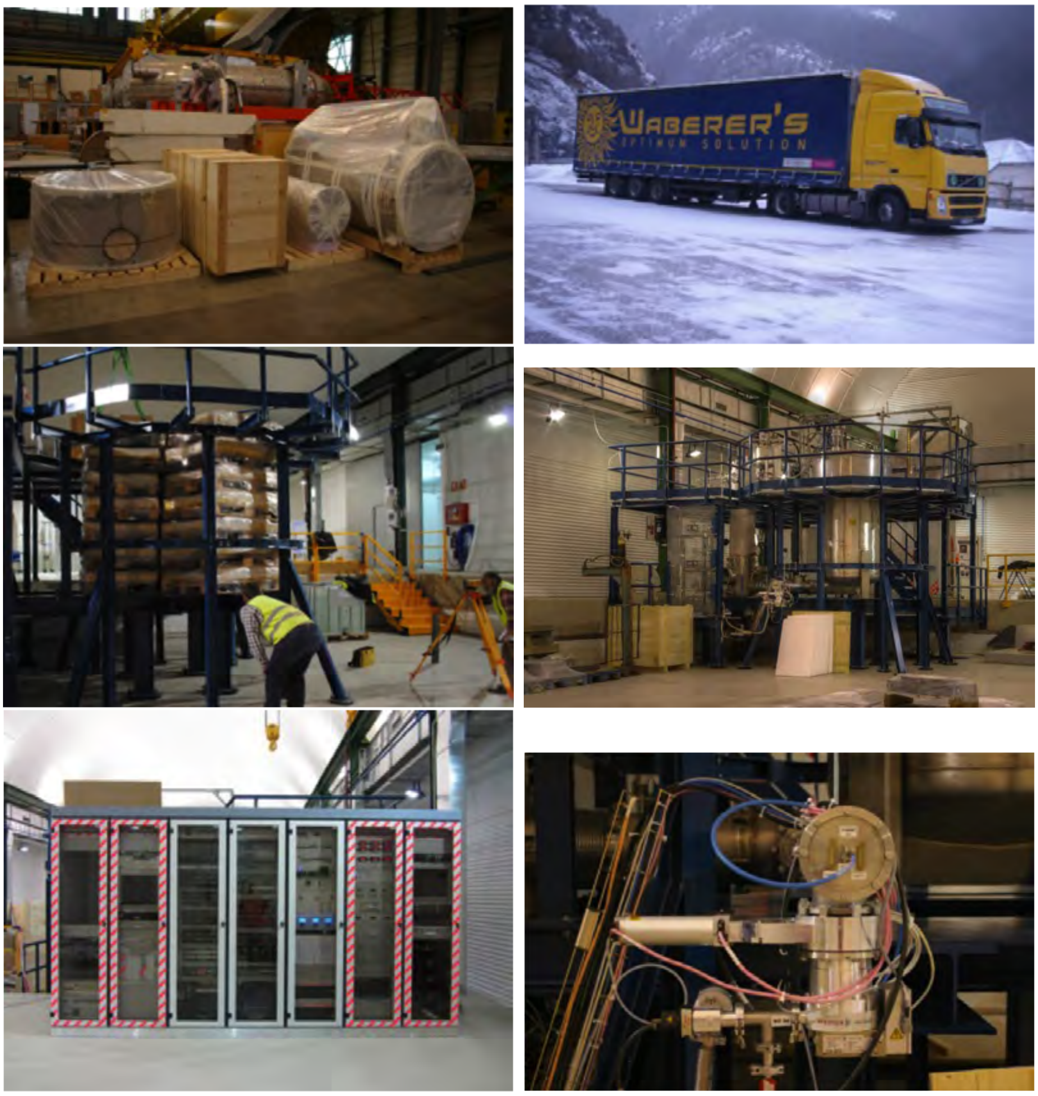

Figure 3.20: (Top left) ArDM detector vessel and cryogenic hardware packed at CERN and prepared for transport. (Top right) Transport of the ArDM experiment from CERN to LSC by lorry. (Middle left) Load test of the ArDM supporting structure. (Middle right) Detector vessel already installed in the supporting structure. (Bottom left) PLC slow control system. (Bottom right) Detail of a vacuum pump.

successfully during October 2012. There were no interference problems with the previously installed platform or with the vessel infrastructure, and the installation went smoothly. After this first phase, the lateral neutron shield structure, consisting of trapezoidal polyethylene tiles prepared by the CIEMAT workshop, reached up to the level of the first floor of the ArDM platform. The tiles were installed forming the shape of an octagonal tube with a wall thickness of ∼50 cm. The next step, consisting of mounting the bottom part of the shield, just under the detector vessel, was performed in September 2013, some time after the installation of the main detector parts.

After performing a dedicated study of the PMTs QE and in order to ensure their best possible performance, the TPB coating of all the 24 PMTs was renewed in late 2012, keeping PMTs in dark boxes at the end of the process to avoid TPB degradation. Before sending them to LSC, they were assembled in the top/bottom arrays together with the top/bottom reflectors and sealed in plastic bags filled with dry nitrogen at ETH Zurich in January 2013. Finally, the ArDM detector was installed underground in hall A at LSC in February 2013, including relevant improvements in its original design.

The assembly of the detector was almost totally performed in ultra-pure atmosphere inside the LSC clean room, reducing the total time in which detector components were exposed to ordinary laboratory atmosphere to less than three hours in total. Firstly, operating with the crane in hall A, the top flange was dismounted from the ArDM dewar and transported to the area where the PMTs were being stored in the same hall. Secondly, the top PMT array was unpacked and attached to the top flange, which was right afterwards mounted on a specifically designed supporting structure and transported to the LSC clean room. Inside the clean room, the installation of the top PMT array cabling, the field shaping rings and the side reflectors was performed. The side reflectors sheets had been freshly coated and transported to LSC in aluminium boxes to protect them from dust and light right before starting the detector assembly. However, due to the height of the clean room, it was not possible to install the bottom array inside, so the system was moved again into hall A, where the bottom array and the corresponding cabling were installed, while the detector was hanging from the crane. Finally, after finishing the whole detector assembly, it was introduced into the ArDM dewar, which was closed tightly and pumped right after. A summary of whole installation process is shown in pictures of Figure 3.21.

Figure 3.21: (Top left) Assembly of the top PMT array. (Top right) Installation of the field shapers, reflectors and top PMT connections inside the LSC clean room. (Middle left) Field cage completely mounted inside the clean room. (Middle right) Installation of the bottom PMT array. (Bottom left) Field cage hanging from the laboratory crane. (Bottom right) Connecting PMTs of the bottom array.

.

Chapter 4

ArDM backgrounds and discrimination techniques

Experiments aiming at detecting low event rates require both underground operation, in order to avoid interactions induced by cosmic rays, and powerful event rejection tools. Relevant backgrounds for the ArDM experiment are the ones caused by radioactivity of the surrounding rock and the detector materials (U/Th natural decay chains), muon-induced neutrons and the internal ^{39}Ar.

Detecting two signals simultaneously, such as charge and light, yields a powerful discrimination against background events, which are mostly interactions with electrons, as opposed to WIMPs and neutrons scattering off nuclei. Electron recoils can be effectively discriminated with respect to nuclear recoils thanks to the differences in ratio between S1 and S2 signals, which gives a rejection of two orders of magnitude, and in the scintillation pulse shape, providing $\sim 10^6$ or more discrimination. However, neutrons coming from natural radioactivity of the surrounding laboratory rock and detector components constitute an irreducible background, which has to be evaluated by detailed screening measurements of the detector components, in the case of internal radioactive contamination, and absorbed by neutron shielding (made of polyethylene in ArDM) for the case of external neutrons.

4.1 Electronic and gamma background

The electronic events are mainly originated by electrons from radioactive decay of the internal ^{39}Ar isotope. Natural argon making up $\sim 1\%$ of the Earth atmosphere is composed by the stable isotope ^{40}Ar. Apart from ^{40}Ar, commercially available Ar, which is obtained by liquefaction of the air, contains radioactive isotopes, such as ^{37}Ar and ^{41}Ar, which are short-lived ($T_{1/2}$ are 35 days and 109 min, respectively) and their cosmogenic production is negligible in an underground laboratory. Among the long-lived ones, ^{42}Ar ($T_{1/2} = 32.9$ y) is expected to be present in natural argon because of thermonuclear tests in the atmosphere, with a concentration with respect to natural Ar of ^{42}Ar/nat(Ar) $< 6\cdot 10^{-21}$ g/g (at 90% CL) [126], thus it is considered negligible for ArDM. Another long-lived Ar isotope is ^{39}Ar, a beta emitter produced by the interaction of cosmic rays with atmospheric Ar, which decays into ^{39}K with a half-life of 269 years,

$$^{39}\mathrm{Ar} \rightarrow ^{39}\mathrm{K} + e^- + \bar{\nu}_e. \tag{4.1}$$

As ^{39}Ar decays in the atmosphere, its concentration is maintained at a stable level by cosmogenic neutron activation on the stable argon isotope, ^{40}Ar(n,2n). The ^{39}Ar presents a typical continuous beta spectrum with and endpoint of 565 keV and mean energy of 220 keV, as it is shown in the plot of Figure 4.1 (left).

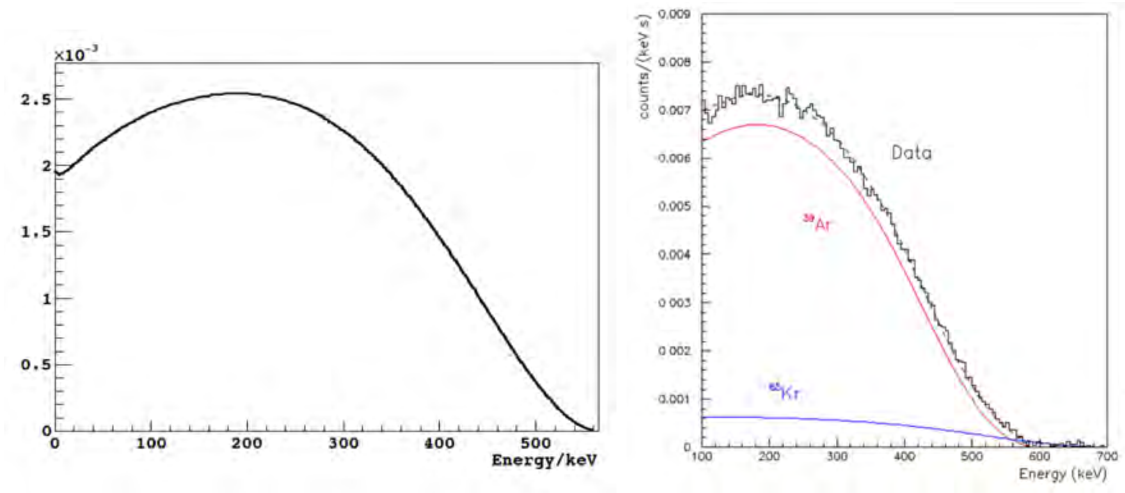

Figure 4.1: (Left) ^{39}Ar beta decay spectrum from LBNL [127]. (Right) Observed energy spectrum in the WARP chamber after subtraction of the expected contribution from external γ rays. The main contribution to the spectrum comes from the beta decay of the ^{39}Ar together with the ^{85}Kr [95].

Human activities, such as nuclear bomb tests and nuclear power plants, also contribute to the production of ^{39}Ar, but this contribution is estimated to be relatively small compared to the cosmogenic one. The most precise estimate of the ^{39}Ar specific activity in LAr, measured by the WARP collaboration [95], is 1.41 ± 0.11 Bq/L, or 1.01 ± 0.08 Bq/kg of natural Ar, also expressed as the contamination ratio ^{39}Ar/nat(Ar) of $(8.0 \pm 0.6) \cdot 10^{-16}$ g/g. In the WARP collaboration study, ^{85}Kr, mainly produced as fission product of uranium and plutonium, was also considered, as shown in the plot of Figure 4.1 (right). ^{85}Kr is a beta emitter characterised by the parameters written in Table 4.1 and a 0.43% branching ratio for beta decay on a metastable state of ^{85}Rb, which then decays by emitting a gamma ray of energy

514 keV, with a half-life of 1.01 μs [127]. Its abundance in the atmosphere is of the order of 1 Bq/m^3, corresponding to about $4 \cdot 10^{-15}$ g(^{85}Kr)/g(nat(Ar)) in air. However, the ^{85}Kr half-life is ~25 times shorter than that of the ^{39}Ar. In addition, the distillation procedure for the production of liquid argon substantially reduces the ^{85}Kr fraction; thus, it will not be considered in our study.

Isotope	**Half-life (y)**	**β end-point (keV)**	**β mean energy (keV)**
^{39}Ar	269	565	220
^{85}Kr	10.8	687	251

Table 4.1: Characteristics of the ^{39}Ar and ^{85}Kr β decays.

Despite the relatively low abundance of ^{39}Ar, the influence of the background due to ^{39}Ar decay is remarkable in a large scale detector using atmospheric Ar. Considering ~1 ton of atmospheric LAr present in ArDM sensitive volume, the ^{39}Ar decay rate is approximately 1 kHz, which means 3×10^{10} decays within one year in total [128] and of the order of 10^9 evt/yr in the energy range of interest for ArDM. According to this estimation and in order to achieve zero background contribution, a combined rejection power of about 10^9 is required. Compared to ^{39}Ar, gammas from U/Th natural contamination of the detector components produce an interaction rate which is about three orders of magnitude smaller. For this reason, this gamma background contribution is considered negligible compared to ^{39}Ar and only the neutrons coming from these natural decay chains will require a dedicated evaluation.

Another possibility to mitigate the ^{39}Ar problem in Dark Matter searches and, in particular, in ArDM, is the use of Ar with low ^{39}Ar content, also called depleted argon. However, the traditional methods for isotope separation (centrifugation and thermal diffusion) become prohibitively expensive and time-consuming on a ton-scale experiment. Therefore, it is necessary to find a natural occurring location where depleted Ar is available at large quantities. Due to the cosmogenical origin of the ^{39}Ar isotope in natural Ar, depleted Ar is expected to be found underground in gas wells, where it has been shielded from cosmic rays, responsible for the ^{39}Ar formation in the atmosphere. Consequently, current experiments based on LAr technology are developing dedicated techniques to extract Ar from underground sources and use it as target in their respective detectors.

A future Ar-TPC experiment called Argo based on this depleted argon target has been recently proposed. With 300 tons of depleted LAr, Argo is expected to achieve a background free exposure of 1000 ton × year and a sensitivity of 9×10^{-49} cm^2 at 1 TeV WIMP mass. The Argo experiment is expected to start operation in 2024 after installation and commissioning underground at LNGS [129].

4.2 Neutron background

Neutron radiation constitutes the most important background in ArDM due to the fact that fast neutrons (with $\sim$ 1 MeV or higher energy) can induce nuclear recoils in the detector volume, which makes them indistinguishable from WIMP events on an event by event analysis.

Neutrons arising from radioactive decays, for example in a fission process or produced in (α,n) reactions following α-decay of trace contaminations of heavy radioisotopes, have energies limited to a few MeV. In contrast, neutrons produced through interaction of high energy cosmic-ray muons with matter can reach energies of several GeV. Consequently, while radioactivity neutrons may be effectively controlled by appropriate shielding constructions and selection of radio-pure building materials, removing cosmic-ray induced neutrons is more difficult, with the most effective solution being to go deep underground where the muon flux is reduced by several orders of magnitude compared to that at the surface [130].

Due to the presence of two different neutron background contributions, a double strategy to address this background was developed. Firstly, an screening campaign of ArDM materials was carried out in order to evaluate the internal neutrons from radioactivity in detector components. Secondly, an in-situ measurement of the neutron background in hall A of LSC, where ArDM is installed, was developed to evaluate the impact of environmental neutrons.

4.2.1 Neutrons from radioactivity in detector components

Among all unstable isotopes that are present on Earth, there are few ones that are long-lived, thus the entire decay chain can still be present in nature. Particularly, natural isotopes ^{238}U (half-life=4.5 billion years) and ^{232}Th (half-life=14 billion years) are present in detector materials, thus they can be detected via their decay products in the screening process of the materials composing the ArDM detector. Unstable nuclei can decay through different mechanisms, emitting one or more particles. As a result, several isotopes are formed leading to successive α, β and γ emissions as an intermediate step in the normal radioactive decay chains, through which ^{238}U and ^{232}Th decay into ^{206}Pb and ^{208}Pb respectively, which are stable nuclides, as shown in the scheme of Figure 4.2. As it has been mentioned previously, the γ background from the ^{238}U and ^{232}Th natural decay chains, as well as from ^{40}K, is negligible compared to the one coming from ^{39}Ar, since it gives a three times smaller interaction rate. For this reason, only nuclides capable of generating neutrons will be taken into account as relevant contributions in the present study.

In the case of nuclei that have too many protons to ensure stability, α decay occurs because of the repulsion among protons in the nuclei, resulting in the emission

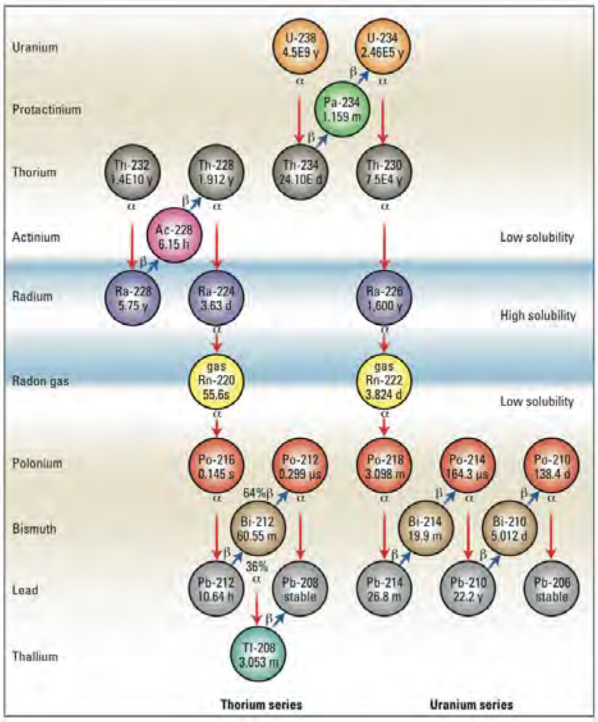

Figure 4.2: ^{238}U and ^{232}Th natural radioactive decay chains.

of an α particle, as it happens with ^{238}U:

$$^{238}_{92}\text{U} \rightarrow ^{234}_{90}\text{Th} + \alpha \tag{4.2}$$

The α particles emitted in the decay chains can produce neutrons through (α,n) reactions, which is usual among low weight atoms. Furthermore, very large nuclei can undergo spontaneous fission (SF) as it is typically the case of ^{238}U. About 2 neutrons in average are emitted per spontaneous fission with a spectrum described by [128]:

$$\frac{d\text{N}}{d\text{E}} \propto \sqrt{E}\text{e}^{-E/1.29}. \tag{4.3}$$

The α particles emitted in the ^{238}U and ^{232}Th decay chains, with α energies between 3.5 and 11 MeV, undergo (α,n) reactions, producing neutrons with energies in the MeV range. The cross section depends on the material and on the energy of the α, but typical yields are 10^{-8} to 10^{-5} neutrons per α. However, considering that ^{238}U decays by SF with a half-life of $\sim 10^{16}$ years, the ^{238}U α decay is a much more probable process (half-life of $\sim 10^{9}$ years). Therefore, the number of neutrons arising from these two processes is roughly of the same order of magnitude.

Since this internal background cannot be removed, it is necessary to minimise it by selecting radiopure materials for the detector construction and developing a complete screening campaign to evaluate their ^{238}U and ^{232}Th contamination. All the mentioned radioactive contaminants can be identified by the gamma lines associated with their decay, allowing the evaluation of their expected contribution to the neutron background. In order to measure the intrinsic radioactivity of a sample material, high purity germanium detectors are frequently used, exploiting their excellent energy resolution, together with the very low background spectrum of dedicated counting setups [131].

4.2.2 Neutrons from the surrounding rock

The minerals constituting the surrounding rock at the LSC underground laboratory, where ArDM is installed, contain a small amount of the natural radioactive ^{238}U and ^{232}Th elements, which depends on the composition of the rock and is usually of the order of hundreds of ppb. Apart from the rock, a concrete layer covers the walls of the laboratory, which also affects the neutron radiation flux. Typically, external shields made of polyethylene or water are used against (1-10) MeV neutrons, as it has been done in ArDM.

Before designing the ArDM neutron shield, several studies were carried out to evaluate the effect of a shield in the neutron flux by simulating the number of neutrons coming from rock and concrete and reaching different depths of the CH_2 shielding with GEANT4 [124]. According to the results, the neutron flux decreases by approximately one order of magnitude after every 10 cm of CH_2 at energies up to 6 MeV, while for higher energies the suppression is slightly less [128]. Finally, based on these results, the CIEMAT group built a polyethylene neutron shield, with a minimum thickness for neutrons to traverse of 50 cm, which reduces the flux of neutrons capable to produce a nuclear recoil detectable with ArDM (the ones with an energy above 100 keV) by about six orders of magnitude.

Another source of neutron background comes from cosmic muons, which penetrate deep underground and interact with the laboratory rocks, resulting in neutron production by spallation, photonuclear processes, or by secondary interactions of muon-induced hadronic showers.

The muon spallation process, in which a muon (μ), with P and E initial momentum and energy, interacts with a nucleus (N), producing a neutron (n) is schematically illustrated in Figure 4.3. The final momentum and energy of the muon are denoted as P' and E' respecively.

The μ-N cross section of this process is calculated as [132]

$$\sigma_{\mu-N} = \quad \frac{N_\gamma(\nu)\sigma^{\mathrm{virt}}_{\gamma-N}(\nu)}{\nu}\mathrm{d}\nu, \tag{4.4}$$

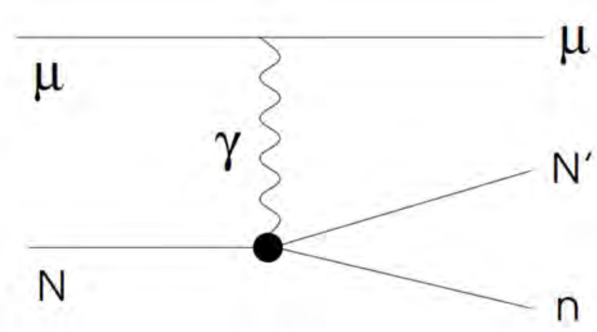

Figure 4.3: Feynman diagram of a muon spallation process [132].

where $\nu = E - E'$ and $N_\gamma(\nu)$ is the virtual photon energy spectrum. These virtual photons are often treated according to the Weizsäcker-Williams approximation [133], in which the passage of a charged particle in a slab of material produces the same effects as the ones of a beam of quasi-real photons. A general expression of the Weizsäcker-Williams formula is given by [134]:

$$N_\gamma(\nu) = \frac{\alpha}{\pi}\left[\frac{E^2+E'^2}{P^2}\ln\frac{EE'+PP'-m^2}{m\nu} - \frac{(E+E')^2}{2P^2}\ln\frac{(P+P')^2}{(E+E')\nu} - \frac{P'}{P}\right]. \quad (4.5)$$

The strategy to address this external neutron background is based on an in-situ neutron flux and neutron spectrum measurement in order to be able to quantify sensitivity limits or systematic correction due to this background contribution. According to previous measurements, performed at the centre of hall A of LSC by CUNA collaboration, this neutron flux is $\Phi = (3.44 \pm 0.35) \times 10^{-6}\mathrm{cm}^{-2}\mathrm{s}^{-1}$ [135]. For this measurement, six large high-pressure ^{3}He proportional counters were used, each one embedded in a polyethylene neutron moderation block of different size in a manner analogous to a Bonner Sphere Spectrometer. The flux distribution as a function of neutron energy was also well determined in the range of 1 eV-10 MeV. However, no data with a naked proportional counter was taken. In addition, these measurements where performed before ArDM or any other experiment was installed in the laboratory and in the centre of hall A, far from the current ArDM position. For this reasons, a new measurement of the neutron flux in hall A of LSC is required. The procedure to perform this measurement will be described in Chapter 7.

4.3 Discrimination techniques

As it has been already introduced on Section 2.2.1 of Chapter 2, in argon there are two different background discrimination methods to distinguish between electron recoils and nuclear recoils: charge to light ratio and scintillation pulse shape discrimination. In a LAr-TPC the relative amount between the produced and extracted electrons depends on the charge track density (besides the drift field). Consequently, the ratio between the two amplitudes of the primary and secondary scintillation signals, S1 and S2, is different for nuclear recoil and electron recoil interactions, which constitutes a background discrimination tool.

Additionally, argon provides another powerful discrimination tool against background: the scintillation pulse shape discrimination, which is illustrated in the plots of Figure 4.4.

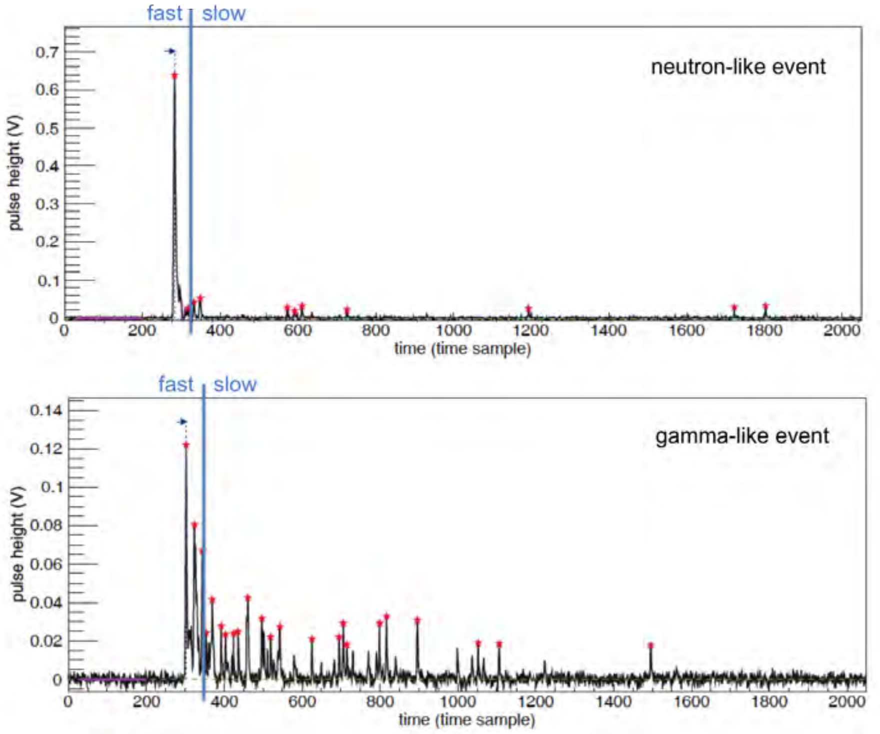

Figure 4.4: PMT signals measured by ArDM for a neutron event (top) and a gamma event (bottom). The events were recorded while the detector was irradiated with an ^{241}Am-Be source. The red stars indicate the peaks found by the peak finding algorithm while the blue arrows point to the peak time [136].

The population ratio of the two Ar excited molecular states, $r = p(^1\Sigma_u^+)/p(^3\Sigma_u^+)$, depends strongly on the ionisation density of the track, which is directly determined by the incident particle. Consequently, the scintillation pulse shape will be different for nuclear recoils and electron recoils, as it is shown in the schemes of Figure 4.4. These plots, which correspond to ^{241}Am-Be data taken on surface at CERN, show the comparison of the signal from a neutron-like event, with practically no tail, on the top plot with a gamma-like signal, with a much higher triplet component, on the bottom one.

The component ratio (CR), defined as the collected light of the fast scintillation component divided by the total collected scintillation light, can be used to parametrise the pulse shape, as it is shown in the plot of Figure 4.5, where CR has been plotted as a function of the total light collected in photoelectrons (p.e.) for ^{241}Am-Be data taken on surface at CERN. Two groups of events are visible: the electronic recoil events with CR$\sim$0.3 and the nuclear recoil events with CR$\sim$0.7 [136].

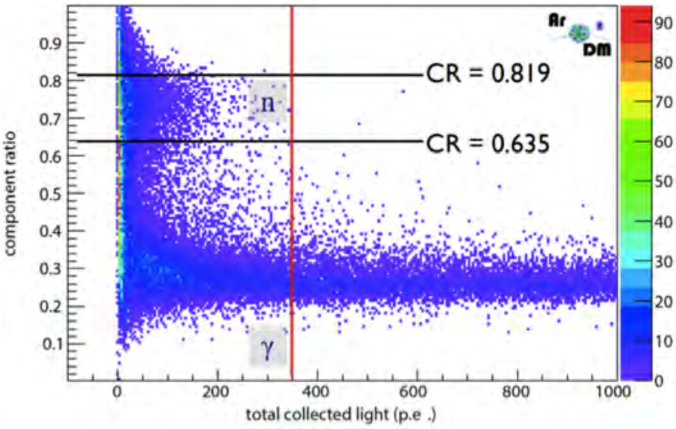

Figure 4.5: Distribution of the component ratio as a function of the integral of the collected scintillation light for the events from the ^{241}Am-Be source. Two groups of events are visible: the electronic recoil events with CR$\sim$0.3 and the nuclear recoil events with CR$\sim$0.7. The maximum energy of the nuclear recoil events is about 350 p.e.. This corresponds to a maximum nuclear recoil energy of 1.9 MeV$_{\mathrm{nr}}$ [136].

Since neutrons can interact with the target nuclei producing nuclear recoils like WIMPs, they can constitute, in principle, an irreducible background that cannot be discriminated from the WIMP signal. However, differently from WIMPs, many neutrons scatter more than once, which would in principle make possible to distinguish them from WIMPs. This fact is shown in the plot of Figure 4.6, obtained from a Monte Carlo simulation, where the number of scattering events with energy higher than 10 keV due to neutrons is presented, shows that $\sim$ 70% of events correspond to a multiple scattering [137]. However, it is necessary to reduce neutron background as much as possible by carefully choosing the detector materials and using a neutron shield.

In order to evaluate the contamination of the internal detector materials, a dedicated screening campaign of a sample of each material, which allows to obtain the contamination in ppb of ^{238}U and ^{232}Th, has been carried out. In parallel, the number of neutrons produced by the decay chains for a given contamination of 1 ppb of ^{238}U and 1 ppb of ^{232}Th has been calculated. Finally, the total number of neutrons expected for our detector has been obtained taking into account results from screening and neutron production and considering the total amount of each screened material in ArDM. Furthermore, an estimation or measurement of the neutron flux in the experimental site is a must to determine the sensitivity of the experiment.

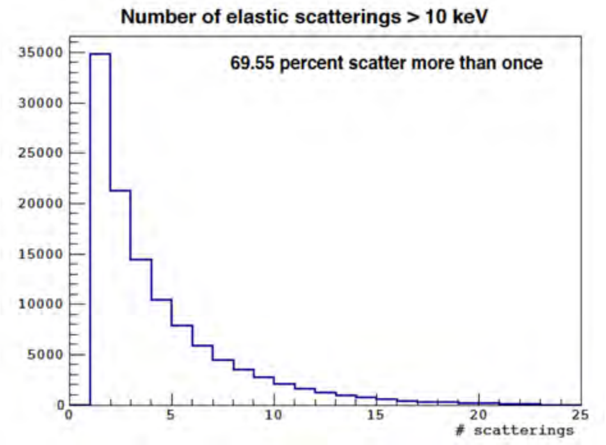

Figure 4.6: Simulated neutron multiple scattering plot showing that ~70% of neutron events above 10 keV scatter more than once, making possible to distinguish them from events due to WIMPs.

4.4 ArDM screening with LSC High Purity Germanium detectors

The internal isotope contamination of detector materials may represent an important contribution to the detector background, thus the development of a complete screening campaign to evaluate the impact of this component becomes essential in any direct Dark Matter search experiment. The screening process detects the presence of radioactive isotopes coming from the natural U and Th decay chains in the different materials through gamma emission. In this section, we will firstly introduce the screening measurements of different sample materials used for the ArDM construction, which have been performed at LSC using germanium detectors. Secondly, a detailed calculation of the neutron flux and energy coming from these materials will be presented. Finally, combining both the measurement of the contamination and the calculated spectra for the different materials, the expected number of neutrons coming from each detector component will be obtained. This result of the neutron background has to be used to evaluate the projected sensitivity for ArDM.

The ArDM material screening campaign started in September 2012 with the support from LSC, using some samples of the different materials present in ArDM that had been previously sent to LSC for screening. The radioactive contamination of the different samples was measured with a high-purity germanium (HPGe) detector, GeTobazo, installed in a dedicated facility, called LSC Radiopurity Service, which has been created for ultralow level measurements and is placed underground in hall C of LSC. There are seven ∼2 kg semiconductor HPGe detectors currently installed and taking data in this facility, as shown in Figure 4.7. These detectors, with extremely high relative efficiency (close to 100%), have been made by Canberra and are capable of detecting activities less than 1 mBq/kg [138].

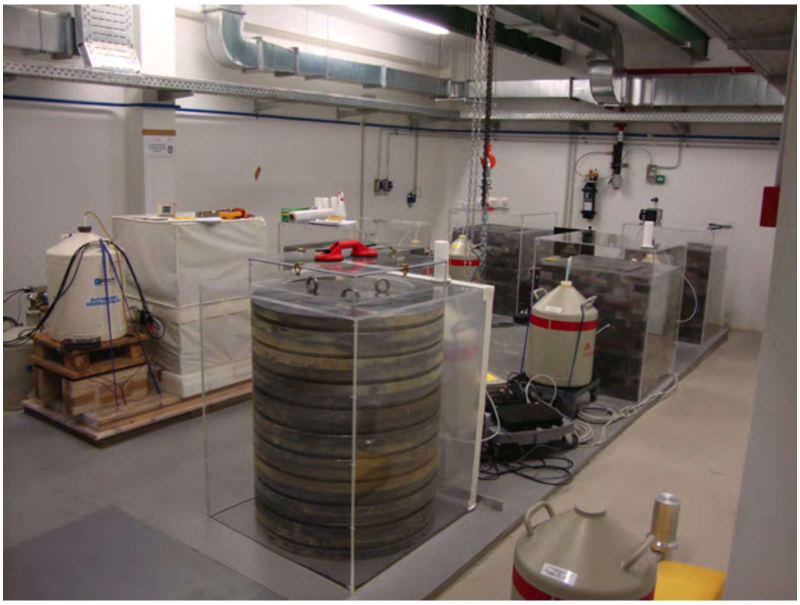

Figure 4.7: The LSC Radiopurity Service, showing some of the HPGe detectors with their lead shieldings and individual cooling systems [138].

A HPGe is a semiconductor ionisation-type detector in which the gamma ray energy is directly converted into electrons, with a signal proportional to the deposited energy of the gamma ray. The basic principle of HPGe gamma ray spectroscopy is to transfer the energy of the incident photon into electron-hole pairs via photoelectric absorption, Compton scattering, and pair production. One of the most remarkable advantages of using a semiconductor detector is that the ionisation energy, the energy required to release an electron to the conduction band, is very small

($\sim$ 3 eV). The HPGe energy resolution, which results from the efficient conversion of the gamma ray into electrons, is typically around 0.1-0.2% FWHM of the gamma ray energy, nearly two orders of magnitude better than a typical NaI detector [139].

The main drawbacks of HPGe detectors are the difficulty of producing large size detectors, needed to detect small amount of radiation in short periods of time, and the high cost per detector, which makes it expensive to use large numbers of them. In addition, the detectors must be cooled down to low temperature, which requires the use of liquid nitrogen or special mechanical or thermoelectric devices to ensure their correct performance.

Description	**Quantity**	**Start**	**Stop**	**Days**
PMT glass Hamamatsu R5912-02MOD Small pieces in plastic film ellipsoid (cylinder) form, D=130 mm	746.7 g	03/08/2012	17/09/2012	45
PMT electrode part Cylindrical shape D=71.5 mm, H=80 mm	197.0 g	17/09/2012	05/11/2012	49
HV resistors 50 MΩ, ∅8 mm × 40 mm, wires ∅1 mm × 35 mm, 36 pieces	242.7 g	30/01/2013	20/02/2013	21
PMT base 1 PCB fully mounted	1 unit	20/02/2013	11/04/2013	50
Polyethylene for PMT holder 12 small parallelepiped pieces	63.2 g	11/04/2013	07/06/2013	57
Stainless Steel for PMT holder Cut in 5 sectors piled up one another	2072.1 g	07/06/2013	07/08/2013	61
Polyethylene for neutron shield 6 small blocks piled up one another	937.6 g	08/08/2013	10/09/2013	33

Table 4.2: Different ArDM materials screened at LSC. The quantity of material screened, the screening period and the total number of screening days are specified.

The different ArDM materials screened with the HPGe detector described above include: one PMT, together with its support and PMT base, field cage high voltage (HV) resistors, polyethylene used for PMT holder and the one used for the neutron shield. The details of the screened samples can be checked on Table 4.2, where the quantity of material screened, the screening period and the total number of screening days are specified. The contamination of the sample usually determines how many days the screening process lasts, with few days for the cases in which the contamination is higher and longer periods for the less contaminated materials.

Each sample was carefully cleaned with alcohol and prepared for screening separately. In the case of the PMTs, two 8” cryogenic PMTs (Hamamatsu R5912-02MOD-LRI), which were previously operated inside the ArDM detector at CERN, were found cracked and hence unusable in the future. Consequently, one of these PMTs was prepared for screening and sent to LSC. The glass tube of the PMT was broken into small pieces and wrapped in a plastic film, to form a cylinder of 130 mm in diameter with a mass of 746.7 g. Other samples of the different PMT parts, such as the polyethylene and the stainless steel PMT holder were also cut in pieces, cleaned and prepared in a similar way for the screening process. Regarding the HV resistors and due to their small size, 36 pieces of 50 MΩ were screened together.

In addition to the already mentioned materials, the possible contribution to the ArDM background given by fission and (α,n) neutrons produced in the inner part of the polyethylene shield has to be also considered, thus the radioactive contamination of a polyethylene sample was measured in September 2013. The polyethylene sample consisted of six small pieces of the material used to build the neutron shield, that were piled up, wrapped in plastic film and placed in the germanium detector setup as shown in the pictures of Figure 4.8. The results of the polyethylene screening are plotted together with the ones of the stainless steel sample in the plots shown in Figure 4.9. In both cases, each sample spectrum is plotted on top of the reference background for comparison, showing high purity of the samples, specially in the polyethylene case, which is not only of the same order of the background, but also almost indistinguishable from it.

The intrinsic gamma background of the germanium detector has to be taken at least once a year, in order to be sure that the spectra taken on different months do not vary significantly over time. In addition, calibration runs with several radioactive sources have been taken after removing a sample from the detector and before introducing the following one.

Once the screened spectra for the different samples has been obtained, a dedicated analysis, which will be described in the next section, is required to calculate their corresponding gamma activity.

4.4.1 Methodology and results from material screening

In order to study the HPGe detector efficiency, a detailed Monte Carlo (MC) simulation of the GeTobazo detector has been performed by the laboratory staff. Monochromatic gammas are emitted uniformly and isotropically from all the sam-

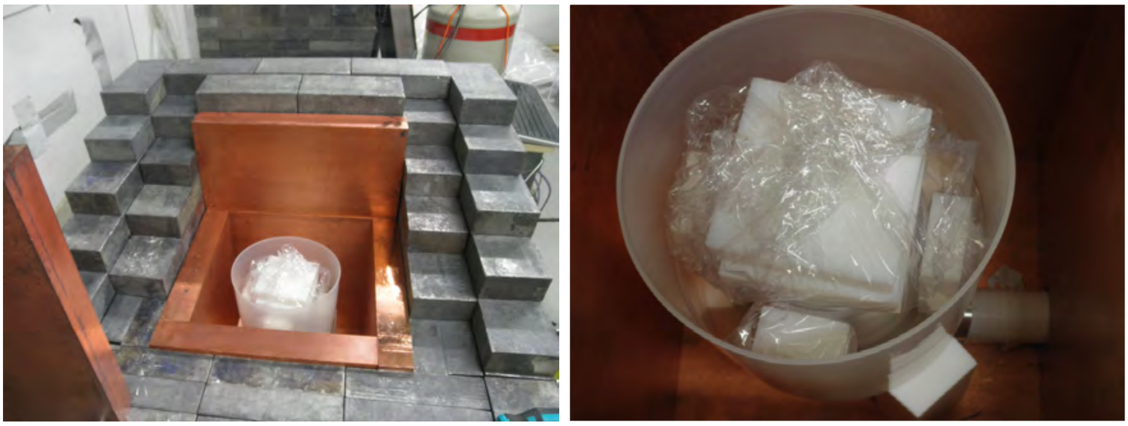

Figure 4.8: (Left) General view of the opened HPGe LSC detector, GeTobazo, in which the shielding lead bricks and the copper inner part containing the detector and the sample are visible. (Right) Detail of the polyethylene sample placed inside GeTobazo for screening.

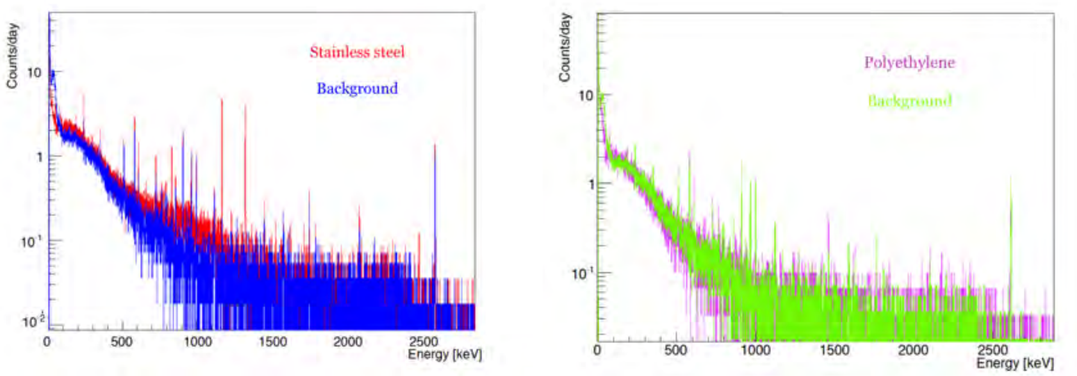

Figure 4.9: (Left) Spectrum of the stainless steel screened sample (red) compared to background (blue). (Right) Spectrum of the screened polyethylene neutron shield sample (magenta) compared to background (green).

ple bulk as shown in Figure 4.10. The energies of the simulated gammas are 40 keV, 50 keV, 75 keV, 100 keV, 150 keV, 200 keV,..., 2850 keV, increasing in steps of 50 keV for energies higher than 100 keV. The corresponding spectra are used to evaluate the detector efficiency, ε, which is calculated as the ratio between the number of counts in a specific photoelectric peak to the total number of simulated events ($\sim 10^7$). These results for the efficiencies will be used later in the calculation of the activity of the sample.

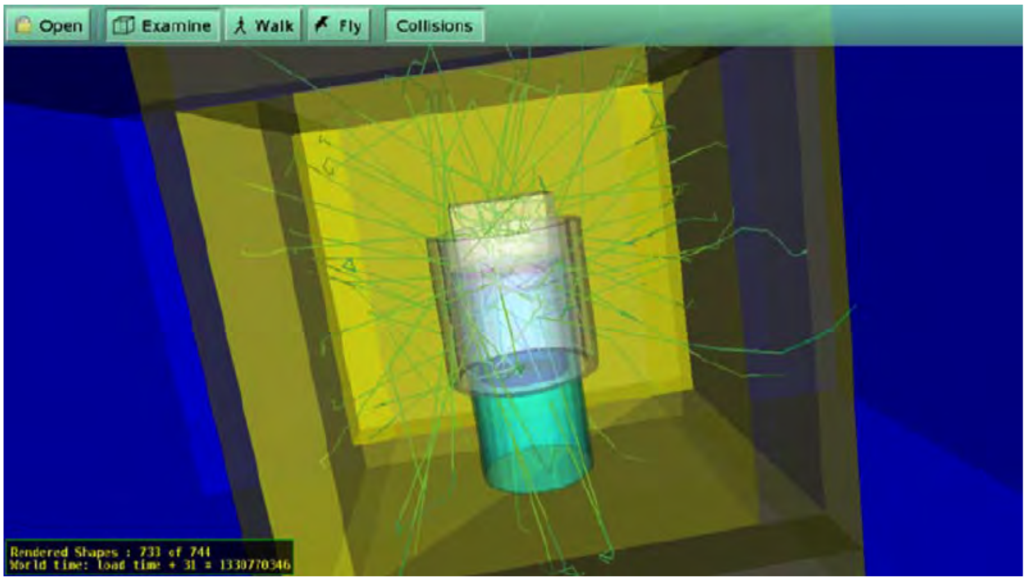

```
Rendered Shapes : 733 of 744
World time: load time + 31 = 1330770346
```

Figure 4.10: GEANT4 Monte Carlo simulation of the HPGe LSC detector called GeTobazo.

After completing the MC simulation, the first step in the analysis is to look qualitatively at the total spectrum of the sample, which is obtained by summing up all the partial spectra, corresponding to ∼1 day of data, taken during the screening campaign. In order to reject data due to environmental contaminations, if great differences are observed in partial spectra when comparing with the average, the corresponding partial spectrum is not summed. Due to the high radon contamination accumulated when the detector is opened to change the sample or for calibration, the first 1-3 days of data taken are usually discarded.

Once the spectrum has been obtained, the next step is the identification of the peaks, whose energy values will be used as initial input for the main part of the analysis, and identify the corresponding isotopes that might produce them in the particular sample under study. In the plot shown in Figure 4.11 we have a sample spectra measured with the HPGe GeTobazo, in which the most relevant peaks have been identified. The lines coming from the decay chains of ^{238}U and ^{232}Th have been depicted in red and blue colours respectively. The efficiency for each energy is extracted from the MC. If the energy is between two MC values, the mean is calculated.

The main analysis of the spectra is performed following the general strategy already applied in Gran Sasso Underground Laboratory (LNGS) [140]. The analysis program uses three different spectra: the summed detector background spectrum, the summed sample spectrum and the ^{152}Eu calibration spectrum. This last calibra-

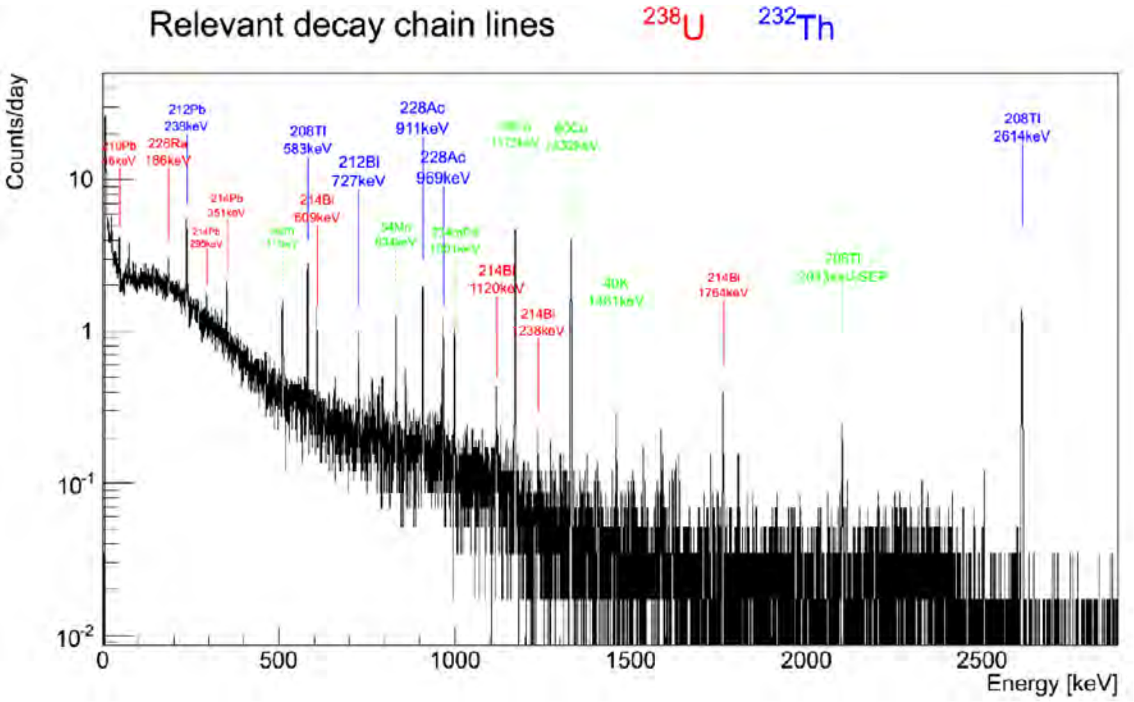

Figure 4.11: Screened spectrum in which the most relevant gamma peaks have been identified, including the lines coming from the decay chains of ^{238}U (red) and ^{232}Th (blue).

tion spectrum is used to obtain the dependency of sigma (FWHM) of the peaks with energy, by considering the energies corresponding to the main ^{152}Eu peaks, which are the following ones: 121.78 keV, 244.7 keV, 778.92 keV, 867.39 keV, 964.13 keV, 1085.9 keV, 1112.1 keV and 1408.6 keV. A Gaussian + linear fit is used for each peak and the obtained sigma is plotted as a function of energy, giving the dependency of sigma with the energy: $\sigma = a \cdot E + b$. Finally, the detector background is subtracted from the sample spectrum and we search for all the peaks in an energy region around the initially identified peaks and fit them with a Gaussian and a linear polynomial. As input values for the central peak, the searched energy and the sigma obtained from calibration are imposed.

In parallel, using the function $\sigma = f(E)$, the integral in the region under study $(E - 3\sigma, E + 3\sigma)$, S, is calculated and then the remaining Compton background, B_C, calculated as the area under the line previously obtained in the same interval, is subtracted. The background in the peak region, B, obtained by calculating the integral in the same region $(E - 3\sigma, E + 3\sigma)$ of the background spectrum, is also subtracted. The decision on whether the signal exceeds the background is based on the net signal number of counts, which has the following expression:

$$S_{net} = S - B \cdot t_S/t_B - B_C, \tag{4.6}$$

where t_S and t_B are the measuring times for signal and background, respectively. The so-called detection limit, L_d, which is the level of a true net signal that can be detected, is defined as [141]:

$$L_d = 2.86 + 4.78 \sqrt{B_C + B \cdot \frac{t_S}{t_B} + 1.36}. \tag{4.7}$$

The HPGe measurement yields either an actual measurement value, if the detection limit is exceeded ($S_{net} > L_d$), or, in case of a too low signal ($S_{net} < L_d$), an upper limit on the activity. In the first case, the specific activity, in units of Bq/kg is calculated as follows:

$$A = \frac{S_{net}}{r \cdot \varepsilon \cdot m \cdot t} \tag{4.8}$$

with S_{net} given by Equation 4.6, r the branching ratio for a specific line, ε the peak efficiency determined by MC simulations as explained before, m the mass of the sample in kg and t the measuring time.

In the present analysis, the contribution of the individual isotope of the decay chain in the case of a too low signal ($S_{net} < L_d$) was not taken into account to obtain the final activity coming from the respective reactions. Special attention was paid to the metastable isotope ^{234}Pa with respect to the other elements appearing later in the decay chain of ^{238}U to check for the possibility of a broken equilibrium in the decay of the parent element. The activity due to the presence of ^{232}Th and ^{238}U was then determined as the average of the activity of the individual lines. In the case of ^{238}U, the elements taken into account are $^{234\mathrm{m}}$Pa, ^{226}Rn, ^{214}Pb and ^{214}Bi; while for ^{232}Th the considered individual lines are ^{228}Ac, ^{212}Pb and ^{208}Tl. The results of the ^{238}U and ^{232}Th contamination for the different screened samples are summarised in Table 4.3 in units of parts per billion (ppb).

According to the screening results, the highest contamination is obtained for the PMT components, in particular for the PMT base and PMT glass. This is one of the reasons that has motivated the investigation of other types of PMTs, such as SiPMTs, within the collaboration to improve the ArDM light readout at the same time that the ^{238}U and ^{232}Th contaminations are significantly reduced. Regarding the resistors for the drift cage, measurements of contamination showed relatively high results with respect to the other screened components. As a consequence, the impact of this contribution on backgrounds was investigated and different models of resistors were proposed to substitute the original ones. Although the ^{235}U contamination in detector materials was also measured, it has not been considered in the present study since its contribution was negligible compared to the ^{238}U and ^{232}Th contaminations.

Contamination of the different ArDM screened materials [ppb]		
Material	**^{238}U**	**^{232}Th**
PMT glass	55.63 ± 3.51	31.84 ± 7.32
PMT base	916.63 ± 39.38	3264.66 ± 245.68
PMT electrodes	34.19 ± 3.12	28.89 ± 10.06
HV resistors	152.20 ± 8.19	471.38 ± 43.92
Stainless steel (PMT support)	3.87 ± 0.05	4.40 ± 0.05
Polyethylene (PMT support)	5.12 ± 0.97	38.16 ± 16.46
Polyethylene (neutron shield)	2.06 ± 0.12	3.16 ± 3.65

Table 4.3: Results of the ^{238}U and ^{232}Th contaminations [ppb] for the different ArDM screened samples.

In parallel with the measurements of the material contamination, the simulations necessary to predict the neutron background in ArDM were carried out. The code SOURCES was used to estimate the flux and the energy spectrum of the neutrons produced by the material contamination through fission and (α,n) reactions from the ^{238}U, ^{232}Th, following the procedure presented in next Section.

4.5 Calculation of the neutron flux and energy spectrum from the detector materials

The calculation of the neutron flux and energy spectrum was performed with SOURCES 4A [142], a computer code that determines neutron production rates and spectra from (α,n) reactions, spontaneous fission and delayed neutron emission due to the decay of radionuclides. It consists of a FORTRAN 77 (F77) source code, a user-created input file, up to five output files, and four library files. The SOURCES code has been under development for several years with continuing improvements implemented in calculation methods and data. The original version of SOURCES (SOURCES 1x) was actually named POFEAL and was primarily used for calculating Pi OF E-ALpha (i.e., the probability of an (α,n) interaction with nuclide i by an α-particle prior to stopping in the material). SOURCES 2x was based on the original POFEAL code and included spectra calculations and improvements in the calculational algorithm. The difference of SOURCES 3A, with respect to older ones was the ability to handle two-region interface problems, which has been improved recently to three-region interface problems in SOURCES 4A.

The SOURCES 4A code, available for both Unix and PC platforms, is capable of calculating (α,n) source rates and spectra in four different types of problems: homogeneous media (i.e., a mixture of α-emitting source material and low-Z target material), two-region interface problems (i.e., a slab of α-emitting source material in contact with a slab of low-Z target material), three-region interface problems (i.e., a thin slab of low-Z target material sandwiched between α-emitting source material and low-Z target material), and (α,n) reactions induced by a monoenergetic beam of α-particles incident on a slab of target material. Spontaneous fission spectra are calculated with evaluated half-life, spontaneous fission branching, and Watt spectrum parameters for 43 actinides. The (α,n) spectra are calculated using an assumed isotropic angular distribution in the centre-of-mass system with a library of 89 nuclide decay α-particle spectra, 24 sets of measured and/or evaluated (α,n) cross sections, product nuclide level branching fractions and α-particle stopping cross sections for Z<106. The delayed neutron spectra are taken from an evaluated library of 105 precursors. The code outputs the magnitude and spectra of the resultant neutron source and also provides an analysis of the contributions to that source by each nuclide in the considered problem. The physics underlying both (α,n) and spontaneous fission process that are implemented in the SOURCES code will be described in the following Sections.

4.5.1 (α,n) in SOURCES

The calculation of the (α,n) neutron production in a material requires detailed knowledge of the slowing and stopping of α-particles in that material, which is described by the stopping power:

$$S_p(E) = -\frac{\mathrm{d}E}{\mathrm{d}x}. \tag{4.9}$$

From Equation 4.9, the stopping cross section, σ_S, is defined in a straightforward way:

$$\sigma_S(E) = -\frac{1}{N}\frac{\mathrm{d}E}{\mathrm{d}x}. \tag{4.10}$$

We can also determine the energy loss of an α-particle of initial energy E after travelling a distance L, by integration of the stopping power written in Equation 4.9,

$$\Delta E = E_\alpha - E'_\alpha = \int_0^L -\frac{\mathrm{d}E}{\mathrm{d}x} \, \mathrm{d}x. \tag{4.11}$$

This energy loss corresponds to a travelled distance expressed as

$$L = \int_{E_\alpha}^{E'_\alpha} \frac{1}{\frac{\mathrm{d}E}{\mathrm{d}x}}\mathrm{d}E. \tag{4.12}$$

During the slowing down of the α-particles within the material, neutrons may be produced by (α,n) reactions with the nuclides contained in that material. The probability of (α,n) interaction with nuclide i by an α-particle that slowed from E_α to E'_α is

$$p_i(E_\alpha \to E'_\alpha) = \int_{E_\alpha}^{E_\alpha} \frac{N_i \sigma_i(E)}{\frac{\mathrm{d}E}{\mathrm{d}x}} \mathrm{d}E = \int_{E_\alpha}^{E_\alpha} \frac{N_i \sigma_i(E)}{\left(-\frac{\mathrm{d}E}{\mathrm{d}x}\right)} \mathrm{d}E, \tag{4.13}$$

where N_i is the atom density of the nuclide i and σ_i is the microscopic (α,n) cross section for the nuclide i.

Thus, the probability of an α-particle undergoing an (α,n) reaction with nuclide i before stopping in the material is given by the thick-target neutron production function,

$$P_i(E_\alpha) = \int_{0}^{E_\alpha} \frac{N_i \sigma_i(E)}{\left(-\frac{\mathrm{d}E}{\mathrm{d}x}\right)} \mathrm{d}E. \tag{4.14}$$

Both probabilities written in Equations 4.13 and 4.14 can be expressed as a function of the stopping cross section given in Equation 4.10 as follows:

$$p_i(E_\alpha \to E'_\alpha) = \frac{N_i}{N} \int_{E_\alpha}^{E_\alpha} \frac{\sigma_i(E)}{\sigma_S(E)} \mathrm{d}E, \tag{4.15}$$

and

$$P_i(E_\alpha) = \frac{N_i}{N} \int_{0}^{E_\alpha} \frac{\sigma_i(E)}{\sigma_S(E)} \mathrm{d}E. \tag{4.16}$$

In the case of an homogeneous problem, in which the material will be composed by J different constituents homogeneously distributed, σ_S is obtained adding all possible contributions from the J materials

$$\sigma_S(E) \simeq \frac{1}{N} \sum_{j=1}^{J} N_j \sigma_{Sj}(E), \tag{4.17}$$

where

$$N = \sum_{j=1}^{J} N_j. \tag{4.18}$$

In the decay of a nuclide k, the α particles will be emitted with one of L possible energies. Therefore, considering a thick-target material containing I nuclei, we can define the fraction of nuclide k decays resulting in an (α,n) reaction in that material with non-negligible (α,n) cross sections as

$$R_k(\alpha, n) = \sum_{l=1}^{L} f^{\alpha}_{kl} \sum_{i=1}^{I} P_i(E_l), \tag{4.19}$$

with f^{α}_{kl} the fraction of all decays of nuclide k resulting in an α-particle of energy E_l and P_i obtained from Equation 4.16. It is important to point out that to compute the neutron emission per decay of nuclide k due to (α,n) reactions, it is necessary to know the (α,n) cross section and the atom fraction (N_i/N) for each target nuclide, the intensity for emission of each of L α-particles (f_{kl}^{α}) and the energy of each of the L α-particles (E_l). All these quantities are available on SOURCES in different libraries.

The (α,n) energy spectra of the emitted neutrons will be calculated assuming an isotropic neutron angular distribution in the centre-of-mass system with a library of 89 nuclide decay α spectra and 24 sets of product-nuclide level branching fractions.

4.5.2 Spontaneous Fission in SOURCES

The spontaneous fission of an actinide nuclide k is accompanied by the emission of an average number of ν_k(SF) neutrons. The fraction of nuclide k decays that are spontaneous fission events are given by the SF branching fraction:

$$P_i(E_l) = \frac{\lambda_k^{\mathrm{SF}}}{\lambda_k}. \tag{4.20}$$

Therefore, the average number of SF neutrons emitted per decay of nuclide k is

$$R_k(\mathrm{SF}) = F_k^{\mathrm{SF}} \nu_k(\mathrm{SF}). \tag{4.21}$$

The spontaneous fission neutron spectra are approximated by a Watt type fission spectra using two evaluated parameters, a and b, in the following form:

$$\chi_k^{\mathrm{SF}} = R_k(\mathrm{SF})\mathrm{e}^{-E/a}\mathrm{sinh}\sqrt{bE}. \tag{4.22}$$

Thus, to compute the neutron production due to spontaneous fission per decay of nuclide k, the SF branching fraction and average number of neutrons per spontaneous fission must be known. All these quantities together with a and b evaluated parameters for 43 different fissioning nuclides are available in SOURCES from libraries.

Once we have reviewed the physically relevant parameters for the (α,n) and spontaneous fission neutron production included in SOURCES, we will present the main results of the neutron flux and spectra calculations for the different ArDM screened materials in the next Section.

4.5.3 Results of neutron production for ArDM

In order to obtain the total neutron flux and neutron energy spectrum for each screened material, the contributions of all isotopes in the ^{238}U and ^{232}Th decay chains were included, with a separate treatment for each decay chain. The results presented in this Section are the ones from (α,n) processes for ^{238}U and ^{232}Th and spontaneous fission from ^{238}U, considering the contribution of spontaneous fission reaction from ^{232}Th negligible compared to the other dominant reactions. In addition, due to the fact that ^{235}U contamination in detector materials had been measured to be negligible, the contribution from ^{235}U has not been considered.

Both the neutron energy spectra and neutron flux were obtained using the SOURCES software, taking into account the atomic density and the exact chemical composition of each detector material, expressed as percentage in weight of the different atomic elements with respect to total weight of the material. The detailed composition of the different ArDM screened samples is specified in Tables 4.4 and 4.5.

Composition in weight of the different ArDM screened materials [%]							
Stainless Steel		**HV resistors**		**Borosilicate** (PMT glass)		**Polyethylene**	
Fe	68.85	Al	52.93	O	53.96	C	85.63
Cr	17	O	47.07	Si	37.72	H	14.37
Ni	12			B	4.01		
Mn	2			Na	2.82		
C	0.15			Al	1.16		
				K	0.33		

Table 4.4: Results of the ^{238}U and ^{232}Th contaminations [ppb] for the different ArDM screened samples.

Since all the information that we have just presented refers to the specific target material, it still remains to obtain the density of atoms (atoms/cm^3) of each source nuclide forming the ^{238}U and ^{232}Th decay chains, which is also required as an input in SOURCES. Assuming 1 ppb of contamination, a custom made program called raconv, which has been developed at CIEMAT by R. Santorelli and B. Montes, calculates the density of atoms composing the sample for all the nuclides of the mentioned decay chains. The code has been included in this Thesis as Appendix A.

Once all the required inputs have been calculated, SOURCES code has been run separately for each decay chain in each material, resulting the spectra that have been plotted in Figure 4.12. In these plots the expected neutron flux is shown in units of n/s/MeV/cm^3 as a function of the energy in MeV units for the different screened materials. The (α,n) contribution from ^{238}U and ^{232}Th correspond to the solid black and blue curves respectively, while the red dashed curve represents the spontaneous fission contribution from ^{238}U. As expected, we observe that the shape and average energy of the spectrum varies depending on the considered material. In addition, for almost all the cases, the dominant contribution comes from (α,n) reactions of the ^{238}U.

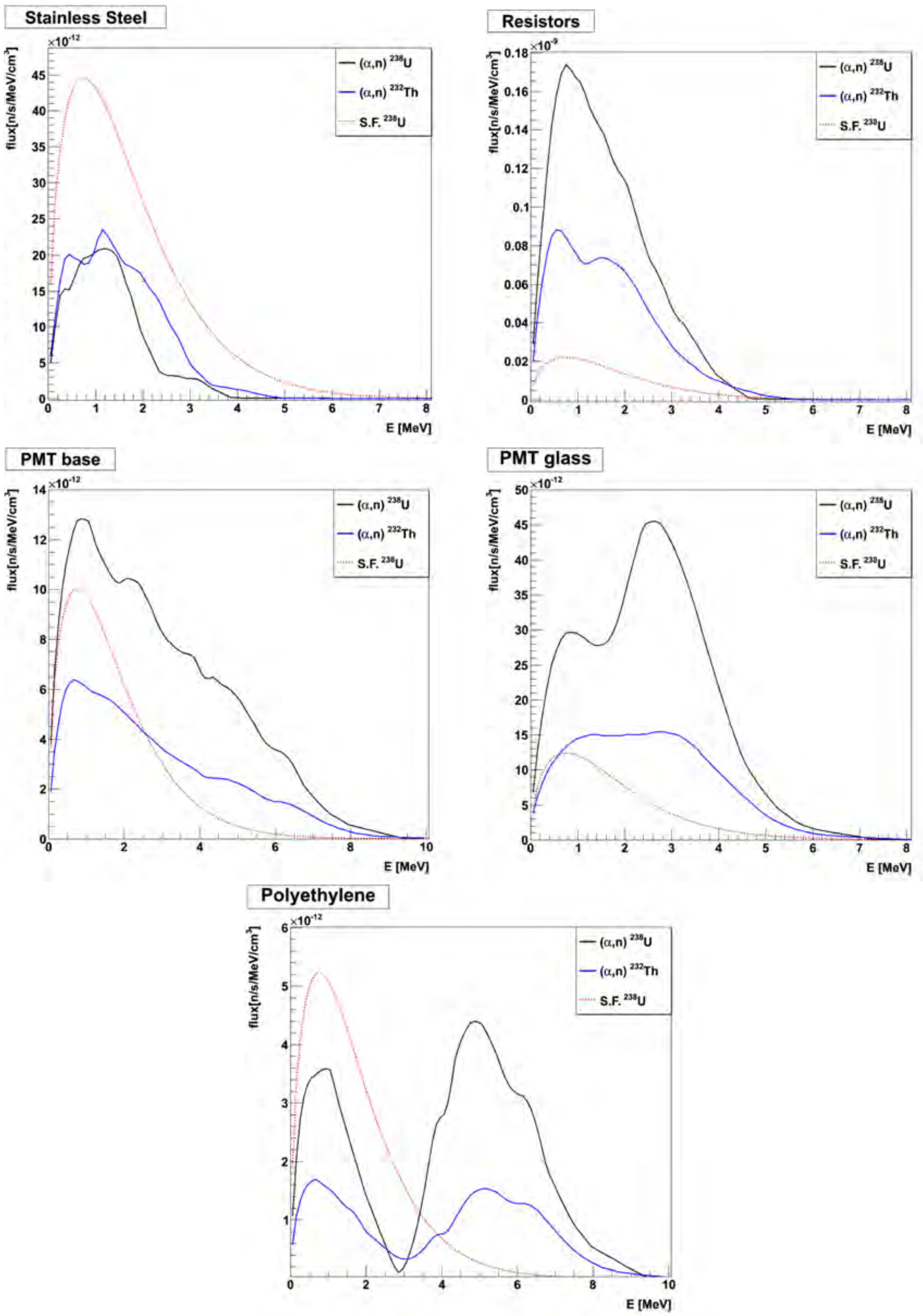

Figure 4.12: Total neutron spectra for the different screened materials. The (α,n) contributions from ^{238}U and ^{232}Th correspond to the solid black and blue curves respectively, while the red dashed curve represents the spontaneous fission contribution from ^{238}U.

Composition in weight of ArDM screened FR4 (PMT base) [%]			
E-glass (60%)		**Epoxy (40%)**	
SiO_2	54	$C_{19}H_{20}O_4$	56
CaO	19	$C_{10}H_{18}O_4$	24
Al_2O_3	13	$C_9H_{22}N_2$	20
MgO	2.5		
B_2O_3	7.5		
TiO_2	0.8		
Na_2O	1		
K_2O	1		
Fe_2O_3	0.5		
F_2	0.7		

Table 4.5: Composition in fraction of weight (%) for each chemical compound forming the FR4 (PMT base). Both e-glass (60%) and epoxy (40%) have been included.

The total neutron flux from the different materials is obtained by integration of the spectra shown in the plots of Figure 4.12. The integral is computed as the sum of bin contents in the considered range, while the error is computed using error propagation from the individual bin errors, assuming that all the bins are uncorrelated. The calculated neutron flux and average energy are reported in Table 4.6. The results have been obtained considering 1 ppb contamination of ^{238}U and ^{232}Th. The highest flux is produced by the PMT high voltage resistors and the PMT glass, made of borosilicate. These results have to be combined with the activity measured with the Ge detector in order to obtain the actual neutron flux from detector materials. Dedicated MC simulations have been carried out in order to calculate the rate of single scattering nuclear recoils expected in ArDM based on the calculated neutron flux.

4.6 Final results of single-scatter neutron recoils from ArDM screening

The results obtained in previous Sections were used as input for the GEANT4 simulations of the ArDM detector to evaluate the expected fraction of single-scatter neutron recoils. The corresponding results of the neutron flux for the measured contaminations obtained from screening are presented in Table 4.7 (contamination [ppb]×neutron flux [n/s/cm^3/ppb]). Thus, the total number of neutrons per day for

Calculated neutron production [1 ppb]					
Material	**Source**	**Neutron flux ($n/s/cm^3/ppb$)**		**Average neutron E (MeV)**	
		(α,n)	**S.F.**	**(α,n)**	**S.F.**
Stainless steel (SS)	^{238}U	$(3.86\pm0.77)\cdot10^{-11}$	$(1.09\pm0.18)\cdot10^{-10}$	1.29	1.69
	^{232}Th	$(5.17\pm0.93)\cdot10^{-11}$	$(9.8\pm1.7)\cdot10^{-16}$	1.51	1.60
PMT HV	^{238}U	$(3.81\pm0.68)\cdot10^{-10}$	$(5.38\pm0.90)\cdot10^{-11}$	1.56	1.69
	^{232}Th	$(2.13\pm0.36)\cdot10^{-10}$	$(4.84\pm0.84)\cdot10^{-16}$	1.64	1.60
FR4	^{238}U	$(5.37\pm0.68)\cdot10^{-11}$	$(2.45\pm0.41)\cdot10^{-11}$	2.88	1.69
	^{232}Th	$(2.47\pm0.32)\cdot10^{-11}$	$(2.20\pm0.38)\cdot10^{-16}$	2.76	1.60
Borosilicate	^{238}U	$(1.45\pm0.21)\cdot10^{-10}$	$(3.04\pm0.51)\cdot10^{-11}$	2.48	1.69
	^{232}Th	$(6.28\pm0.89)\cdot10^{-11}$	$(2.73\pm0.47)\cdot10^{-16}$	2.49	1.60
Polyethylene	^{238}U	$(1.90\pm0.21)\cdot10^{-11}$	$(1.28\pm0.22)\cdot10^{-11}$	4.02	1.69
	^{232}Th	$(8.11\pm0.97)\cdot10^{-12}$	$(1.15\pm0.20)\cdot10^{-16}$	3.90	1.60

Table 4.6: Neutron flux and average neutron energy calculated with SOURCES for the different material contributions in ArDM, considering 1 ppb contamination of ^{238}U and ^{232}Th for each material.

each detector component is given by [137]:

$$\begin{aligned} \text{neutrons/day} &= \text{fraction of single scattering events} \\ &\times \text{component volume } [\text{cm}^3] \\ &\times \text{contamination [ppb]} \times \text{neutron flux } [\text{n/s/cm}^3/\text{ppb}] \\ &\times 3600 \text{ s/h} \times 24 \text{ h/day} \end{aligned} \tag{4.23}$$

The fraction of elastic single-scatter events is determined from the MC simulation by counting the scattering events taking place within the LAr volume. In order to reduce the expected neutron background, different fiducial volume and recoil energy cuts were studied, always trying to preserve the maximum of LAr mass. The studies of the distribution of single-scatter events along the z-axis and their radial position as a function of the recoil energy showed that the cuts $-500 < z < 450$ mm and $r < 345$ mm suppress most of the neutron background coming from the screened materials and preserve, at the same time, a reasonable fiducial volume of 508 kg. The analysis cuts are related to the requirement of a single energy deposit in LAr of more than 10 keV, which represents a S2 proportional scintillation threshold to discriminate against multiple scattering events. This is due to the fact that, as described previously, more than 69% of neutrons scatter more than once in the large LAr target of ArDM. Additionally, the sum of the overall deposited energy, which was required to lie within 30 and 100 keV, establishing a S1 primary scintillation

Total neutron production from detector materials					
Material	**Source**	**Neutron flux ($n/s/cm^3$)**		**Average neutron E (MeV)**	
		(α,n)	**S.F.**	**(α,n)**	**S.F.**
SS (PMT support)	^{238}U	$(1.49\pm0.30)\cdot10^{-10}$	$(4.22\pm0.70)\cdot10^{-10}$	1.29	1.69
	^{232}Th	$(2.27\pm0.41)\cdot10^{-10}$	$(4{,}31\pm0.75)\cdot10^{-15}$	1.51	1.60
SS (PMT electrodes)	^{238}U	$(1.32\pm0.29)\cdot10^{-9}$	$(3.73\pm0.70)\cdot10^{-9}$	1.29	1.69
	^{232}Th	$(1.49\pm0.59)\cdot10^{-9}$	$(2.8\pm1.1)\cdot10^{-14}$	1.51	1.60
PMT HV resistors	^{238}U	$(5.8\pm1.1)\cdot10^{-8}$	$(8.2\pm1.4)\cdot10^{-9}$	1.56	1.69
	^{232}Th	$(1.00\pm0.19)\cdot10^{-7}$	$(2.28\pm0.45)\cdot10^{-13}$	1.64	1.60
FR4 (PMT base)	^{238}U	$(4.92\pm0.66)\cdot10^{-8}$	$(2.25\pm0.39)\cdot10^{-8}$	2.88	1.69
	^{232}Th	$(8.1\pm1.2)\cdot10^{-8}$	$(7.2\pm1.4)\cdot10^{-13}$	2.76	1.60
Borosilicate (glass)	^{238}U	$(8.1\pm1.3)\cdot10^{-9}$	$(1.69\pm0.30)\cdot10^{-9}$	2.48	1.69
	^{232}Th	$(2.00\pm0.54)\cdot10^{-9}$	$(8.7\pm2.5)\cdot10^{-15}$	2.49	1.60
Polyethylene (support)	^{238}U	$(9.7\pm2.1)\cdot10^{-11}$	$(6.6\pm1.7)\cdot10^{-11}$	4.02	1.69
	^{232}Th	$(3.1\pm1.4)\cdot10^{-10}$	$(4.4\pm2.0)\cdot10^{-15}$	3.90	1.60
Polyethylene (shield)	^{238}U	$(3.91\pm0.49)\cdot10^{-11}$	$(2.64\pm0.48)\cdot10^{-11}$	4.02	1.69
	^{232}Th	$(2.6\pm3.0)\cdot10^{-11}$	$(3.6\pm4.2)\cdot10^{-16}$	3.90	1.60

Table 4.7: Total neutron flux and average neutron energy for the different material contributions in ArDM, considering the measured contaminations from screening.

threshold. Further analysis showed that the optimal cuts for the scintillation signals were thresholds of $S1 > 50$ keV and $S2 > 2$ keV.

After applying the mentioned cuts, the remaining fraction of single-scatter events yields a total irreducible neutron-induced background of 0.22 ± 0.08 single recoils per day, with the different detector component contributions represented in the pie chart of Figure 4.13. A large fraction of these neutrons are originated from the HV resistors and the PMT bases, as we already pointed out previously, and they will be significantly reduced ($\sim$ 35%) by replacing them with lower radioactive components for ArDM Run II. The largest contribution however comes from the PMTs, which account for $\sim$ 50% of neutrons, even though they are made of low-radioactive borosilicate glass and have orders of magnitude lower activities compared to the ordinary ones. Due to the fact that the polyethylene contamination is at least one order of magnitude lower than the one of the other screened components, its influence is negligible compared to the other contributions and, for this reason, it has not been included in the final fraction of single-scatter events calculation.

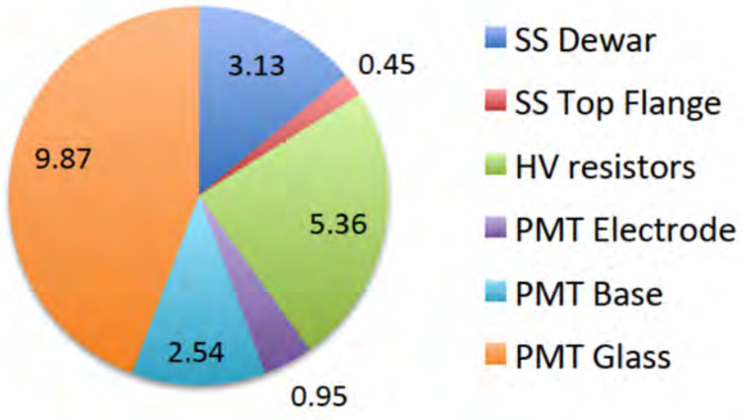

Figure 4.13: Total number of irreducible WIMP-like background events expected in ArDM due to elastic scattering of neutrons from individual detector components. The exposure time is 100 live days and the fiducial volume after the analysis cuts is 508 kg LAr, resulting in a total number of 22.3 ± 7.7 neutrons [137]. However, the largest contributions will be significantly reduced for ArDM Run II by replacing the HV resistors and the PMT bases.

Chapter 5

ArDM underground commissioning: warm and cold argon gas data

The main goal of the first underground argon gas tests performed at LSC was the commissioning of the ArDM detector and the detection of the scintillation signals in the underground environment. Due to the fact that argon scintillation light is emitted in the VUV range, it was also necessary to evaluate the effectiveness of the wavelength conversion performed by the TPB. During these tests we also studied the stability of the DAQ and the PMTs, the performance of the LAr recirculation system, the energy dependence of the light yield and the background in deep underground environment. Since the ArDM detector has been designed to obtain a uniform light collection, it was also important to study the uniformity of the light yield. In addition, even with the neutron shield partially opened during this operation phase, these gas tests have provided a first glimpse on the background, which has helped to understand the possible underground sources of gamma radiation.

5.1 Dry commissioning of ArDM

The first underground data taking at LSC was carried out for two weeks in April 2013 with the detector filled with pure warm (room temperature) argon gas. Since the aim of this first test was to detect the argon scintillation signals, a low-activity ^{241}Am alpha source was installed inside the detector vessel. This source was selected since its signals are easy to detect due to the fact that the alphas emitted by the source provide a localised and well-defined high energy deposition. The evaluation of the light yield, which is a fundamental aspect of this research since it provides the detector energy threshold, was firstly performed with the ^{241}Am alpha source and then with several gamma sources during the later warm and cold argon gas tests.

After opening the dewar to uninstall the alpha source, some improvements in the detector and a test of the liquefaction of argon in the external bath were performed as a first step to prepare the detector for future cryogenic operation. The bath test was performed by filling the cooling bath jacket, which is a thin layer between the vessel main volume and the insulation vacuum, with a small amount of about 200 L of liquid argon. During this test and also in the later cryogenic operation, the gaseous argon was delivered in gas bottles to LSC and then condensed using cryocoolers, which is a slow process, since it takes about one week to fill the cooling jacket with LAr and to cool down all the steel and instrumentation. This LAr bath test allowed to gain vital experience on the in-situ operation of the cryocoolers and the entire ArDM cryogenic and monitoring system and it also allowed to assess and directly verify the impact of an eventual long-term ArDM cryogenic operation in hall A. For instance, the impact of the noise level (80 dBm) and the heat dissipation ($\sim$14 kW) of the cryocoolers, together with the stopping and the controlled venting of the LAr bath were tested.

Another data taking campaign started around the end of May 2014, consisting of more than five months of single gas phase operation, with continuous data taking in warm (room temperature) and then cold (LAr temperature) argon gas. Several calibration measurements to assess the light yield of the detector were performed during the single warm gas phase data taking period, using external ^{57}Co and ^{83}Kr gamma sources. The energy dependence of the light yield has been evaluated together with its uniformity. In addition, the stability of the DAQ and the PMTs, together with the recirculation and purification systems have been tested during this warm argon gas data taking. Finally, a detailed analysis of isotope contamination coming from the ^{238}U and ^{232}Th decay chains has been carried out in order to evaluate the sources of internal gamma background contamination.

After the first test in warm argon gas, ArDM transitioned to the cryogenic operation mode with data taking in cold gas, which is approximately three times denser argon gas, at the beginning of September 2014. The main goal of this cold gas test was the commissioning of the detector in cryogenic conditions, including the monitoring of the DAQ and PMTs stability, together with the uniformity and the energy dependence of the light yield. The same strategy already presented in warm gas was followed in cold gas data taking, with several ^{57}Co and ^{83}Kr calibration measurements to assess the light yield and compare with previous results.

5.2 ^{241}Am alpha calibration source data

In order to detect the gas argon scintillation and to study the event position reconstruction, a low activity ^{241}Am alpha source was installed inside the ArDM detector vessel. The $\sim$5.5 MeV alpha particles emitted by the source provide at the same time a well-defined peak for full energy deposition and a relatively well localised scintillation photons emission, since the alpha average track in warm gas argon at the pressure of 1 bar is ∼4 cm.

The ^{241}Am alpha source, produced at CIEMAT in the Metrology laboratory with a total activity of ∼500 Bq, was made of an electro-deposited ^{241}Am layer, to ensure a stable attachment. The support for the deposition was a 1-mm-thick stainless steel disc, sealed with a thin Mylar protection layer, which was placed in a Teflon PTFE source holder, shown in Figure 5.1 (Left). This ^{241}Am source, together with a ^{57}Co gamma source and a ^{252}Cf neutron source, whose specifications are detailed in Table 5.1, have been provided by CIEMAT for the calibration of the ArDM detector.

Nuclide	**Type**	**Energy**	**Half-life**	**Activity (time)**	**Support**
^{241}Am	alpha	∼5.5 MeV	432.3 y	500 Bq (13/3/2013)	Electro-deposited
^{57}Co	gamma	122 keV	271.8 d	400 kBq (1/11/2013)	Encapsulated
^{252}Cf	neutron	0-13 MeV	2.645 y	10 kBq (1/4/2013)	5 mL vial

Table 5.1: Specifications of the sources provided by CIEMAT for ArDM calibration.

The energy spectrum of the alphas emitted has been measured showing negligible energy loss in the Mylar protection layer. Alpha emission is accompanied by 60 keV gammas for 36% of alpha decays, with a gamma emission rate which is estimated to be 180 Hz over 4π, however, half of them, which are emitted upwards, are absorbed by the stainless steel substrate.

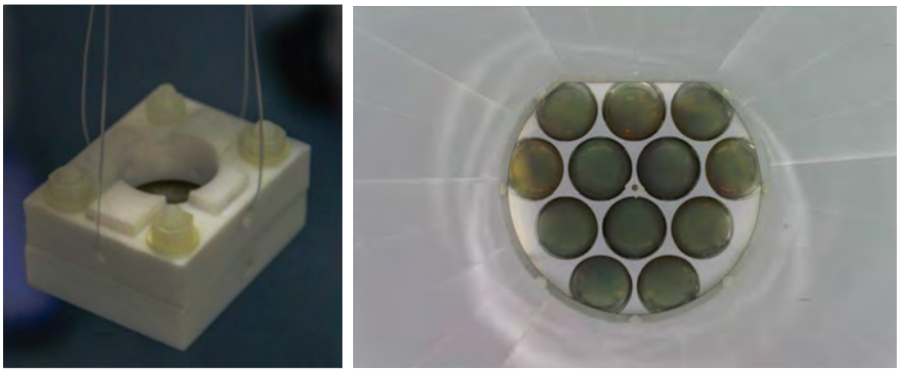

Figure 5.1: (Left) Alpha source inside the source holder hanging from a nylon thread. (Right) Bottom view of the ArDM active volume inside the lateral reflectors, showing the ^{241}Am source, which is hanging in the middle of the top PMT array.

In order to be able to move the source vertically from the cathode up to the extraction grids along the axis of the cylinder, the source holder was hanging from a nylon thread along the axis of the cylindrical active volume, as shown in the picture of Figure 5.1 (Right). Due to the possibility to change the height of the source inside the active volume, with the aid of a spool mounted onto a rotary motion feedthrough, the light yield and the event position reconstruction as a function of the drift coordinate (z) could be studied in a straightforward way.

Since the gas recirculation and purification system was not operative during this data taking period, the data were taken for 5-7 hours/day, limited by the degradation of the gas argon purity due to the outgassing, causing the loss of VUV light, which is absorbed by impurities, mainly oxygen and water. In order to cope with the lack of the gas recirculation and purification system, the detector was evacuated during the night and filled with pure argon gas the next day, monitoring constantly the argon quality by measuring the characteristic time of the scintillation light. The signals of each PMT array were analog summed, with a requirement of a coincidence within 100 ns of at least two photoelectrons for both PMT arrays. Furthermore, dedicated runs for the PMT calibration were taken using LEDs, with a variation of the gain among the PMTs within 5% for the entire data taking period.

In the analysis of the data mentioned above, we define the total light (Total [p.e.]) as the sum of the number of photoelectrons detected by every PMT placed on both top and bottom PMT arrays. We distinguish between the light detected by the top PMT array ($\mathrm{Total_{top}}$) and the bottom one ($\mathrm{Total_{bottom}}$); thus, we define the top to total ratio as

$$\mathrm{TTR} = \mathrm{Total_{top}}/(\mathrm{Total_{top}} + \mathrm{Total_{bottom}}). \tag{5.1}$$

Since that the scintillation light is emitted isotropically, the TTR is a measurement of the z coordinate of the source, as it is illustrated in the plots of Figure 5.2, where we present the TTR versus the total light detected by both arrays of PMTs for two different positions of the alpha source. The red blob visible in Total > 2000 p.e. moves in TTR as the z position of the source changes, indicating that those events are due to the alpha particles from the source, appearing in TTR ~ 0.6 for $z \sim 84$ cm from cathode, as it is shown in the plot of Figure 5.2 (left), and in $0.4 <$ TTR < 0.5 for $z \sim 47$ cm, as shown in the plot of Figure 5.2 (right).

Moving the source upwards makes TTR of these full energy alpha events increase, since more light is collected on the top PMT array and less on the bottom one. The total light collected varies within 10% with the source position, which represents a first result that proves the uniformity of the reflectors and the TPB deposition. The specific geometry of the source affects the rate of alpha particles emitted into gas argon, which is estimated to be ~100 Hz. In addition, since the source was placed downwards, the geometry of the source holder also reduces the rate, shadowing partially the top PMT array, and actually creates two types of alpha particle tracks, as shown in the scheme of Figure 5.3 (right).

Taking the plot of Figure 5.3 (left) as a reference, two main TTR-Total regions can be identified:

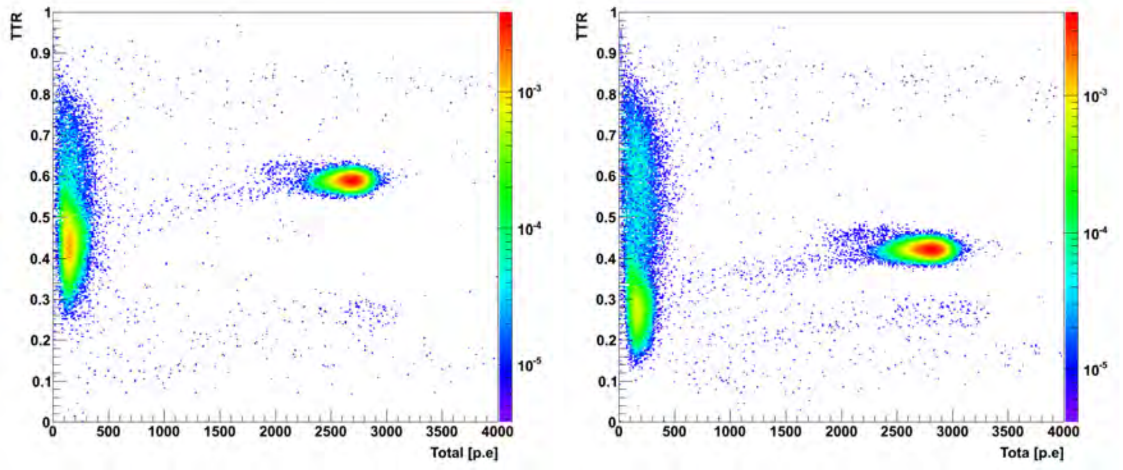

Figure 5.2: Top-to-total ratio (TTR) plotted as a function of total light detected in photoelectrons [p.e.] for data taken in warm gas at two different positions of the ^{241}Am alpha source: ∼84 cm from cathode (left) and ∼47 cm (right).

1. Events with Total $>$ 2000 p.e., which are due to the alpha particles depositing their full energy in gas argon.
2. Events with Total $<$ 500 p.e., which are due to background events distributed all over the active volume ($0.3 <$ TTR < 0.8 for z ∼84 cm from cathode) and also to the alpha particles hitting the source holder and, therefore, depositing only a fraction of the energy in gas argon ($0.3 <$ TTR < 0.6 for z ∼84 cm from cathode).

The light yield (LY) is defined as the number photoelectrons detected (p.e.) corresponding to a certain energy (keV), so it is expressed in p.e./keV. First LY tests were performed on surface at CERN with a ^{241}Am which was sealed with a palladium layer and had the energy peaked at 4.8 MeV. The number of photoelectrons detected with this source was at most 850 p.e., which gives LY=0.2 p.e./keV, being also significantly dependent on the position of the source. Furthermore, using 511 keV photons from a ^{22}Na source in a previous liquid argon test at CERN with no electric field a light yield of 0.7 p.e./keV was measured [143, 144].

Comparing with these surface tests performed at CERN in warm argon gas, the light yield of the detector assembled underground improved notably, with ∼2700 p.e. detected with no remarkable effect of the source position. Taking into account that the source used for the underground test delivers alphas with energy of 5.5 MeV, giving LY=0.5 p.e./keV, the gain in the light yield is a factor of 3. However, it is necessary to take into account that the light yield measured underground with the ^{241}Am source is affected by the shadowing effect produced by the source holder.

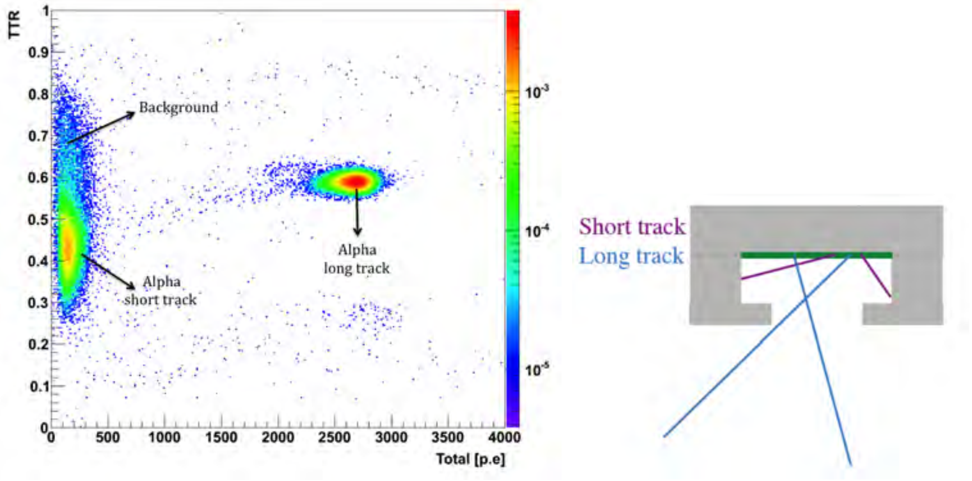

Figure 5.3: (Left) TTR versus total light detected for data taken in warm gas with the ^{241}Am source at $z \sim 84$ cm above the cathode. Two main different regions corresponding to the alpha long tracks and to background with alpha short track events superimposed are distinguishable. (Right) Scheme of the source holder indicating the two different type of alpha tracks.

5.3 ^{57}Co gamma calibration source data

Since several sources, such as ^{57}Co (85.6% $E = 122$ keV and 10.7% $E = 136$ keV) and ^{75}Se (58.3% $E = 136$ keV and 58.9% $E = 265$ keV), were suggested as possible candidates for gamma calibration, a detailed Monte Carlo simulation was required in order to investigate the type and activity of the gamma source needed to efficiently calibrate the Ar-TPC. For the calibration setup modelling, a point like gamma source with isotropic emission was placed at medium height and 40 mm distance from the outer dewar wall, which is approximately the distance where the vertical calibration pipe, described in Section 3.6, is installed, as it is shown in the simulation drawing of Figure 5.4 (left). The calibration pipes, made of corrugated plastic and installed between the ArDM vessel and the polyethylene shield, provide the possibility of scanning in xy and z coordinates by changing the horizontal position and height of the calibration sources.

The MC simulation was performed in liquid argon, which is the final goal for ArDM, using GAMOS [145], a framework for fast and flexible GEANT4 application developed at CIEMAT. The ArDM detector vessel was simulated with the real thickness of the four different stainless steel dewar walls, meaning that the gammas have to travel 6 cm to reach the inner detector volume, from which 2 cm correspond to stainless steel. The energy range considered for the scanning simulation goes from 100 keV up to 450 keV with steps of 50 keV, although smaller steps of 25 keV were considered for the most interesting energy range (100 - 200 keV). In order to have enough statistics, $2 \cdot 10^6$ events were simulated for energies above 150 keV and $4 \cdot 10^6$ events for lower energies. As an example, the spectra for 125 keV and 175 keV gammas are shown in the plot of Figure 5.4 (right).

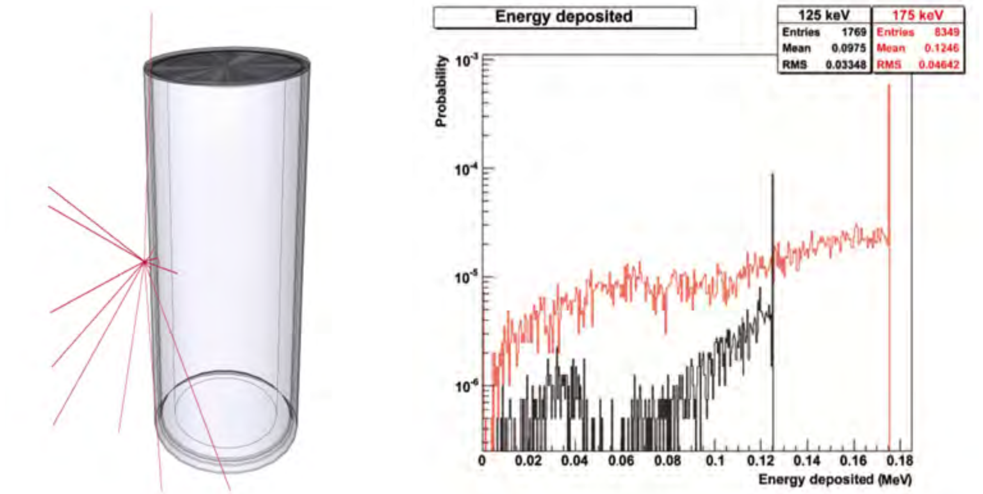

Figure 5.4: (Left) Dewar geometry used for energy scanning simulations. Some primary gamma tracks are depicted in red. (Right) Energy deposited in the sensitive volume by 125 keV and 175 keV gamma sources for the lateral pipe calibration setup.

The spectra for 125 keV gammas and the one for 175 keV gammas have a similar structure, consisting of the full energy peak, including both multiple and single (photoelectric) interaction, and a tail composed by multiple interaction events, which correspond to the not fully absorbed gammas, Compton dispersed, that interact before entering the sensitive volume or after leaving it.

Although the higher energy photons (175 keV) are more penetrating and they have a bigger interaction probability, the ratio between photoelectric and Compton interactions is lower: $(1.65 \pm 0.14) \cdot 10^{-2}$ for 175 keV and $(4.25 \pm 0.51) \cdot 10^{-2}$ for 125 keV [146]. Because of this and since we are interested in the lower energy range, the ^{57}Co source was selected for gamma calibration. In spite the fact that this simulation was carried out in liquid, which is the main goal for ArDM, later simulations in gas proved that some events are detected in gas phase, so the source is still useful for calibrations during the dry commissioning of ArDM.

The first gamma calibration source used during single warm gas phase underground commissioning of ArDM is a 180 kBq ^{57}Co source (originally 400 kBq), with a half-life of 271.8 days. This source, which gives ∼1 emission of 122 keV photon for each decay (dominant line, 85.6% Ig), was purchased from Eckert & Ziegler by the CIEMAT group. It is encapsulated in a small ~ 3 mm in diameter stainless steel cylinder, which can be attached to a specifically designed supporting system to be introduced inside the drawer of the ArDM polyethylene shield, as it has been already described in Section 3.6.

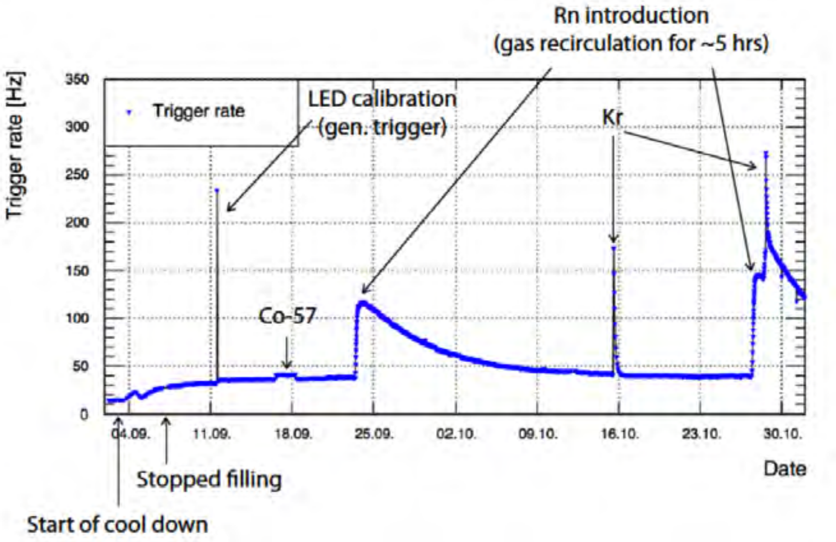

Figure 5.5: Time evolution of trigger rate (blue line) over the entire period of cold argon gas underground runs.

During the single gas phase data taking underground, several runs have been taken with ^{57}Co source placed in the polyethylene drawer, so that the gammas are emitted isotropically. The evolution of the trigger rate was monitored during the whole data taking period, as it is shown for cold gas in the plot of Figure 5.5. In the calibration run taken with ^{57}Co, a slight increase of the trigger rate of about 5 Hz was detected. There are also two rises of trigger rate corresponding to the switch-on of the recirculation system, so that they can be explained with the introduction of Rn inside the detector (see Section 5.5.). After each rise, the trigger rate decreases according to the Rn half-life of 3.8 days. The injection of Kr for two different calibration runs it is also translated into a rise of the trigger rate. In this case, the trigger rate decays much faster, following the Kr half-life (1.83 h).

The additional fluctuations ($\sim$1 Hz) of the trigger rate which have been registered with the detector in stable conditions can be eventually explained by tiny ($\sim$mV) fluctuations in the DC offset level of the electronic modules, possibly related to the temperature and humidity variations in hall A of LSC, where ArDM is installed.

Figure 5.6 shows the distribution of low energy events for both a background run (left) and isotropic ^{57}Co data (right) in warm gas by plotting the TTR versus total light in the region Total < 500 p.e., in which the ^{57}Co peak is expected to be found.

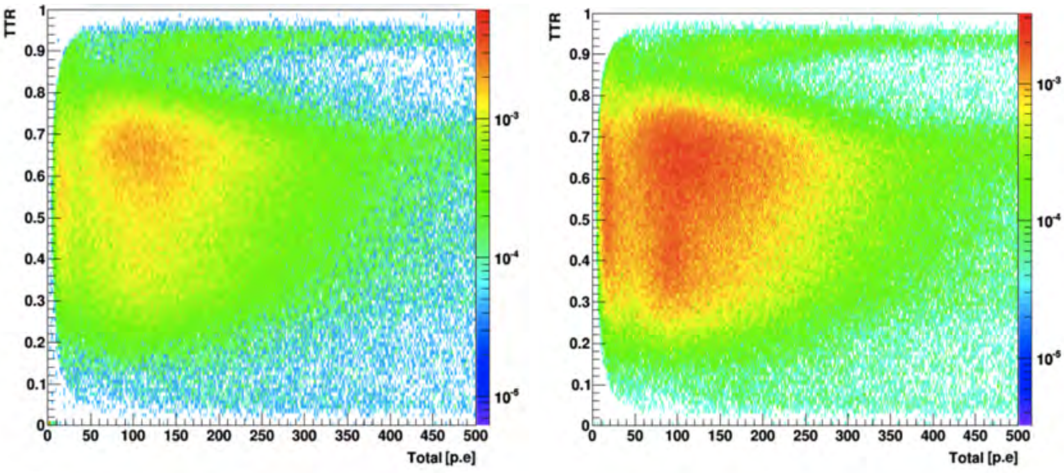

Figure 5.6: TTR versus total light detected in p.e. in warm gas for background (left) and with ^{57}Co events isotropically distributed (right) in the gas argon volume.

The colour scale represents the number of detected events and it is normalised by the data taking time, indicating a clear increase of rate in the central part of the detector, $0.3 < \text{TTR} < 0.75$, and around Total < 200 p.e for ^{57}Co data with respect to a background run.

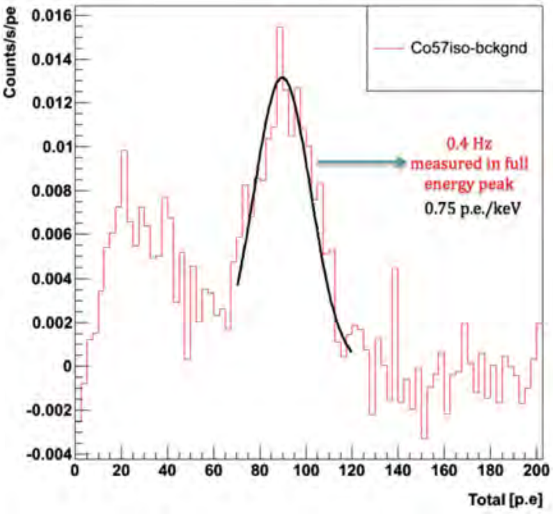

Figure 5.7: Gaussian fit to the 122 keV ^{57}Co peak of the total light spectrum collected with the source in warm gas, giving a light yield of 0.75 p.e./keV.

In order to assess the light yield from the ^{57}Co 122 keV gamma calibration line, a Gaussian fit was performed to the energy spectrum of the ^{57}Co data after subtracting the background, as shown in Figure 5.7. The light yield value obtained from this fit is LY = 0.75 p.e./keV, with a statistical error lower than 1%, which improves the result of LY = 0.5 p.e./keV obtained with the ^{241}Am source. The lower light yield result from alphas respect to gammas was expected since alpha particles are partially shielded by the effect of the source holder.

The measured energy spectrum of isotropic ^{57}Co data along with the background spectrum for a cold gas run are plotted in Figure 5.8 (left). The light yield was evaluated in analogy to the warm gas data, performing a Gaussian fit of the peak, as it is plotted in Figure 5.8 (right). The resulting light yield from the fit, calculated as 105.9 p.e./122 keV, is (0.8680 ± 0.0033) p.e./keV, with the error given by the statistical uncertainty from the fit. This value is slightly higher than the result previously obtained in warm gas (0.75 p.e./keV). In summary, an increase of the light yield from warm to cold gas argon is observed due to the improvement in the scintillation yield, which was expected given the fact that ion pairs are produced with a higher density in denser cold gas argon.

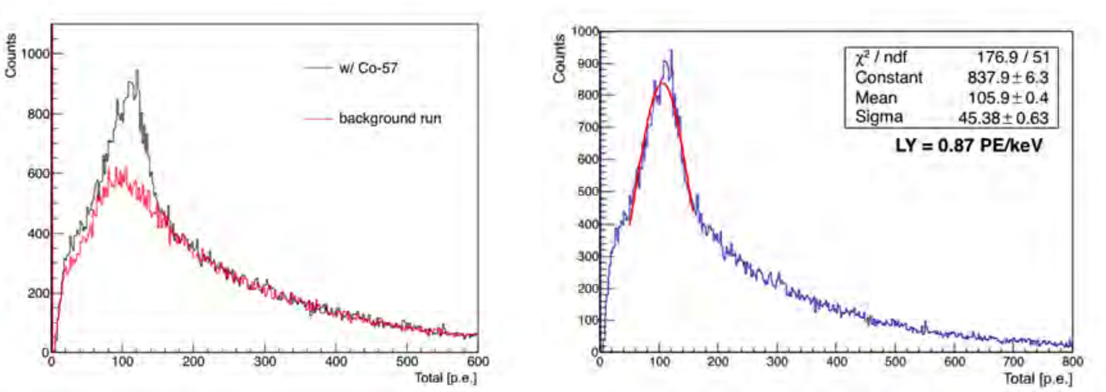

Figure 5.8: (Left) Total light detected in p.e. of the ^{57}Co runs compared to the background runs in cold gas, with the ^{57}Co peak clearly visible. (Right) Gaussian fit to the 122 keV peak for the data taken with the ^{57}Co source in cold gas, which indicates a light yield of 0.87 p.e./keV.

5.4 ^{83}Kr gamma calibration source data

The second gamma source used during ArDM underground commissioning is a 100 kBq ^{83}Rb/^{83}Kr source, which has been chosen for internal calibration because, as a noble gas, it disperses uniformly in all regions of the detector, providing the possibility to perform a study of the uniformity of the LY. In addition, it provides a gamma calibration at low energies, near the ArDM Dark Matter expected energy threshold ($\sim 10\,\mathrm{keV_{ee}}$) and the resulting ^{83}Kr isotope is stable, which is required to avoid introducing internal radioactive contamination in the detector.

The ^{83}Kr source consists of ^{83}Rb nuclides, which are produced by proton bombardment (27 MeV) of natural krypton gas via the reaction Kr(p,xn)^{83}Rb. The ^{83}Rb isotope decays dominantly (∼75%) into the metastable isomer $^{83\mathrm{m}}$Kr, which is left in any of the excited states of ^{83}Kr lying below the Q-value of the Rb decay (910 keV). Independently of the initial krypton excited state, the nucleus rapidly de-excites within picoseconds to the isomeric state $^{83\mathrm{m}}$Kr, located 41.5 keV above the ground state, which then decays to the first ^{83}Kr excited state (9.4 keV) with a half-life of 1.83 h, as it is shown in the scheme of Figure 5.9. Although typical intermediate metastable states have a half-life which is of the order of ps, the half-life of the $^{83\mathrm{m}}$Kr state (1.83 h) is long enough to use it for gamma calibration. Finally, ^{83}Kr excited state decays to the ground state with a half-life of 154 ns. Therefore, a $^{83\mathrm{m}}$Kr decay is indicated by two S1 pulses (32.1 keV and 9.4 keV) whose separation in time is characterised by a decaying exponential with $t_{1/2}$ = 154 ns [147]. Although is is difficult to distinguish the two transitions because of the small energy difference between both of them, they could be in principle separated by time since ∼5 ns is enough for the PMTs to distinguish two signals. However, the scintillation signal of Ar is not that fast since the slow component has a decay time of $\sim 1.6\,\mu$s.

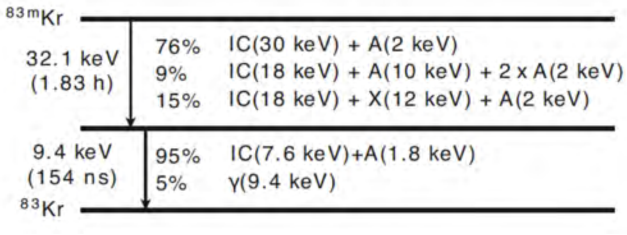

Figure 5.9: Decay and emission scheme of the metastable isomer $^{83\mathrm{m}}$Kr.

The ^{83}Rb isotopes that compose the ^{83}Kr source are attached to small grains of zeolite, which have been installed in the ArDM setup at LSC in a small vacuum-tight tube connected to the main detector volume. The $^{83\mathrm{m}}$Kr emanates from the zeolite, accumulating in the small tube. Zeolite was chosen as the host material due to the strong adhesion of the Rb atoms to it, as well as a high emanation efficiency for the Kr daughter nuclei. The firm fixation of the Rb atoms to the zeolite has been thoroughly investigated in previous studies [147, 148, 149], concluding that no release of Rb atoms from the zeolite could ever been detected to the level of $1 \cdot 10^{-10}$. This result is important because the presence of a Rb contamination inside the detector volume would constitute a permanent radioactive background source. The UHV (ultra high vacuum) source assembly has been installed in the gas recirculation circuit of the ArDM setup, as a bypass with two manual bellows sealed valves, as it is shown in Figure 5.10. The zeolite grains (2 mm in diameter), which are contained in the central compartment of the piece, have been separated by a perforated disk from the gas line, so that the whole system can be pumped and evacuated through its connection to the gas recirculation system. In order to perform a calibration, these radioactive atoms can be swept and distributed homogeneously into the ArDM detector volume via the gas argon recirculation circuit.

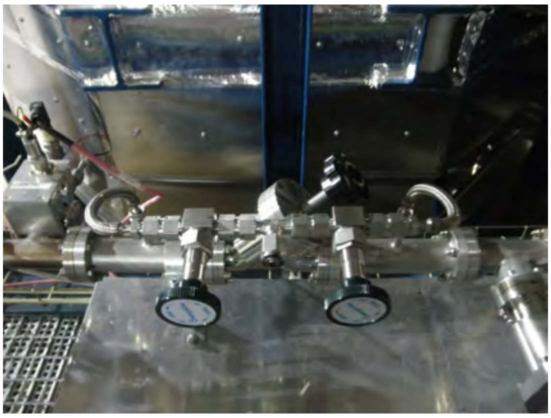

Figure 5.10: The ^{83}Rb/$^{83\mathrm{m}}$Kr source assembly mounted as a bypass to the gas recirculation circuit of ArDM.

The characteristic decay of 1.83 hours from $^{83\mathrm{m}}$Kr was obtained from an exponential fit to the evolution of the trigger rate with time, as shown in the plot of Figure 5.11, obtaining a result of 1.7 hours. Comparing both ^{83}Kr runs shown in Figure 5.5, the rate increased for at least 140 Hz when the source was injected in the first one; while, in the second run, the gas recirculation was switched on some hours before the source was injected, leading to a higher increase of the trigger rate, which reached 230 Hz. This higher increase in the trigger rate, due to introduction of radon in the system, was expected since, as it has been mentioned before, radon emanation depends on the total surface and switching on the gas recirculation adds the surface of the recirculation pipes to the inner detector surface.

A distribution of the events after sweeping the ^{83}Kr source into the detector is shown for a ^{83}Kr calibration run in the TTR versus total light detected plot of Figure 5.12 (left). As it can be inferred from this plot, the ^{83}Kr events are uniformly distributed within the detector, with the highest rate in the range $0.3 < \mathrm{TTR} < 0.75$ and around Total < 30 p.e.. This uniform distribution of the events was expected, since the source has been introduced in the gas argon volume via the gas recirculation system. The detected signal from the ^{83}Kr data indicates a sensitivity of the ArDM detector to a low energy threshold below $\sim$20 keV$_{\mathrm{ee}}$, thus confirming the expectation for the Dark Matter run.

In order to evaluate the light yield of the detector from ^{83}Kr data, the same

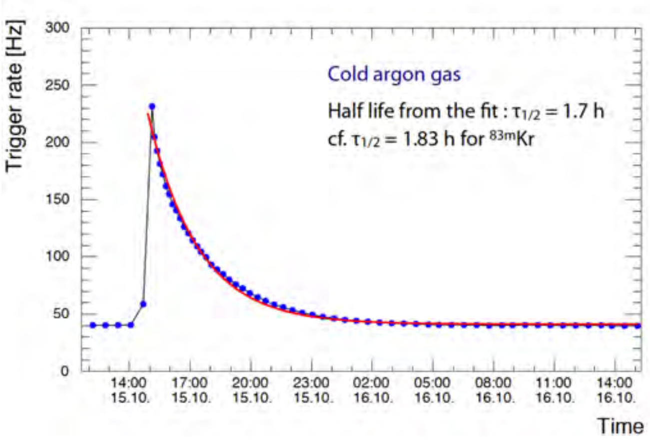

Figure 5.11: Half-life of $^{83\mathrm{m}}$Kr obtained from an exponential fit to the evolution of the trigger rate with time.

approach was followed as in the case of ^{57}Co. Figure 5.12 (right) shows the spectrum of the total light detected, with a Gaussian fit to the krypton peak. The light yield is calculated as 37.2 p.e./41.5 keV, resulting in (0.8961 ± 0.0012) p.e./keV for the light yield in warm gas, with the error given by the statistical uncertainty from the fit.

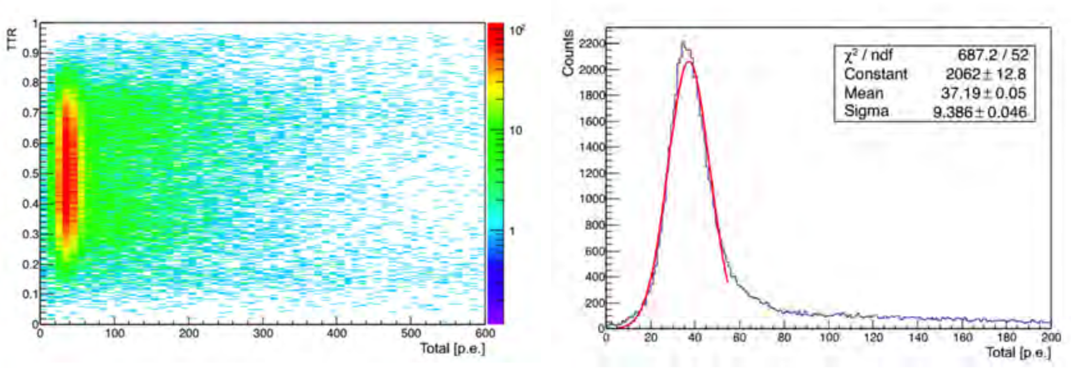

Figure 5.12: (Left) TTR as a function of the total light detected for data taken in warm gas with the ^{83}Kr source. The Kr events are isotropically distributed in the detector volume, as expected. (Right) Total light spectrum in p.e. for the ^{83}Kr data and Gaussian fit to the peak. The corresponding mean of the distribution gives a value for the light yield of 37.2 p.e./41.5 keV = 0.9 p.e./keV.

The spectrum of the ^{83}Kr source compared to the background as well as the fit to the ^{83}Kr peak for cold gas data are both shown in Figure 5.13 (left) and (right) respectively. From this data taken in cold gas phase, a value of $(1.0467 \pm$

0.0012) p.e./keV for the light yield is obtained from the fit. This result is in good agreement with the previous result from ^{57}Co and it is again slightly higher than the result obtained from ^{83}Kr in warm gas (0.9 p.e./keV). This increase was expected from the fact that the W-value is lower in targets with higher density [52], as it happens with cold argon gas with respect to warm gas.

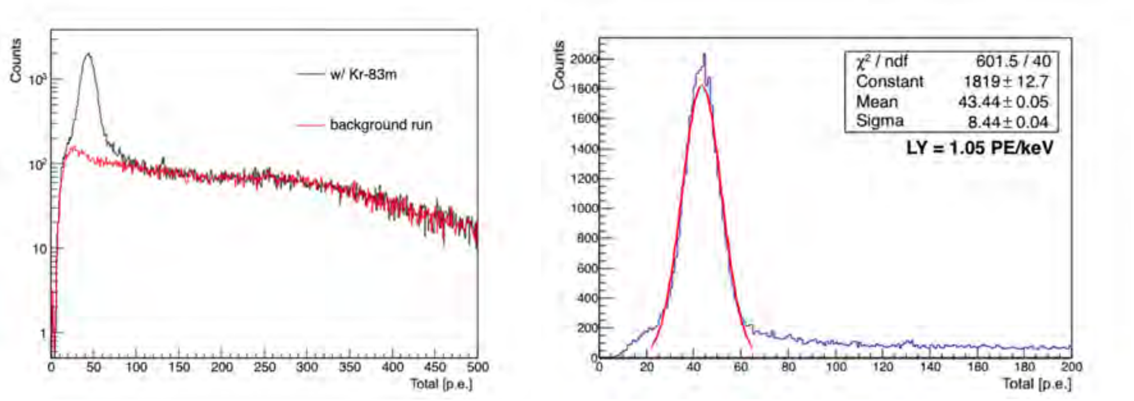

Figure 5.13: (Left) Total light spectrum of the first ^{83}Kr taken in cold gas argon compared to a background run. (Right) ^{83}Kr spectrum with background subtracted and a Gaussian fit to the peak, giving a value for the light yield of 43.44 p.e./41.5 keV = 1.05 p.e./keV.

5.5 Background studies: radon and daughter products

As we already mentioned in previous Chapters, among all unstable isotopes that are present on Earth, there are few ones that are long-lived, thus the entire decay chain can still be present in nature. Particularly, natural isotopes ^{238}U (half-life = 4.5 billion years) and ^{232}Th (half-life = 14 billion years), which can be detected via their decay products, are present in laboratory rock walls and also in detector materials. In Figure 5.14 we show both decay chains of ^{238}U and ^{232}Th, in which we see that radon is formed as an intermediate step in the mentioned radioactive decay chains, until ^{206}Pb or ^{208}Pb stable isotopes are produced.

Since radon is an inert gas at typical atmospheric pressure and temperature, the small contamination of ^{238}U and ^{232}Th in the detector materials is expected to produce a continuous emanation of ^{222}Rn (half-life = 3.8 days) and ^{220}Rn (half-life = 55.6 s) gas inside the active volume, producing a background of alpha particles originated from natural decays. This effect can be enhanced by the gas recirculation system since the Rn emanation depends on the total surface. The Rn is accumulated

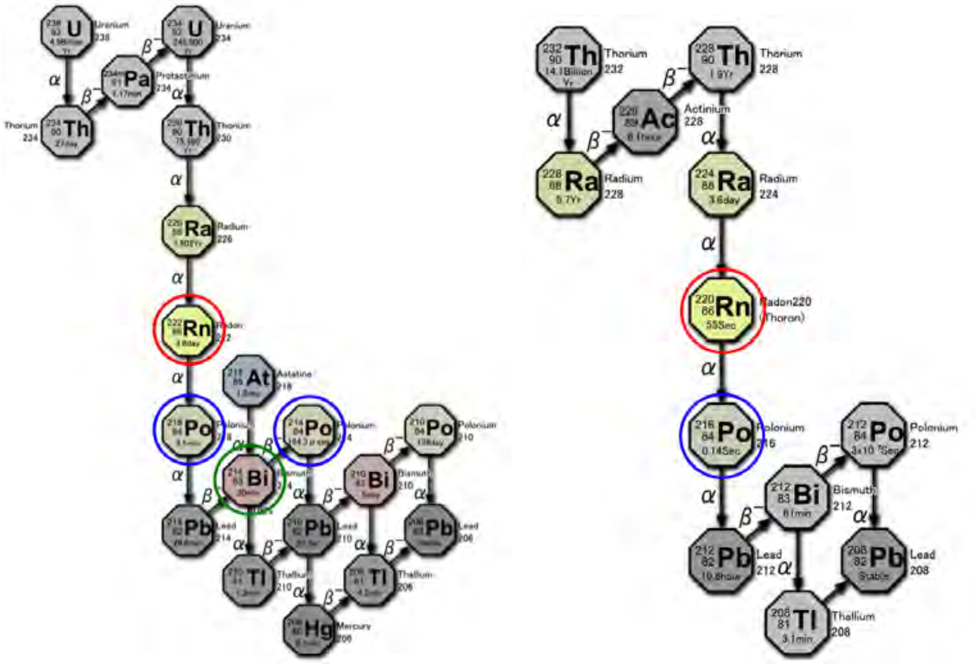

Figure 5.14: ^{238}U (left) and ^{232}Th (right) natural radioactive decay chains. ^{222}Rn and ^{220}Rn isotopes are marked with red circles, while the Po isotopes and decays (Bi-Po) that have been identified in the present analysis are marked with blue and green circles respectively.

in the recirculation pipes, creating a medium rich in Rn that is introduced inside the detector volume when the recirculation system is switched on. It is expected that radon diffuses uniformly inside the detector and, once it decays, ions are generated. These ions can be drifted by an electric field and attach to inner detector surfaces.

In the plot of Figure 5.15 we present the TTR (top to total ratio of light collected by the two PMT arrays as defined in Section 5.2), which parametrises the detector z coordinate, as a function of the total light detected (Total [p.e.]). Different arc-like structures and "blobs" appear in the range between 3000 and 7000 photoelectrons (p.e.) of total light detected when switching the gas recirculation system. These structures can be interpreted as alpha emissions inside the detector and are compatible in energy with the alphas originated from the radon decays that come from the purification cartridges and are flushed through the vessel by the recirculation system. The "blobs" are compatible with radon decay products (positive ions) that are drifted towards the photocathode of the top PMTs by a small residual electric field present in the active volume and stick onto the PMTs on the top array (negatively charged). For low values of total light (Total$<$ 1500 p.e.) a beta contribution is observed and the region Total$<$ 1500 p.e. and TTR$>$ 0.85, which will be analysed in more detail in Section 5.6, is in principle compatible with Po nuclei from alpha decays recoiling into the gas argon phase. Finally, the regions with 0.7 <TTR< 0.95 or 0.05 <TTR< 0.35 and Total> 4000 p.e. are compatible with alpha particles from top and bottom PMT arrays respectively.

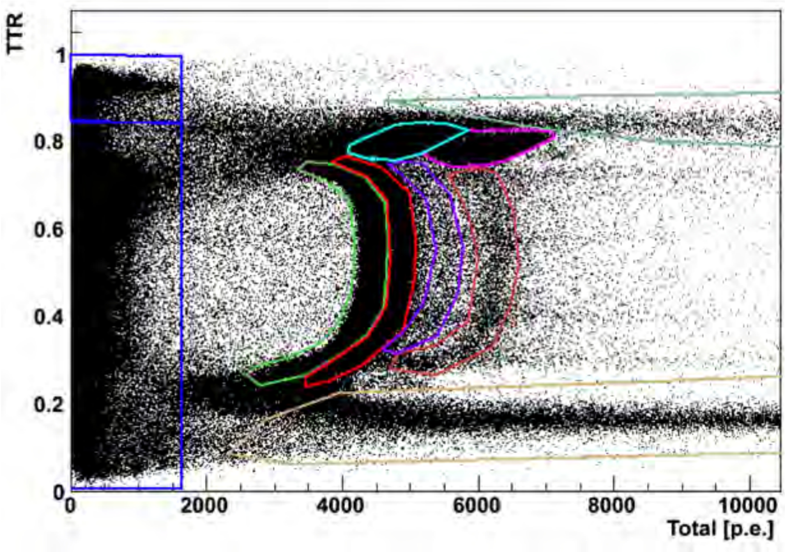

Figure 5.15: Regions selected for the rate study to distinguish different isotope contributions.

In order to study the rate due to the different contributions from Rn and its daughters, several regions in the TTR versus scintillation plane have been selected, presenting the percentage of events in each selection with respect to total events detected and their corresponding contribution to the measured rate in Table 5.2. These results show that the highest contribution to the total event rate comes from beta particles and from radon itself, while the lower rates correspond to contributions that are compatible with Rn daughters.

The spectra (Total [p.e.]) for all events is shown on the plot of Figure 5.16 (right) (black histogram), in which three peaks are visible. These peaks can be compatible with ^{222}Rn, ^{218}Po and ^{214}Po isotopes coming from the ^{238}U decay chain. In order to study the contributions from the different isotopes depending on their position inside the detector, two selections have been performed on TTR, corresponding to the middle and top regions of the detector, where we observe the arc-like structures and the blobs respectively. These bands are depicted in red ($0.45 < \mathrm{TTR} < 0.55$) and blue ($0.75 < \mathrm{TTR} < 0.8$) in the plot shown in Figure 5.16 (left) and the spectra for these TTR selections are plotted with the mentioned colours in Figure 5.16 (right) together with the total spectrum. The comparison of the spectra for the different TTR selections shows that the contribution from Rn is nearly uniform inside the

Element	**Region**	**LY**	**TTR**	**% Events**	**Rate (Hz)**
Betas	**Region 1**	< 1600	0 – 0.85	68.3	18.0
Po nuclei	**Region 2**	< 1600	0.85 – 1	3.3	0.9
^{218}Po	**Region 3**	4100 – 5600	0.75 – 0.85	3.2	0.8
^{214}Po	**Region 4**	5200 – 7200	0.74 – 0.83	3.2	0.9
^{222}Rn	**Region 5**	2500 – 4700	0.22 – 0.76	9.2	2.4
^{218}Po	**Region 6**	3400 – 5100	0.22 – 0.76	3.0	0.8
^{216}Po	**Region 7**	4600 – 5800	0.3 – 0.75	0.3	0.1
^{214}Po	**Region 8**	4600 – 6600	0.25 – 0.75	0.6	0.1
-	**Region 9**	5000 – 45000	0.7 – 0.95	0.6	0.2
-	**Region 10**	4500 – 45000	0.05 – 0.35	2.6	0.7
Total	–	–	–	94.3	24.9

Table 5.2: Rn and daughters rate study, showing the percentage of events and the rate corresponding to each region selected in the TTR-Total distribution.

detector while its daughters accumulate near the top PMT array. This effect can be eventually explained recalling that Rn is an inert gas, so it is neutral and diffuses within the detector volume, but its daughter isotopes produced in the Rn decay are positively charged. As a consequence, they are drifted towards the windows of the PMTs that are negatively charged and due to the slow drift velocity ($\sim$ min) of the positive ions, a vertical arc-like structure remains in the detector, while the isotopes that have arrived to the top PMT array generate the observed blobs at TTR$= 0.8$. One important result, inferred from the curved shape of the structures created by the ion drift, is that the light collection is not completely uniform in height.

In addition, if we plot the spectra for the same TTR selections in logarithmic scale (Figure 5.17), we can distinguish two more contributions to the spectrum of total light detected, which are compatible with ^{216}Po and ^{212}Po coming from ^{220}Rn in the ^{232}Th decay chain. The explanation for this very small contribution of ^{220}Rn daughters is the short half-life of ^{220}Rn, which implies that many of these isotopes may not have enough time to enter the active volume before decaying.

Finally, in order to obtain an energy calibration, the high energy part ($>$4000 p.e.) of the spectrum has been fitted with five different Gaussians over a small constant background in the plot of Figure 5.18 (left), four of them corresponding to the contributions compatible with ^{222}Rn, ^{218}Po, ^{216}Po and ^{214}Po isotopes detected in our experimental system. The fifth one, between ^{218}Po and ^{216}Po, is compatible in energy with the ^{220}Rn isotope from the ^{232}Th decay chain. In the case of ^{216}Po, which decays to ^{212}Pb with a half-life of 0.145 s, there is no enough time for the ion to be drifted to the top PMT array, thus there is no blob at TTR ~ 0.8 corresponding to this isotope. In Figure 5.18 (right), the mean values of the four physical Gaussians

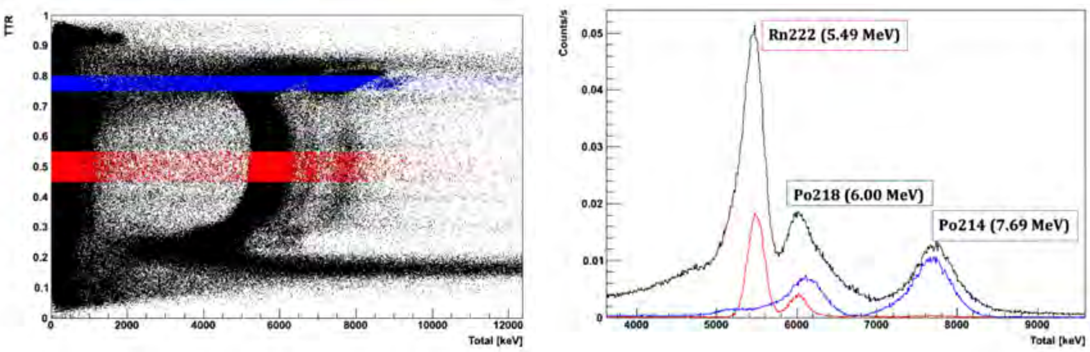

Figure 5.16: Selected TTR vs total light slices to study different isotope contributions (left) and ^{222}Rn, ^{218}Po and ^{214}Po peaks contributing to the total light detected can be distinguished depending on the selected slice (right). After applying an energy calibration, the positions of the peaks are in good agreement with the expected energies from each decay.

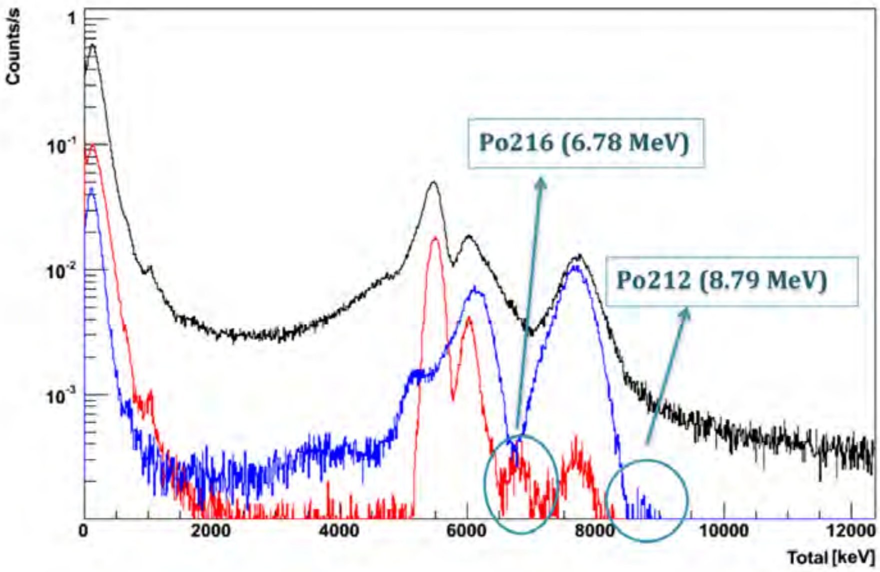

Figure 5.17: Gamma peaks compatible with ^{216}Po and ^{212}Po isotopes from ^{232}Th decay chain.

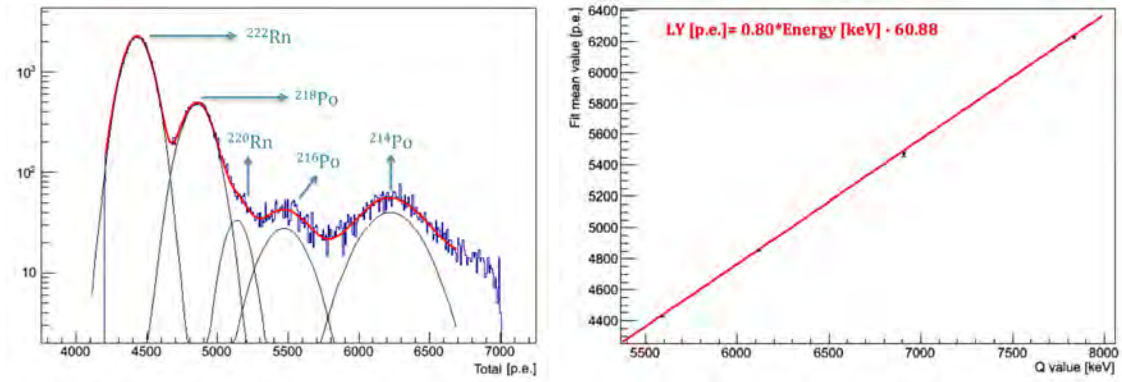

Figure 5.18: (Left) Rn and Po peaks fitted with Gaussians to obtain the energy calibration and (Right) linear fit obtained from previous four pair of values of total light detected in p.e. and corresponding energy in keV. The error bars are calculated from the errors of the fit.

have been plotted as function of the Q-values of the alpha decay of ^{222}Rn and the mentioned Po isotopes. The Q-value has been used in place of the alpha energy since both alpha and recoil nucleus deposit their kinetic energy inside the active volume. The fit proves a very good linear behaviour of the detector, also at high energies, and provides the conversion from p.e. to keV, obtaining a light yield of 0.8 p.e./keV. This result is in perfect agreement with the ones reported previously from ^{57}Co and ^{83}Kr gamma calibrations, which allows to conclude that the calibration in warm gas is not dependent on the energy. In cold gas, we have structures different from the arc-like and “blob” ones present before in warm gas. This is possibly given by the fact that at lower temperatures, Rn is condensed directly on the reflector walls.

5.6 Bi-Po analysis

Although the previous analysis is compatible with the presence of Po isotopes within the detector, it is not sufficient to distinguish them unequivocally. An independent way to confirm the results of this isotope analysis is to measure the time delay between beta and alpha decays, which allow to measure the isotope half-life.

Let us apply this method to our data. According to the previous scenario, alpha events are selected as the ones in the 5600 p.e.$<$Total$<$ 7000 p.e. range of total light detected, as it is shown in Figure 5.20 (left), and then the difference in time (μs) with the previous event is calculated. In Figure 5.20 (right), we show the plot of the selected events with the corresponding calculation of the isotope half-life in warm gas. The distribution shows an exponential decay and a flat contribution due to random coincidences with previous events, which below 500 μs corresponds to 3% of

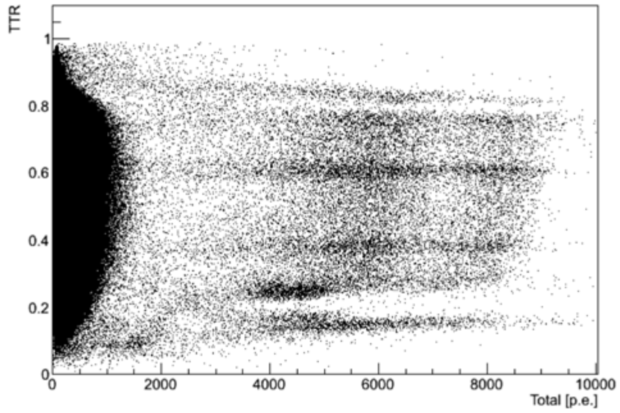

Figure 5.19: TTR versus scintillation plane in cold gas. Different structures from the ones present in warm gas appear probably due to condensation of Rn on the reflector walls.

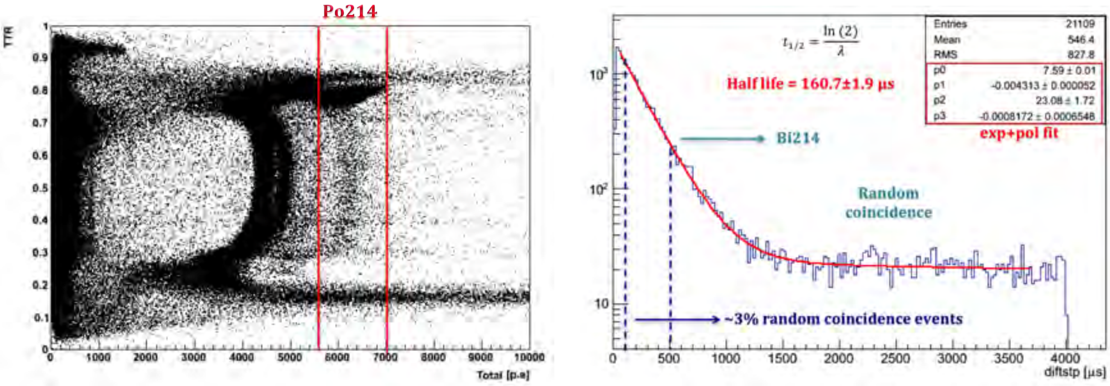

Figure 5.20: ^{214}Po event selection (left) and calculation of ^{214}Po half-life (right) in warm gas. The result for the half-life is compatible with the expected value within 2σ, showing also a low contribution from random coincidences with previous events, of the order of 3% below 500 μs.

total events. After a exponential+first order polynomial fit, the calculated half-life is $t_{1/2} = 160.7 \pm 1.9\,\mu$s, with the error obtained from the statistical uncertainty of the exponential parameter, p_1, from the fit. This result is consistent with the expected value of ^{214}Po, 164.3 μs, within 2σ, thus confirming our previous hypothesis of the presence of ^{214}Po isotopes coming from Rn in our detector.

Once we have identified the ^{214}Po isotopes, let us recall that Po decays happen mainly on the window of the PMTs, thus it is reasonable to assume that only roughly 50% of times, the subsequent alpha decay deposits its energy inside the active volume, while in the other 50% of the cases the alpha hits the windows and the recoil nucleus enters the argon gas region, releasing typically 100-300 keV. These nuclear recoils can be identified by their low energy, their position close to the top PMT array and BiPo analysis. We can therefore redo the BiPo analysis for these events by selecting them with a simple cut in TTR (TTR>0.85) and total light (Total<1600) as it is shown in Figure 5.21 (left).

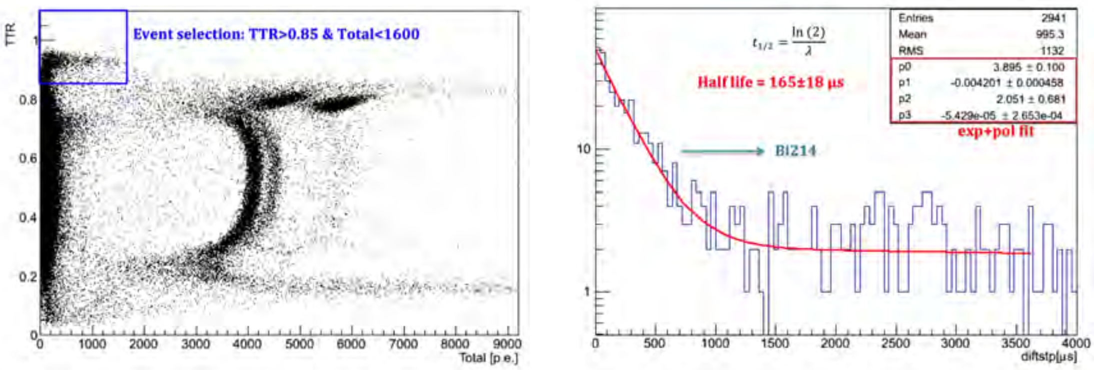

Figure 5.21: Selection of nuclear recoils (left) and calculation of ^{214}Po half-life in warm gas for nuclear recoil events (right).

The result for the Po half-life, $t_{1/2} = 165 \pm 18\,\mu$s, obtained again with a exponential+first order polynomial fit of the time distribution shown in the plot of Figure 5.21 (right), is well consistent with the real value, which confirms that these events are compatible with ^{214}Po, allowing us to identify them as nuclear recoils.

Finally, in order to perform the BiPo analysis in cold gas, alpha events are selected considering a wider selection (Total>4000 p.e.) compared to the previous one in warm gas (5600 p.e.<Total< 7000 p.e.) since we do not have the arc-like and "blob" structures any more, as shown in the plot of Figure 5.22 (left). Then the difference in time (μs) with the previous event is calculated in cold gas, as shown in the plot of Figure 5.22 (right). The time distribution shows again an exponential decay due to ^{214}Bi and a background flat contribution due to random coincidences with previous events, which below 500 μs corresponds to 7% of total events. After a exponential+first order polynomial fit, the calculated ^{214}Po half-life, $t_{1/2} = 169.0 \pm 4.3\,\mu$s, is compatible with the expected value, $164.3\,\mu$s, within 2σ.

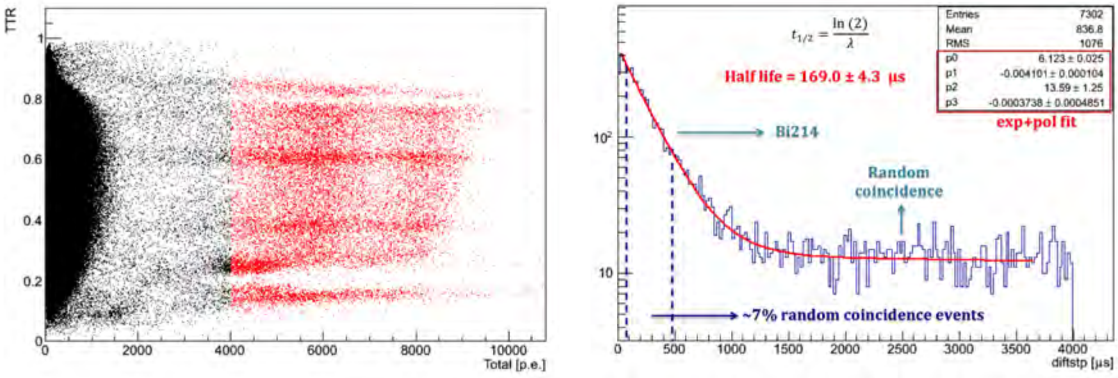

Figure 5.22: (Left) Events selected for the ^{214}Po study in cold gas are depicted in red and total events are shown in black in the TTR versus total light plane. (Right) Calculation of ^{214}Po half-life in cold gas. The result is compatible with the expected value within 2σ.

In Figure 5.23 we compare the positions of the ^{214}Bi events in cold gas (red dots) with the ones in warm gas (black dots) by plotting the TTR versus total light distribution of these events. The majority of them are distributed between 0.2 and 0.9 in TTR with a more homogeneous distribution of events in cold gas, which also spreads in a wider range of total light detected, as expected from the wider ^{214}Po event selection.

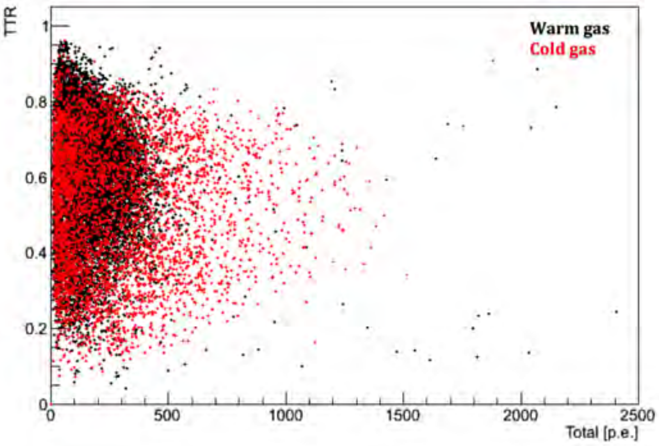

Figure 5.23: Position of ^{214}Bi events in the TTR-Total light plane for warm gas (black dots) and cold gas (red dots).

5.7 Position reconstruction with neural networks

The reconstruction of the interaction position is crucial to understand the response of any Dark Matter detector and to improve the uniformity of the signal. This is particularly important for ArDM due to the fact that the Ar-TPC is not operative yet, meaning that there is no information on the interaction position at this moment. Since ArDM has operated in single phase during Run I, we have developed an Artificial Neural Network (ANN) algorithm based on the S1 signal detected by the two arrays of PMTs in order to have minimal information on the xy position. In the future, once the TPC will be in place and operative, this algorithm could be used through the S2 signal, measured in gas by the top PMT array, to have a much more straightforward reconstruction of the xy interaction position.

5.7.1 Artificial neural networks

Artificial neural networks (ANN) are algorithms inspired by human brain which are composed by interconnected processing units called “neurons” or nodes made of mathematical functions that produce a certain value corresponding to a determined input. The information is processed separately by each neuron and passed to another one distributed in the network via weighted links, called synapsis. There are several types of ANN, the most typical application is based on the reconstruction of the relationship between an input and a known output and the guessing of an unknown output corresponding to a determined input [150].

The perceptron is a simple ANN composed by individual neurons distributed in two interconnected layers, one for the input and one for the output. One or more hidden layers can typically be used between input and output layers, as it is shown in the scheme represented in Figure 5.24, where a multilayer perceptron contains an input layer with three neurons, one hidden layer with four neurons and an output layer with two neurons. In this example, the neurons of the different layers are connected feedforward, which means that each neuron of the layer i is connected to all the neurons of the following layer $i+1$, so that the data flows in one direction. Opposite to this case, we have recurrent ANN, in which data flows in a loop and is useful when the problem is consistent with a time evolution.

Typically each neuron makes the sum of its inputs, p_i, through weights, $w_{i,j}$, which is feed to the so-called activation functions, here denoted as F_j, such that the output,q_j, from the j neuron is written as

$$q_j = F_j\left(\sum_i w_{i,j}\cdot p_i\right). \tag{5.2}$$

ANN may use different types of activation functions, such as the sign function, linear function, sigmoid function and hyperbolic tangent function. These various

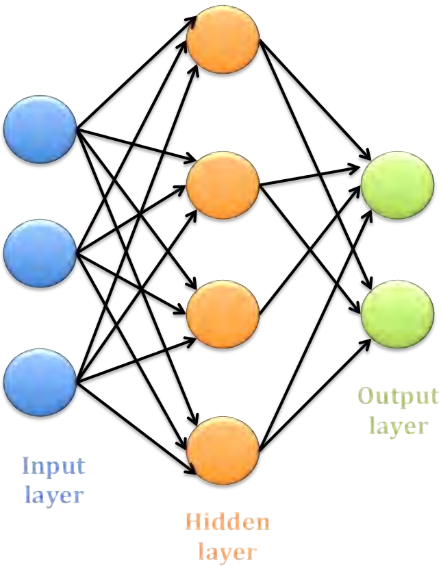

Figure 5.24: Simple feedforward ANN with an input layer, one hidden layer and an output layer.

types of activation functions allow the hidden and output neurons to model non-linear relationships between the input parameters and output values. In our present study, we will use the hyperbolic tangent, represented in the plot of Figure 5.25, since it is conveniently applied to both function approximation and classification problems.

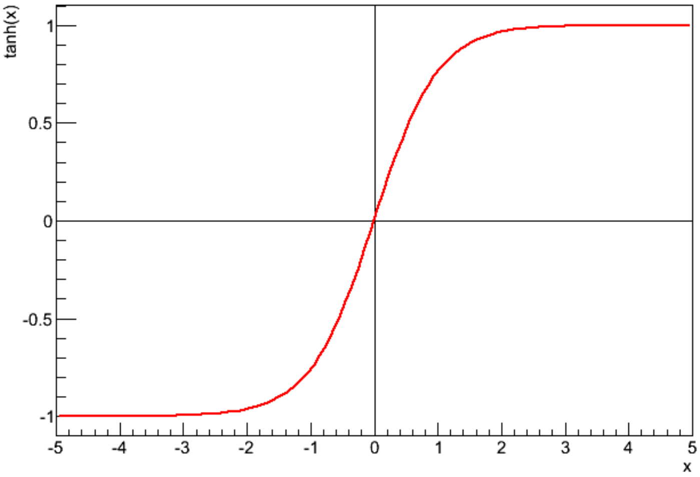

Figure 5.25: Hyperbolic tangent used as activation function in the neural network.

5.7.2 Training of artificial neural networks

As it has been mentioned before, the main characteristic of ANN is their learning ability, which is the capacity of finding correlations between an input and an output. The training process of an ANN, which is performed with a high statistics sample of events with known outputs, is a supervised learning that adapts the weights of the links until they fit the input-output relationships of the underlying data. The training algorithm extracts correlations between the given inputs and determines a set of weights that minimise the total sum of squared errors, which, for a single input vector n, is typically expressed as

$$e^n = \frac{1}{2} \sum_l \left(y_l^n - T_l^n \right)^2 , \tag{5.3}$$

where T_l is the target output value for the output neuron l.

However, the global optimization is not trivial because it is difficult to determine the error term associated with each hidden node. In order to address this problem, a learning algorithm known as backpropagation, which takes into account the errors for neurons at layer $k+1$ to estimate the errors for neurons at layer k, has been used. The basic computation of backpropagation can be divided into two phases: forward phase, in which the outputs of the neurons at level k are computed prior to computing the outputs at level $k+1$, and the backward phase, in which the weights at level $k+1$ are updated before the weights at level k are updated.

The key computation for ANN training algorithm is finding out the best weight vectors applied in the model. The free parameters are first initialised to small random values and then the algorithm keeps updating the weight parameters in each iteration until the ANN is consistent with the outputs of the training dataset. The new weight is a combination of the original weight and a part based on the prediction error. If the prediction is correct, then the weight remains unchanged; otherwise, it is modified. In the weight update algorithm, the links that contribute the most to the prediction error are the ones that require the largest adjustment. The weight algorithm has a learning rate parameter λ, which takes values between 0 and 1, to control the amount of adjustment made in each iteration. If λ is close to 0, then the new weight is mostly influenced by the value of the old weight. On the other hand, if λ is close to 1, then the new weight is sensitive to the amount of adjustment performed in the current iteration.

During our training we used a specific backpropagation algorithm called resilient backpropagation, in which the network parameters are updated only after the error has been computed for the whole training set. In this case, the final error is computed as the average error as follows:

$$E = \frac{1}{N} \sum_{n=1}^{N} e^n . \tag{5.4}$$

An important issue that has to be taken into account during the training is the over-training of the network, which means that the ANN perfectly fits the training set but it will not be able to guess the output for other events. In order to minimise the possibility of over-training, two data sets were used during the training process: the training and the validation sets. The error given by Equation 5.4 is also calculated for the validation set, but without updating the network parameters with it, so that the validation set ensures that when the error with the training set decreases, the error with the validation set also decreases. The network is trained for a certain number of cycles until the error converges to a global minimum.

In the present analysis, we have used Java Neural Network Simulator (JavaNNS), a simulator for neural networks developed at the Wilhelm-Schickard-Institute for Computer Science (WSI) in Tübingen, Germany, which works on Windows, Mac and UNIX platforms [151]. This software supports several types of ANN models and provides a useful graphical interface for network creation and training. An example of the graphical interface of the JavaNNS program is shown in Figure 5.26. In this picture, the structure of the network is shown with the neurons depicted in different colours depending on their weights. The chosen resilient propagation algorithm together with its parameters and the number of training cycles is also shown in the top right part of the picture. Finally, the evolution of the average error for both training and validation sets, which decreases as the training process evolves, is plotted as function of the number of cycles passed on the bottom right part of this picture.

5.7.3 Monte Carlo performances

As it has been mentioned previously, during the first tests carried out underground, ArDM was operated in single gas phase, so that only the primary scintillation signal was detected. However, given the large PMT coverage of the active volume, it is still conceivable to infer the interaction position information with sufficient resolution in case of sophisticated ANN algorithms. Therefore, a routine based on ANN techniques has been developed in order to reconstruct the 3D position of the interaction based on the light pattern detected by the top and bottom PMT arrays.

A first test has been carried out using an ANN based on three layers with 24 input neurons corresponding to the PMT signals, 24 neurons in the hidden layer with hyperbolic tangent as activation function and 3 neurons in the output layer corresponding to the x, y, z position of the interaction. The input signals have been normalised for the total light collected, thus only the fraction of the light detected by each PMT is known to the ANN. In that way, the ANN output is nearly independent of the absolute magnitude of the signal, apart from the intrinsic statistical fluctuations given by the PMT signals that can be more relevant at lower energy. The ANN has been trained on $8 \cdot 10^4$ MC alpha events generated uniformly

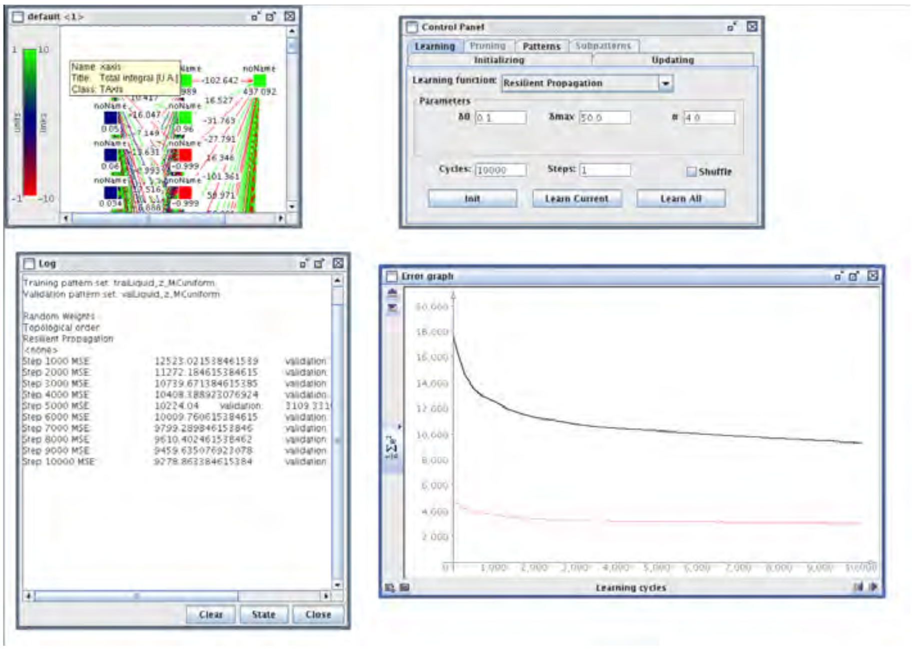

Learning function: Resilient Propagation

Parameters

Δ0 0.1 Δmax 50.0 α 4.0

Cycles: 10000 Steps: 1 ☐ Shuffle

```
Training pattern set: traiLiquid_z_MCuniform
Validation pattern set: valLiquid_z_MCuniform

Random Weights
Topological order
Resilient Propagation
<none>
Step 1000 MSE:          12523.0215384615З9      validation
Step 2000 MSE:          11272.184615384615      validation
Step 3000 MSE:          10739.671384615385      validation
Step 4000 MSE:          10408.388923076924      validation
Step 5000 MSE:          10224.04     validation:     3109.311
Step 6000 MSE:          10009.760615384615      validation
Step 7000 MSE:          9799.289846153846       validation
Step 8000 MSE:          9610.402461538462       validation
Step 9000 MSE:          9459.635076923078       validation
Step 10000 MSE:         9278.863384615384       validation
```

Figure 5.26: Model of JavaNNS graphical interface showing the trained ANN, with the different colours indicating the weights of each neuron (top left), the chosen resilient propagation algorithm together with its parameters and the number of training cycles (top right), the written details on the training (bottom left) and the evolution of the average error function for both training and validation sets (bottom right).

in the sensitive region and its performances have been evaluated on a different set of $2 \cdot 10^4$ MC alpha events and on the real data taken during this first detector operation in gas.

In Figure 5.27 we have plotted the MC x, y and z distributions of values that have been used for the validation of the ANN training process (black) together with the ANN reconstructed coordinates (red). The two distributions present quite similar behaviour for each coordinate if we compare MC values with results from ANN, covering the same ranges in each case with small differences in the borders. These differences are mainly due to the fact that the reconstruction of the position made by the ANN becomes more and more challenging as we approach to the borders since there are less MC values to train the ANN.

In the plots shown in Figure 5.28, the errors between the ANN output and the MC position are shown for the x and z variables, proving the possibility of the position reconstruction with a resolution of the order of few centimetres for most of the events. In particular, performing a Gaussian fit to the difference between the simulated MC position and the result obtained from the ANN gives a difference of

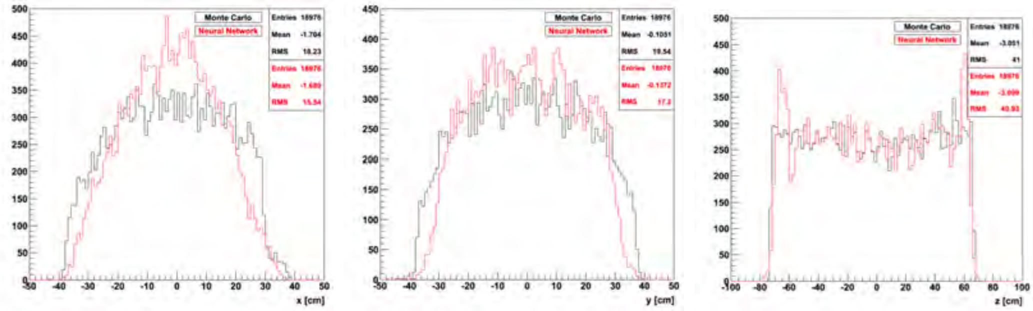

Figure 5.27: Comparison between MC values and results after training the ANN for x (left), y (middle) and z (right) positions. Both distributions cover the same range for each coordinate, with slight differences in the borders.

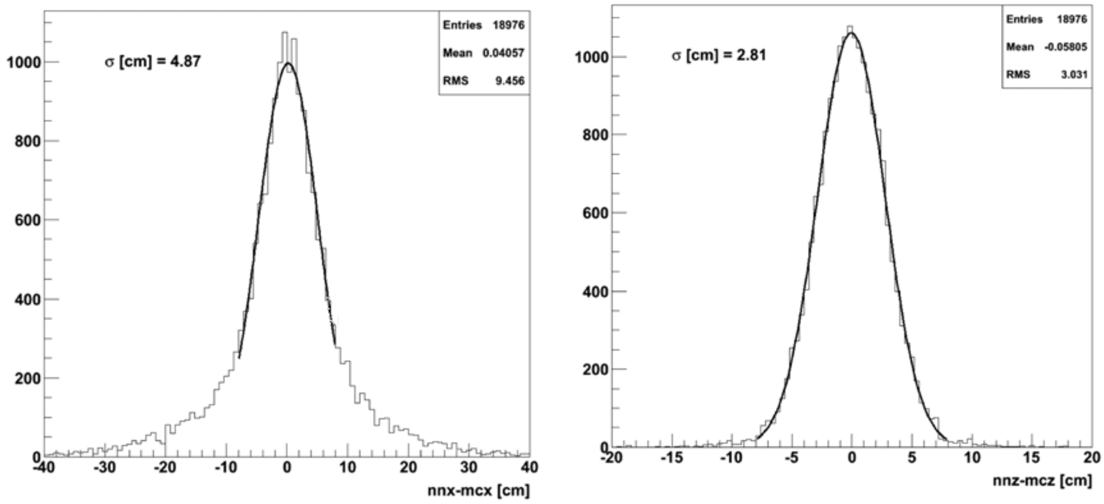

Figure 5.28: Position reconstruction error between the ANN and the MC on x (left) and z (right). A similar result to x has been obtained for y.

$\sim$ 5 cm for the x coordinate and a lower difference of $\sim$ 3 cm for the z coordinate. The better result for the z coordinate is due to the intrinsic vertical symmetry of the detector; while the x and y coordinates, which give similar results from the ANN, suffer from the lack of symmetry caused by the field shapers flat part in the xy plane.

In Figure 5.29 we have the reconstruction error map in the MC xy plane. The colour scale in the z axis accounts for the difference between the ANN output and the MC position, proving once again the possibility of the position resolution of the order of few centimetres for most of the events.

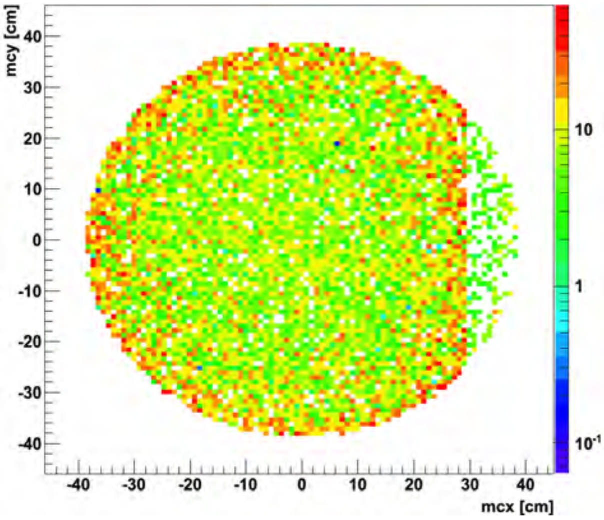

Figure 5.29: Error map for neural network. The colour scale in the z axis illustrates differences between event coordinates and reconstructed position in each point of the MC xy plane.

5.7.4 Neural networks results from alpha source data

Different runs taken with the ^{241}Am source inside the detector have been analysed in order to compare the reconstructed positions with the positions of the source holder, which are known with an uncertainty at the level of the centimetre. It has to be noted that the holder has not been considered in the MC geometry used for the ANN training, thus the reconstruction algorithm can be biased by the significant shadowing effect of the holder itself on the top PMT array. In order to minimise that effect, runs with the source in the three positions which are closer to the bottom part of the detector have been chosen for this study.

In the plot of Figure 5.30 the position of the holder for the three selected runs is compared with the map of the reconstructed events. While a systematic shift of the reconstructed position is evidenced at higher holder position, possibly explained by the shadow effect, the ANN output is few centimetres away from the real source position. In order to improve the results, more sophisticated ANNs have been also studied, in which the structure of the ANN has been changed adding another hidden layer or including more neurons. The latest results show an improvement of the order of 10% in each variable respect to the first results.

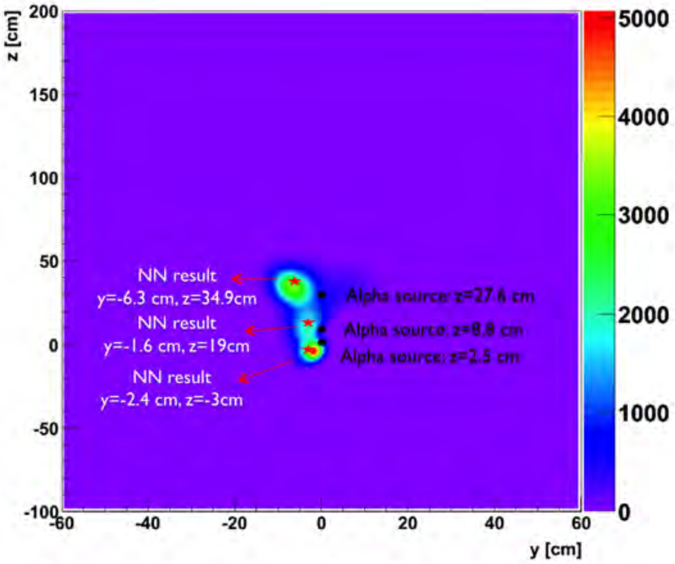

Figure 5.30: Comparison between ANN results marked with red stars and real source positions represented as black points.

5.7.5 Neural networks results from background data

The ANN described in Section 5.7.3 has also been used for position reconstruction of background data taken in warm and cold gas argon some months after ^{241}Am, during underground operation of the ArDM detector in pure gas argon phase. The results for the z coordinate in mm are shown as a function of the energy [keV] in Figure 5.31, reproducing the characteristic arc-like and blob structures caused by the radon and polonium isotopes present in the uranium and thorium natural decay chains, which have been already discussed in previous Sections. From the comparison of this plot with the one for TTR shown in Figure 5.15, we conclude that the ANN reproduces the expected behaviour of TTR showing the same structures corresponding to beta, radon and polonium that we have in real data. The correlation of the TTR value and the z coordinate in cm reconstructed by this ANN is shown in Figure 5.32, together with the drift length of the detector and the extraction and cathode grids delimiting its sensitive volume. According to this plot, any position in TTR can be directly interpreted as a position along the z axis, having a quite linear relationship between the two variables.

The ANN can be also used to reconstruct the position in the xy plane. In Figure 5.33 we show the reconstructed xy position (cm) for two different types of events in warm gas. The vertical axis represents the number of events detected per second during the data taking. First, we select the inner part of the detector in height by requiring an absolute value of the z coordinate lower than 500 mm,

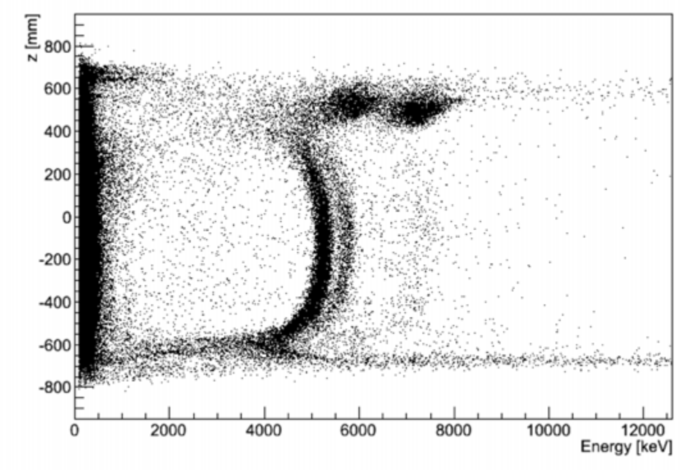

Figure 5.31: z coordinate (cm) from ANN warm gas results plotted as a function of the energy (keV), showing characteristic arc-like and blob structures of the radon and daughter isotopes.

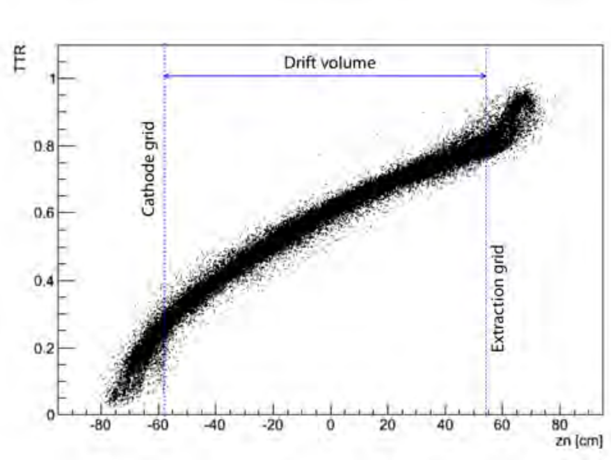

Figure 5.32: TTR as a function of the reconstructed ANN z coordinate (cm) from warm gas data, with the lines indicating the position of the detector. Considering this correlation, any position in TTR can be directly interpreted as a position along the z axis.

then we apply a cut in energy (less than 1 MeV), obtaining a quite homogeneous result for the position reconstruction in xy, shown in the plot of Figure 5.33 (left). In Figure 5.33 (right) we select events with energies between 2 and 9 MeV and z coordinate greater than 500 mm. In this case, the reconstructed events appear to be much less homogeneously distributed. In particular, those events are clustering around the centre of the PMTs, which is consistent with previous hypothesis of positive ions (daughter isotopes from Rn) attaching to the negatively charged PMTs.

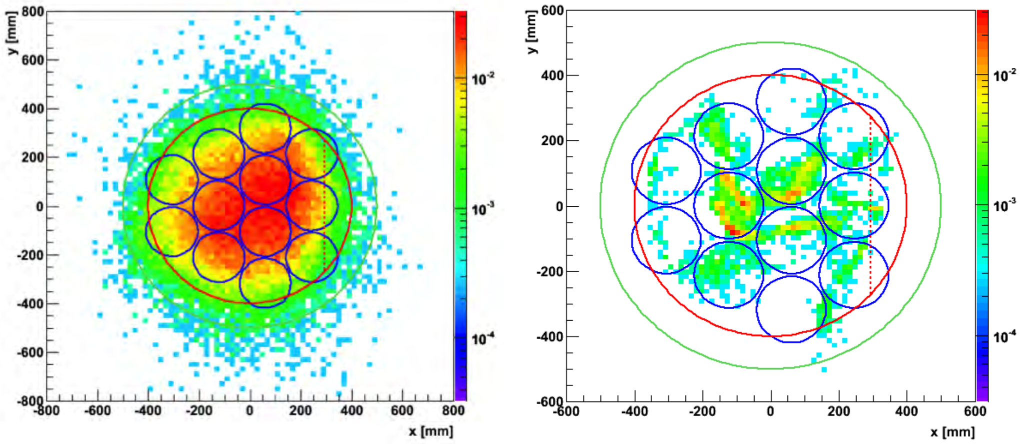

Figure 5.33: Reconstructed xy interaction position (mm). (Left) Energy $< 1\,\mathrm{MeV}$ and $|z| < 500$ mm. (Right) $2\,\mathrm{MeV} < E < 9\,\mathrm{MeV}$ and $z > 500\,\mathrm{mm}$. The PMT positions have been included (blue circles) as well as the dimensions of the detector in the xy plane.

Chapter 6

ArDM data taking and analysis in liquid

ArDM achieved a major milestone in February 2015, when the filling of the detector vessel with approximately 2 t of liquid argon (LAr) was finally completed, thus the experiment entered the first period of physics data taking in single-phase pure LAr operation mode [2]. The main goal of this first underground LAr run was the wet commissioning of the detector in cryogenic conditions, providing at the same time a first glimpse in the Dark Matter path. In addition, this first LAr data taking was aimed to study the stability of the DAQ and the PMTs, the performance of the LAr recirculation system, the energy dependence and uniformity of the light yield and the background in deep underground environment. Differently from gas, in which the contribution of ^{39}Ar was small ($\sim$1 Hz) due to the low mass of Ar contained inside the detector vessel, ^{39}Ar becomes the dominant electron background in liquid ($\sim$1 kHz), thus measuring its contribution to the energy spectrum constitutes one of the LAr run main goals.

During this LAr operation phase, different calibration runs were taken not only with ^{57}Co and ^{83}Kr gamma sources, which had been already used in gas, but also with a ^{252}Cf neutron source. Studies on the distribution and discrimination of nuclear recoil events respect to electron recoil events have been also developed. Finally, the tools that have been already presented in gas data were used to perform BiPo studies and event position reconstruction with Artificial Neural Network (ANN) using LAr data.

After completing this first LAr data taking period, the neutron shield, which had remained partially opened in the top part during both gas and liquid data taking periods to ensure a quick access to the detector vessel, was completely closed in order to study the reduction of the trigger rate by comparing with previous data, thus fully evaluating the detector background for the first time.

A total of 3.3 billion events were recorded resulting in 215 TB of raw data, which were compressed by a factor of 4 for storage. The data obtained with the polyethylene shield closed amounts to approximately 2 billion events, the rest being with the shield open.

Finally, at the beginning of August 2015, ArDM was emptied and warmed up in order to prepare the detector upgrade that will allow the experiment to face the second period of physics data taking in the double-phase TPC operation mode in 2016.

6.1 Filling of the ArDM detector with liquid argon

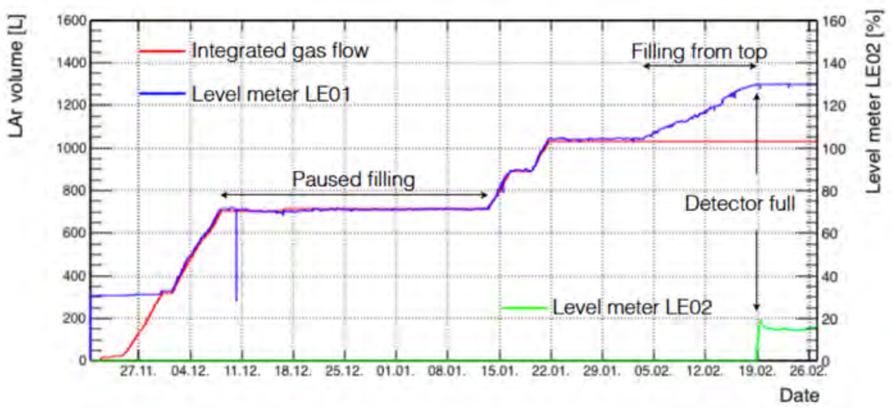

Figure 6.1: Evolution of the filled LAr volume measured by a flow meter (red curve) and the level meters LE01 (blue line) and LE02 (green line) for the whole filling period.

After performing the first tests in gas argon and completing a full risk assessment study to ensure the safety of the experimental setup, ArDM finally obtained permission from the LSC laboratory to fill the detector vessel with LAr in the end of November 2014. The entire filling process of the detector vessel, which is detailed in Figure 6.1, lasted for about three months with several periods in which the filling was paused for technical reasons, and also during the Christmas break for safety reasons since the access to the laboratory was restricted within this period. During this filling phase, pure (99.9999%) gaseous argon from standard batteries of 16 - 200 bar gas bottles at room temperature was allowed to condense into the system using the 300 W Gifford-McMahon cryocoolers.

In the plot of Figure 6.1, the time evolution of LAr volume in litres introduced into the system is represented as a function of time. The condensed amount of LAr was controlled continuously by three methods: the pressure of the argon gas battery, the integrated input-gas flow read and recorded by a flow meter (red curve) and a $\sim$ 1.5 m-long cylindrical capacitive level meter (LE01, blue curve) installed inside the detector vessel. Since the bottom of LE01 is approximately at the top of the bottom PMTs, it started to register the LAr level values only after the system had already held 300 L.

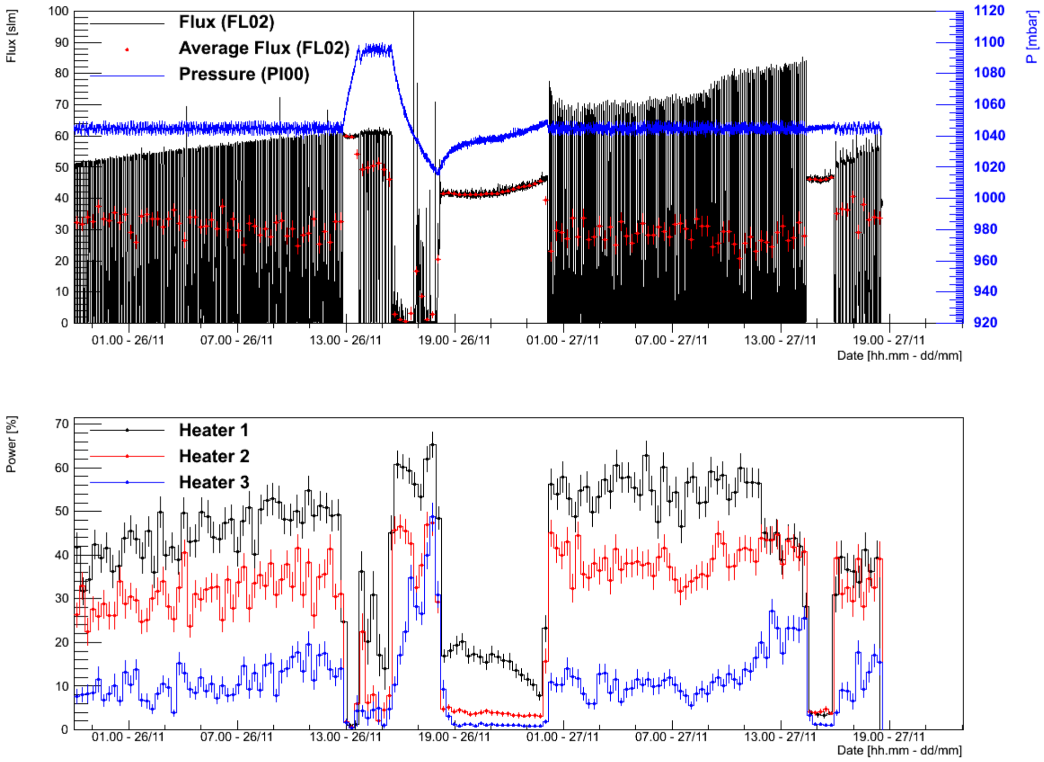

Figure 6.2: (Top) Evolution of the pressure inside the detector vessel (PI00) represented in blue, together with the total and average LAr flux entering the vessel in standard litres per minute (slm), presented with a black line and red points respectively, for a $\sim$2 days period of the LAr filling process. (Bottom) Evolution of the operation power for the three different cryocoolers during the same period.

During most of the time, argon was condensed in a cooling coil, which is completely immersed in the cooling argon bath volume and connected to the bottom of the vessel. Although this method provided the highest efficiency, it was changed into filling from the top flange of the vessel for the last 20% of the process, in order to deal with increasing hydrostatic pressure inside the vessel and to ensure the safety of the system. This last part of the filling was monitored by three small capacitive level meters, which are mounted $\sim$ 5 cm below the bottom end of the top PMTs, at the final desired level of liquid. This level, represented for one of the level meters

(LE02) by the green curve in the plot of Figure 6.1, was achieved on 18 February 2015.

In the top plot of Figure 6.2, the pressure inside the detector vessel (PI00) is represented together with the total and average fluxes of LAr entering the vessel in standard litres per minute (slm) for ∼2 days during the filling period. Several tests were performed within this period by modifying the gas argon flow that enters the system from the battery of bottles. In the first hours, the average flux (FL02) is maintained around ∼30 slm, which makes PI00 quite stable; but when FL02 is increased to more than ∼50 slm, PI00 starts to rise, dropping again as FL02 decreases some hours later. A short interval in which the average flux is extremely low due to an exchange of the gas-bottle bank is observed on 26/11. The corresponding operation power (%) was also monitored for the three cryocoolers (see Section 3.1), as it is shown in the bottom plot of Figure 6.2, showing that less heating power is needed for higher values of the average flux (FL02).

At the end of the process, ArDM had been filled with a total mass of 2 tons of LAr (∼870 kg of active target) and was fully ready for the first data taking in liquid. At that moment, ArDM was the first ton-scale LAr detector to start underground operation.

6.2 Calibration measurements

During the LAr commissioning phase of ArDM in deep underground environment, several calibration measurements were performed with ^{57}Co and ^{83}Kr gamma sources aiming to study the energy dependence and uniformity of the light yield in LAr cryogenic conditions. In addition, ^{252}Cf neutron source measurements were performed to investigate the discrimination of electron recoils versus nuclear recoil events, thanks to differences in the pulse shape between both events. Although we already started monitoring the detector stability and we had a first look on the LY during the filling of the detector, the data presented in this Section correspond to the runs taken with the detector completely filled and the neutron shield partially opened.

6.2.1 ^{57}Co and ^{83}Kr gamma sources

In order to evaluate the light yield (LY) in liquid of ArDM and to compare with previous measurements in gas, several calibration runs have been taken with the detector already filled with liquid, using the same external ^{57}Co source (122 keV line) and injecting internally the ^{83}Kr source (41.5 keV line) which were used in the gas argon data taking and have been described in the previous chapter. The analysis of these data and the consequent calculation of the LY has been performed considering different selections of TTR with the goal of studying the LY dependency with the detector height, represented in this case by TTR, and to evaluate its stability in time comparing data from different runs.

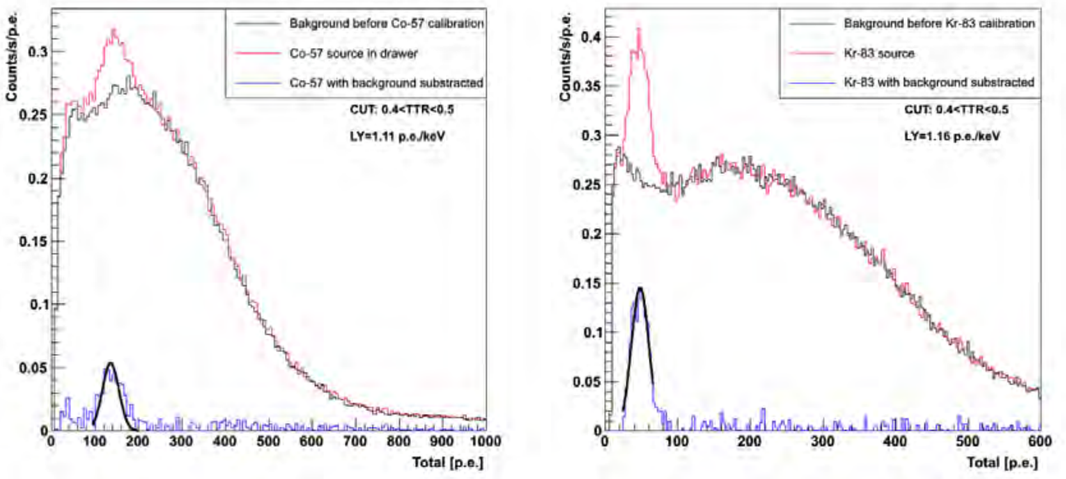

Figure 6.3: Evaluation of the LY in LAr from ^{57}Co (left) and ^{83}Kr (right) spectra for the data selection $0.4 < \mathrm{TTR} < 0.5$. The result obtained from the fit to the gamma peak for ^{57}Co, LY=1.11 p.e./keV, is compatible with the one calculated for ^{83}Kr, LY=1.16 p.e./keV.

The TTR selections used in the present analysis cover the range $0.1 < \mathrm{TTR} < 0.9$ in slices of 0.1. Two examples of the obtained spectra from both sources after a TTR selection and the fits to the corresponding gamma peaks are shown in the plots of Figure 6.3. In this case, for $0.4 < \mathrm{TTR} < 0.5$, the fits provide LY results that are in good agreement between each other, in particular 1.11 p.e./keV for ^{57}Co (left plot) and 1.16 p.e./keV for ^{83}Kr (right plot). These results are higher than the ones obtained for gas argon data (LY=0.9 p.e./keV in warm gas and LY=1.05 p.e./keV in cold gas).

The comparison among the different considered TTR ranges is illustrated in Figure 6.4 for four independent calibration runs (two ^{57}Co runs and two ^{83}Kr runs) taken with several days of time difference. The LY results go from 0.9, for higher TTR selections, up to 1.2, showing in general higher values of the LY for the selections that are closer to the detector centre in height. In addition, a slight decrease in the LY is observed for the more recent runs taken with the ^{83}Kr source.

In summary, the LY in liquid ($0.9 < \mathrm{LY} < 1.2$) slightly improves with respect to gas (LY=0.9 p.e./keV in warm gas and LY=1.05 p.e./keV in cold gas). This increase was expected from the fact that the W-value is lower in targets with higher density [52], as it happens with liquid argon with respect to gas. However, the increase was not as much as expected (~2 p.e./keV) for reasons that are still unknown, but could

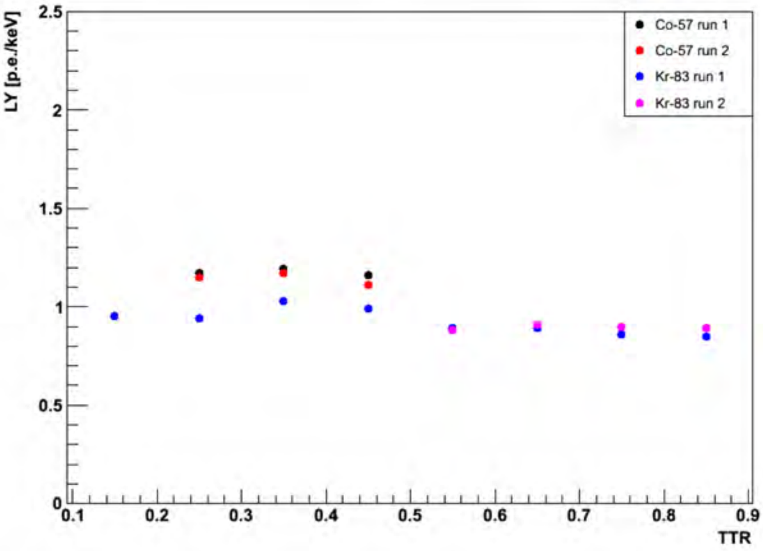

Figure 6.4: LY comparison for different TTR selections on several ^{57}Co and ^{83}Kr runs taken with the neutron shield partially opened. The results are contained in the range $0.9 < \mathrm{LY} < 1.2$, with higher values for TTR selections corresponding to the middle height of the detector.

be eventually explained by certain degradation of the wavelength shifter or to some contaminations condensing on the main reflector and thus lowering its reflectivity. Those effects were estimated in the simulations and have the strongest influence on the total light yield when changed.

6.2.2 ^{252}Cf neutron source and pulse shape discrimination

First neutron runs in LAr were taken in March 2015 with a ^{252}Cf from CIEMAT which emits $\sim$ 600 neutrons/s via spontaneous fission. The goal of this data taking with the neutron source was to produce nuclear recoil events and to evaluate the response of the ArDM detector to these events and the achievable pulse shape discrimination with respect to electron recoil events.

The trigger rate from background with the neutron shield partially opened, which was 1.97 kHz, increased up to 2.23 kHz when the ^{252}Cf source was placed inside the calibration drawer. In this configuration we took several runs with the ^{252}Cf source in different positions, but the great part of the data were taken with the source inside the calibration drawer. The different background and ^{252}Cf spectra are shown in the plot of Figure 6.5. In all the cases two small bumps corresponding to the gammas of ^{40}K ($\sim$1500 p.e.) and Tl ($\sim$2600 p.e.) are visible and the main difference of ^{252}Cf in the drawer with respect to the background spectrum is visible for energies above

4000 p.e. (~ 4 MeV), with a bump around 6000 p.e. (~ 6 MeV). This bump may be due to production of ^{41}Ar from neutron capture on ^{40}Ar ($Q = 6.1$ MeV).

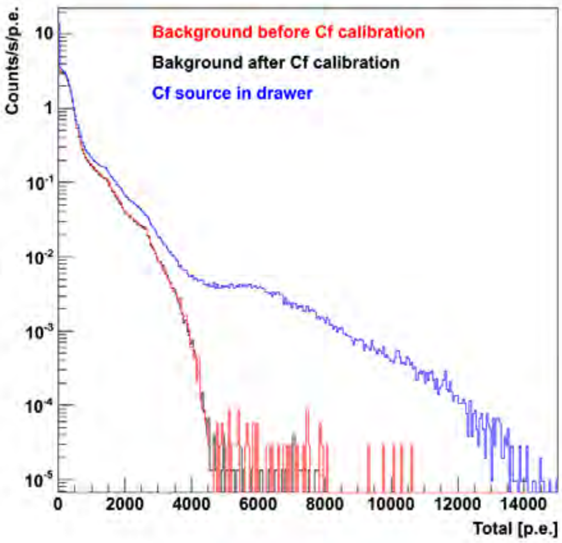

Figure 6.5: Background spectra before (red) and after (black) the calibration with the ^{252}Cf source and with the source placed inside the calibration drawer (blue). The main difference of the ^{252}Cf spectrum with respect to the background one is visible above 4000 p.e. (~ 4 MeV).

Signals from neutrons coming from the ^{252}Cf source were identified by pulse shape discrimination (PSD) since, as described in Chapter 2, the population ratio of the two Ar excited molecular states $r = p(^1\Sigma_u^+)/p(^3\Sigma_u^+)$, depends strongly on the ionisation density of the track, which is directly determined by the incident particle. This means that light particles, such as electrons and gammas will lead to a ratio of $r \simeq 1/2$, while heavier particles, including α particles and fission fragments, will have $r \simeq 4/5$, as it is shown in the event displays of Figure 6.6.

In these plots the pulse height (V) is presented as a function of time, showing relevant differences in the pulse shape between an electron recoil and a nuclear recoil event, particularly in the slow component. As consequence, thanks to the differences in fast/slow scintillation components, it is possible to discriminate between electron and nuclear recoil events. For this purpose, the component ratio (CR) is defined as the fast component of the scintillation light divided by the entire scintillation signal. The fast component is calculated in a 108 ns time interval which includes the highest signal peak and is defined as: $[t_{\mathrm{main\ peak}}$-60 ns, $t_{\mathrm{main\ peak}}$+48 ns$]$. Therefore, signals from neutrons were identified in the high CR region, as shown in the plots of Figure 6.7, in which TTR is plotted versus CR for background (left) and

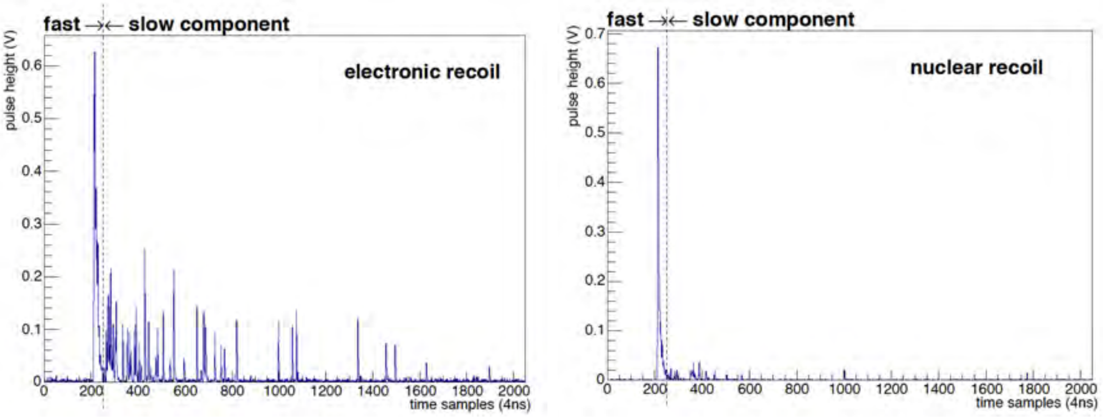

Figure 6.6: Event display of an electron recoil (left) and a nuclear recoil (right) registered in ArDM during the liquid argon underground commissioning. Relevant differences are observed in the pulse shape between electron recoils and nuclear recoils.

^{252}Cf (right). Neutrons coming from the ^{252}Cf source, which have a higher ratio of fast/slow scintillation light with respect to particles producing electron recoils, appear as high CR events, CR ~ 0.75.

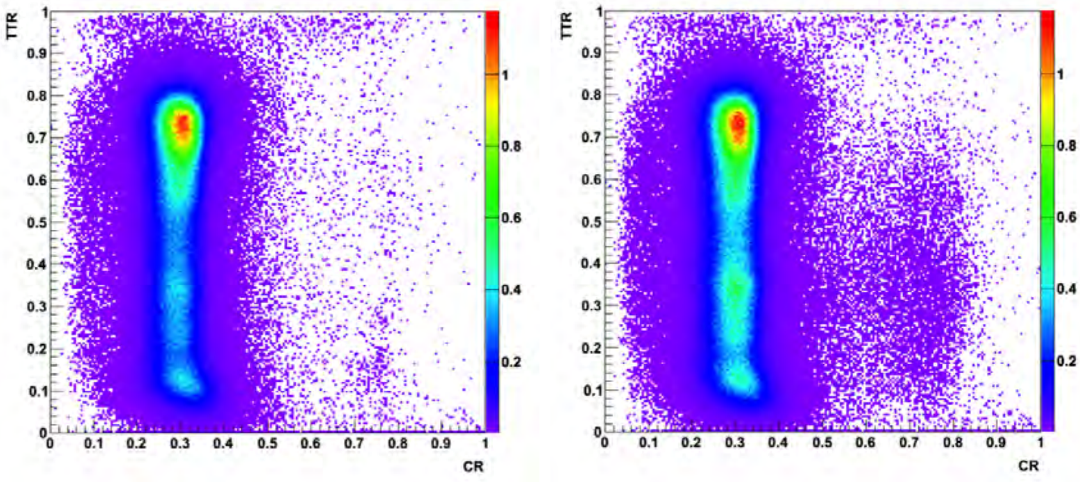

Figure 6.7: TTR versus CR for background (left) and ^{252}Cf data (right), where neutrons present higher CR values than electron recoils, CR ~ 0.75.

6.3 Background studies

One of the main goals of the LAr run is to study the different background contributions present in data. Firstly, in order to ensure that the analysis is performed with a clean data sample, certain basic quality cuts related to the light detected and to the signal shape are applied on data to reject misreconstructed events. Secondly, in contrast with argon gas data, in which the contribution of ^{39}Ar was negligible ($\sim$1 Hz) due to the low mass of Ar contained inside the detector vessel, ^{39}Ar becomes the dominant electron recoil background in liquid ($\sim$1 kHz), thus measuring its contribution to the energy spectrum becomes extremely important. Finally, it is also important to study the possible presence of BiPo events inside the detector following a similar analysis scheme to the one already used in gas to evidence the radon contribution.

6.3.1 Data quality and selection

Since this has been the first data taking with ArDM in pure LAr phase, it is important to obtain a clean data sample for the analysis. For this reason, some low level quality cuts, conditions related to the light detected by the PMTs and to the peak time of the scintillation light, were developed and applied to data taken with the shield partially opened. The aim of these cuts is to discard from the analysis misreconstructed events, electronic noise and other signals different from argon scintillation, trying to maintain at the same time a low effective energy threshold. The basic quality cuts that have been applied to the data are the following ones:

1. MaxPMTdetTop/Top < 0.9. Maximum fraction of photons detected by one PMT on the top PMT array lower than 90% of the total light detected on that array.
2. MaxPMTdetBottom/Bottom < 0.9. Maximum fraction of photons detected by one PMT on the bottom PMT array lower than 90% of the total light detected on that array.
3. Top > 8 p.e. Minimum number of photons detected by the top PMT array.
4. Bottom > 8 p.e. Minimum number of photons detected by the bottom PMT array.
5. $220 <$ PeakTime < 260. Peak time position selection, which ensures that the maximum peak of the signal is found in a particular time range expressed in samples unit.

Cuts 1 and 2 ensure that the events produced right on the window of the PMTs, that can be due to ions sticking to the PMT surface, are rejected; while cuts 3 and 4 select events with a minimum detection of 8 p.e. in each PMT array in order to ensure that we have a reliable TTR. The last cut, referred to the peak time position, rejects misreconstructed events in which the event trigger has not been set to the proper position due to a problem in an ADC board. The individual effect of each of the above described cuts and the combined effect of all of them is written in Table 6.1 in terms of events rejected with respect to total events. In the plots of Figure 6.8 we show the TTR versus total light detected distributions for all events in black and the events rejected by each cut in red. The combined effect of all cuts (shown in the bottom right plot) represents a rejection of 31.8% of total events detected. We mainly remove low energy events, with more than 90% of events in the region of interest for Dark Matter passing the cuts. After applying all the mentioned cuts, the misreconstructed events were suppressed very efficiently, yet preserving relatively low effective threshold.

Cut	**% Events rejected**
MaxPMTdetTop/Top < 0.9	22.2%
MaxPMTdetBottom/Bottom < 0.9	20.9%
Top > 8 p.e.	26.8%
Bottom > 8 p.e.	15.4%
$220 <$ PeakTime < 260	2.73%
All cuts combined	31.8%

Table 6.1: Percentage of events rejected respect to total events detected by each quality cut and by the combination of all of them.

Finally, the plots of Figure 6.9 show the difference in CR for both background and ^{252}Cf source data before (black histograms) and after (red histograms) applying the described quality cuts. After rejecting the great part of misreconstructed or non physical events, the electron recoil and nuclear recoil distributions can be distinguished, observing higher number of events in the nuclear recoil distribution for the ^{252}Cf source data ($\sim 10^{-1}$ counts/s), due to neutrons coming from the source, compared to background data ($\sim 10^{-2}$ counts/s). The event rate in the NR region for background data, probably due to internal alpha contamination, has still to be understood.

Although the quality cuts that have just been presented should be optimised in the future for further lowering the effective energy threshold with the best rejection of the misreconstructed events, the current strategy will make possible to perform a preliminary nuclear/electron recoil event analysis and to evaluate the achievable ArDM rejection power.

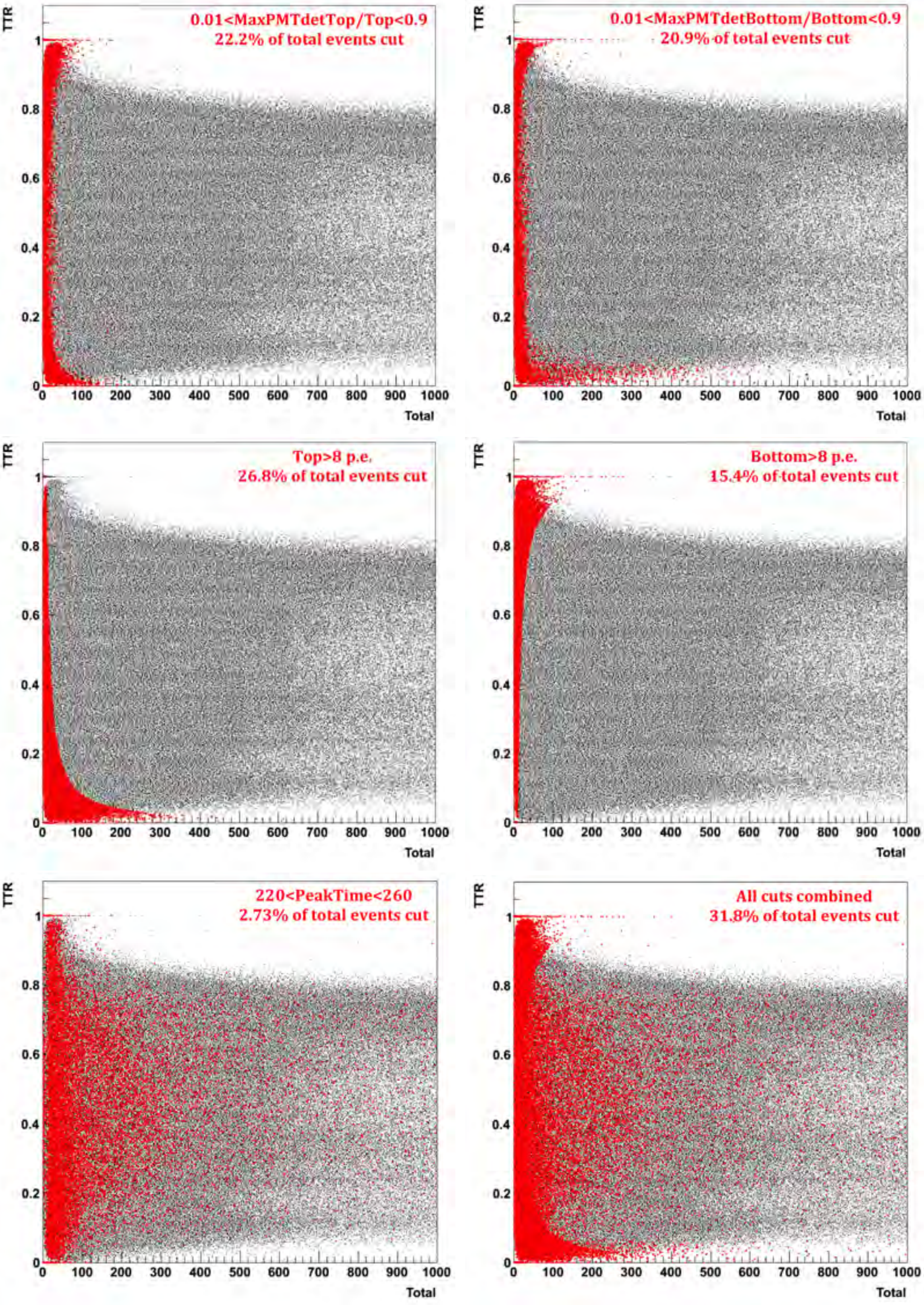

Figure 6.8: Individual effect of the quality cuts related to the light detected on the top and bottom PMT arrays (top left and right and middle left and right) and to the peak time (bottom left). The combined effect of all cuts (bottom right) rejects 31.8% of total events detected.

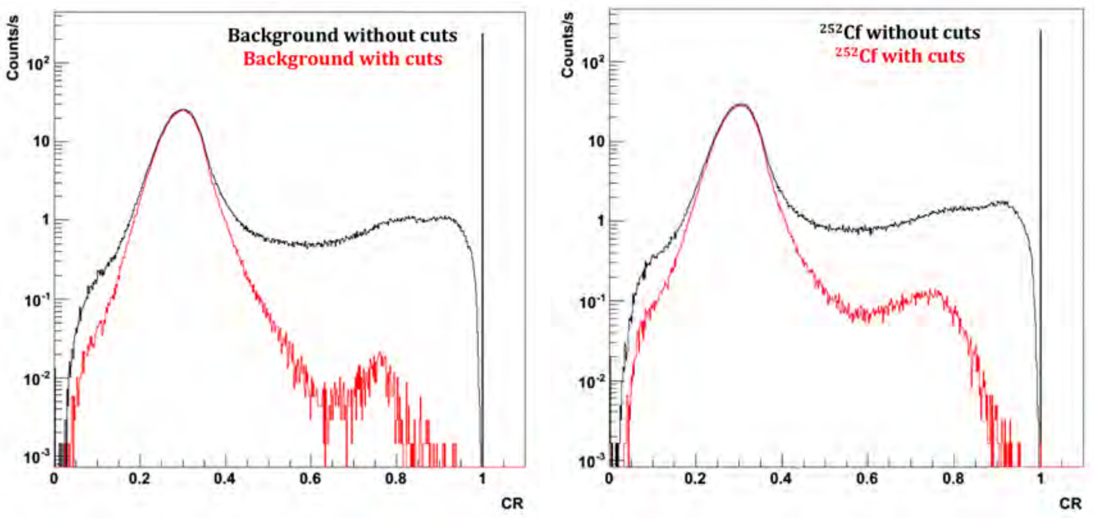

Figure 6.9: CR event distribution for background (left) and ^{252}Cf data (right) before (black histograms) and after (red histograms) applying the defined quality cuts, which reject great part of the misreconstructed events (31.8% of total events detected), giving rise to clean electron and nuclear recoil event distributions.

6.3.2 Contribution of ^{39}Ar to the background energy spectrum

As it has been already introduced in previous Chapters, natural argon making up $\sim$ 1% of the Earth atmosphere is composed by the stable isotope ^{40}Ar and also by radioactive isotopes, such as ^{39}Ar, a beta emitter produced by the interaction of cosmic rays with atmospheric Ar, which decays into ^{39}K with a half-life of 269 years. The ^{39}Ar presents a typical continuous beta spectrum with and endpoint of 565 keV and mean energy of 220 keV.

After closing the neutron shield, we could perform a more detailed background analysis. In order to evaluate the quantity of electron recoil background in ArDM, we have investigated the beta spectrum due to the presence of ^{39}Ar in our target, which represents the most important electron recoil background contribution in LAr phase [152]. The theoretical shape of the distribution is given by:

$$\frac{\mathrm{d}N}{\mathrm{d}w} \sim pw(w_0 - w)^2 F(Z,w) S(w), \tag{6.1}$$

where p is the beta momentum, $w = (m_e c^2 + E_e^{\mathrm{kin}})/m_e c^2$ is the total energy of the electron in unit $m_e c^2$ and $w_0 = w + E_{\bar{\nu}}/m_e c^2$ is the total energy available for both the e$^-$ and the $\bar{\nu}$ together, with $E_{\bar{\nu}}$ denoting the energy of the anti-neutrino. The recoil energy taken by the nucleus is considered negligible due to its large mass.

Z is the atomic number, $F(Z, w)$ is the Fermi correction and $S(w)$ is a correction function for the forbiddenness of the transition [153, 154].

For this analysis of electron recoil background, a data set containing 5.1×10^7 events collected after the closing of the neutron shield was used. The electron recoil events were selected by PSD and afterwards quality cuts were applied together with the cut TTR > 0.2, which was required to reject events below the bottom edge of the TPB coated main reflector. Finally, 3.1×10^7 events were left for the analysis after applying all cuts. The final electron recoil background energy spectrum obtained after performing the event selection is shown in red in the plot of Figure 6.10.

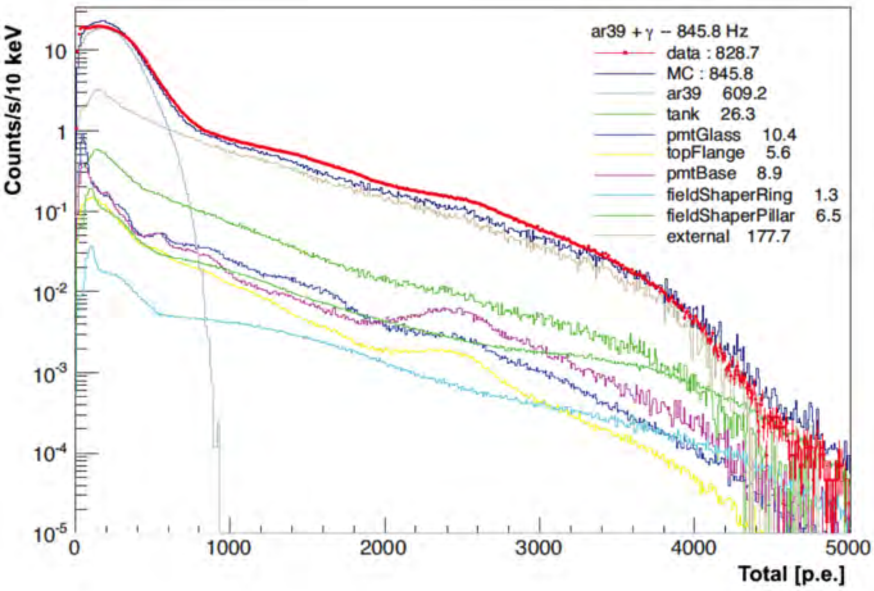

Figure 6.10: Raw energy spectrum of electron recoils after selection cuts (red) compared to various backgrounds derived from the MC simulation. The dominant contribution at low energy is described by the beta spectrum of ^{39}Ar decays.

The raw experimental data were found to be well described by a fit function which is the sum of a smeared ^{39}Ar beta spectrum with an exponential background:

$$f(E) = C_1 \times \frac{\mathrm{d}N}{\mathrm{d}E} \otimes \mathrm{Gauss}(0, \sigma) + C_2 \times \mathrm{e}^{-E/E_0}. \tag{6.2}$$

The specific activity of ^{39}Ar is obtained from the integral of the fit function in the range 0-1500 keV$_{\mathrm{ee}}$. The run time is 37025 s and the target mass corresponding to the TTR>0.2 cut is 733 kg. The measurement yields 0.903 ± 0.002 (stat) Bq/kg. Systematic errors however are much larger, and are estimated to be 7%. They originate mainly in the precision of the determination of the resulting target volume

(6%), as well as in the exponential background description by the fit (4%). Our result is in agreement with previous work (1.01 ± 0.02(stat) ± 0.08 (syst) Bq/kg) performed by the WARP collaboration [95].

A GEANT4 MC developed by the ArDM collaboration was used to estimate the internal and external gamma backgrounds in order to compare to the experimental data, paying special attention to the electron recoil events. In particular, the ^{39}Ar spectrum was simulated and the radiogenic background from the different detector components were estimated based on the screening results. The decay chains of ^{238}U and ^{232}Th, which were assumed to be in equilibrium, as well as contributions from ^{60}Co and ^{40}K were considered. Contributions from environmental flux in hall A were also estimated using the full detector simulation and assuming an isotropic and uniform flux from ^{238}U and ^{232}Th chains as well as ^{40}K.

The simulation computed spectra for different source contributions, including all the internal detector components, the environmental flux and ^{39}Ar, are shown in the plot of Figure 6.10 compared to the experimental raw energy spectrum of electron recoils (red). Each contribution is adjusted to its estimated activity derived from the screening results and the environmental flux measurement, while the value for ^{39}Ar was set to the measured value 1 Bq/kg. The sum of all contributions calculated by MC, shown in dark blue, is in very good agreement with the observed experimental spectrum (red) over the full energy range. The result identifies ^{39}Ar and the environmental flux as the dominant contributions to the e^--like background, before considering any PSD or fiducialisation.

The total observed rate in the detector with the shield closed is about 828.7 Hz, while the total background prediction is 845.8 Hz. This level of agreement represents a major milestone in the analysis and in the first operation of ArDM. From the total background of 845.8 Hz predicted by MC, 609.2 Hz correspond to ^{39}Ar and 177.7 Hz are due to external sources. The internal backgrounds are 26.3 Hz from the main tank vessel steel, 5.6 Hz from the top flange, 10.4 Hz from the PMT glass, 8.9 Hz from the PMT bases, and the field shaper rings and pillars contribute 7.8 Hz. These results indicate that after ^{39}Ar the second most dominant source of background is external.

6.3.3 BiPo studies

The BiPo study that was performed with gas argon data, already presented in Chapter 5, has been redone for the liquid data taken with the shield partially opened. We select events in the high light yield and CR regions as it is shown in Figure 6.11 (left) and then calculate the difference in time [μs] with the previous event. The selection in liquid, shown as black dots in Figure 6.11 (Left), is CR>0.6 for the component ratio and Total>1000 p.e. of total light detected. Apart from this data selection, the quality cuts described previously have been also applied.

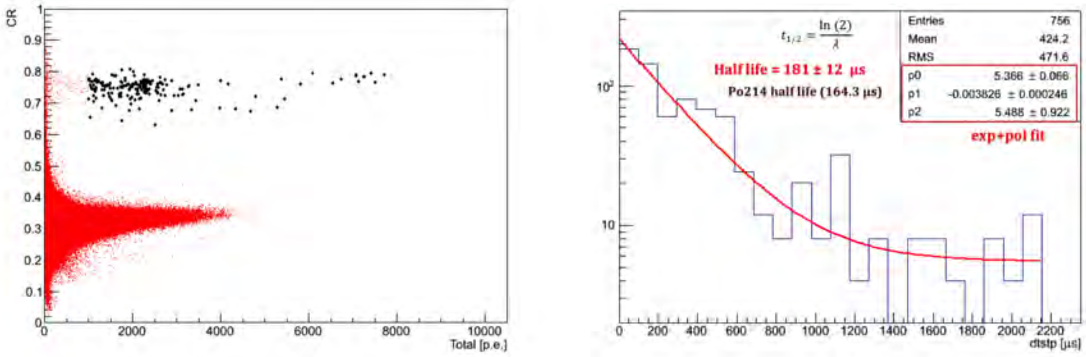

Figure 6.11: (Left) BiPo event selection in LAr. The selected events, CR>0.6 and Total>1000 p.e, have been represented as black dots. (Right) Difference in time of the selected events with respect the previous one [μs]. The ^{214}Po half-life obtained from the exponential+first order polynomial fit liquid data is $181 \pm 12\,\mu$s.

In Figure 6.11 (right) we show the plot of the selected events. As it happened in gas, the distribution shows an exponential decay and a flat contribution due to random coincidences with previous events. After an exponential+first order polynomial fit, the calculated half-life, $181 \pm 12\,\mu$s, is compatible with the ^{214}Po value, $164.3\,\mu$s, within 2σ, which may indicate the presence of ^{214}Po - ^{214}Bi isotopes from the ^{238}U decay chain in the LAr volume.

Comparing with previous gas results, a $\sim$0.06% of events have been selected respect to total events detected, while this selection was higher in gas with 1.4% of total events in warm gas and 0.88% in cold gas. On the other hand, the result from the fit in liquid is in principle further from the ^{214}Po half-life value, $181 \pm 12\,\mu$s, than the results obtained in gas ($160.7 \pm 1.9\,\mu$s in warm and $169.0 \pm 4.3\,\mu$s in cold gas) and the error from the fit is higher in liquid since we have less statistics. Considering the errors, the result in liquid is compatible with the one obtained in cold gas since there is an overlap between these two values. It will be important to redo this analysis during ArDM Run II, when we will achieve a very good position reconstruction with the TPC in place. However, the fact that these events in the high CR region are compatible with the Po decay, indicate that they may be given by alphas.

6.4 Position reconstruction with neural networks

Following the same strategy already used with gas data, the 3D position reconstruction has been performed also in liquid with JavaNNS, based on the light pattern detected by the top and bottom PMT arrays. After a first test with a single ANN for the x, y, z position reconstruction, a system of three separate ANN, one for each coordinate, has been chosen in order to minimise the errors in the position. Each of these ANN is composed by three layers: an input layer with 24 input neurons corresponding to the PMT signals, 24 neurons in the hidden layer with hyperbolic tangent as activation function and 1 neuron in the output layer corresponding to the x, y or z position of the interaction. As it was already performed in gas, the input signals have been normalised for the total light collected.

A new MC in LAr was also developed in order to train these networks. In the new MC, $\sim 10^6$ events of 5 MeV alpha particles were emitted isotropically inside the LAr detector volume. The uniform distribution of events is shown for the xy and xz planes in the plots of Figure 6.12 (left) and (right) respectively. The xz plot shows the internal shape of the detector, which is delimited in its central part by the lateral reflectors, while the top and bottom parts are wider. Due to the fact that the LAr level has been established to be ~4 cm above the lateral reflectors, the wide area on top is thinner than the bottom one. The visible gap with no events in the right part of the plot corresponds to the field cage flat sector, in which no particles are emitted. In the xy plot, a flat transverse section of the detector is visualised at 300 mm and the area between 300 and 400 mm shows a lower concentration of events, as expected, since it corresponds to the region with the gap due to the flat sector shown in the xz plot.

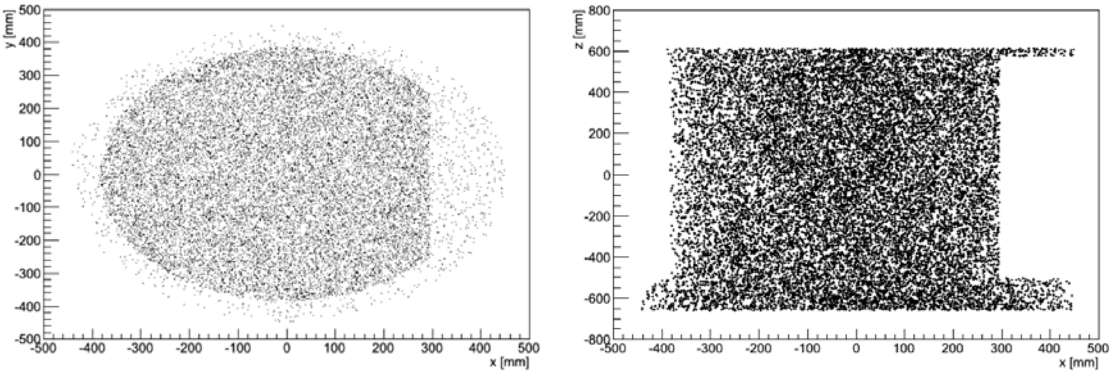

Figure 6.12: Distribution of MC events in the xy and xz planes.

The three ANN previously mentioned were trained separately over the described MC sample, from which $\sim 2.5 \cdot 10^5$ were extracted, using 80% of events for the training set and 20% of events for validation. Comparing the reconstructed position with the MC values, errors of 6.9 cm have been obtained for both x, y coordinates, while the error of the reconstructed z coordinate is of the order of 4.2 cm, as shown in the plots of Figure 6.13.

Several LAr runs taken with the neutron shield partially opened have been analysed using the three trained ANN to obtain the 3D event position reconstruction with ^{57}Co data, taken in the calibration drawer. The comparison plots between

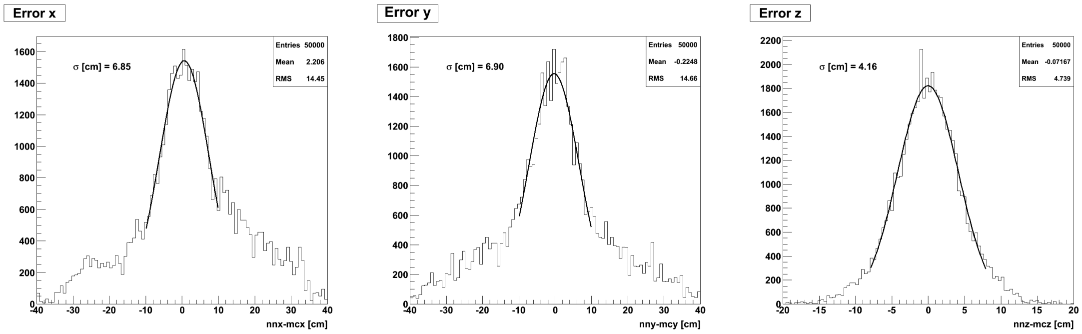

Figure 6.13: Difference between the NN reconstructed position and the MC value for x (left), y (centre) and z (right). A Gaussian fit of the distributions provides the corresponding error in the reconstructed position for the x, y, z coordinates.

background and ^{57}Co source data are shown in Figure 6.14 (left) and (right) respectively, for TTR (top plots) and reconstructed z coordinate in mm (bottom plots) as a function of the energy, with the colour scale normalised to total run time. In both cases, the contribution of the ^{57}Co source, which represents an increase of ∼30 Hz in the trigger rate respect to background, has been marked with a red circle. Comparing top and bottom right plots, we see that the z reconstructed position, whose distribution around ∼-600 mm is consistent with the position of the cathode grid, spreads in a wider range, pointing out the presence of a compression effect in TTR.

Apart from ^{57}Co data taken in the calibration drawer, more runs have been taken in different source positions in height (z coordinate). In Figure 6.16 the plot of the reconstructed position in the xy plane is shown for four different runs, each one corresponding to a different z position of the ^{57}Co source. The distance written in the plots has been measured from the top part of the detector, meaning that higher distances correspond to lower positions of the source, decreasing from the top left plot to the bottom right plot. Since the background position distributions have been subtracted, the displayed events correspond to the ^{57}Co source, showing displaced distributions for lower positions and more centred ones for higher positions. This is due to the fact that the detected light pattern is more clear for the runs in which the source is placed lower in height and thus closer to the bottom array of PMTs.

Finally, performing Gaussian fits to the 1D position distributions for both TTR and reconstructed z coordinate, we can establish a relation between the mean values of these magnitudes and the corresponding distance to the cathode for each source position, as shown in the plots of Figure 6.16. In these plots, the sigma of the Gaussian fit has been taken as the error in the mean to give and estimate of the spread of the data, while the error in the distance to the cathode has been experimentally evaluated to be 25 mm. The increasing behaviour of the TTR and the flat tendency above distance of the cathode of 600 mm are reproduced by the reconstructed z

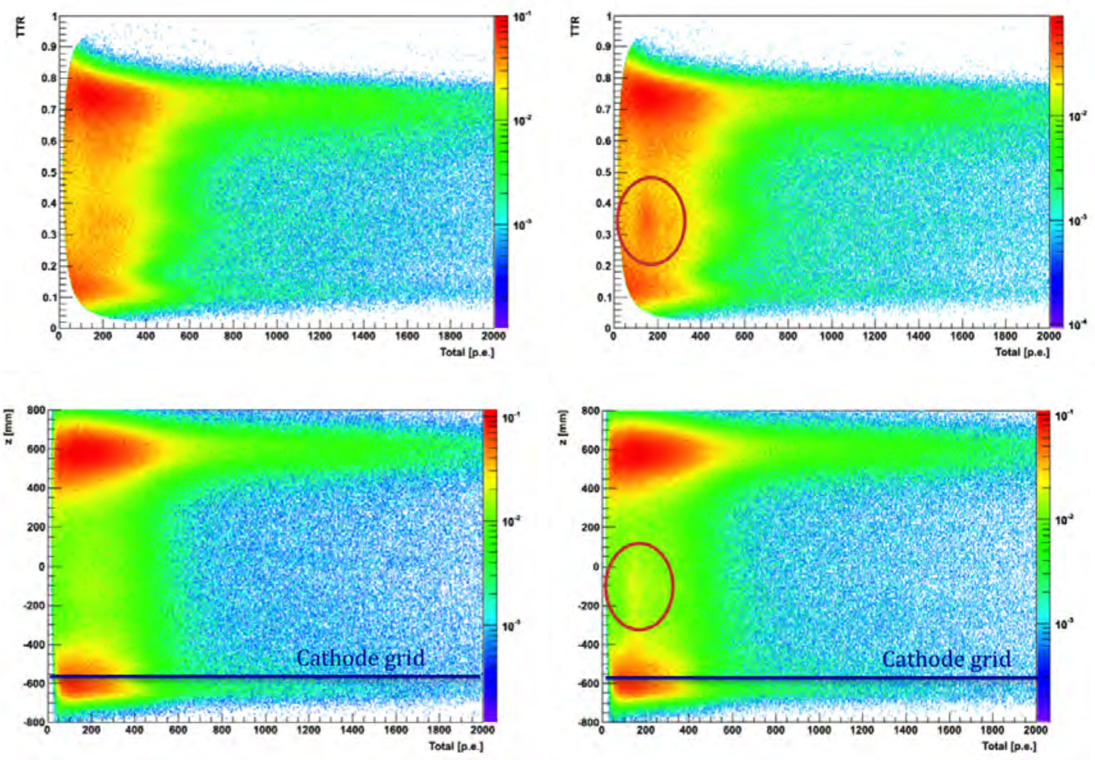

Figure 6.14: TTR versus total light detected for background (top left) and data taken with the ^{57}Co source (top right) compared with the reconstructed z position for background (bottom left) and ^{57}Co data (bottom right). The position of the ^{57}Co has been marked with a red circle in both cases. The TTR distribution shows a compression effect with respect to the reconstructed z coordinate.

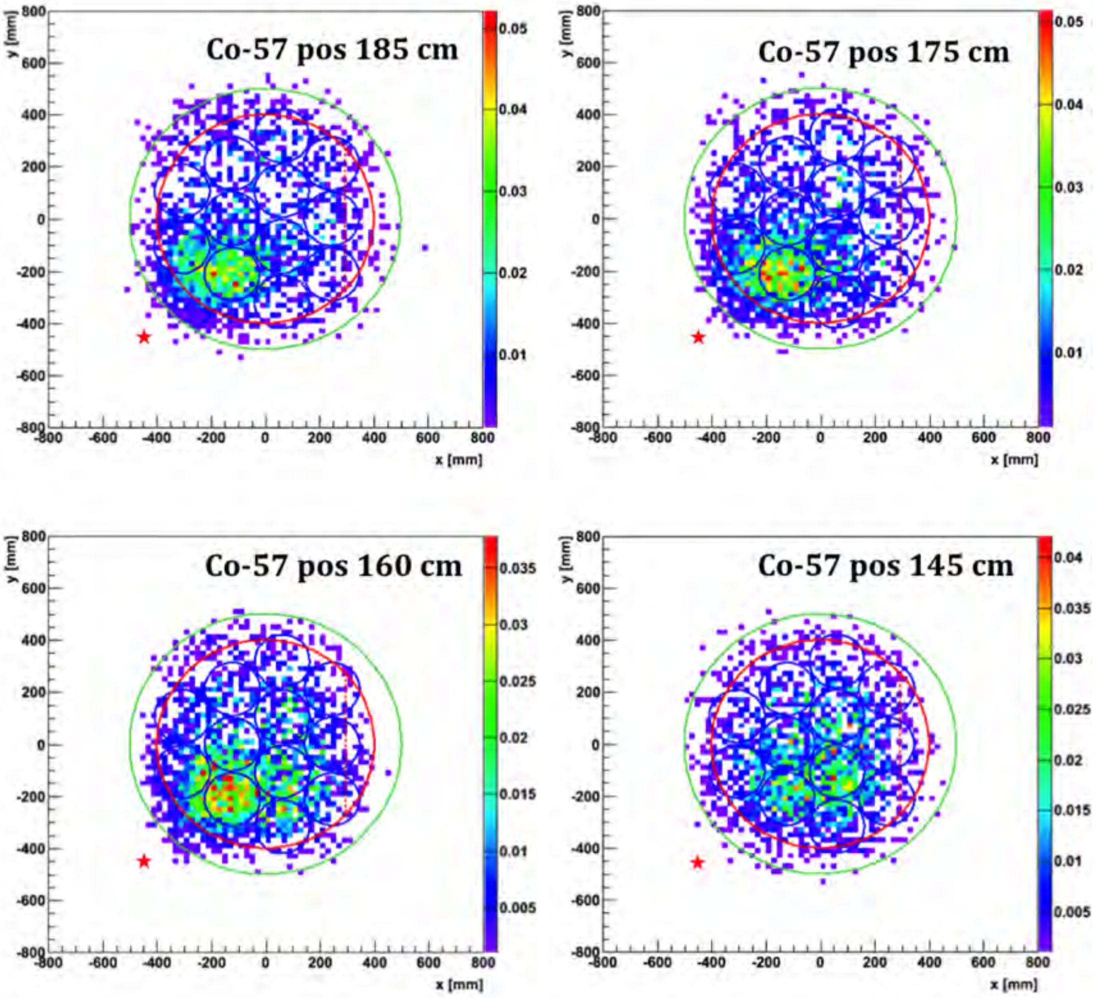

Figure 6.15: Reconstructed xy coordinates with background subtracted for four different positions of the ^{57}Co source in height, z, measured from the top part of the detector. The real position of the source in the xy plane is (x,y) = (-450,-450) [mm]±10 mm and it has been marked with a red star in the plots. Lower z positions (higher distances from top part) show a clear displaced pattern, agreeing with the real position of the source, due to the presence of the source near the bottom PMT array, while the intermediate ones, represented by the bottom right plot, present a much more centred pattern.

coordinate.

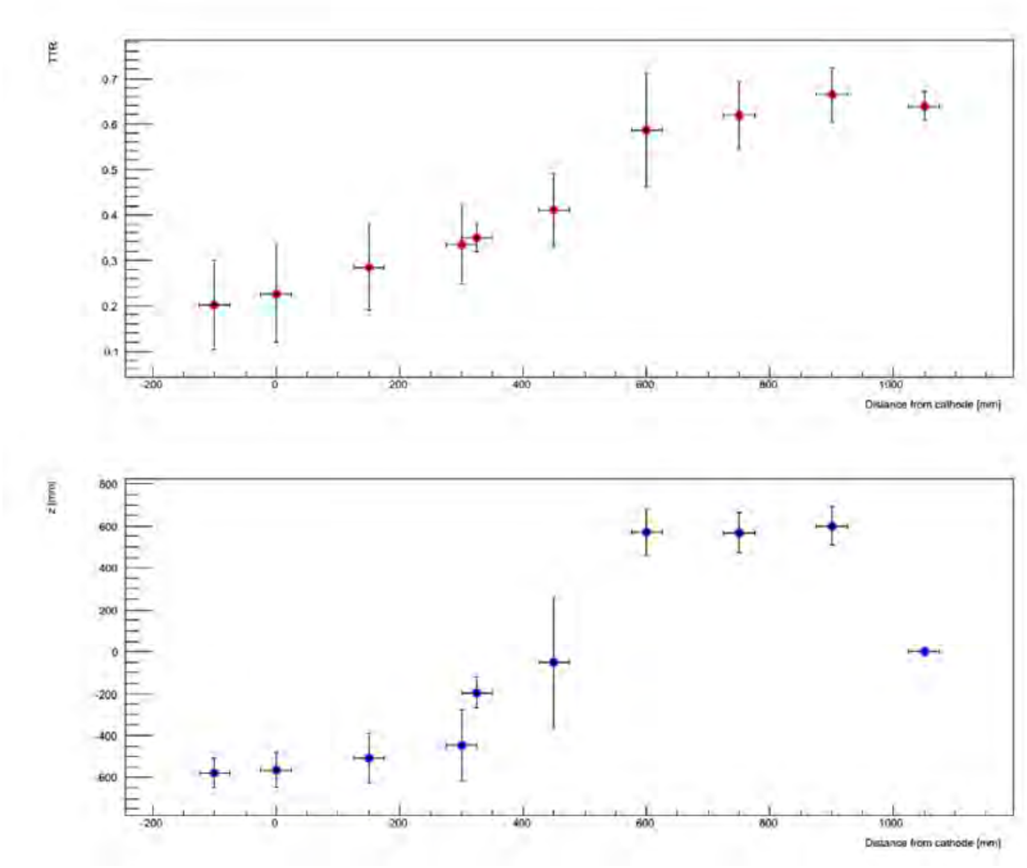

Figure 6.16: Mean of the Gaussian fits for the TTR (top) and reconstructed z distributions as a function of the ^{57}Co distance from the cathode (bottom). The mean TTR positions show an increasing behaviour with the distance to the cathode, which then tends to be flat for distances higher than 600 mm. This behaviour is reproduced by the reconstructed z coordinate.

Comparing to the results obtained in gas, the position reconstruction error between the ANN and the MC result is better for z (4.16 cm) than for x (6.85 cm), given the symmetry of the detector, as it already happened in gas (2.81 cm error for z and 4.87 cm error for x), with similar results if we compare z and y coordinates. On the other hand, this reconstruction error has increased a factor ~ 1.4 in liquid with respect to the gas.

In conclusion, as it has been mentioned in the gas analysis, this position reconstruction study has been particularly important due to the fact that the Ar-TPC is not operative yet, meaning that there is no information on the interaction position at this moment. Once the detector Ar-TPC will be fully operative, the results obtained for the reconstructed z from the ANN algorithm, based on the S1 signal detected by the two arrays of PMTs position, could be compared with the ones obtained from the S2 scintillation signal. The S2 signal will provide more precise results and a much more straightforward reconstruction of the xy interaction position.

6.5 Data with the shield closed

During the first phase of ArDM data taking in pure warm and cold gas argon and in liquid argon, the neutron shield was partially opened in the top part in order to ensure the quick access to the detector in case it was required. However, after completing the z scan runs with the ^{57}Co source, the neutron shield was completely closed in order to evaluate subsequent reduction in the trigger rate. The evolution of the trigger rate in this period, evaluated after performing the quality cuts is shown in Figure 6.17. A clear increase of ∼80 Hz in the trigger rate is observed in ^{57}Co data with respect to background (∼1.3 kHz). However, the highest difference appears by comparing background before closing the shield with the background after closing it, which implies a reduction of ∼320 Hz in the trigger rate.

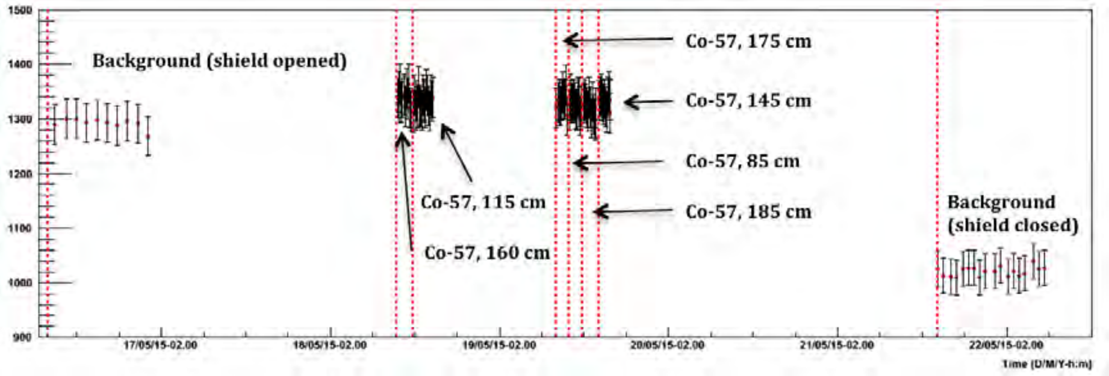

Figure 6.17: Rate evolution in time for the background (before and after closing the neutron shield) and for ^{57}Co runs after quality cuts. The reduction of the trigger rate after closing the shield is ∼320 Hz.

It is necessary to investigate those events which have been reduced, studying the TTR distribution and the energy spectra comparing data before and after closing the neutron shield. In Figure 6.18, we compare the TTR versus total light detected plot for background before (left) and after (right) closing the neutron shield. According to these results, the events with TTR> 0.6 have been substantially reduced by closing the neutron shield. In particular, from 0.08 counts/s to 0.04 counts/s below 400 p.e. and from 0.01 counts/s to 0.002 counts/s above 400 p.e.. This relevant reduction effect for large values of TTR was expected, as the top part of the detector was completely uncovered before the closing operation.

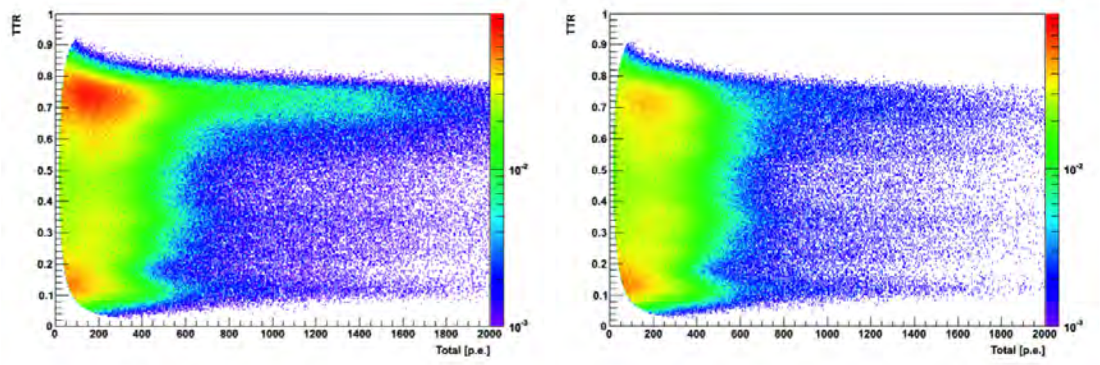

Figure 6.18: TTR versus total light detected distributions for background before (left) and after (right) closing the neutron shield. An important rate reduction is observed after closing the shield for events with TTR> 0.6.

The background spectra before (black) and after (red) closing the neutron shield is plotted in Figure 6.19 along with the subtraction of both, plotted in blue. The highest reduction of the rate occurs in the range 700 <Total (p.e.)< 2700, where the ^{40}K (~1500 p.e.) and the Tl (~2500 p.e.) gamma peaks have been reduced accordingly.

Apart from the reduction of the gamma rate, an important change in the neutron rate was also expected after closing the polyethylene shield. However, if we compare the CR versus total light plots shown in Figure 6.20 before (left) and after (right) closing the neutron shield, there is no evidence of significant reduction of rate in the region CR > 0.6, where we expect to find neutrons.

In order to perform a more detailed comparison, we can plot the TTR versus total light detected for all events (red dots) and for the CR > 0.6 selection (black dots) before and after closing the shield, as shown in the top left and right plots of Figure 6.21 respectively. We can also perform this comparison between shield opened and shield closed after applying the previously defined quality cuts (QC), as shown in the bottom left and right plots of Figure 6.21 respectively. According to these plots, most of the CR > 0.6 events have energy lower than 200 p.e., with higher density of events in the bottom part of the detector (TTR < 0.3) for energies higher than 200 p.e..

The results of the rates calculated for total events and CR > 0.6 events are presented in Table 6.2, showing a difference of 24 Hz between the shield opened and closed for CR > 0.6 events. However, after applying the QC, we still have a rate of ~1 Hz for CR > 0.6 events in both cases, meaning that the closing of the shield

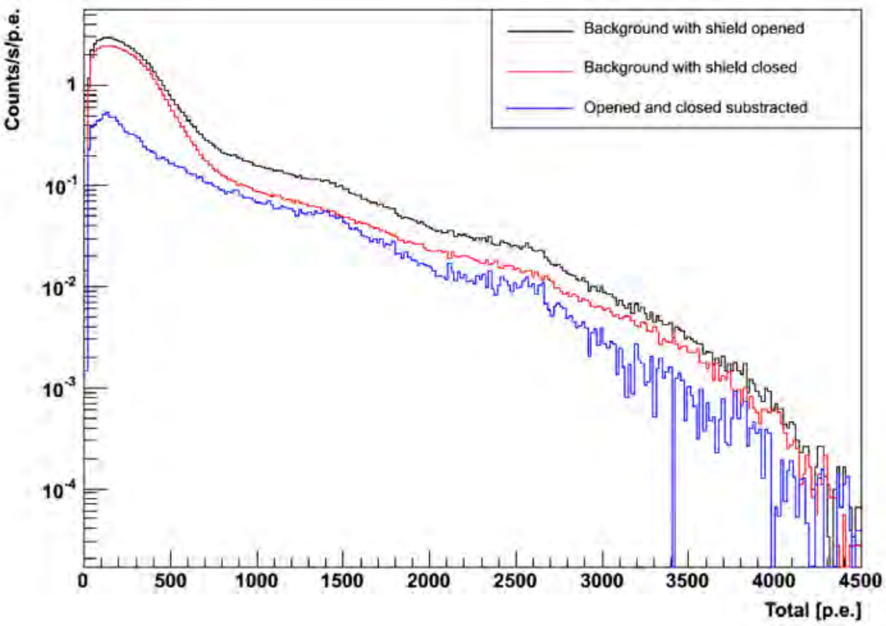

Figure 6.19: Background spectra before (black) and after (red) closing the neutron shield. The subtraction of both spectra is plotted in blue.

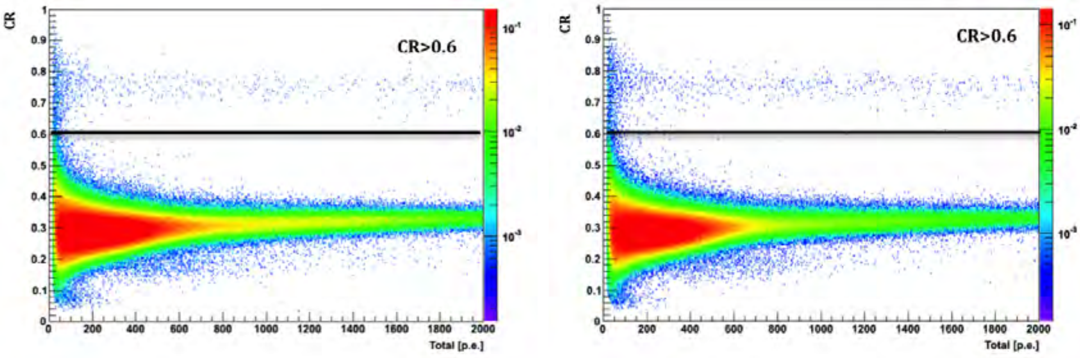

Figure 6.20: CR versus total light detected for the shield opened (left) and same for shield closed (right). The selection of CR > 0.6 corresponds to the range in which we expect to find neutrons.

does not affect the detection rate of those events.

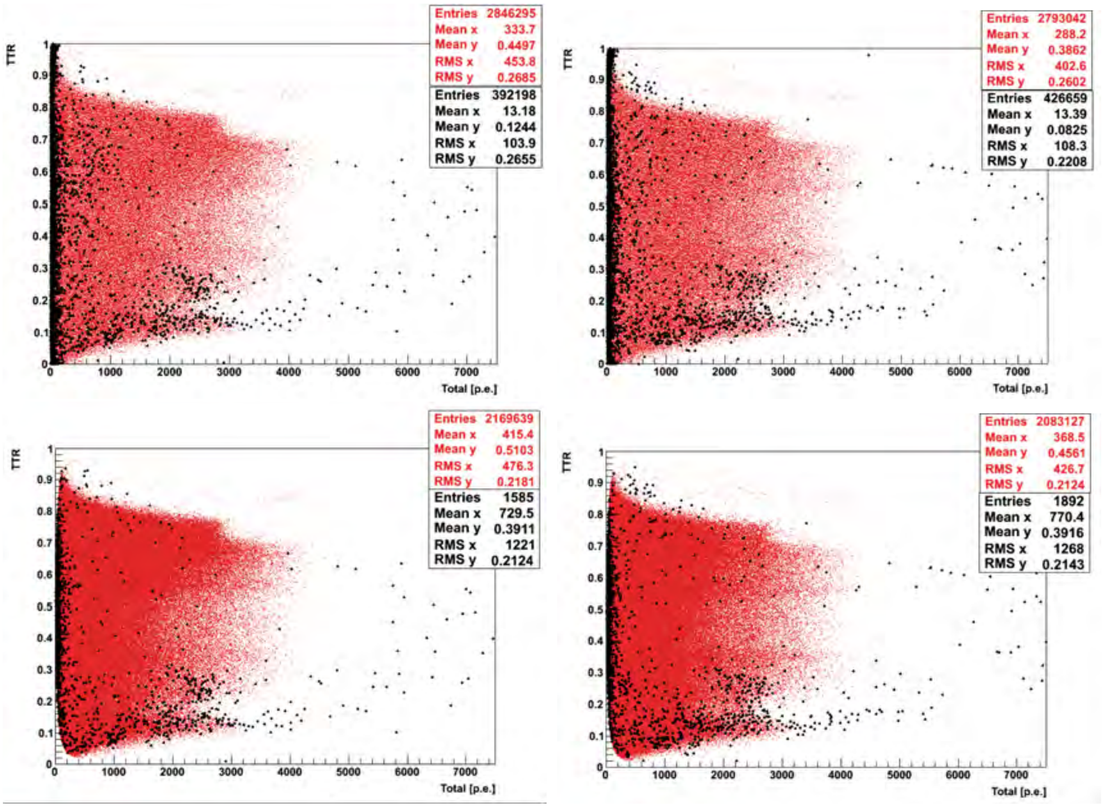

Figure 6.21: (Top) TTR versus total light detected plot before (left) and after (right) closing the neutron shield. The black dots correspond to CR > 0.6 events. (Bottom) Same with quality cuts.

The first possible explanation of this unexpected ∼1 Hz of CR > 0.6 events is that they are real neutrons coming for example from internal contamination of the detector materials. Neutrons can be produced in (α,n) reactions or by spontaneous fission from ^{238}U, with typical neutron yields of $1 \cdot 10^{-2}$ n/g(^{238}U) and $1.39 \cdot 10^{-2}$ n/g(^{238}U) respectively. If this is the case and these events correspond to real neutrons, the mass of ^{238}U necessary to produce a neutron flux like the one detected would be ∼100 g. However, according to the screening measurements of the ArDM detector components, giving a typical material contamination of ∼10-100 ppb for most of the materials, the total mass of ^{238}U is of the order of ∼0.1 g, which is three orders of magnitude lower than the required one to explain the CR > 0.6 ∼ 1 Hz event rate.

Once we have discarded neutrons, the remaining possibility is that those CR > 0.6 events are due to internal alpha contamination. In this case, the 3D position reconstruction of the events can provide a valuable piece of information. Consequently, the ANN that had been already trained in LAr has been used to reconstruct the position of data with the shield opened and closed for all the events and for the CR > 0.6 selection. The results for the reconstructed z of all events as a function of total light is shown before (left) and after (right) closing the neutron shield in the top plots of Figure 6.22, while the reconstructed z coordinate for the CR > 0.6 selection is shown in the bottom plots for shield opened (left) and closed (right). Once again, the results present a similar behaviour before and after closing the shield with less events around ∼600 mm in height for the shield closed (0.06 ev/s compared to 0.1 ev/s) in the total event distribution; while no clear differences between shield opened and closed are observable for the CR > 0.6 selection. In the bottom plots of Figure 6.22 we see that these CR > 0.6 events are distributed in a thin band below 200 p.e., which spreads over the total height of the detector and also in wider bands around the cathode grid and the top/bottom PMT arrays positions. This fact can represent an indication of internal isotope contamination, since isotopes generated inside the detector volume would stick on the lateral reflectors covering the detector walls and on other surfaces, such as the grids and the PMT arrays. The BiPo analysis presented in Section 6.3.3 could indicate that those events may be given, at least partially, by alphas. Another possibility is that these events, specially in the low energy region, populate the NR band instead of the ER band due to a baseline error, that mainly affects the slow component of the scintillation light since it is long in time (μs). If a pulse is too near from the previous one, the first pulse could modify the baseline. However, an inspection of the data excluded that those events are misreconstructed.

Shield	**Cuts**	**Rate (Hz)**
Opened	–	1689
Closed	–	1370
Opened	QC	1288
Closed	QC	1022
Opened	CR > 0.6	233
Closed	CR > 0.6	209
Opened	CR > 0.6, QC	0.94
Closed	CR > 0.6, QC	0.93

Table 6.2: Total and CR > 0.6 event rate for the shield opened/closed and with/without QC. No significant event rate decrease is observed in the region CR > 0.6 after closing the neutron shield.

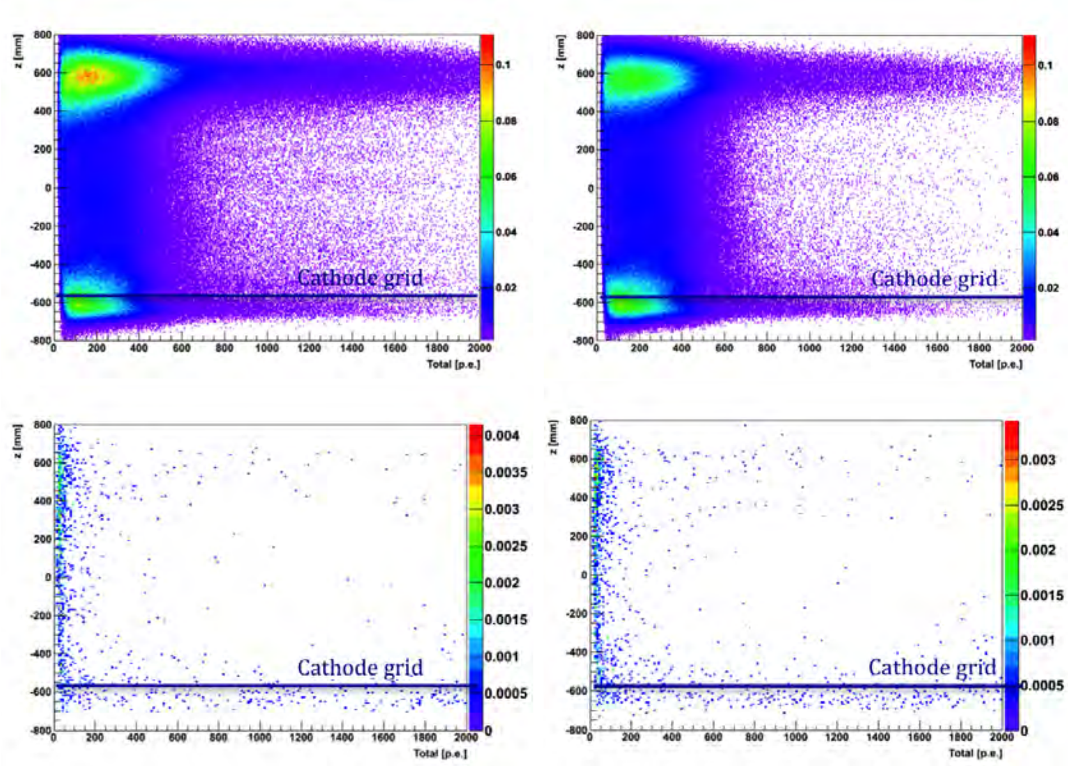

Figure 6.22: Reconstructed z position from ANN for all events (top plots) and CR $>$ 0.6 selection (bottom plots). The left plots correspond to data taken with the shield opened while the right plots account for data with the shield closed. The CR $>$ 0.6 events with low total light ($<$ 200 p.e.) are distributed all over the detector height, while the ones with higher total light detected are mainly located around the cathode grid/bottom PMT array and also on the top part of the detector, near the top PMT array.

6.6 Electron recoil statistical rejection power during Run I

The ^{252}Cf and background data taken during the ArDM Run I (single phase) allow to quantify, for the first time, the discrimination of the ER versus the NR events through the pulse shape analysis. The data set used for this study consists of 47 background runs, which correspond to $4.15 \cdot 10^6$ events collected in 2173 s, and 50 ^{252}Cf runs, corresponding to $4.52 \cdot 10^6$ events registered in 2093 s. The ER rejection power has been evaluated by studying the separation between the two bands as function of the energy for 99.7%, 97.6%, 84.0% and 50% NR acceptance. Even though the results show that, for the full 3σ acceptance, the NR and ER are largely overlapping at 20 p.e., the rejection power necessary for some days of data taking in ER background free mode can be obtained with an higher threshold and a smaller NR acceptance.

6.6.1 Nuclear recoil and electron recoil bands: separation and rejection power

The ^{252}Cf and background data taken with ArDM in pure LAr phase allow to evaluate the discrimination of ER versus NR events by studying the distribution of events in the ER and NR bands and the separation between them using the CR. Obtaining the rejection power is one of the fundamental goals of the first ArDM underground run. The plots of Figure 6.23 show the CR versus energy for background (left) and ^{252}Cf (right), allowing to distinguish the NR and ER populations. The plots have been obtained with very loose cuts (QC) in order to reject spurious triggers not produced by the argon scintillation or events that are not well reconstructed, given, for example, by a shift of the trigger position, which could affect the proper pulse shape reconstruction. As an example, more than 96.7% of the events passed the cuts on the region [15,210] p.e.

The ER band, which is dominated by the presence of ^{39}Ar, is placed at CR ~ 0.3, and the NR band, with events mainly due to neutrons (or maybe alphas in case of background data), is placed at CR ~ 0.75. The population of events between the two bands is not produced by statistical fluctuation or misreconstruction of the signal but it is interpreted as physical triggers given the contemporary detection of a nuclear recoil and a gamma interaction typically produced by the prompt deexcitation of the fragments following the ^{252}Cf fission. That NR-ER pile-up tends to arbitrarily average the CR value of the two interactions, however the cleaner sample of NR events with CR>0.65 is sufficient to carry out a statistical analysis of the band separation.

As shown in the CR plots of Figure 6.24, the events are distributed, in average,

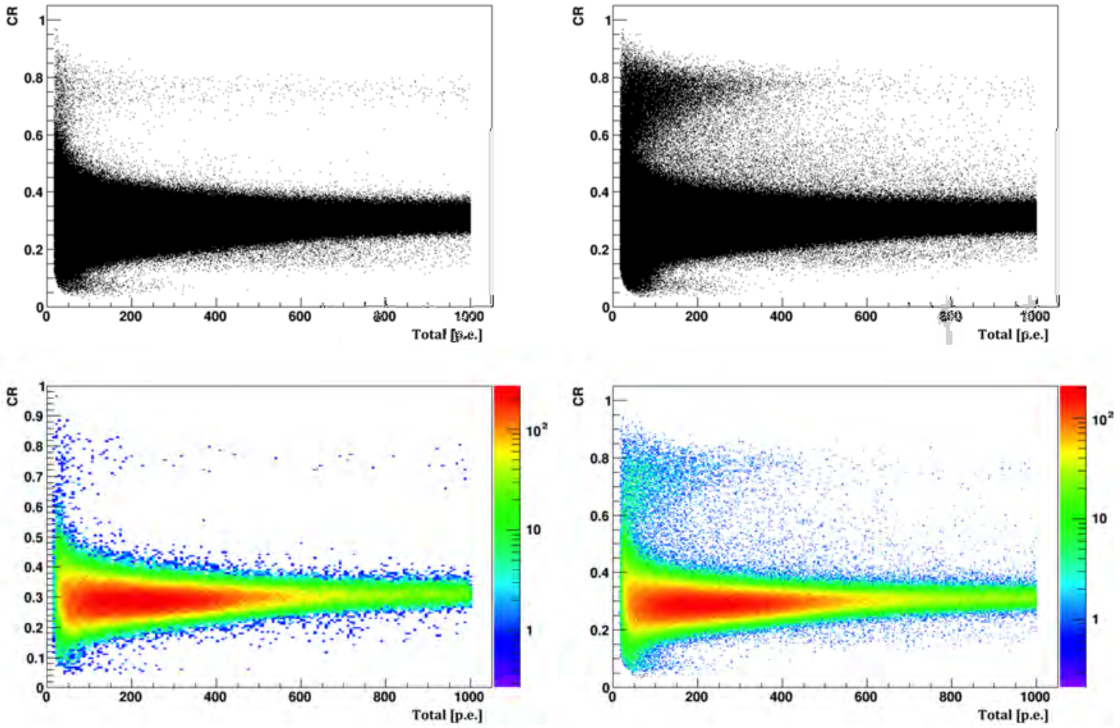

Figure 6.23: CR versus total light detected for background (left) and ^{252}Cf (right) with and without colour scale. The ER band, dominated by ^{39}Ar, is placed at CR $\sim$ 0.3, and the NR band, mainly populated by neutron events (or alphas), is placed at CR $\sim$ 0.75.

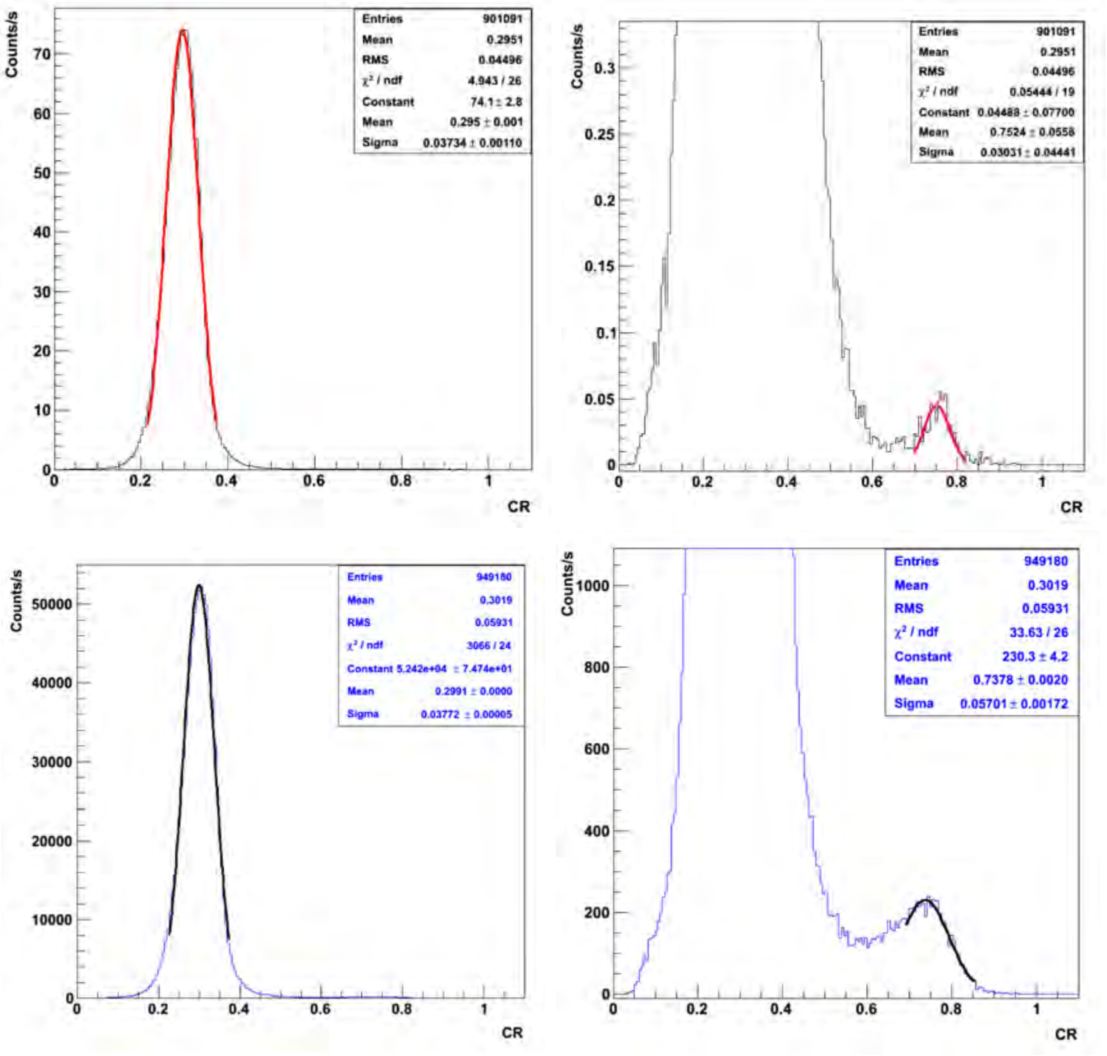

Figure 6.24: Gaussian fits to the ER (left) and NR (right) distributions for background (top) and ^{252}Cf data (bottom).

according with two Gaussian functions. In order to evaluate the statistical separation between the NR and the ER bands, Gaussian fits have been performed to both distributions, and the results for the mean of the ER and NR distributions obtained for background ($m_{ER} = 0.295$ and $m_{NR} = 0.75$) and ^{252}Cf data ($m_{ER} = 0.299$ and $m_{NR} = 0.74$) are compatible within the statistical uncertainties (Figure 6.25).

Taking into account the mean and the sigma of the Gaussian fits, the separation between the two bands and the statistical leakage of the electron recoils into the nuclear recoil region can be evaluated through:

$$L_{ER} = \frac{m_{NR} - N \cdot \sigma_{NR} - m_{ER}}{\sigma_{ER}} \tag{6.3}$$

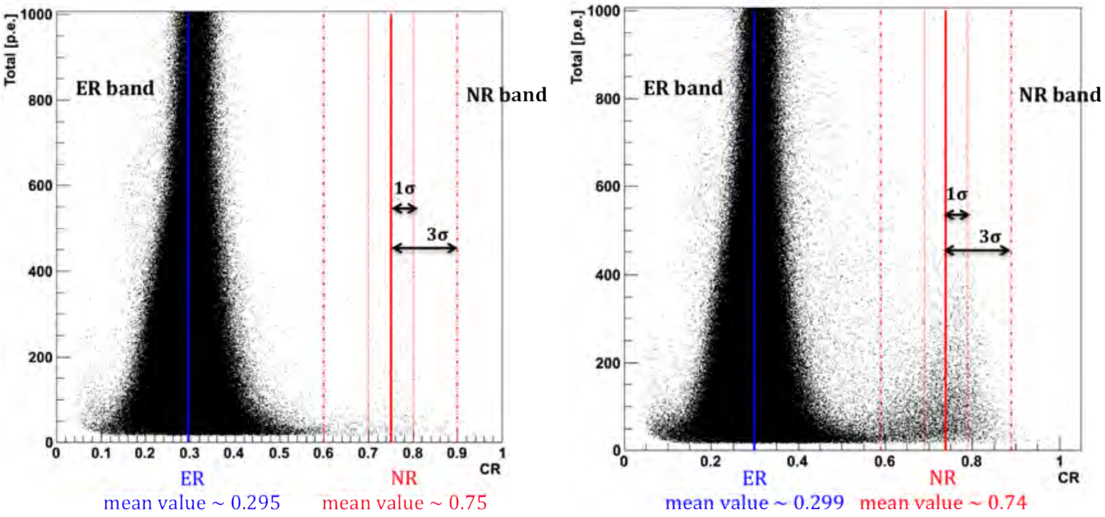

Figure 6.25: Total light detected versus CR for background (left) and ^{252}Cf data (right). The mean values obtained from the Gaussian fits to the ER and NR bands are shown as blue and red solid lines. The 1σ and 3σ NR acceptance regions are marked with dotted and dashed dotted lines respectively.

where N=3 in case of 99.7% signal acceptance (NR band defined as $m_{NR} \pm 3\sigma_{NR}$).

We can quickly calculate the average separation between the NR and ER bands below 200 p.e. In Figure 6.26 the Gaussian fits to the background ER band below 200 p.e. are shown (blue line) with the mean value of the NR band obtained from ^{252}Cf data (red line). The red dashed lines correspond to the $\pm 3\sigma_{NR}$ limits. According to the results, the average separation between ER and NR bands below 200 p.e. is 5.5σ, meaning that the probability to have one ER event statistically leaking into the NR band below 200 p.e. is of the order of 10^{-8}.

Since the acceptance region can be arbitrarily defined, we can use that additional degree of freedom in order to get a better ER rejection power and a smaller statistical leakage in the region between the two bands. That can be effective to eliminate the ^{39}Ar background in the CR region between the bands at the price of a reduction of the acceptance corrected DM exposure. In that sense, alternative NR limits, such as $[m_{NR} - 2\sigma_{NR}, m_{NR} + 3\sigma_{NR}]$ (97.6% acceptance), $[m_{NR} - \sigma_{NR}, m_{NR} + 3\sigma_{NR}]$ (84.0% acceptance) or $[m_{NR}, m_{NR} + 3\sigma_{NR}]$ (50.0% acceptance) can be considered. In next Section we will calculate the ER rejection power as function of the energy with different definitions of the NR band.

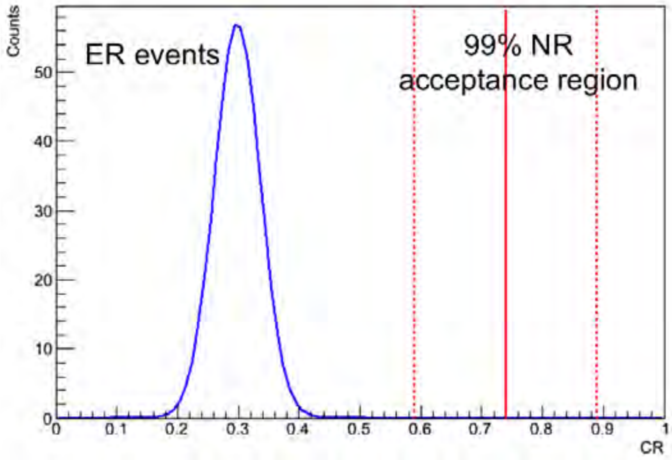

Figure 6.26: CR distribution showing the Gaussian fit to the ER band from background data in blue and the mean value of the NR band from ^{252}Cf data. The 99.7% NR acceptance region is delimited by red dashed lines.

6.6.2 ER rejection power as function of energy and signal acceptance

Since the band widths and ER-NR separation strongly depend on the number of photoelectrons detected, it is essential to carry out an analysis of the rejection power as function of the visible energy. In order to do that, we divide the CR distribution into energy slices and perform Gaussian fits to the NR and ER distributions from ^{252}Cf and background data respectively. The mean and the sigma obtained from the fits define, through Equation 6.3, the separation between ER and NR bands, and thus the rejection power at each energy slice. We can divide the range below 200 p.e. into 10 p.e. slices and perform the mentioned fits, obtaining the results shown Figure 6.27. The event pile-up between the two bands for the ^{252}Cf data tends to arbitrarily change the CR value, making difficult the fit procedure at low energy. In order to minimise the contamination of the pile-up between a neutron and a gamma interaction, the fits for the NR band definition have been carried out

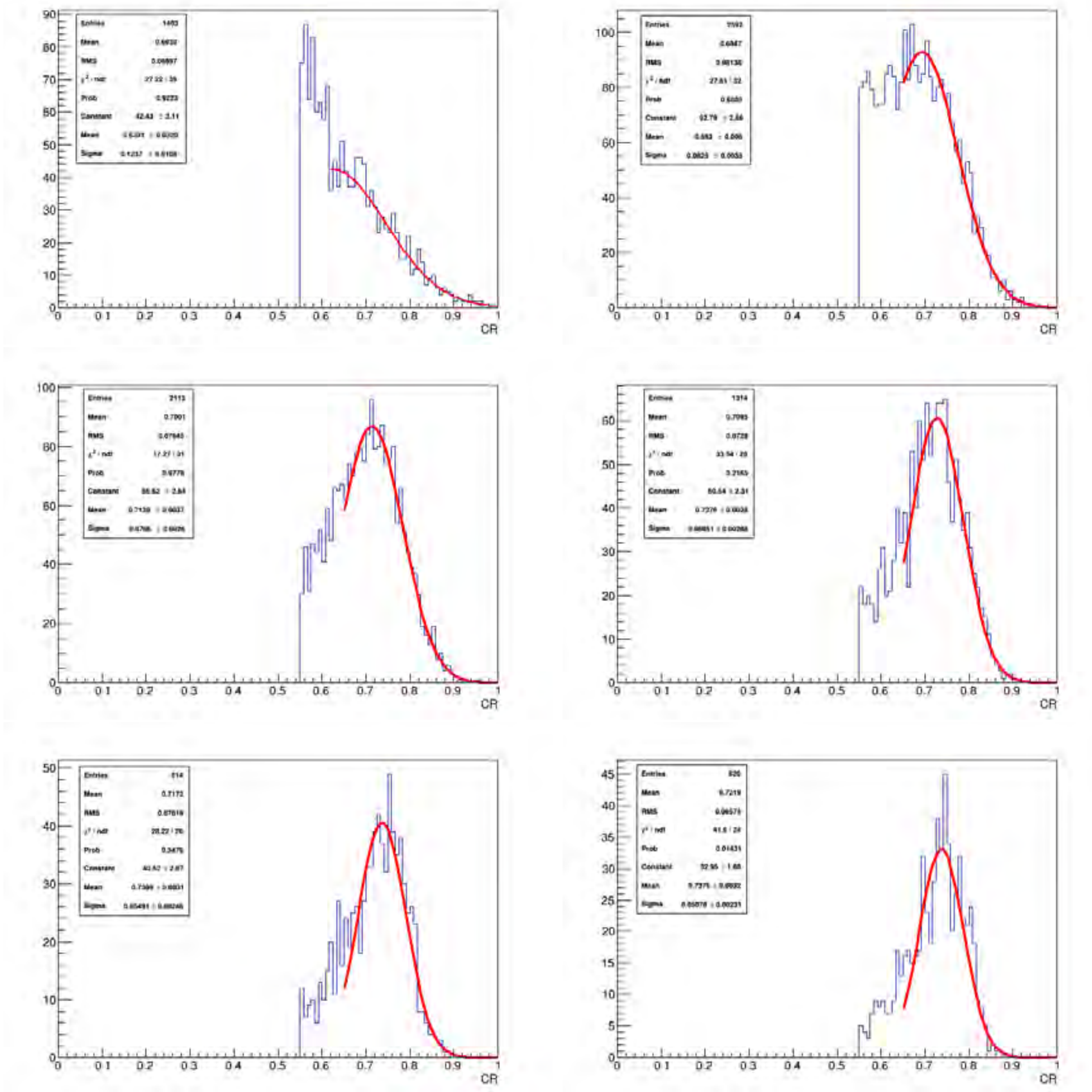

Figure 6.27: Gaussian fits of the CR histogram in the NR region for some energy bins (20, 40, 60, 90, 130 and 150 p.e. - ^{252}Cf data). The asymmetry of the distribution, given eventually by NR overlap with a low energy ER, is evident particularly for the first energy bin. For that reason, the fits of the NR slices have been carried out only for CR> 0.65.

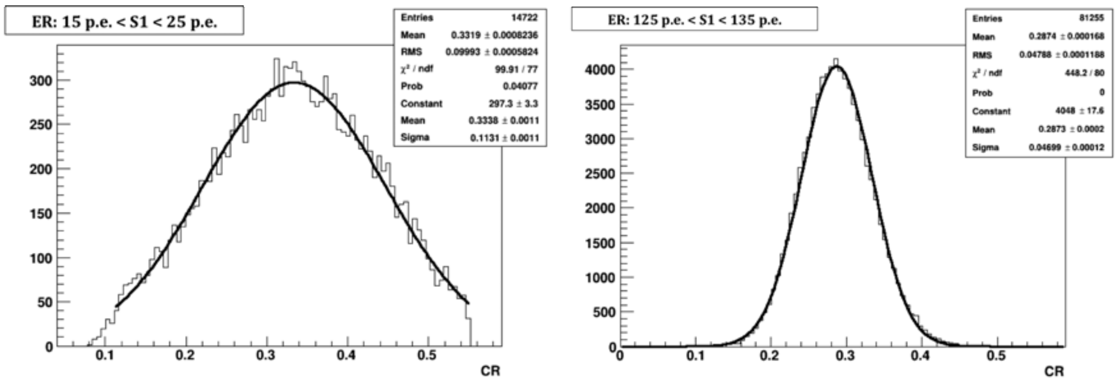

Figure 6.28: Gaussian fit of the CR histogram in the ER region for 20 p.e. (left) and 130 p.e. (right). Nearly perfect Gaussian fits have been obtained for all the energy slices of the ER band.

for CR>0.65 in each slice. The ER band has been well fitted by a Gaussian in all the energy slices (Figure 6.28).

The same fit procedure has been carried out on the background data to compare the results obtained from the two sets of data, even though the poor statistics of the NR events at low energy made necessary to adopt larger bin size (20 p.e.) for the background set. In the plots of Figure 6.29 the mean values obtained from the fits are superimposed to the event distributions. The vertical error bands account for $\pm\sigma$ of each Gaussian fit, while the horizontal error bars mark the ±5 p.e. or ±10 p.e. of the energy slices.

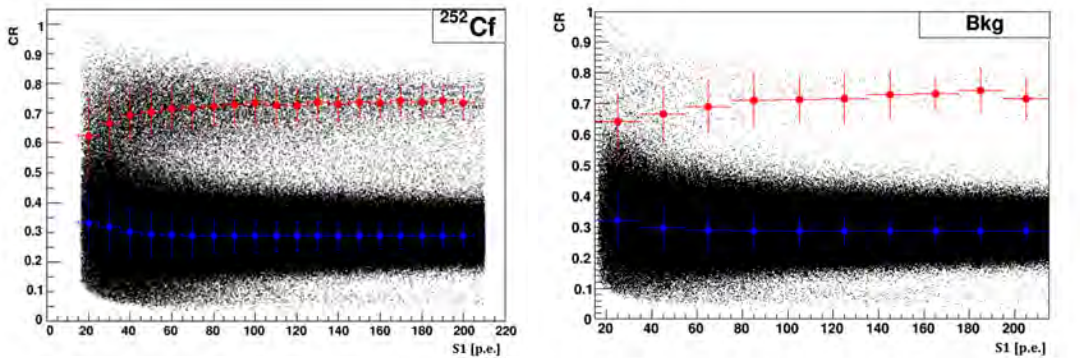

Figure 6.29: CR versus S1 light signal [p.e.]. The mean and sigma (dots and vertical error bars) of each energy slice are shown for both NR (red) and ER (blue) events in the case of ^{252}Cf (left) and background data (right).

Both the separation between bands and the rejection power obtained as a function of the energy have been summarised in Tables 6.3, 6.4, 6.5 and 6.6 for 99.7%, 97.6%, 84.0% and 50% NR acceptance regions respectively. The figure of merit is defined as $FOM = (MV_{NR} - MV_{ER})/(FWHM_{NR} + FWHM_{ER})$, with MV the mean value and FWHM the full width at half maximum of the Gaussians, and it gives the quality of the NR-ER band separation. The band separation has been calculated using Equation 6.3. The probability that an ER event lies in the NR band is given by the normalised integral of the ER-Gaussian distribution in that energy slice between the limits: $(m_{NR} - N\sigma_{NR}, m_{NR} + 3\sigma_{NR})$, where N is 0,1,2 or 3. Finally, the ER rejection power based on the pulse shape discrimination, defined as the number of events that can be rejected before getting one background event statistically leaking into the NR band, has been calculated as the inverse of the leakage probability.

According to the results, the separation between bands and, consequently, the rejection power, increases with the energy. In particular, for 99.7% NR acceptance the separation increases from ∼0.50 σ (3.2 rejection) at 30 p.e. to ∼5.05 σ (4.5×10^6 rejection) at 100 p.e., indicating that a poor ER discrimination can be achieved by ArDM at such low energy considering the full acceptance. At the same time, the rejection greatly improves reducing the acceptance, as it is shown in the plot of Figure 6.30, that summarises the results from Tables 6.3, 6.4, 6.5 and 6.6. The rate of events expected per second in each energy bin from the ^{39}Ar decay is reported in the last column of the tables for comparison.

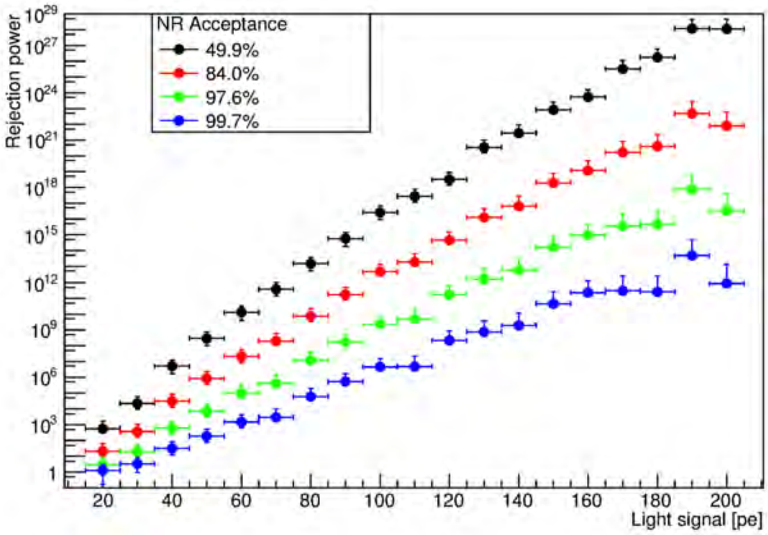

Figure 6.30: Statistical ER rejection power for different NR acceptance definitions as function of the S1 light signal.

The narrowness of the bands together with their separation in terms of pulse shape discrimination represent a first indication of the background rejection power of LAr detectors at the ton scale, even though, in the region below 50 p.e., the ER discrimination strongly depends on the number of photoelectrons detected. The detailed study of PSD, which depends on a precise description of the distribution tails, is subject of the upcoming next run of ArDM in the double phase operational mode.

S1 [p.e.]	**NR**		**ER**		**Figure of Merit**	**Band separation**	**ER leaking probability**	**Rejection power**	**^{39}Ar events/s**
	Mean	**Sigma**	**Mean**	**Sigma**					
20	0.623	0.124	0.332	0.0999	0.55	/	0.79	1.2	1.3×10^1
30	0.665	0.101	0.318	0.0886	0.77	0.50σ	0.31	3.2	1.3×10^1
40	0.693	0.0825	0.302	0.0771	1.04	1.86σ	3.1×10^{-2}	3.2×10^1	1.3×10^1
50	0.704	0.0765	0.294	0.0707	1.18	2.55σ	5.3×10^{-3}	1.9×10^2	1.4×10^1
60	0.714	0.0706	0.29	0.0662	1.31	3.20σ	6.7×10^{-4}	1.5×10^3	1.4×10^1
70	0.717	0.0725	0.288	0.0622	1.35	3.4σ	3.4×10^{-4}	3.0×10^3	1.5×10^1
80	0.724	0.0638	0.288	0.0589	1.50	4.15σ	1.6×10^{-5}	6.1×10^4	1.5×10^1
90	0.728	0.0605	0.288	0.0559	1.60	4.62σ	1.9×10^{-6}	5.3×10^5	1.5×10^1
100	0.733	0.0586	0.287	0.0535	1.69	5.05σ	2.2×10^{-7}	4.5×10^6	1.5×10^1
110	0.727	0.0604	0.287	0.0511	1.67	5.06σ	2.0×10^{-7}	4.9×10^6	1.5×10^1
120	0.727	0.0519	0.287	0.0495	1.84	5.74σ	4.6×10^{-9}	2.2×10^8	1.5×10^1
130	0.737	0.0549	0.287	0.0479	1.85	5.95σ	1.3×10^{-9}	7.8×10^8	1.6×10^1
140	0.731	0.0539	0.287	0.0462	1.88	6.11σ	5.0×10^{-10}	2.0×10^9	1.6×10^1
150	0.738	0.0508	0.287	0.0453	1.99	6.59σ	2.2×10^{-11}	4.6×10^{10}	1.6×10^1
160	0.734	0.0485	0.288	0.044	2.04	6.83σ	4.3×10^{-12}	2.4×10^{11}	1.6×10^1
170	0.742	0.0526	0.288	0.0431	2.01	6.87σ	3.2×10^{-12}	3.2×10^{11}	1.6×10^1
180	0.737	0.0538	0.288	0.042	1.99	6.85σ	3.8×10^{-12}	2.7×10^{11}	1.6×10^1
190	0.741	0.0481	0.287	0.041	2.16	7.55σ	2.1×10^{-14}	4.7×10^{13}	1.6×10^1
200	0.734	0.0544	0.288	0.0403	2.00	7.02σ	1.1×10^{-12}	8.9×10^{11}	1.6×10^1

Table 6.3: NR and ER mean and sigma values from the Gaussian fits of each 10 p.e. slice, band separation, ER events leaking probability and rejection power for 99.7% NR acceptance region.

6.7 Background and signal modelling in a frequentist analysis framework

Even though during Run I ArDM did not reach the status for a possible Dark Matter analysis because we did not have the TPC in full operation, we developed a first profile likelihood study that could be used for the Dark Matter analysis during Run II. This study, which was performed during Gran Sasso Summer Institute 2014 (GSSI2014) and has been recently published [155], was developed as an statistical approach to model signal and background for the XENON100 2011 direct Dark Matter search results, setting the basis for the future Dark Matter data analysis of the ArDM experiment.

In the present study, calibration data (AmBe for nuclear recoils and ^{60}Co gamma source for electron recoils) have been used in order to build a signal and background

S1 [p.e.]	**NR**		**ER**		**Figure of Merit**	**Band separation**	**ER leaking probability**	**Rejection power**	**^{39}Ar events/s**
	Mean	**Sigma**	**Mean**	**Sigma**					
20	0.623	0.124	0.332	0.0999	0.55	0.43σ	0.33	3.0	1.3×10^{1}
30	0.665	0.101	0.318	0.0886	0.77	1.63σ	0.05	19.6	1.3×10^{1}
40	0.693	0.0825	0.302	0.0771	1.04	2.93σ	1.7×10^{-2}	3.2×10^{2}	1.3×10^{1}
50	0.704	0.0765	0.294	0.0707	1.18	3.63σ	1.4×10^{-4}	1.9×10^{3}	1.4×10^{1}
60	0.714	0.0706	0.29	0.0662	1.31	4.27σ	9.7×10^{-6}	1.0×10^{5}	1.4×10^{1}
70	0.717	0.0725	0.288	0.0622	1.35	4.57σ	2.5×10^{-6}	4.0×10^{5}	1.5×10^{1}
80	0.724	0.0638	0.288	0.0589	1.50	5.23σ	8.2×10^{-8}	1.2×10^{7}	1.5×10^{1}
90	0.728	0.0605	0.288	0.0559	1.60	5.71σ	5.8×10^{-9}	1.7×10^{8}	1.5×10^{1}
100	0.733	0.0586	0.287	0.0535	1.69	6.15σ	4.0×10^{-10}	2.5×10^{9}	1.5×10^{1}
110	0.727	0.0604	0.287	0.0511	1.67	6.24σ	2.1×10^{-10}	4.8×10^{9}	1.5×10^{1}
120	0.727	0.0519	0.287	0.0495	1.84	6.80σ	5.5×10^{-12}	1.8×10^{11}	1.5×10^{1}
130	0.737	0.0549	0.287	0.0479	1.85	7.10σ	6.1×10^{-13}	1.6×10^{12}	1.6×10^{1}
140	0.731	0.0539	0.287	0.0462	1.88	7.28σ	1.7×10^{-13}	5.8×10^{12}	1.6×10^{1}
150	0.738	0.0508	0.287	0.0453	1.99	7.71σ	6.1×10^{-15}	1.6×10^{14}	1.6×10^{1}
160	0.734	0.0485	0.288	0.044	2.04	7.93σ	1.1×10^{-15}	9.2×10^{14}	1.6×10^{1}
170	0.742	0.0526	0.288	0.0431	2.01	8.09σ	2.9×10^{-16}	3.4×10^{15}	1.6×10^{1}
180	0.737	0.0538	0.288	0.042	1.99	8.12σ	2.2×10^{-16}	4.6×10^{15}	1.6×10^{1}
190	0.741	0.0481	0.287	0.041	2.16	8.72σ	1.3×10^{-18}	7.6×10^{17}	1.6×10^{1}
200	0.734	0.0544	0.288	0.0403	2.00	8.37σ	2.9×10^{-17}	3.4×10^{16}	1.6×10^{1}

Table 6.4: NR and ER mean and sigma values from the Gaussian fits of each 10 p.e. slice, band separation, ER events leaking probability and rejection power for 97.6% NR acceptance region.

S1 [p.e.]	**NR**		**ER**		**Figure of Merit**	**Band separation**	**ER leaking probability**	**Rejection power**	**^{39}Ar events/s**
	Mean	**Sigma**	**Mean**	**Sigma**					
20	0.623	0.124	0.332	0.0999	0.55	1.67σ	4.7×10^{-2}	2.1×10^{1}	1.3×10^{1}
30	0.665	0.101	0.318	0.0886	0.77	2.78σ	2.7×10^{-3}	3.6×10^{2}	1.3×10^{1}
40	0.693	0.0825	0.302	0.0771	1.04	4.01σ	3.1×10^{-5}	3.2×10^{4}	1.3×10^{1}
50	0.704	0.0765	0.294	0.0707	1.18	4.71σ	1.2×10^{-6}	8.3×10^{5}	1.4×10^{1}
60	0.714	0.0706	0.29	0.0662	1.31	5.34σ	4.7×10^{-8}	2.1×10^{7}	1.4×10^{1}
70	0.717	0.0725	0.288	0.0622	1.35	5.73σ	5.0×10^{-9}	2.0×10^{8}	1.5×10^{1}
80	0.724	0.0638	0.288	0.0589	1.50	6.31σ	1.14×10^{-10}	7.6×10^{9}	1.5×10^{1}
90	0.728	0.0605	0.288	0.0559	1.60	6.79σ	5.6×10^{-12}	1.8×10^{11}	1.5×10^{1}
100	0.733	0.0586	0.287	0.0535	1.69	7.24σ	2.2×10^{-13}	4.5×10^{12}	1.5×10^{1}
110	0.727	0.0604	0.287	0.0511	1.67	7.43σ	5.5×10^{-14}	1.8×10^{13}	1.5×10^{1}
120	0.727	0.0519	0.287	0.0495	1.84	7.84σ	2.2×10^{-15}	4.5×10^{14}	1.5×10^{1}
130	0.737	0.0549	0.287	0.0479	1.85	8.25σ	8.0×10^{-17}	1.2×10^{16}	1.6×10^{1}
140	0.731	0.0539	0.287	0.0462	1.88	8.44σ	1.5×10^{-17}	6.5×10^{16}	1.6×10^{1}
150	0.738	0.0508	0.287	0.0453	1.99	8.83σ	5.0×10^{-19}	2.0×10^{18}	1.6×10^{1}
160	0.734	0.0485	0.288	0.044	2.04	9.03σ	8.3×10^{-20}	1.2×10^{19}	1.6×10^{1}
170	0.742	0.0526	0.288	0.0431	2.01	9.31σ	6.2×10^{-21}	1.6×10^{20}	1.6×10^{1}
180	0.737	0.0538	0.288	0.042	1.99	9.41σ	2.5×10^{-21}	4.0×10^{20}	1.6×10^{1}
190	0.741	0.0481	0.287	0.041	2.16	9.9σ	2.1×10^{-23}	4.8×10^{22}	1.6×10^{1}
200	0.734	0.0544	0.288	0.0403	2.00	9.72σ	1.2×10^{-22}	7.8×10^{21}	1.6×10^{1}

Table 6.5: NR and ER mean and sigma values from the Gaussian fits of each 10 p.e. slice, band separation, ER events leaking probability and rejection power for 84% NR acceptance region.

S1	**NR**		**ER**		**Figure of**	**Band**	**ER leaking**	**Rejection**	^{39}**Ar**
[p.e.]	**Mean**	**Sigma**	**Mean**	**Sigma**	**Merit**	**separation**	**probability**	**power**	**events/s**
20	0.623	0.124	0.332	0.0999	0.55	2.91σ	1.7×10^{-3}	5.5×10^{3}	1.3×10^{1}
30	0.665	0.101	0.318	0.0886	0.77	3.91σ	4.4×10^{-5}	2.2×10^{4}	1.3×10^{1}
40	0.693	0.0825	0.302	0.0771	1.04	5.07σ	2.0×10^{-7}	5.1×10^{6}	1.3×10^{1}
50	0.704	0.0765	0.294	0.0707	1.18	5.80σ	3.3×10^{-9}	3.0×10^{8}	1.4×10^{1}
60	0.714	0.0706	0.29	0.0662	1.31	6.40σ	7.5×10^{-11}	1.3×10^{10}	1.4×10^{1}
70	0.717	0.0725	0.288	0.0622	1.35	6.90σ	2.6×10^{-12}	3.8×10^{11}	1.5×10^{1}
80	0.724	0.0638	0.288	0.0589	1.50	7.40σ	6.7×10^{-14}	1.5×10^{13}	1.5×10^{1}
90	0.728	0.0605	0.288	0.0559	1.60	7.87σ	1.7×10^{-15}	5.7×10^{14}	1.5×10^{1}
100	0.733	0.0586	0.287	0.0535	1.69	8.33σ	3.8×10^{-17}	2.6×10^{16}	1.5×10^{1}
110	0.727	0.0604	0.287	0.0511	1.67	8.61σ	3.6×10^{-18}	2.7×10^{17}	1.5×10^{1}
120	0.727	0.0519	0.287	0.0495	1.84	8.89σ	3.0×10^{-19}	3.2×10^{18}	1.5×10^{1}
130	0.737	0.0549	0.287	0.0479	1.85	9.40σ	2.9×10^{-21}	3.5×10^{20}	1.6×10^{1}
140	0.731	0.0539	0.287	0.0462	1.88	9.61σ	3.6×10^{-22}	2.7×10^{21}	1.6×10^{1}
150	0.738	0.0508	0.287	0.0453	1.99	9.96σ	1.2×10^{-23}	8.4×10^{22}	1.6×10^{1}
160	0.734	0.0485	0.288	0.044	2.04	10.14σ	1.9×10^{-24}	5.2×10^{23}	1.6×10^{1}
170	0.742	0.0526	0.288	0.0431	2.01	10.53σ	3.0×10^{-26}	3.3×10^{25}	1.6×10^{1}
180	0.737	0.0538	0.288	0.042	1.99	10.69σ	5.6×10^{-27}	1.8×10^{26}	1.6×10^{1}
190	0.741	0.0481	0.287	0.041	2.16	11.07σ	8.5×10^{-29}	1.2×10^{28}	1.6×10^{1}
200	0.734	0.0544	0.288	0.0403	2.00	11.07σ	9.1×10^{-29}	1.1×10^{28}	1.6×10^{1}

Table 6.6: NR and ER mean and sigma values from the Gaussian fits of each 10 p.e. slice, band separation, ER events leaking probability and rejection power for 50% NR acceptance region.

model; while the science data are the ones collected by XENON100 from February 2011 to March 2012. The approach used here is described in more detail in [156]. In Figure 6.31 the nuclear recoil (NR), electron recoil (ER) and dark matter (DM) distributions are shown in the "linearised" log (S2/S1) (here called delta) vs S1 (in photoelectrons) parameter space.

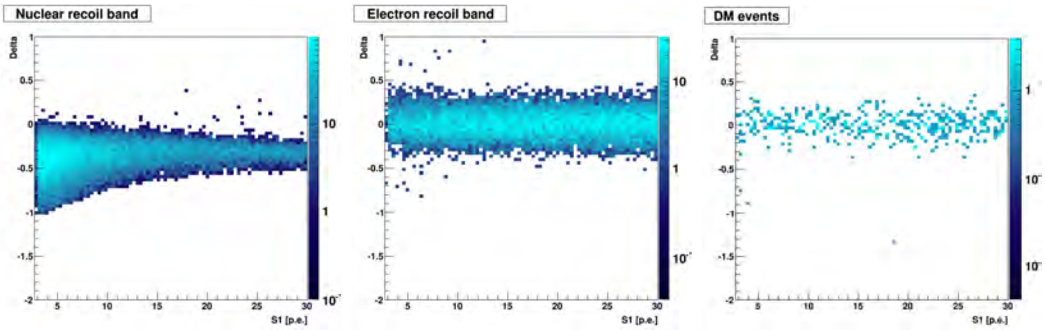

Figure 6.31: (Left) Nuclear recoil (NR), (centre) electron recoil (ER) and (right) Dark Matter (DM) distribution plots. In the plots we represent delta ("linearised" log of the ratio S2/S1) vs S1 signal in photoelectrons. Clear differences in shape and position are observed between NR and ER.

The first goal of this study is to calculate the number of signal events that maximises the likelihood describing our science data. Therefore, we construct 12 bands in the delta vs S1 parameter space in order to have the same number of NR events in each band as it is shown in Figure 6.32 (left). We then apply these bands to the ER, Figure 6.32 (centre), and science data, Figure 6.32 (right). This adaptive binning model allows us to have consistent signal statistics per bin.

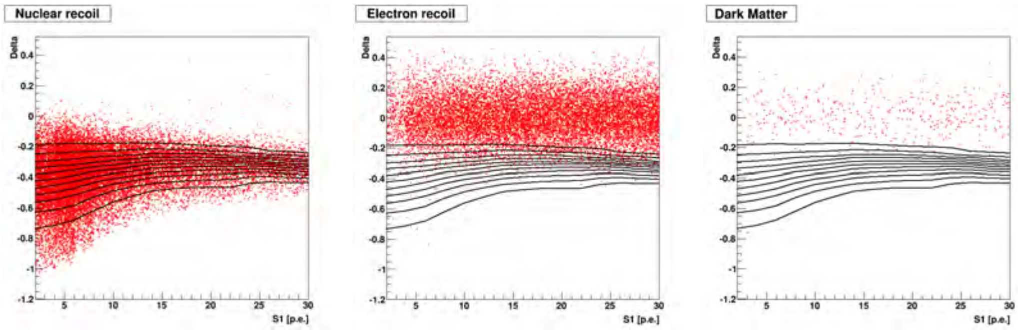

Figure 6.32: Modelling of the signal and background distributions by constructing delta bands (left). There are the same number of signal events in each band. The same bands are applied to the ER (centre) and science data (right) distributions.

We can then calculate how many events we will have in each band for the different data sets (Figure 6.33). The signal distribution (NR) is flat (by construction) compared to background (ER) and science data (DM).

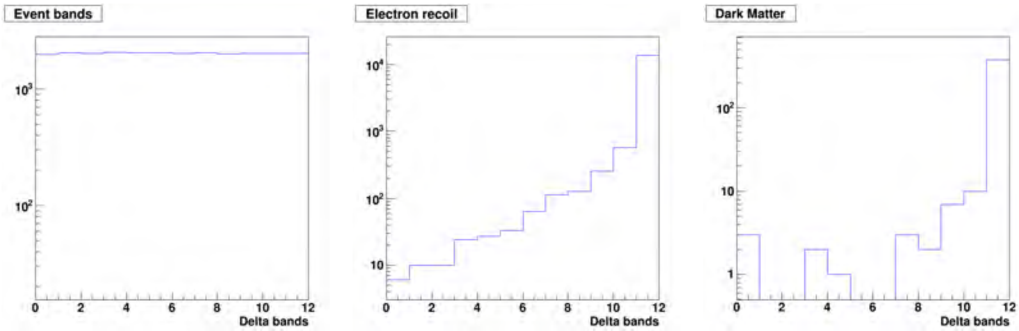

Figure 6.33: Number of events in each band. (Left) NR events show a flat distribution while for ER (centre) and science data (right) the number of events in each bin follows a Poisson distribution.

Assuming Gaussian errors, the number of events in each bin should follow a Poisson distribution. The mean of this distribution in principle varies bin by bin, since we are only interested in finding the maximum of the likelihood function and minimisers are more straightforward from an implementation standpoint than maximisers, we will focus on minimising the negative log of this likelihood function (nLL). Given a set of n_i science data points in a certain bin i, shown in Figure 6.33 (right), nLL is defined as follows:

$$nLL_i(N_s) = -n_i log\theta_i - \theta_i \tag{6.4}$$

The likelihood function depends on the expectation value of our signal and background in each bin, θ_i, which is function of the number of signals, N_s. The signal and background distributions are also required and they will be calculated from our histograms (Figure 6.33).

$$\theta_i(N_s) = N_s \cdot \;{}^{i}_{s} + N_b \cdot \;{}^{i}_{b} \tag{6.5}$$

The signal and background distributions are calculated as the number of events in the band normalised to total number of events:

$${}^{i}_{s} = \frac{NR_i}{\sum_i NR_i} = \frac{NR_i}{NR} \tag{6.6}$$

$${}^{i}_{b} = \frac{ER_i}{\sum_i ER_i} = \frac{ER_i}{ER} \tag{6.7}$$

The number of background events is obtained from data subtracting the number of signals:

$$N_b = Data - N_s = \sum_i Data_i - N_s \tag{6.8}$$

Taking all these aspects into account, the nLL is obtained as a function of N_s, with N_s calculated as the minimum of the function. However, this approach assumes that the histograms constructed from our calibration exactly follow the true background and signal distributions, which is not exactly true as Poisson fluctuations will make the number events in each bin differ from the actual expectation value. In order to cope with this effect, nuisance parameters, which represent the occupancy probability for each bin, can be introduced in a more advanced step of the study. All the mentioned tools represent a solid basis, which, after a final tuning, will be certainly required for the Dark Matter analysis of the future ArDM physics runs.

6.8 Conclusions and prospects for Run II

The calibration performed with the ^{252}Cf source during ArDM Run I has allowed to calculate the separation between NR and ER bands and the rejection power of ArDM through pulse shape discrimination. The neutron source has been proven to be active enough to produce a significant number of nuclear recoil events inside the detector, so it will be possible to use the same source in future to carry out the periodical neutron calibrations of the detector necessary during the ArDM Run II. Additionally, it will be possible to place the source further from the detector with a lead shield in front of it in order to stop the gamma emission from the source itself. That would allow to reduce the pile-up between the NR and ER given by the de-excitation following the ^{252}Cf fission, thus reducing the uncertainty on the measurement of the rejection power at low energy.

Given the relatively low ^{238}U and ^{232}Th contamination measured in the detector materials we cannot explain the events populating the NR band with the shield fully closed, shown in Figure 6.23 (top/bottom left plots), as produced by the neutron flux. Although these events could be due in principle to alpha particles sticking on the detector walls, this cannot be ensured due to the lack of a TPC during Run I. During Run II, the TPC will be operative, which will improve the event position reconstruction, allowing to reject events due to alphas. Furthermore, during the double phase operations, an additional selection of the nuclear recoils will be performed measuring the relationship between charge and light. It is expected that two more orders of magnitude electronic background rejection, with respect to what we measured during the first data taking, will be granted by the combined use of the two event discrimination tools.

Even though a higher light yield, in principle close to ≈ 2 p.e./keV$_{\mathrm{ee}}$, was expected, only ≈ 1 p.e./keV$_{\mathrm{ee}}$ has been obtained during Run I. That evidence, together with the high background measured in the NR band, prevented to carry out a preliminary DM analysis of the data. We are planning to improve the light yield during the next Run by replacing the tetratex reflector foils with a new aluminised mylar reflector from 3M company with freshly deposited TPB. The preparation of the new reflector is currently carried out at the CIEMAT laboratory. The possible improvement of the light yield, together with the reduction of the neutron background given by the replacement of the PMT bases with new radiopure materials, open interesting prospects for the first Dark Matter data taking to be carried out during Run II. According to the latest MC simulations and considering 500 kg fiducial mass of LAr, the number of single interactions due to neutrons would be reduced to 0.045 single scattering evt/day, in the energy range 50-100 keV$_{\mathrm{nr}}$, for the next Run foreseen by the project.

For 500 kg LAr fiducial mass, exposures of 4000, 6000 and 8000 kg×day can be obtained with 8, 12 and 16 live days respectively. In these cases, the expected improvement on the light yield up to 2 p.e./keV$_{\mathrm{ee}}$ would be sufficient to get a sensitivity similar or better than DarkSide-50 (1422±67 kg×day)[56] in a few weeks. In a conservative scenario, it will be possible to carry out background free data taking in the range 60-105 keV$_{\mathrm{nr}}$ considering 50% nuclear recoil acceptance and 90% C.L.. Given the 0.045 single scattering nuclear recoils per day calculated based on the screening results and the MC simulation, the background due to neutrons would be less than one event for all the data taking periods considered above. The background due to ^{39}Ar is calculated in evt/day as follows:

$$\sum_{\mathrm{bin}} \frac{^{39}\mathrm{Ar\ evt/s}}{\mathrm{Combined\ rejection\ power}} \times 3600\ \mathrm{s/h} \times 24\ \mathrm{h/day}, \tag{6.9}$$

with ^{39}Ar evt/s and rejection power taken from the last two columns of Table 6.6 and bin taking values from 40 p.e. (equivalent to ∼60 $\mathrm{keV_{nr}}$ or ∼20 $\mathrm{keV_{ee}}$) to 70 p.e. (equivalent to ∼105 $\mathrm{keV_{nr}}$ or ∼35 $\mathrm{keV_{ee}}$). The combined rejection power is obtained by multiplying the table values by the additional factor 10^2 thanks to the operative LAr-TPC during Run II. Considering 60-105 $\mathrm{keV_{nr}}$, the number of background events due to ^{39}Ar is less than one for all the data taking periods mentioned above. In this case, the ArDM expected sensitivity as function of the WIMP mass is shown in the plot of Figure 6.34. For the 60 $\mathrm{keV_{nr}}$ threshold, ArDM would achieve DarkSide-50 sensitivity with approximately 6000 kg×day exposure, calculated with the tools developed in Chapter 2, which only corresponds to 12 live days. In a bit more aggressive approach, shown in Figure 6.35, lowering the threshold to 50 $\mathrm{keV_{nr}}$, we would also achieve background free exposures of 4000, 6000 and 8000 kg×day. In this case, only with approximately 4000 kg×day (8 live days), ArDM would achieve the DarkSide-50 sensitivity. Thus it will be possible to set the most competitive DM limit with an Ar-TPC in the world after a bit more than week of data taking, starting to explore the CMSSM preferred parameter regions from Bayesian theoretical predictions [157] during ArDM Run II.

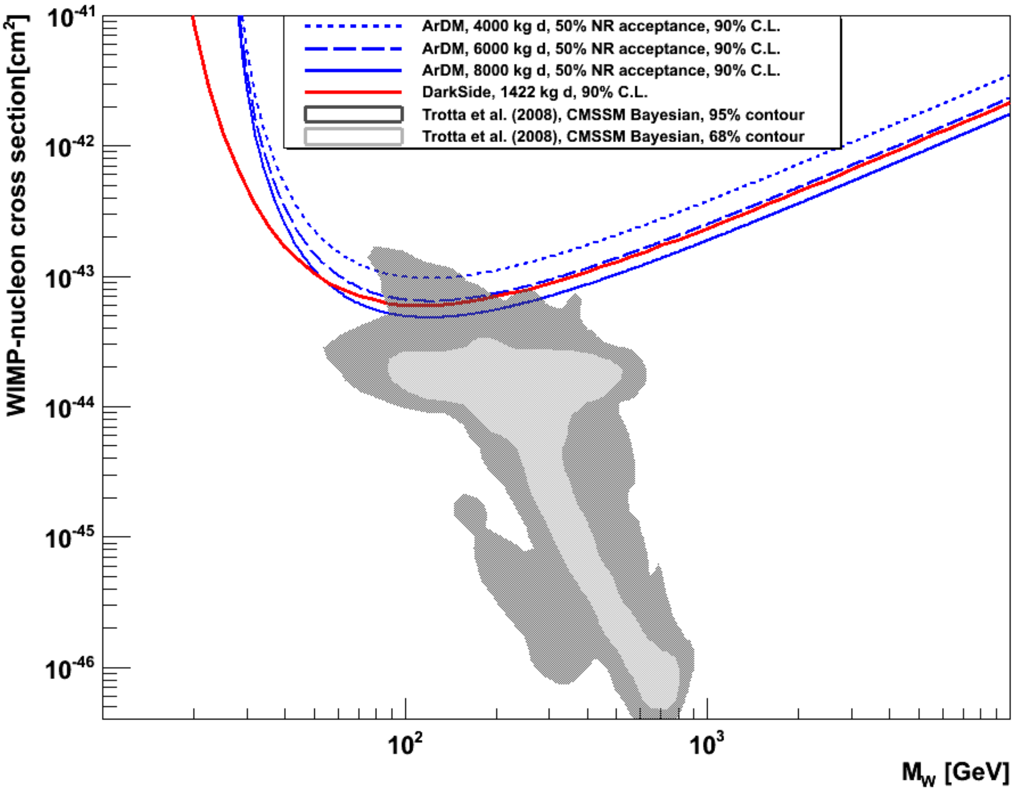

Figure 6.34: Projected sensitivity of the ArDM experiment for exposures of 4000, 6000 and 8000 kg×day (blue lines), assuming 50% NR acceptance and 90% C.L., which gives ^{39}Ar background free data in the range 60-100 keV$_{\mathrm{nr}}$. Only with 11.4 days of data taking and considering 500 kg fiducial mass of LAr, ArDM can achieve the latest limit set by DarkSide-50 (red line), which corresponds to 1422±67 kg×day [56]. The CMSSM preferred parameter regions from Bayesian theoretical predictions are depicted in grey [157].

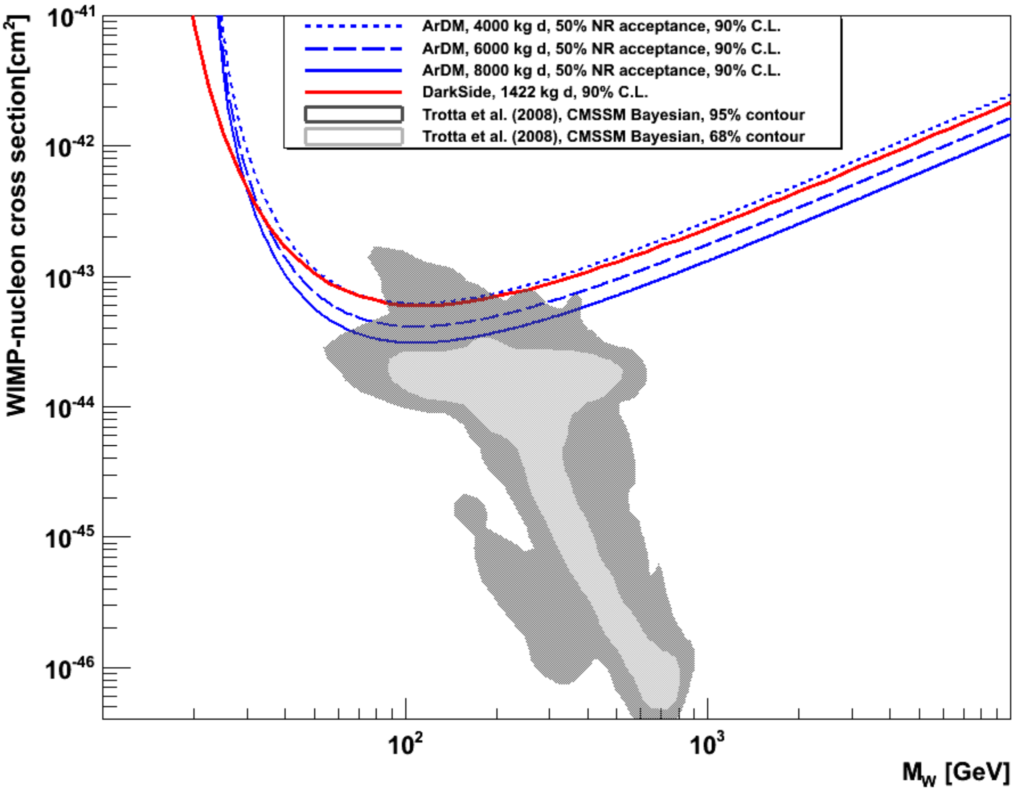

Figure 6.35: Projected sensitivity of the ArDM experiment for exposures of 4000, 6000 and 8000 kg×day (blue lines), assuming 50% NR acceptance and 90% C.L. in the range 50-100 keV$_{\mathrm{nr}}$. Only with 5.7 days of data taking and considering 500 kg fiducial mass of LAr, ArDM can achieve the latest limit set by DarkSide-50 (red line), which corresponds to 1422±67 kg×day [56]. The CMSSM preferred parameter regions from Bayesian theoretical predictions are depicted in grey [157].

Chapter 7

Neutron background @ LSC

As it has been mentioned in Chapter 4, neutron radiation constitutes the most important background in Dark Matter experiments due to the fact that fast neutrons (with $\sim$ 1 MeV or higher energy) induce nuclear recoils in the Dark Matter energy region of interest, which makes them indistinguishable from WIMPs on an event by event analysis. In a deep underground site, such as LSC, background neutrons are produced from three major sources: cosmic ray muon interactions, spontaneous fission of ^{238}U and (α, n) reactions, following α-decay of trace contaminations of ^{238}U and ^{232}Th in detector materials or laboratory rock. Neutrons arising from radioactive decays, for example in a fission process or produced in (α,n) reactions, have energies limited to $\sim$10 MeV. In contrast, neutrons produced through the interaction of high energy cosmic ray muons with matter can reach energies of several GeV.

We investigated a possible way to measure the neutron flux in the experimental hall A, where the ArDM detector is installed, to evaluate the contribution of environmental neutrons. In order to explore the neutron flux in the energy range of interest for ArDM (1-$\sim$10 MeV), a BC501A liquid scintillator detector, foreseen for fast neutron spectroscopy (few keV to 20 MeV), was installed underground in hall A. This option is motivated by similar measurements performed with liquid scintillators at the CPL laboratory in the range 1.5-6 MeV [165]. An extensive work has been performed to find out the optimal setup and conditions to tentatively measure the neutron flux, including several tests on surface at CIEMAT before moving underground to LSC. This study has been carried out in the context of ArDM, but it can be considered a possibility to explore a general measurement in the laboratory. If this technique is proved to be successfully applied to measure and monitor the neutron flux in the experimental hall, we will plan to keep functioning the liquid scintillator over the ArDM data taking.

Other measurements have been performed in the past at LSC. In particular, the energy distribution of the neutron background was measured for the first time at hall A by CUNA collaboration [135]. For this purpose they used six high-pressure

^{3}He proportional counters embedded in individual polyethylene blocks of different thickness to moderate neutrons. In this way not only the integral value but also the neutron flux distribution as a function of energy was determined in the range from 1 eV to 10 MeV by combining the response of the six proportional counters.

7.1 Detector description

Scintillation detectors can be made of crystals, plastic scintillators or organic liquids. Organic crystals usually present anisotropies in light production and they cannot be easily machined, nor can they be grown in large sizes; hence they are not very often used. Plastic scintillators, consisting of a solid solution of organic scintillating molecules in a polymerised solvent, do not provide neutron gamma discrimination or provide a poor discrimination in the case of the most recently synthesised compounds, so they are often used for other type of measurements that require fairly high light output and a relatively quick signal. Finally, liquid scintillators have been extensively used for neutron detection in the presence of background gamma radiation, due to the possibility to discriminate between neutron and gamma incident particles thanks to their fast time response.

In most organic scintillators, the scintillation light is composed by a prompt fluorescence and a longer-lived contribution, corresponding to the delayed fluorescence, called fast and slow components of the scintillation respectively. Compared with the prompt decay time of a few nanoseconds, the slow component typically has a characteristic decay time of several hundred nanoseconds. Although the majority of the light yield occurs in the prompt scintillation, the long-lived tail presents a useful property, similarly to LAr: the fraction of light in the tail depends on the nature of the exciting particle. One can therefore make use of this dependence to distinguish between different incident particles that deposit the same energy in the detector. This scintillation pulse shape discrimination (PSD) process is widely applied to eliminate gamma-ray-induced events when organic scintillators are used as neutron detectors [158, 159].

Among the different liquid scintillators, BC501A, which is an aromatic hydrocarbon, $C_6H_4(CH_3)_2$, provides the highest discrimination between neutrons and gammas. The BC501A liquid scintillator, manufactured by Saint-Gobain Crystals, has a density of 0.874 g/cm^3 and a refractive index of 1.5 [160]. Its scintillation light presents three characteristic fluorescence components ($\tau_2 \sim 3.16$ ns, $\tau_3 \sim 32.3$ ns and $\tau_4 \sim 270$ ns) [161], whose relative contribution to the total light output depends on the specific energy loss of the ionising particle. These decay times of the different scintillation components are obtained from a χ^2 fit to experimental points, as shown in the plot of Figure 7.1 (left). The lifetime of the slow component, τ_4, is obtained from the slope of the decay curve in the interval 200-500 ns, while the lifetime of the intermediate component, τ_3 is estimated from the slope in the interval 50-100 ns after subtracting the contribution of the slow component in this region. The emission spectrum of BC501A, which is shown in Figure 7.1 (right), presents a maximum of emission for a wavelength of 425 nm [160].

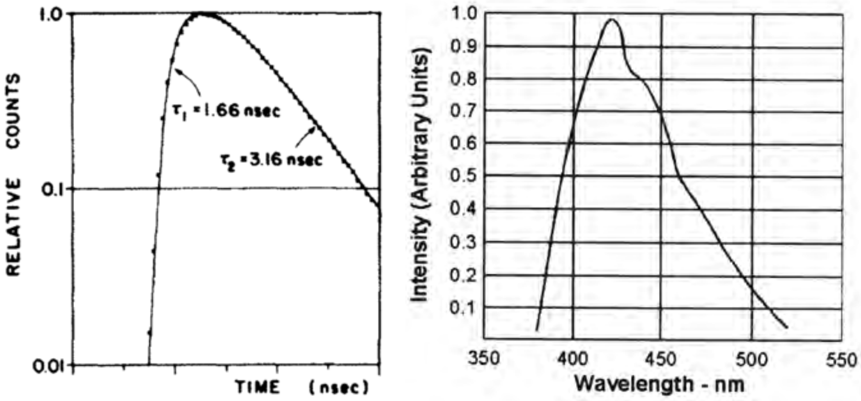

Figure 7.1: (Left) Time dependence in the early portion of the scintillation produced by gamma rays in BC501A. The curve is a χ^2 fit to experimental points [161]. (Right) Emission spectrum of BC501A showing a maximum of emission for a wavelength of 425 nm [160].

A BC501A liquid scintillator detector specifically designed for low background measurements, in order to avoid neutrons from material contamination, was selected to perform the neutron flux and spectra measurements at LSC. The BC501A is encapsulated in a cylindrical 12.7 × 12.7 cm stainless steel cell, which has a quartz window in one side as shown in Figure 7.2 (left). The quartz window is directly connected to a 5-inch diameter R877-01 Hamamatsu PMT through optical grease. This PMT, which is made of borosilicate glass and has a bialkali photocatode, is placed in a copper housing that includes a built-in voltage divider, which is connected to the PMT by soldering, as shown in Figure 7.2 (right).

7.2 Experimental setup and detector characterisation at CIEMAT laboratory

The characterisation of the low background BC501A liquid scintillator detector was carried out at CIEMAT in collaboration with the Nuclear Innovation Unit. The optimal electronic setup has been investigated in order to guarantee both the linearity of the detector response and the neutron-gamma separation using PSD. Two different energy ranges were defined: 0.1 - 7 $\mathrm{MeV_{ee}}$ (corresponding to 0.7 - 10 $\mathrm{MeV_n}$ of neutron energy) for neutrons from radioactive decays and fission and 0.1 - 14 $\mathrm{MeV_{ee}}$

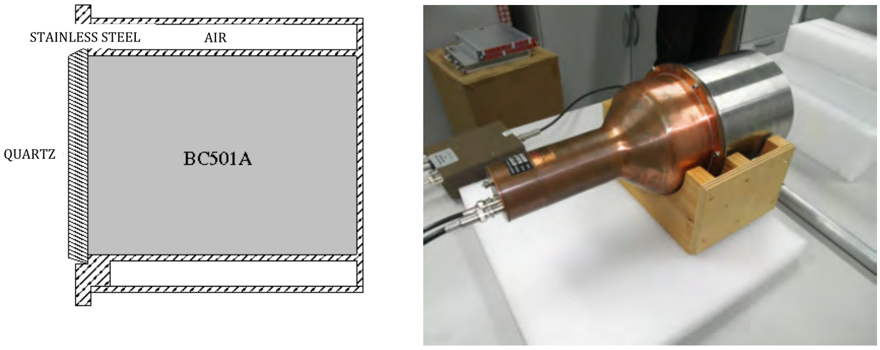

Figure 7.2: (Left) Scheme of the BC501A capsule with the quartz optical window that is connected to the detector PMT. (Right) BC501A at the Nuclear Innovation Unit laboratory (CIEMAT), showing the stainless steel case of the liquid scintillator and the copper housing of the detector PMT.

(corresponding to 0.7 - 20 MeV_n of neutron energy) for neutrons produced through the interaction of high energy cosmic ray muons with matter.

The setup that has been used for the measurements, which includes the BC501A detector, electronic modules and a DAQ, is schematically shown in Figure 7.3. The detector is connected to a high voltage (HV) power supply and its output signal is introduced in a fast amplifier in order to be able to measure the two different energy ranges, adapting to the 2 V dynamical range of the digitiser and preserving the linearity of the response. In addition, the detector output signal is introduced in a time filter amplifier (TFA), a constant fraction discriminator (CFD) and a gate generator (GDG) to create the trigger signal. Then, the signals are digitised by the DAQ.

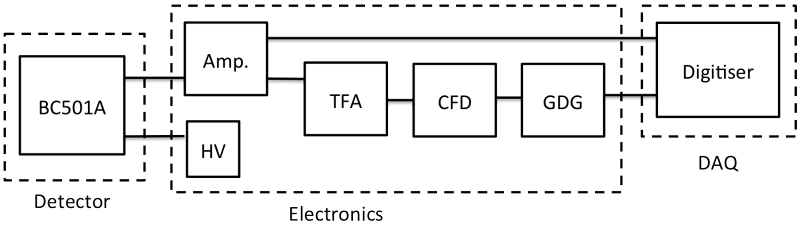

Figure 7.3: Scheme of the final neutron setup tested at CIEMAT before installation at LSC. The output signal from the BC501A detector is amplified and digitised. In order to generate the trigger signal, the amplified signal passes through a time filter amplifier, a constant fraction discriminator and a gate generator.

Several tests were performed at CIEMAT with different electronic modules and configurations to evaluate which ones provided the highest efficiency and the best conditions for the measurements. Finally, a 16CH CAEN N979B fast amplifier, an ORTEC 474 TFA, a DIFF DISC 583B CFD and an ORTEC GG8020 GDG were chosen to compose the final setup that was tested and moved to LSC. In this final setup, shown in the scheme of Figure 7.4, the detector output signal is amplified once in the fast amplifier (factor 2 of amplification) and introduced to channel 1 of the CAEN digitiser for the energy range $0.7-20$ $\mathrm{MeV_n}$. In the case of the range $0.7-10$ $\mathrm{MeV_n}$, the BC501A output signal is amplified a second time in another CAEN fast amplifier with a factor 2 of amplification, so the resulting total amplification is a factor 4. Then this amplified signal passes through an external DC level remover before being introduced in the channel 0 of the CAEN digitiser.

The HV power supply for the detector is a N470 model from CAEN. The CAEN digitiser (N6720) has a sampling rate of 250 Gsamples/s (each sample corresponds to 4 ns), a vertical resolution of 12 bits, corresponding to 4096 points, and a fixed input range of 2 V. In order to perform the analysis, the digitised signals are transferred by USB connection to a computer, which has an external hard drive for data storage.

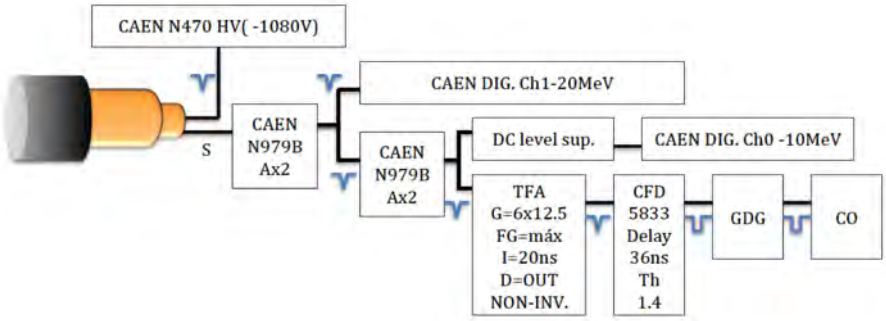

Figure 7.4: Scheme of the BC501A setup and electronics.

In order to characterise the detector response (light spectrum), we have used standard calibration gamma sources and we have carried out the following procedure for each measurement:

1. Firstly, by convention, the detector response to gamma rays is calibrated in electron equivalent energy units, which correspond to the energy deposited by the gamma through Compton effect mainly. Experimentally, the relation L(keVee) = $E_{compton}$ - 5.0 (keV) is fulfilled in the energy range of 50 keV up to 20 MeV. The use of a ^{22}Na (511 and 1275 keV gamma-rays) and an ^{88}Y (898 and 1893 keV) gamma sources have provided a wide range for calibration.
2. Secondly, the pulse height spectrum of each gamma source is obtained as the total integral of the waveform, which is calculated from 15 samples (60 ns) before the signal amplitude up to 75 samples (300 ns) after it. As an example

the spectrum for ^{22}Na is plotted in Figure 7.5 (left) in area units [A.U.]. The spectrum shape corresponds to the superposition of the Compton continuum from both gamma-rays emitted by the source.

3. The region of the Compton edge for each gamma-ray has a structure similar to a peak due to the finite experimental resolution, and its right position corresponds to a point between the maximum of the peak and the 50% in the upper part of the peak. Typically, the position of the 80% is accepted for the Compton edge position. By fitting a Gaussian function we have determined the Compton edge position for the various gamma-rays.
4. A calibration plot is shown in Figure 7.5 (right), in which, for every gamma line of ^{22}Na and ^{88}Y, its Compton energy is associated to the corresponding area value in the spectrum. The linear fit to these four points provides the relationship between the energy [keV$_{ee}$] and the area for data taken with input HV = 1080 V.

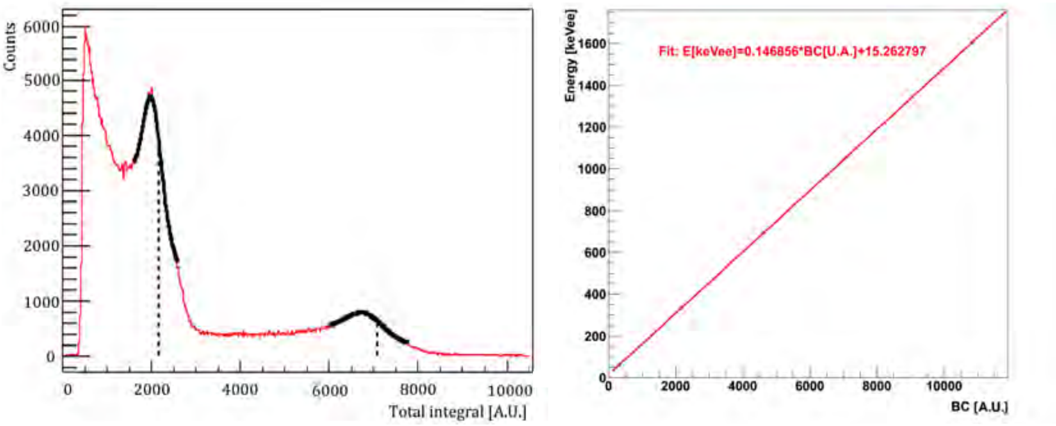

Figure 7.5: (Left) ^{22}Na spectrum taken at HV = 1080 V with Gaussian fits to the 511 keV and 1275 keV Compton peaks. The Compton edges, taken as the energies corresponding to the 80% of the maximum, are depicted with dashed lines. (Right) Detector calibration with ^{22}Na and ^{88}Y gamma sources for data taken with HV = 1080 V.

The linearity of the detector response (light spectrum) was evaluated by studying the relationship between the signal amplitude and the equivalent energy (or total area). Sometimes depending on the PMT characteristics, at high voltages the charge collected at the anode can be affected by screening effect and therefore the signal amplitude is not linearly proportional to the signal area. The signal is then saturated and the separation capability can be affected, thus a linear behaviour is preferred.

The linearity has been studied for different input voltages (1250 V, 1180 V, 1100 V and 1050 V). The amplitude of the signal (measured in the range 0 - 2000 mV) has been plotted as a function of the signal area calibrated in equivalent energy (keV$_{\mathrm{ee}}$), also named as equivalent light. A linear fit has been performed to a set of amplitude - energy signal points. The results obtained for the different HV values are shown in the plot of Figure 7.6 (left). According to them, a relatively low input voltage (1050-1100 V) has been set in order to guarantee a linear response. The amplitude of the signal is plotted as a function of the energy in the range for 1080 V in the plot of Figure 7.6 (right), showing the linearity of the response uo to 7 MeV$_{\mathrm{ee}}$.

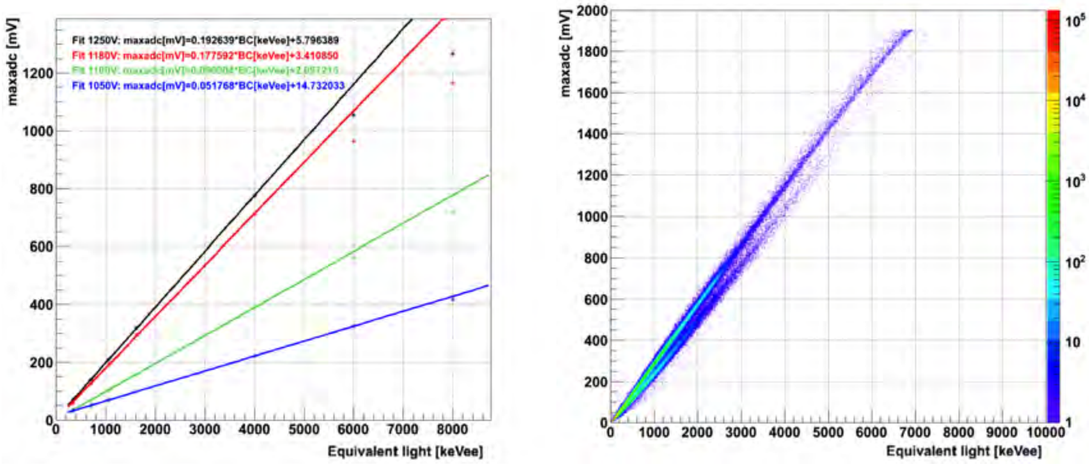

Figure 7.6: (Left) Study of the linearity of the detector response by plotting the variation of the amplitude of the signal (mV) with the energy (keV$_{\mathrm{ee}}$) for four different voltages. The linearity up to 8 MeV$_{\mathrm{ee}}$ is only ensured for the minimum studied value of the voltage. (Right) Amplitude of the signal as a function of the energy for background data taken at the final operation input voltage of 1080 V, confirming the linear response of the detector.

7.2.1 Study of the neutron gamma separation

Comparing signals produced by neutron and gamma particles, the neutron pulse shape shows a longer tail than the gamma ones. This is due to the fact that the slow decay components fraction depends on the rate of energy loss $\mathrm{d}E/\mathrm{d}x$ of the exciting particle and should be great for particles with large $\mathrm{d}E/\mathrm{d}x$. Consequently, the ratio between the integrated signal within the total time interval and the one corresponding to the tail of the signal, I_{tail}/I_{total}, determines the incident particle type. This method is the so-called digital charge integration discrimination and it is one of the most broadly used Pulse Shape Analysis (PSD) methods [162].

In order to compare both particles, we obtained average neutron and gamma signals by extracting and summing up several hundreds of signals that had been previously normalised to their amplitude. Neutron calibrations were performed with a ^{252}Cf source, procured by Eckert & Ziegler with a nominal activity of 10 kBq (1st of January 2011) [163]. The liquid source of chemical form $Cf(NO_3)_3$ in 0.1M HNO_3 is contained inside a sealed 5 mL V-vial. In Figure 7.7 (left) we plot the summed gamma and neutron signals extracted from data taken at CIEMAT with the ^{252}Cf source at an input voltage of 1100 V, showing the difference in the tail that allows to distinguish between them. In Figure 7.7 (right) the ratio of the tail integral and the total integral is plotted as a function of the equivalent light or energy deposited in the detector in keV$_{\mathrm{ee}}$. Two populations corresponding to neutrons, with higher I_{tail}/I_{total} ratio, and gammas, with lower I_{tail}/I_{total} can be distinguished for energies higher than $\sim$1.6 MeV$_{\mathrm{ee}}$, with a separation between them that increases with the energy.

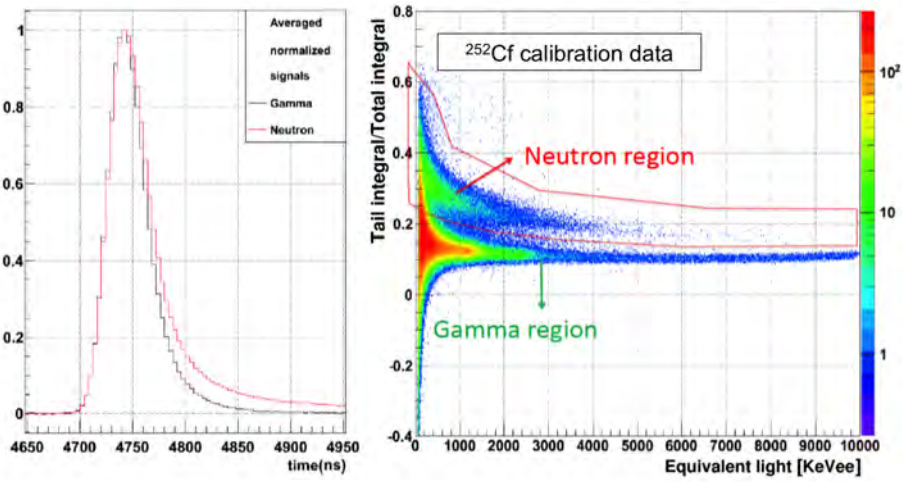

Figure 7.7: (Left) Average neutron (red) and gamma (black) signals, showing clear differences in the signal tail due to the fact that the slow component depends on the rate of energy loss $\mathrm{d}E/\mathrm{d}x$ of the particle. (Right) Ratio of the tail integral and the total integral plotted as a function of the equivalent light or energy deposited in the detector in keV$_{\mathrm{ee}}$. Neutron and gamma event distributions appear in different I_{tail}/I_{total} ratio.

In order to discriminate between neutron and gamma events of lowest possible energy, it is necessary to optimise the time interval of the tail integral, selecting the one that maximises the difference between neutrons and gammas. With this aim, the total integral has been calculated in the range from 15 samples (60 ns) before to 75 samples (300 ns) after the signal amplitude and the integral of the signal tail has been calculated in six different time intervals to choose the one providing optimal neutron-gamma separation. The integration intervals for the signal tail were defined as follows:

1. Tail integral 1 from 8 samples (32 ns) to 75 samples (300 ns) after the signal amplitude.
2. Tail integral 2 from 10 samples (40 ns) to 75 samples (300 ns) after the signal amplitude.
3. Tail integral 3 from 12 samples (48 ns) to 75 samples (300 ns) after the signal amplitude.
4. Tail integral 4 from 14 samples (56 ns) to 75 samples (300 ns) after the signal amplitude.
5. Tail integral 5 from 16 samples (64 ns) to 75 samples (300 ns) after the signal amplitude.
6. Tail integral 6 from 20 samples (80 ns) to 75 samples (300 ns) after the signal amplitude.

These time integration intervals have been implemented in the analysis software and they are calculated for each data file. As an example, the histogram of the ratio between the charge in the tail and the total charge at 200 keV$_{\mathrm{ee}}$ (between 185 KeV$_{\mathrm{ee}}$ and 215 KeV$_{\mathrm{ee}}$) taken with an input voltage of 1080 V is shown in Figure 7.8 for the six different tail integrals, fitting the gamma and neutron distributions with Gaussians.

In order to evaluate the quality of the neutron-gamma separation and therefore determine the optimal tail integral range, we define a figure of merit (FOM) as follows [164]:

$$FOM = \frac{S_{n\gamma}}{FWHM_{\gamma} + FWHM_{n}}, \tag{7.1}$$

where $S_{n\gamma}$ is the distance between the centroids of the two Gaussians, and $FWHM_{\gamma}$ and $FWHM_{n}$ are the full width at half maximum of gamma and neutron peaks respectively. This procedure was repeated for different input voltages, summarising the results for the highest and one of the lowest voltages in Table 7.1. According to these results and considering that for higher values of the figure of merit the separation is better, the best choice for the tail integral is the range 48-300 ns, which gives the highest FOM for both input voltages. In addition, for this integral range, $FOM = 1.367$ if 1080 V, while $FOM = 1.107$ if 1250 V, which indicates that a better separation is obtained for lower input voltages. For this reason and taking into account that, according to previous results, the linearity of the detector response is ensured for voltages of the order of 1050 V, 1080 V was chosen as input voltage for underground measurements.

The gamma versus neutron separation is shown for background data taken at 1080 V as function of the energy in the plot of Figure 7.9 (left) considering 48-300 ns for the tail integral. The neutron and gamma populations are visible with a separation that improves at higher energy from $FOM = 1.367$ at 200 keV$_{\mathrm{ee}}$ (between

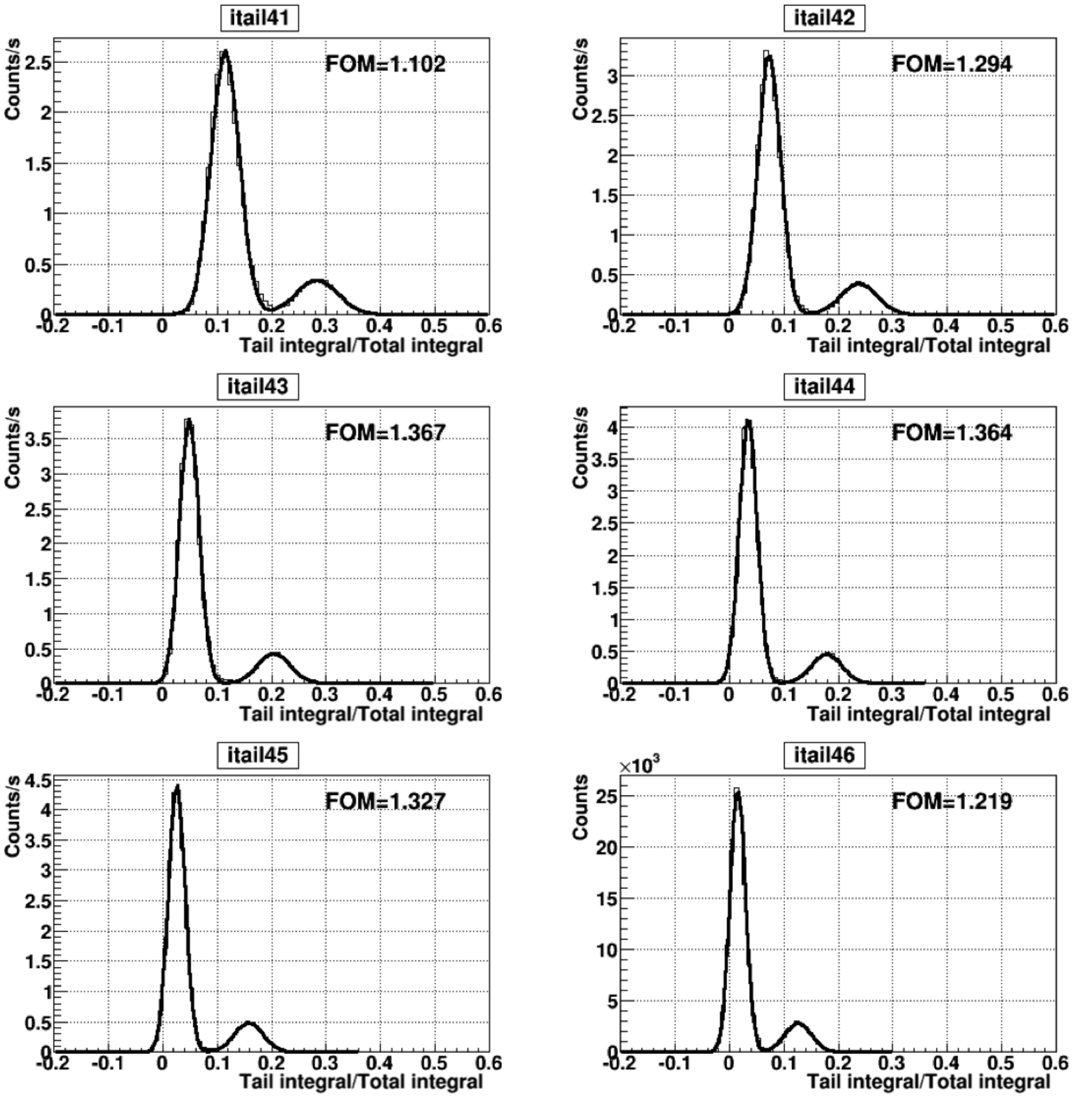

Figure 7.8: Ratio between the charge in the tail and the total charge for different tail integrals and data taken at CIEMAT with HV=1080 V. The neutron-gamma separation at 200 KeV_{ee} (between 185 KeV_{ee} and 215 KeV_{ee}) is obtained by performing Gaussian fits to the neutron and gamma distributions and calculating the figure of merit.

Interval	**Integration limits (ns)**	**FOM(1250 V)**	**FOM(1080 V)**
1	32 - 300	0.943	1.102
2	40 - 300	1.080	1.294
3	48 - 300	1.107	1.367
4	56 - 300	1.073	1.364
5	64 - 300	1.027	1.327
6	80 - 300	0.929	1.219

Table 7.1: Results for the FOM in the different tail integral ranges.

185 $\mathrm{KeV_{ee}}$ and 215 $\mathrm{KeV_{ee}}$), as mentioned previously, which corresponds to 1 MeV energy of the neutron, that is well above the minimal requirements. The energy spectra of the two subsets are shown in the plot of Figure 7.9 (right). The gamma and neutron event rates were measured to be 510 Hz and 5 Hz respectively in the range [0.7,10] $\mathrm{MeV_n}$, expecting a much lower rate inside the underground laboratory.

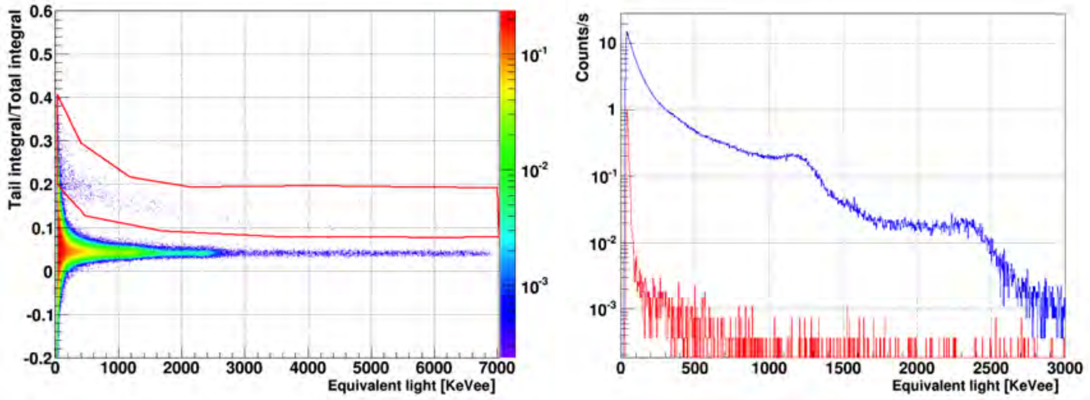

Figure 7.9: (Left) Ratio between tail integral and total integral versus equivalent light ($\mathrm{keV_{ee}}$) of the charge calculated from background signals taken at CIEMAT. The region where the neutron events are located is surrounded by a red line. (Right) The gamma spectrum is depicted in blue and in red we have plotted the neutron spectrum.

Another relevant issue of the signal study is the variation of the pulse shape as function of the signal amplitude. One can compare this variation among different ranges of the signal amplitude for neutrons and gammas. In order to do that:

1. Firstly, we selected several ranges of amplitude.
2. Secondly, we extracted neutron and gamma signals from ^{252}Cf data taken at CIEMAT in each range.

3. Then, we calculated the average signals in each range as the sum of all the extracted signals normalised to the amplitude.
4. Finally, the average signals obtained for the different amplitude ranges are shown in the plots of Figure 7.10 for gammas (left) and neutrons (right). Comparing the different amplitude ranges, we see that while the tail remains almost unchanged in gammas, it decreases with increasing amplitude for neutrons.

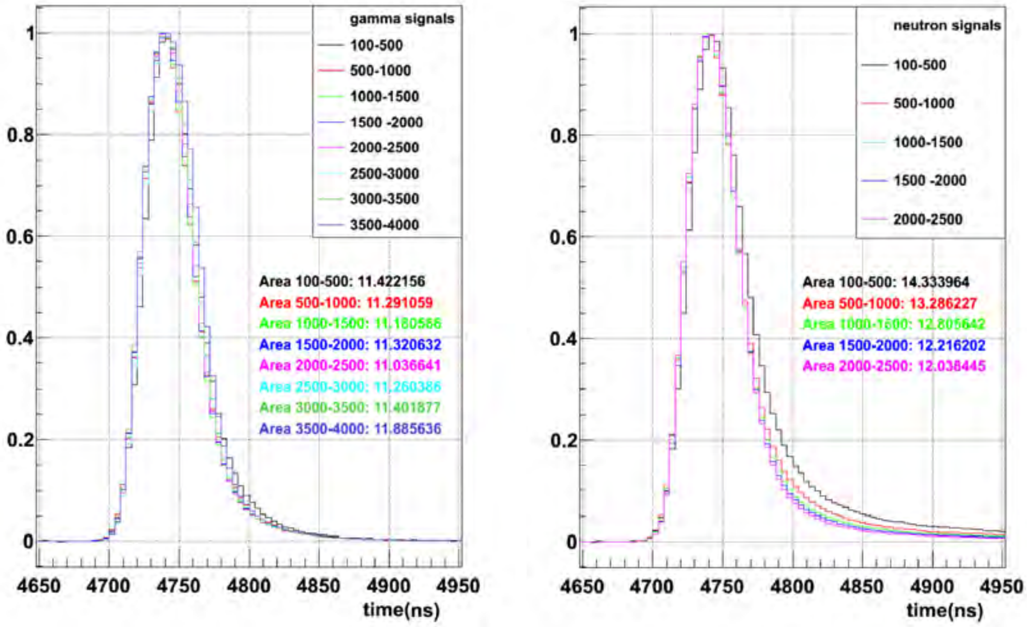

Figure 7.10: Average signals in different amplitude ranges for gammas (left) and neutrons (right). While the tail practically remains unchanged in gammas, it decreases for increasing amplitudes in neutrons.

In order to quantify the differences in the pulse shape for the studied amplitude ranges, we calculated the total integral of the signals shown in the plots of Figure 7.10. The results, which are written in Table 7.2, confirm that the variation in the area for gammas is of the order of 7%, much lower than that of neutrons, which varies within 16%. The PSD study and, in particular, these last results regarding the differences in the slow component of the signals will eventually become highly relevant in the analysis of the data taken underground at LSC.

Range	Amplitude range (U.A)	Integral γ	Integral n
1	100 - 500	11.42	14.33
2	500 - 1000	11.29	13.29
3	1000 - 1500	11.18	12.81
4	1500 - 2000	11.32	12.22
5	2000 - 2500	11.04	12.04
6	2500 - 3000	11.26	-
7	3000 - 3500	11.40	-
8	3500 - 4000	11.89	-

Table 7.2: Total integrals for gammas and neutron signals in the different amplitude ranges.

7.3 Underground commissioning

We worked in collaboration with the Nuclear Innovation Unit from CIEMAT to investigate a possible way to measure the environmental neutron flux and estimate the neutron induced background relevant for Dark Matter. The neutron setup which had been already evaluated at CIEMAT was moved to hall A of LSC, where ArDM is installed. We installed it in a metallic structure placed near the ArDM detector, as it is shown in Figure 7.11 (top left). The BC501A liquid scintillator was held in a wooden support on the top shelf of the metallic structure in order to ensure its safety, while both the DAQ and the computer were placed on a laboratory table next to this structure, as shown in Figures 7.11 (top right) and (bottom left) respectively. In Figure 7.11 (bottom right) the DAQ system containing the electronic modules that have been already described in Section 7.2, is shown in detail. The final detector setup and DAQ settings are the same ones that were selected after the tests performed at CIEMAT and that have been already specified in the scheme of Figure 7.4. The only change was performed in the energy threshold. We established a hardware threshold of 100 $\mathrm{keV_{ee}}$, which allows to measure neutrons with energies $\mathrm{E} > 0.7\,\mathrm{MeV_n}$.

The control of the DAQ and the data taking has been performed by a software specifically designed by the CIEMAT group for these measurements. This program allows controlling the start/stop of the DAQ and continuously monitors the trigger rate. The raw data are stored in .dat files, each of them containing a fixed number of events ($1.5 \cdot 10^5$), which corresponds to a run time of approximately 20 min. Due to the decrease in the trigger rate in the latest measurements with the detector inside a polyethylene shield, this run time per .dat file increased up to 2 hours. Each run is composed by hundreds of these .dat files and typically corresponds to a total run time of several days. In parallel to the data taking, an independent program process the .dat files, extracting relevant variables for the analysis, including: time, baselines, total and tail integrals of the signals, position of the signal maximum and value of this maximum. Then, from each .dat file, it creates a ROOT file with a tree containing those variables. Finally, the .root files are copied periodically to CIEMAT by network connection and further analysed remotely.

Figure 7.11: (Top left) Neutron flux measurement setup installed in hall A at LSC near ArDM. (Top right) BC501A held in its wooden support and placed on the top shelf of the metallic structure. (Bottom left) Computer and electronics. (Bottom right) Detail of the DAQ electronic modules.

The data taking is stopped in order to perform periodical calibrations with ^{22}Na and ^{137}Cs sources and a ^{252}Cf neutron source to check the performance of the detectors and the neutron-gamma separation. The setup for gamma calibration, which is shown on the picture of Figure 7.12 (left), consists of a metal and methacrylate support adjustable in height, in which the disk shaped sources can be placed in front of the cell containing the liquid scintillator lined to its centre. For neutron calibrations, the ^{252}Cf source, shown in the picture of Figure 7.12 (right), was placed directly next to the BC501A detector due to its low activity.

A possible problem that can occur during the data taking is due to the change of the PMT gain with variations in environmental conditions, specially temperature. The detector gain has been monitored during the whole data taking period to check that possible fluctuations do not affect the measurement significantly. Dedicated

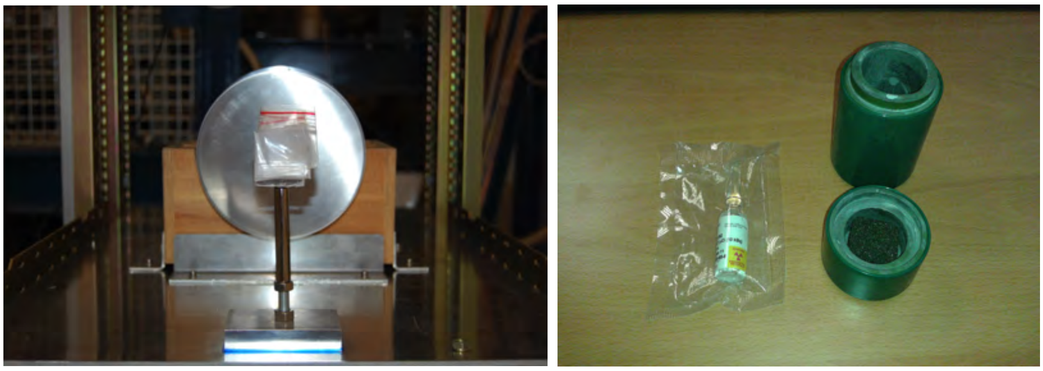

Figure 7.12: (Left) Gamma calibration setup consisting of a methacrylate support adjustable in height which is placed in front of the cell containing the liquid scintillator. (Right) ^{252}Cf source and its lead container designed for safe transport and storage.

checks have been performed in data, daily and also comparing runs taken in different days. As an example of the monitoring, we show the total integral for different runs within the same day in the plot of Figure 7.13 (left) and comparing runs taken in different days in the plot of Figure 7.13 (right). According to the coincidence of the peaks in the spectrum observed in these plots, the PMT gain stability is ensured for runs of short periods of time (days or several weeks).

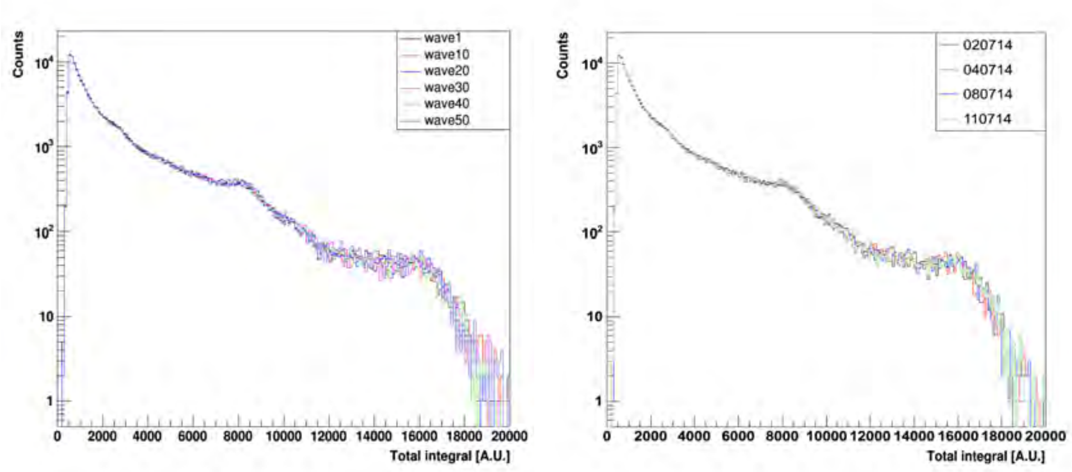

Figure 7.13: (Left) Integral of the signals from different runs taken during the same day. The coincidence of the peaks ensures gain stability. (Right) Comparison of the total integral for runs taken on different days (each histogram plotted with the sum of statistics of the whole run). Same results for the gain stability are obtained.

However, if we consider one year of data taking (May 2014 - May 2015), significant variations of the order of ∼35% have been detected in the detector response, as it is shown in the plot of Figure 7.14, where we present the variation of the ^{208}Tl peak position of the spectrum with time in red. On one hand, a strategy to correct for this effect, based on the variation in time of the position of the ^{40}K and ^{208}Tl lines that are visible in the gamma background spectra, has been developed. On the other hand, we have carried out detailed investigations to correlate these changes in the detector response to variations of environmental parameters in hall A, such as temperature, pressure, humidity and radon concentration, which are represented in the four plots of Figure 7.14. However, no clear correlation has been found with these environmental parameters.

The behaviour of the gamma and neutron response underground is the same as the one observed on the measurements performed at CIEMAT. In the plots of Figure 7.15 (left) we show the tail integral/total integral versus equivalent light plot with the same neutron selection already considered in Figure 7.9. The gamma and neutron spectra have been plotted in blue and red respectively in Figure 7.15 (right). As it was expected, the gamma and neutron event rates measured underground are much lower than the ones measured at ground level (CIEMAT). In particular, for the range [0.7,10] $\mathrm{MeV_n}$ the gamma rate underground is 120 Hz (510 Hz at ground level) and the underground neutron rate is 0.6 Hz (5 Hz at ground level).

7.3.1 Underground data taking

After the commissioning phase at LSC, we started the physics run in April 2014. The detector has been taking data continuously during the last year, obtaining a total live time of 216 days until March 2015. This live time corresponds to more than 65% of the total time, with a total number of $2.57 \cdot 10^9$ recorded events. In order to tentatively obtain a preliminary estimation of the neutron flux inside hall A, the following cuts related to the amplitude and position of the signal, the baseline and the signal area were performed in data:

1. Amplitude of the signal: maxadcBC $>$ 20. This cut removes signals due to electronic noise.
2. Position of the signal maximum: 1586 $<$ maxpBC $<$ 1570. We ensure that the signal maximum is correctly distributed in time.
3. Ratio between the baseline calculated in the left part of the signal with respect to the one calculated in the right part of it: bslaBC/bslbBC>0.99983 and bslaBC/bslbBC $<$ 1.0002. If this ratio is approximately 1, events in which the baseline is not properly calculated are rejected.
4. Value of different tail integrals defining an area per bin of the histogram: (itail42/65)/(itail45/59)>1.16, (itail42/65)/(itail45/59)<1.55 and itail45/itail42<0.76, which eliminates pile-up events

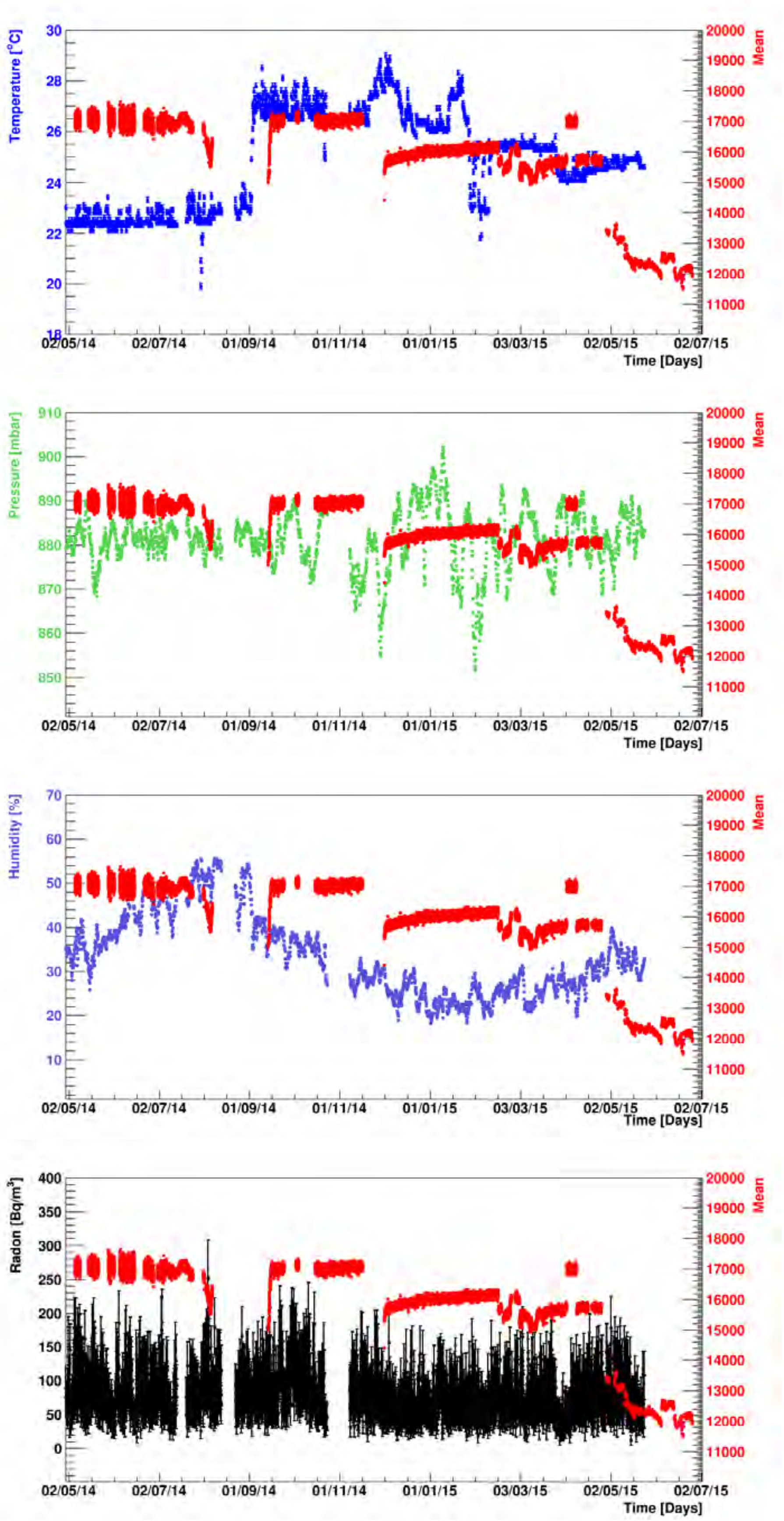

Figure 7.14: Evolution of the environmental parameters on the hall A of LSC for the period May 2014 to May 2015.

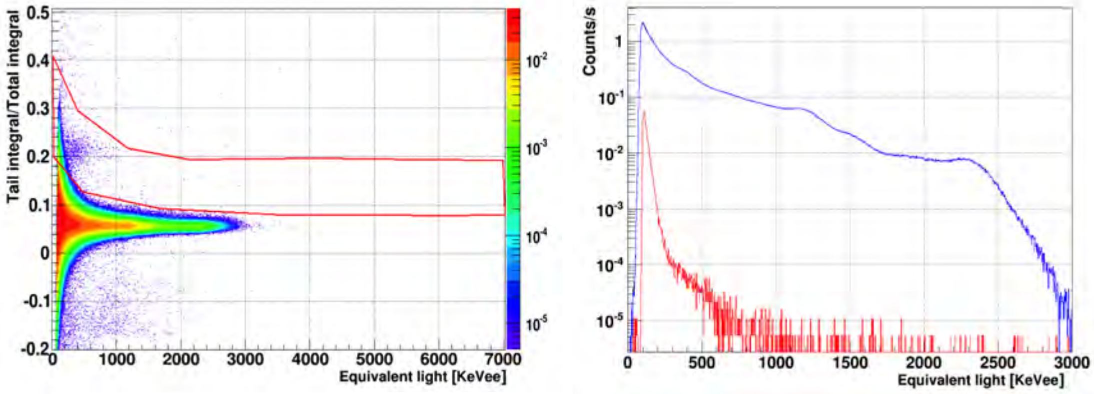

Figure 7.15: (Left) Ratio between tail integral and total integral versus equivalent light (keV$_{\mathrm{ee}}$) of the charge calculated from background signals taken at LSC. The region where the neutron events are located is surrounded by a red line. (Right) The gamma spectrum is depicted in blue and in red we have plotted the neutron spectrum.

The plots in Figure 7.16 (top-left) and (top-right) show the combined effect of cuts 1+2 and of all cuts 1-4 respectively. Finally, once the previous cuts have been applied, neutrons are selected with a two-dimensional cut, rejecting the gamma contribution, as shown in Figure 7.16 (bottom-left). In addition, a cut in the equivalent light ($>$ 200 keV$_{\mathrm{ee}}$ equivalent to $>$1.5 MeV$_{\mathrm{n}}$) is considered in the plot of Figure 7.16 (bottom-right) due to the fact that there is a minimum energy for which the detector does not allow to distinguish between neutrons and gammas.

Considering the restrictive neutron selection from Figure 7.16 (bottom-right), the preliminary result for the estimated neutron flux inside hall A is $6.3 \cdot 10^{-6}$ n/cm^2/s for energies in the range 1-6 MeV ($2.6 \cdot 10^{-6}$ n/cm^2/s for energies in the range 1.5-6 MeV). This result has been obtained considering the 84659 neutrons detected in a time interval of $1.76 \cdot 10^7$ s and taking into account the detector area of 760.06 cm^2. Our preliminary estimated neutron flux is one order of magnitude lower than a similar measurement performed in the CPL laboratory ($\sim$ 1000 m.w.e.), $(3.00 \pm 0.05) \cdot 10^{-5}$ n/cm^2/s, in the same energy range, 1.5-6 MeV [165]. At the same time, our measured preliminary flux is significantly higher than the one measured previously by CUNA in hall A with ^{3}He proportional counters, $(3.44 \pm 0.35) \cdot 10^{-6}$ n/cm^2/s, considering that this last result corresponds to a wider energy range of 1 eV-10 MeV [135].

In order to further investigate these discrepancies, we performed some tests to evaluate possible contributions to the neutron flux from the rock or laboratory materials. Firstly, we took data after covering the detector with perlite, an isolation

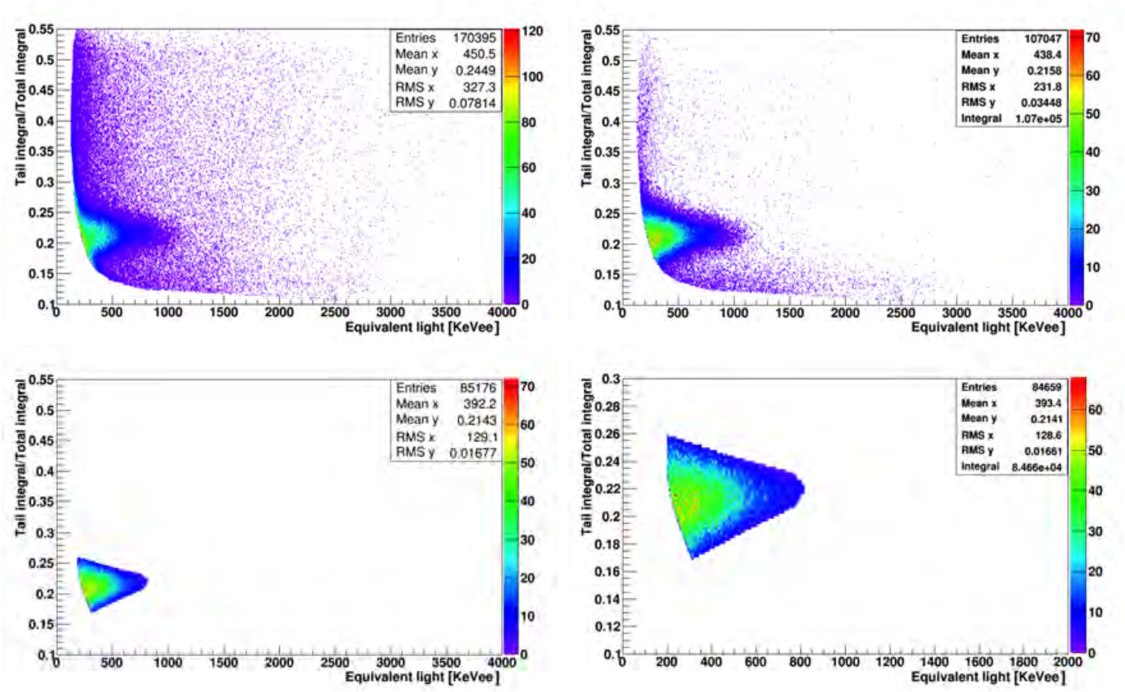

Figure 7.16: Selection of neutron events by applying several cuts to data: amplitude of the signal and position of the signal maximum (top-left), previous cuts plus ratio between baselines and value of tail integrals per bin (top-right), previous cuts plus neutron two-dimensional selection (bottom-left), previous cuts plus equivalent light > 200 keV$_{ee}$ (bottom-right).

material that was being used in ArDM at that moment and had been proven to be contaminated with ^{238}U and ^{232}Th after screening measurements. Secondly, some more data were taken after removing the perlite and placing the detector in the middle of hall A, far from the laboratory walls and from other detector setups, trying to avoid possible neutrons coming from interactions of cosmic muons with the laboratory rock or due to a local increment of the rock activity. The results, which have been summarised in Table 7.3, showed an increase in the gamma rate, from 120 Hz to 135 Hz, for the perlite measurement respect to the usual configuration and a decrease in the rate, from 120 Hz to 103 Hz, in the centre of hall A measurement. The same variation has been observed on the neutron rate, measured considering the restrictive selection from Figure 7.16 (bottom-right), which changed from 0.0056 Hz to 0.0063 Hz (perlite test) and then to 0.0052 Hz (centre of hall A test), remaining statistically consistent among the different measurements. Finally, we carried out a study of possible sources of internal detector background.

Data	**Gamma rate (Hz)**	**Neutron rate (Hz)**
Reference	120 ± 2	0.0056 ± 0.0020
Perlite	135 ± 3	0.0063 ± 0.0028
Centre hall A	103 ± 1	0.0052 ± 0.0018

Table 7.3: Gamma and neutron rate for a reference run taken in the usual configuration with the detector near ArDM, compared to tests performed with perlite and placing the detector in the centre of hall A.

7.4 Intrinsic background studies

The last point concerns the measurement of the intrinsic background of the liquid scintillator. In order to do that, the detector was moved into a castle built with the polyethylene bricks from the ArDM top shield, shown in Figure 7.17, in March 2015. According to the Monte Carlo simulations, it is expected that with the polyethylene shield we cut away the neutrons from outside the region of interest, so we can measure the intrinsic background. This measurement was intended to disentangle the contribution of the neutrons produced inside the detector by the spontaneous fission of ^{238}U and (α,n) reactions from the measured neutron flux.

Although the gamma rate was reduced drastically with the detector inside the shield, in particular it changed from ~120 Hz to ~20 Hz, the neutron rate inside the shield remained statistically consistent with the one measured outside the shield (~0.005 Hz). Since it is expected that the neutron rate has to be lower inside the shield, the results suggest the hypothesis that a large fraction of events in the

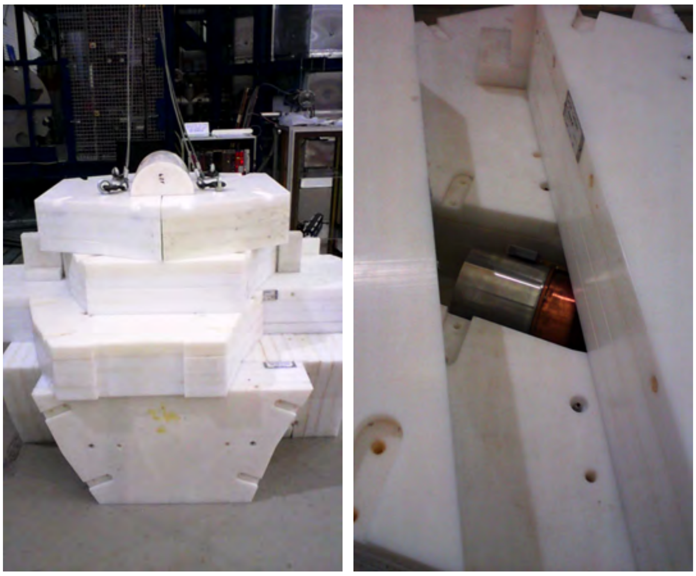

Figure 7.17: (Left) BC501A inside the closed castle made of pieces of the ArDM polyethylene shield. (Right) BC501A inside the opened poly shield.

neutron region were produced by internal detector contamination. However, after calculating the total activity in the ^{238}U and ^{232}Th decay chains ($1.74 \cdot 10^2$ Bq and $4.06 \cdot 10^1$ Bq respectively), the number of detected particles in the neutron region cannot be explained as produced from fission or (α,n) reactions, assuming a reasonable contamination of ^{238}U and ^{232}Th. In addition, this number is not in agreement with the reduction of the gamma rate inside the polyethylene shield.

Several runs with a ^{252}Cf neutron source were taken in order to compare real neutron signals from this source with the signals extracted in the neutron region from background data taken inside the poly shield. In order to select signals in the neutron region, we plotted the ratio between the tail integral and the total integral versus the amplitude of the signal, expressed in ADC units, as shown in Figure 7.18 for both ^{252}Cf data (left) and background data taken with the detector inside the polyethylene castle (right). Five different ranges for the amplitude of the signal have been selected to extract characteristic signals and make this comparison. In Figure 7.19 we show the comparison of the average signals for ^{252}Cf (left) and background data taken in the shield (right), which correspond to the sum of $\sim$100 signals normalised to the amplitude, for all the ranges under study. In the case of ^{252}Cf, the tail of the neutron signals decreases with increasing signal amplitude or energy, accordingly to what we obtained from our neutron measurements on surface at CIEMAT. Differently from those, the background signals extracted from poly data do not show this effect and there is no change in the tail for the different amplitude ranges.

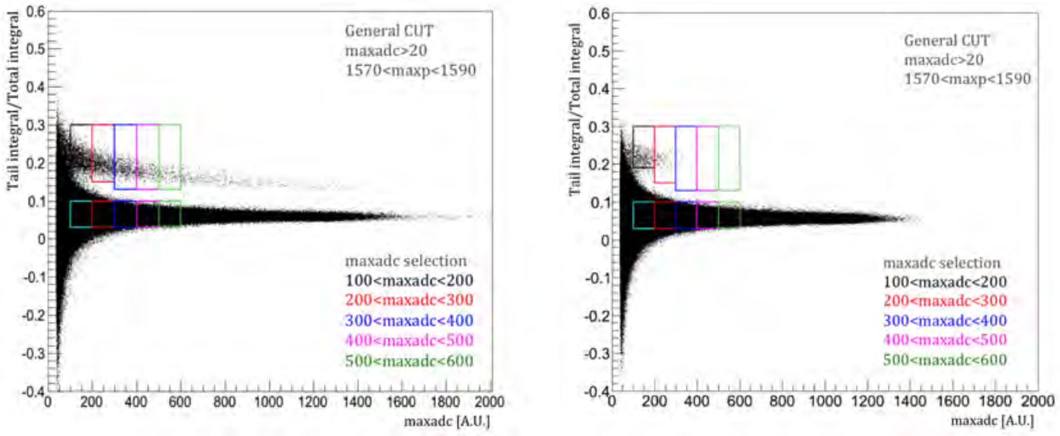

Figure 7.18: Ratio between the tail integral and total integral versus maximum of the signal (maxadc in ADC units) for ^{252}Cf data (left) and background data taken with the detector inside the polyethylene castle (right). Five different ranges of maxadc have been selected in the neutron region in order to compare ^{252}Cf and poly shield signals.

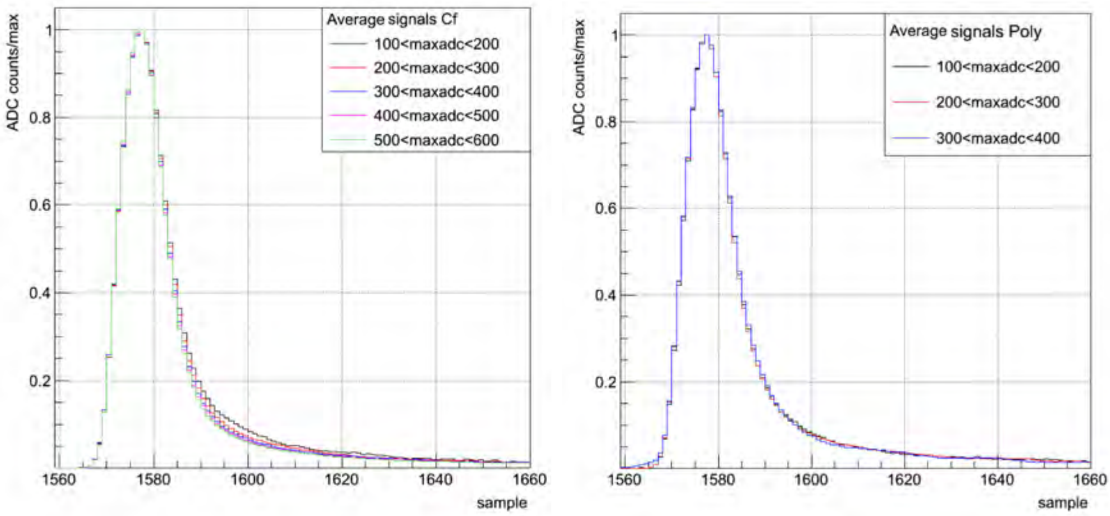

Figure 7.19: Comparison of the average signals extracted in the neutron region corresponding to different ranges of the amplitude for ^{252}Cf (left) and background data taken inside the poly shield (right). The tail of the neutron signals from ^{252}Cf decreases with increasing amplitude while it remains unchanged for background signals from poly shield data.

In order to compare average signals extracted from equivalent regions in energy, the total integral has been calibrated with ^{22}Na and ^{137}Cs gamma sources, so it is possible to express the maximum of the signal in keV$_{\mathrm{ee}}$. In the plot of Figure 7.20 (left) we show the average signals extracted from the neutron region for ^{252}Cf data (blue solid line) and poly shield data (red dashed line) in an equivalent signal amplitude range in energy. The average signals show clear differences in the tail. These differences, which are more relevant in the 1590-1680 sample region, as it is shown in the plot of Figure 7.20 (right), could point out that these partcles are not neutrons, thus explaining the discrepancy in the observed neutron flux with respect to previous measurements.

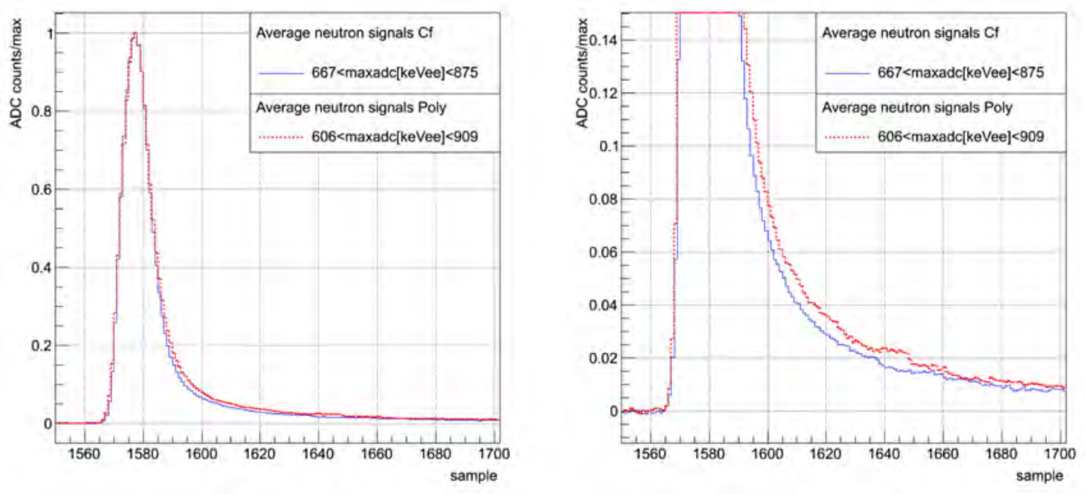

Figure 7.20: (Left) Average signals extracted from the neutron region for ^{252}Cf data (blue solid line) and poly shield data (red dashed line) in an equivalent signal amplitude (maxadc) range in energy. A clear difference is observed between both signals in the tail region. (Right) Zoom in the x axis range 1550-1700 of the left plot for better assessment of the mentioned signal difference.

7.5 Conclusions and plans

In collaboration with the Nuclear Innovation Unit from CIEMAT, we investigated a possible way to measure the neutron flux in the experimental hall A, where ArDM is installed, with a BC501A liquid scintillator detector. The optimal setup and conditions were tested at the CIEMAT laboratory before moving to LSC. After the underground commissioning phase, the detector has been taking data continuously during the last year. According to the results of the first analysis, our preliminary estimated neutron flux inside hall A, $6.3 \cdot 10^{-6}$ n/cm^2/s for energies in the range 1-6 MeV ($2.6 \cdot 10^{-6}$ n/cm^2/s for energies in the range 1.5-6 MeV), is one order of magnitude lower than a similar measurement performed in the CPL laboratory ($\sim$ 1000 m.w.e.), $(3.00 \pm 0.05) \cdot 10^{-5}$ n/cm^2/s, in the same energy range, 1.5-6 MeV [165]. At the same time, our measured preliminary flux is significantly higher than the one measured previously by CUNA in hall A with ^{3}He proportional counters, $(3.44 \pm 0.35) \cdot 10^{-6}$ n/cm^2/s, considering that this last result corresponds to a wider energy range of 1 eV-10 MeV [135].

The detector was then moved into a castle built with the polyethylene bricks from the ArDM shield in order to disentangle the contribution of the neutrons produced inside the detector by the spontaneous fission of ^{238}U and (α,n) reactions from the external neutron flux. Although the gamma rate was reduced drastically with the detector inside the shield, the neutron rate inside the shield remained statistically consistent with the one measured outside the shield. This fact has been interpreted as internal detector contamination, but we keep taking data.

One of the main goals of the future analysis is therefore to evaluate if the difference in the rate, spectrum and in the signals extracted in the neutron region inside and outside the shield is significant. In order to do that, it is necessary that we have comparable statistics inside and outside the shield. In addition, the analysis of the BC501A screening measurements, which are expected to clarify the amount of internal detector contamination, are ongoing.

Chapter 8

Ions drift in liquid argon detectors

A study of the dynamic of migrating electrons and ions in liquid argon (LAr) has been carried out in the context of the future ArDM runs, evaluating their possible impact in the underground operation of the detector. The long drift distances and the small mobility coefficient of the ions ensure that they spend considerably longer time in liquid respect to the electrons, thus giving rise to an accumulation effect of the positive charge. This effect can be eventually worsened by the injection in the active volume of the ions produced by electron multiplying devices located in the gas phase. In the first ArDM design, a Large Electron Multiplier (LEM) system was projected to amplify the electrons in gas phase in order to produce a detectable signal. At that time, we started to investigate the influence of the ions in the detector performance. Although there is no LEM in the current detector, it is possible that primary electrons, which are drifted inside the argon gas phase towards the anode, trigger avalanches near the wires in the anode plane (very close to the wire surface) [166]. Taking this into account, the impact of the positive current on the uniformity of the field has been evaluated as well as the probability of the quenching of the electron signal due to recombination. This study is relevant since one of the discrimination tools in ArDM is based on the detection of both S_1 and S_2 signals, thus it is fundamental not to lose electrons because, in that case, gammas would appear as nuclear recoils and it would not be possible to perform this type of discrimination. This investigation, which in principle has never been carried out, could be important for liquid argon detectors with long drift and charge amplification, such as the ones proposed for neutrino detection.

8.1 Dynamic of the ions at the interface gas/liquid

In the present study, we consider a LAr-TPC with axial geometry and the l axis perpendicular to the surface of the liquid. The drift field $\vec{E}_d$ in liquid is along l, with the anode in the origin ($l = 0$) and the cathode at a positive distance ($l = L$), as shown in the scheme of Figure 8.1. In addition, we assume that the detector is wide enough such that the transverse shape is not relevant for the discussion and the $\vec{E_d}$ is constant in any transverse section of the detector.

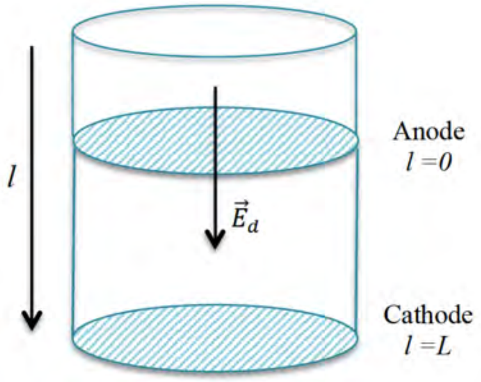

Figure 8.1: Scheme of an LAr-TPC with axial geometry and the l axis perpendicular to the surface of the liquid. The drift field $\vec{E_d}$ in liquid is along l, with the anode in the origin ($l = 0$) and the cathode at a positive distance ($l = L$).

The positive and negative charges present in the LAr bulk drift to the cathode and the anode respectively, following the same field lines. However, the ions have a drift speed orders of magnitude lower than that of the electrons [116, 167], $v_i \ll v_e$, thus they spend longer time in liquid before they get collected on the cathode and neutralised. As a result, the positive charge density is much higher than that of the electrons: $\rho_i \gg \rho_e$. Therefore, it is possible that the positive charge significantly modifies the electric field and, as consequence, the drift lines and the velocity of the electrons produced in liquid. That effect can be particularly relevant in case of a readout foreseeing the charge amplification where positive ions are further created by the avalanche in gas. In this case, the electrons, produced in liquid, drift to the anode and are then extracted and accelerated in gas, with the production of electroluminescence light or Townsend avalanche. The positive ions, produced at the same time in gas, can drift back to liquid surface along the same field lines of the electrons, greatly increasing ρ_i, thus, for large amplification factors, the positive charge density can be dominated by those secondary ions.

Considering the ion as an uniformly charged sphere of radius a, its potential energy can be expressed as:

$$V = \frac{3}{5}\frac{q^2}{4\pi\epsilon a}. \tag{8.1}$$

Taking into account that a is of the order of the Å and the relative permittivity is equal to 1.5 in liquid and 1.0 in gas, a difference in potential energy at the interface of approximately 3 eV favours the injection of the ions into the liquid [168].

For the following study we introduce the parameter G_E defined as the number of positive ions injected into the liquid for each electron extracted. That factor is proportional to the actual signal amplification in the gas G through a constant α ($\alpha < 1$) which takes into account the loss of the positive charge in gas, given by ion diffusion, and the efficiency to pass the liquid-gas interface. If the amplification factor G is large enough, the positive charge density ρ_i in liquid can be widely increased by the secondary ions.

8.2 Calculation of the field lines

Let us consider a negative ion immersed in an external electric field. We would like to determine the volume in which the field lines end in the ion. Analogously, we want to find the flux tube that includes all the flux lines that end in the ion. This problem presents cylindrical symmetry with the origin in the ion and the axis in the direction of the external field.

Let us consider an arbitrary section containing the origin and the axis. The cut of the flux tubes with this section gives the field lines, $r(\varphi)$. Let us consider a coordinate system defined in this section such that the x axis corresponds to the field direction, as it is shown in the scheme if Figure 8.2, where s is the parameter of arc length with arbitrary origin. Due to the cylindrical symmetry, we will only consider the half-plane with positive coordinates.

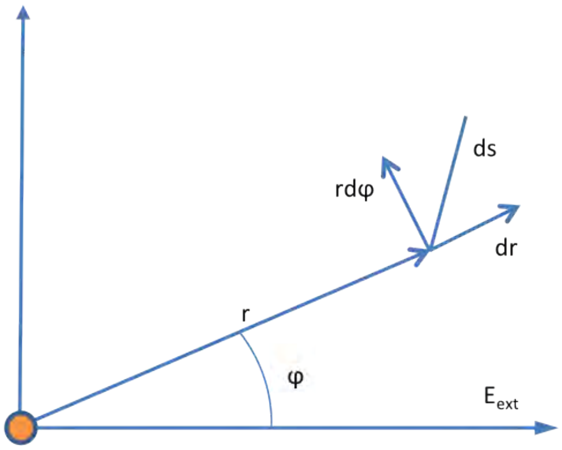

Figure 8.2: Coordinate system with the ion in the origin and the external electric field in the direction of the x axis.

The external electric field in polar coordinates is expressed as follows:

$$\vec{E}_{ext} = \begin{matrix} E_{ext}\cos\varphi \\ -E_{ext}\sin\varphi \end{matrix} \quad . \tag{8.2}$$

The total electric field, which takes into account the external field and the ion field is written as

$$\vec{E} = \vec{E}_{ion} + \vec{E}_{ext} = \frac{q\vec{r}}{4\pi\epsilon r^3} + \vec{E}_{ext} = \begin{matrix} \frac{q}{4\pi\epsilon r^2} + E_{ext}\cos\varphi \\ -E_{ext}\sin\varphi \end{matrix} \quad . \tag{8.3}$$

By definition, the electric field is tangent to any field line, so $\vec{E} = K_0(s)\,\vec{\tau}$, where $\vec{\tau}$ is the unitary vector tangent to a field line in s:

$$\vec{\tau} = \frac{\mathrm{d}\vec{r}}{\mathrm{d}s} = \begin{matrix} \frac{\mathrm{d}r}{\mathrm{d}s} \\ r\frac{\mathrm{d}\varphi}{\mathrm{d}s} \end{matrix} \quad . \tag{8.4}$$

Equalising both expressions of the electric field we get:

$$\frac{q}{4\pi\epsilon r^2} + E_{ext}\cos\varphi = K_0(s)\frac{\mathrm{d}r}{\mathrm{d}s}, \tag{8.5}$$

$$-E_{ext}\sin\varphi = K_0(s)\,r\,\frac{\mathrm{d}\varphi}{\mathrm{d}s}. \tag{8.6}$$

Then, from Equation 8.6 we isolate ds, $\mathrm{d}s = -\frac{K_0(s)r}{E_{ext}\sin\varphi}\mathrm{d}\varphi$, and we substitute this expression in Equation 8.5 to obtain

$$\frac{q}{4\pi\epsilon r^2} + E_{ext}\cos\varphi = -E_{ext}\sin\varphi\,\frac{1}{r}\,\frac{\mathrm{d}r}{\mathrm{d}\varphi}. \tag{8.7}$$

Then, if we multiply Equation 8.7 by r^2/E_{ext}, we have

$$\frac{q}{4\pi\epsilon E_{ext}} + r^2\cos\varphi = -\sin\varphi\,r\,\frac{\mathrm{d}r}{\mathrm{d}\varphi}. \tag{8.8}$$

We perform the change of variable $h = r^2$, $\mathrm{d}h = 2r\mathrm{d}r$ in Equation 8.8 and we also define $K_1 = q/4\pi\epsilon E_{ext}$,

$$\begin{aligned} K_1 + h\cos\varphi &= -\frac{\sin\varphi}{2}\frac{\mathrm{d}h}{\mathrm{d}\varphi} \\ \frac{\mathrm{d}h}{\mathrm{d}\varphi} + \frac{2h}{\mathrm{tg}\varphi} &= -\frac{2K_1}{\sin\varphi}, \end{aligned} \tag{8.9}$$

which is a first order differential equation. The integration factor is:

$$F(\varphi) = \exp\left(\int \frac{2}{\mathrm{tg}x}\mathrm{d}x\right) = \exp\left(\int \frac{2\cos x}{\sin x}\mathrm{d}x\right) = \exp(2\ln(\sin\varphi)) = \sin^2\varphi, \quad (8.10)$$

Taking into account the ingration factor given by Equation 8.10, the solution of Equation 8.9 is given by

$$h = -\frac{1}{F(\varphi)}\int F(x)\frac{2K_1}{\sin x}\mathrm{d}x = -\frac{2K_1}{\sin^2\varphi}\int \sin x\mathrm{d}x = -\frac{2K_1}{\sin^2\varphi}(-\cos\varphi + C). \quad (8.11)$$

As a result, the expression of the field lines, considering the previous change of variable, $h = r^2$, is the following:

$$r(\varphi) = \sqrt{h} = \sqrt{\frac{-q}{2\pi\epsilon E_{ext}}}\frac{\sqrt{C - \cos\varphi}}{\sin\varphi}. \quad (8.12)$$

Equation 8.12 defines the field lines parametrised with the value C. Considering an external electric field of 1 kV/cm, the value of the scale factor $\sqrt{-q/2\pi\epsilon E_{ext}}$ is 0.14 μm. Depending on the value of the parameter C, we distinguish three different cases:

1. If $C > 1$, $r(\varphi)$ is defined in the whole interval $(0,\pi)$ of φ. Since $r(\varphi) \to \infty$ when φ approaches to the limits of the interval, the equation represents a line that goes from $+\infty$ to $-\infty$.
2. There is a value $\varphi_0 \in (0, \pi)$ such that for every $\varphi < \varphi_0$, $r(\varphi)$ is not defined. Since the value of $r(\varphi)$ for φ_0 is null, the equation represents a line from the origin to $-\infty$.
3. If $C < -1$, $r(\varphi)$ is not defined.

The flux tube that includes all the field lines that end in the ion is defined by $C = 1$. The value of the transverse section of the flux tube with $C = 1$ in a point far from the ion is:

$$\pi r_y^2 = \pi r^2\sin^2\varphi = \pi\frac{-q}{2\pi\epsilon E_{ext}}(1 - \cos\varphi) \underset{\varphi\to\pi}{\simeq} \frac{-q}{E_{ext}}, \quad (8.13)$$

Figure 8.3 shows the field lines approaching the ion, positioned at (0,0) which has a negligible size at the micron scale. The lines correspond to different values of C and the green line corresponding to $C = 1$ is the envelope of all the field lines ending in the ion.

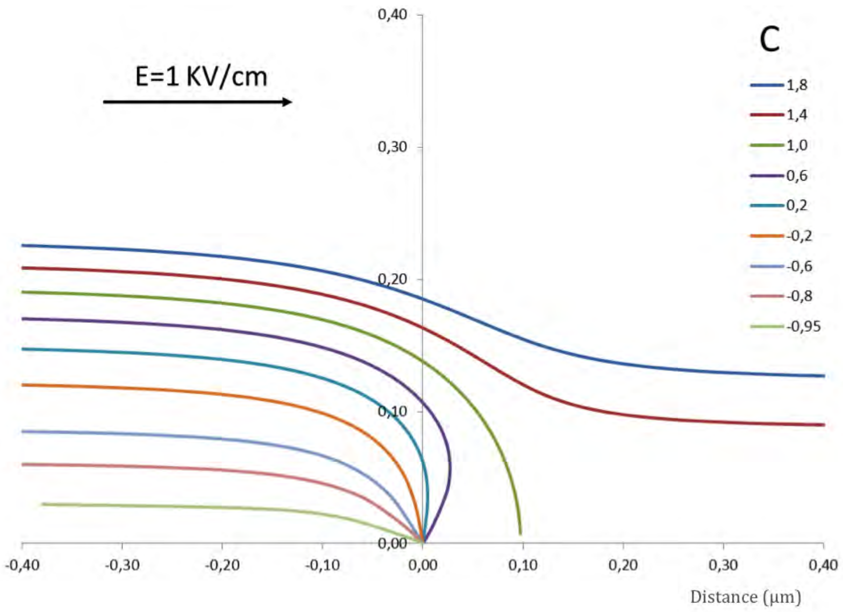

Figure 8.3: Field lines approaching the ion.

8.3 Cross section by recombination

A recombination effect, not related to the parent electron/ion recombination, has to be considered between the primary electrons produced by particle interactions in liquid and the positive charge current from the anode. This effect can cause a significant signal loss that could mimic the electron quenching produced by the electronegative impurities in the active volume.

In order to evaluate the probability of the quenching of the charge signal by recombination, we define the cross section S_{CS} as the transverse area whose field lines end on the ion. This section is the one defined in 8.2 for a negative charge.

The total number of field lines emerging from the ion, q/ϵ, is equal to the number of lines traversing the cross section, $E_d \cdot S_{CS}$, therefore:

$$S_{CS} = \frac{q}{E_d}, \tag{8.14}$$

where q is the elementary positive charge, the absolute permittivity of liquid argon and E_d the magnitude of the drift field. For a typical E_d value of 1 kV/cm, $S_{CS} = 1.2 \ 10^{-7}$ cm^2 is much larger than the ion dimensions. The cross section of individual ions add together, thus the overall S_{CS} of the ion cloud can be macroscopic and the contribution of the recombination cannot be neglected.

We define the ion and electron fluxes as follows:

$$j_i = v_i \rho_i, \qquad j_e = v_e \rho_e, \tag{8.15}$$

where ρ and v are the particle density and the particle velocity respectively, being the last one related to the drift field through the mobility coefficient μ in liquid argon:

$$v_i = \mu_i E_d, \qquad v_e = \mu_e E_d. \tag{8.16}$$

Considering a drift field of E_d =1 kV/cm, the velocity of the electrons was measured to be $v_e \approx 2$ mm/μs [116]. On the other hand, the measured ion mobility in steady state (uninfluenced by liquid motion) is $\mu_i \approx 2{\cdot}10^{-4}$ cm^2 V^{-1}s^{-1} [167]. Therefore, considering E_d ∼1 kV/cm, the expected ion velocity is $v_i \approx 2 \cdot 10^{-6}$ mm/μs, which means that the ion velocity in liquid argon is six orders of magnitude lower than that of the electrons.

The total recombination rate, r, in m^{-3}s^{-1}, is given by the density of ions multiplied by the flux of the electrons and by the cross section for recombination:

$$r = \rho_i \, j_e \, S_{CS}. \tag{8.17}$$

Substituting ρ_i, v_i and S_{CS} from Equations 8.15, 8.16 and 8.14 in Equation 8.17 we obtain:

$$r = \frac{j_i \, j_e}{v_i} \frac{q}{E_d} = j_i \, j_e \frac{q}{\mu_i \epsilon E_d^2}, \tag{8.18}$$

which allows to determine the electron signal loss in liquid. In Equation 8.18, the ion and electron fluxes, which depend on the distance l, $j_i(l), j_e(l)$, are given by the current and field equations.

8.4 Current and field equations

The interactions given by cosmic muons, environmental radioactivity and ^{39}Ar decay are constantly produced within the liquid argon bulk. All those sources are assumed to be uniformly distributed in the volume, so we introduce a constant ionisation rate, h, defined as the average number of ion-electron pairs produced per unit of time and volume.

In stationary state the variation of the density of ions and electrons in any point should be null, therefore:

$$0 = h - r - \frac{dj_i(l)}{dl}, \qquad 0 = h - r + \frac{dj_e(l)}{dl}. \tag{8.19}$$

Note that the electron current diminishes with the axial distance, l, therefore the quantity $dj_e(l)/dl$ is negative.

Replacing the rate of recombination, given by Equation 8.18, in Equation 8.19 we get:

$$\frac{dj_i(l)}{dl} + j_i(l)\, j_e(l)\, \frac{q}{\mu_i \epsilon E_d^2} = h, \qquad \frac{dj_e(l)}{dl} - j_i(l)\, j_e(l)\, \frac{q}{\mu_i \epsilon E_d^2} = -h. \tag{8.20}$$

On the other hand, the variation of the drift field, that we assumed parallel to the detector axis, is determined by the charge density:

$$-\, q\, \rho_e + q\, \rho_i = \frac{dE_d}{dl}. \tag{8.21}$$

Due to the fact that $v_e \gg v_i$, the electrons are drifted by the field while the ions remain. Consequently, $\rho_e \ll \rho_i$ and we can disregard ρ_e. Substituting the density of ions, given by Equation 8.15, in Equation 8.21 and using Equation 8.16, we have:

$$j_i(l) = \frac{v_i}{q} \frac{dE_d}{dl} = \frac{\mu_i\, E_d}{q} \frac{dE_d}{dl} = \frac{1}{2} \frac{\mu_i}{q} \frac{d(E_d^2)}{dl}. \tag{8.22}$$

Equations 8.20 and 8.22 are three coupled differential equations with three functions ($j_i(l)$, $j_e(l)$ and E_d) and one variable l. Those equations can be simplified doing the following change of function:

$$F = \frac{\mu_i}{q}\, E_d^2. \tag{8.23}$$

The 3 coupled linear equations stand:

$$\frac{dj_i(l)}{dl} + \frac{j_i(l)\, j_e(l)}{F} = h, \qquad \frac{dj_e(l)}{dl} - \frac{j_i(l)\, j_e(l)}{F} = -h, \qquad j_i(l) = \frac{1}{2} \frac{dF}{dl}. \tag{8.24}$$

The three boundary conditions required to obtain a particular solution are the following ones:

- The electron current at the cathode is null

$$j_e(L) = 0. \tag{8.25}$$

- The ion current at the anode is given by the electron current at the anode multiplied by the gain

$$j_i(0) = G_E\, j_e(0). \tag{8.26}$$

- The minimal electric drift field is set at the anode

$$E_d(0) = E_{min}. \tag{8.27}$$

The system of equations given by 8.24 can be solved numerically for any particular detector.

In order to approximate the solution of Equations 8.24, let us disregard the recombination factor of the ion current equation. This approximation is valid if the gain is high, so the ionic current is due mainly to the multiplication, or the pair production is small so the product $\rho_i \, j_e$ is very low. Recombination is disregarded for the ions but not for the electrons, so the second Equation of 8.24 still stands. Removing the recombination factor from the first Equation of 8.24:

$$\frac{d\,j_i(l)}{dl} = h \quad \rightarrow \quad j_i(l) = h\,l + j_i(0). \tag{8.28}$$

From the third Equation of 8.24 and using Equations 8.23 and 8.27 we have:

$$F = 2 \int_0^l j_i(l)\,dx = h\,l^2 + 2\,j_i(0)\,l + F_0, \qquad F_0 = F(0) = \frac{\epsilon \mu_i}{q} {E_{min}}^2. \tag{8.29}$$

The value of the drift field is:

$$E_d = \sqrt{\frac{q}{\mu_i}(h\,l^2 + 2\,j_i(0)\,l) + {E_{min}}^2}. \tag{8.30}$$

Therefore, the electron current, second Equation of 8.24, can be written as:

$$\frac{dj_e(l)}{dl} - \frac{j_e(l)\,(h\,l + j_i(0))}{h\,l^2 + 2\,j_i(0)\,l + F_0} = -h. \tag{8.31}$$

This linear differential equation can be solved analytically. Considering the boundary condition of null electron current at the cathode, given in Equation 8.25, the solution is:

$$j_e(l) = -h\,R(l)\,\ln \frac{l + j_i(0)/h + R(l)}{L + j_i(0)/h + R(L)}, \tag{8.32}$$

with

$$R(l) = \sqrt{l^2 + \frac{2\,j_i(0)}{h}\,l + \frac{F_0}{h}}. \tag{8.33}$$

The electron current at the anode can be obtained clearing numerically $j_i(0)$ from Equation 8.32.

8.5 Impact of the ion cloud on a Dark Matter liquid argon detector underground

We can evaluate the space charge effects and the electron quenching probability considering the average ionisation produced in the argon target by the ^{39}Ar decay

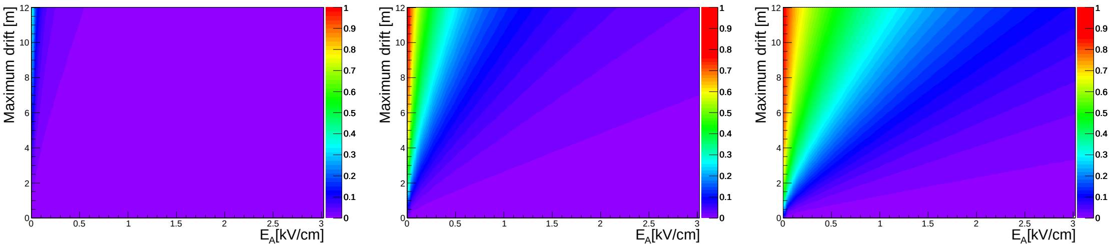

Figure 8.4: Electron-ion secondary recombination probability (colour scale) as function of drift length and field for a detector located underground in case of G_E=0 (left), G_E=20 (middle) and G_E=100 (right).

and by the cosmic muons. Other contributions given, for example, from natural radioactivity or material contamination, are considered negligible.

The quenching of the charge given by electron-ion recombination along the drift can be calculated considering the probability $P(l)$ that an electron created at depth l reaches the anode. That probability is equal to the fraction of the surface S(l) spanned by the field lines ending in the anode respect to the total area $S(0)$ and it is minimal for $l = L$ and one for $l = 0$. Since the number of anodic field lines $(E \cdot S)$ is conserved all along the detector depth, $E(0) \cdot S(0) = E(l) \cdot S(l)$, we obtain from equation 8.30:

$$P(l) = \frac{S(l)}{S(0)} = \frac{E(0)}{E(l)} = \frac{E_{min}}{\frac{q}{\epsilon\mu_i}\left(hl^2 + 2j_i(0)l\right) + E^2_{min}}, \tag{8.34}$$

whose solution can be calculated knowing the constant ionisation rate h, the field at the anode E_{min} and the effective gain G_E.

In an underground facility the dominant contribution to the charge production is typically given by the ^{39}Ar decay, a beta emitter with a Q-value of 565 keV whose activity in natural argon is ≈1 Bq/kg [95], or, for liquid argon, ≈1400 Bq/m^3. We can assume that the average energy deposited per decay in the active volume is approximately one third of the total Q-value. Considering that the accepted value for the average energy required to form an ion-electron pair in liquid argon is W= 23.6 eV [169], a ^{39}Ar decay produces in average $\approx 8 \cdot 10^3$ pairs, therefore the initial ionisation rate h_0 due to ^{39}Ar is $\approx 1.1 \cdot 10^7$ pairs/(m^{3}s). The primary recombination of the electrons with the parent ions is function of the drift field and it is usually approximated with the so-called Birks law $h = \frac{h_0}{1+k_E/E_d}$ [112], which gives the average free charge constantly produced in liquid by the ^{39}Ar decays. The constant k_E has been experimentally measured and it is equal to 0.53 ± 0.04 kV/cm [170].

Taking into account the currently proposed LAr detectors as a possible future for ArDM, the Equation 8.34 has been solved for a detector placed underground considering drift length up to 12 m and fields up to 3 kV/cm. The corresponding secondary recombination probability is plotted in Figure 8.4 as function of the drift length and field for G_E=0, G_E=20 and G_E=100. Without charge amplification the recombination is practically negligible unless very low fields ($\lesssim$ 0.3 kV/cm) and long drift distances ($\approx$ 10 m) are foreseen. At typical field of $\approx$ 1 kV/cm we can expect relatively small charge signal losses ($\leq$ 10%) for a few meters drifts and effective gains of the order of some tens, however, if G_E is of the order of 100, more than 20% of the charge recombines after 6 m drift and more than 50% after 12 m. Consequently, we can conclude that the effect is not relevant for an underground detector, unless it uses a charge amplification of several tens.

8.5.1 Case of neutrino detector placed on surface

In case the detector is located on surface, the contribution to the total ionisation produced in the detector is mainly given by muons. Their flux at sea level is reported to be 168 muons/(m^{2}s) [171]. Considering that most of the muons are at their minimum ionising energy, the energy loss in argon as function of the density is:

$$\frac{dE}{dl} \approx 1.5\,\frac{\mathrm{MeV\,cm^2}}{\mathrm{g}} \tag{8.35}$$

which gives an average deposited energy $dE/dl = 210\,\mathrm{MeV/m}$ or 35 GeV/(m^{3}s) in liquid. Assuming the same a W-value of the beta emission from the ^{39}Ar, the ion production rate is therefore: $h_0 = 1.5 \cdot 10^9$ pairs/(m^{3}s), two orders of magnitude bigger than the one from the ^{39}Ar decay.

The Equation 8.34 has been solved for a detector placed on surface considering G_E=0, G_E=5, G_E=20 and G_E=100, and the corresponding secondary recombination probability is plotted in the plots of Figure 8.5 considering, as for the underground case, drift length up to 12 m and fields up to 3 kV/cm. At typical field of $\approx$ 1 kV/cm we can expect relatively small charge signal losses ($\leq$ 10%) only for a couple of meters drifts and effective gains of the order of 5-10, however a non negligible and measurable recombination ($\approx$ 5-10%) is expected for a single phase detector (G_E=0) placed on surface with maximum drift of some meters. For $G_E \gtrsim$20 and $L \gtrsim$2 m nearly half of the charge is expected to recombine, at the same time, if G_E is of the order of 100, the largest fraction of the charge is quenched in liquid even at higher field or smaller drift distances.

8.6 Conclusions

We calculated the average electron/ion recombination probability assuming a constant ionisation rate with events uniformly distributed in the detector. The approximation is valid for an underground detector, where the ion cloud is given by a large

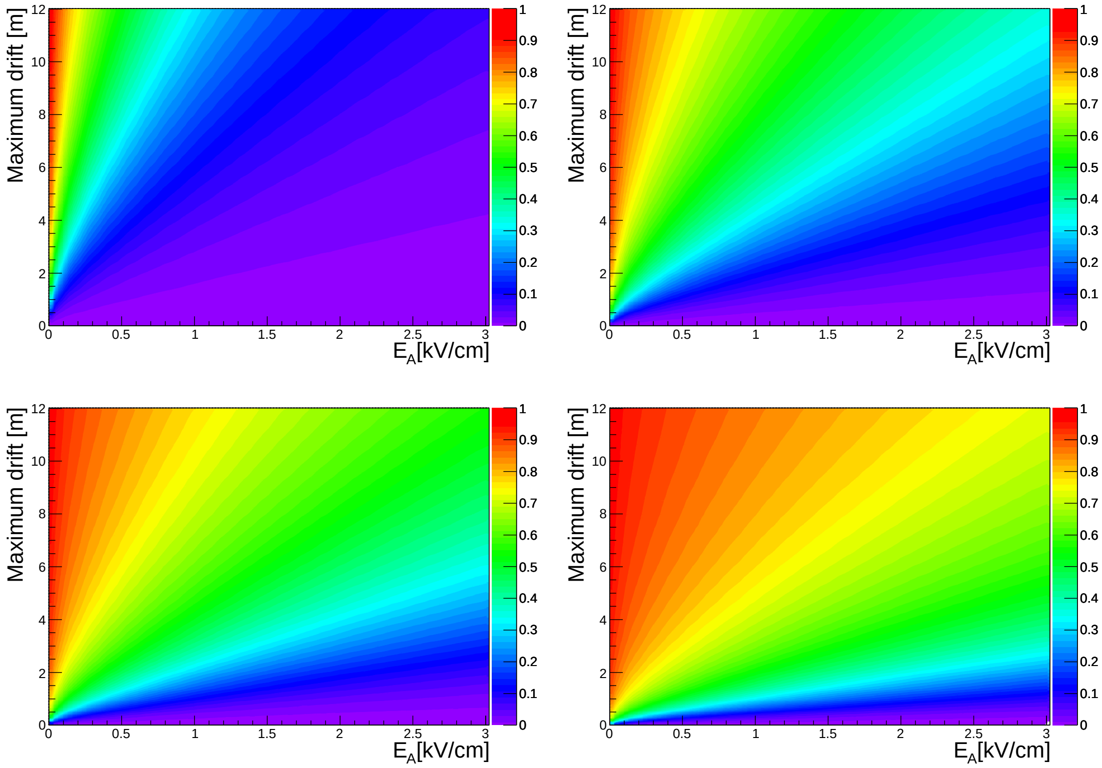

Figure 8.5: Electron-ion secondary recombination probability (colour scale) as function of drift length and field for a detector located on surface in case of G_E=0 (top-left), G_E=5 (top-right), G_E=20 (bottom-left) and G_E=100 (bottom-right).

number of ^{39}Ar decays, with overall dimensions of few μm, uniformly distributed inside the liquid argon volume. On the contrary the ionisation produced by muons is a nearly vertical track with length comparable with the maximum drift L, thus the signal quenching by electron/ion recombination, on an event by event basis, depends on the distance between the signal production and the muon ionisation tracks. Certain specific areas, characterised by high recombination probability, can be locally produced inside the active volume around the muon entry point inside.

At the same time the present discussion has been carried out considering the liquid argon volume in a steady state, although the convection motion given by the temperature gradient inside the detector and the liquid recirculation necessary to keep the required argon purity have to be considered. Given the relatively fast drift time of the electrons ($v_e \approx 2$ mm/μs [116]), their drift is not significantly affected by the liquid motion although that could be the case for the six orders of magnitude slower ions. Even if only extremely powerful recirculation flow (several tens of

m^3/hour) could produce an overall motion barely comparable with the typical drift speed of the ions, convection flows, which have been evaluated to be in the range of mm/s [172], can be comparable with the ion drift velocity and, hence, change their effective mobility.

According to the results, the study is not relevant for ArDM, since it operates underground, has a limited drift length and its current design does not include a dedicated charge amplification system. It could be relevant, in principle, for a massive Dark Matter experiment only if it operates with high gains. However, the present study seems to be extremely relevant for a neutrino detector operating on surface, such as WA105 [172], since a measurable recombination ($\approx$ 5-10%) is expected for a single phase detector (G_E=0) placed on surface with maximum drift of some meters. Considering $G_E \gtrsim 20$ and $L \gtrsim 2$ m, nearly half of the charge is expected to recombine and, at the same time, if G_E is of the order of 100, the largest fraction of the charge is quenched in liquid even at higher field or smaller drift distances.

Conclusions

ArDM took its first underground gas run at LSC in April 2013, after the delay of the construction and the start of operation of the detector, achieving the goal of detecting argon scintillation signals for the first time in the underground environment. Another data taking campaign, consisting of more than five months of single gas phase operation, with continuous data taking in warm (room temperature) and then cold (LAr temperature) argon gas, started around the end of May 2014. During these tests I studied the stability of the DAQ and the PMTs, the performance of the LAr recirculation system, the energy dependence of the light yield and the uniformity of the light collection. In addition, these gas tests have provided a first glimpse on the background, that has helped to understand the possible underground sources of gamma radiation.

Afterwards, ArDM transitioned to single-phase pure LAr operation mode, achieving a major milestone in February 2015, when the filling of the detector vessel with approximately 2 t of liquid argon (LAr) was finally completed. This first underground LAr run in liquid allowed to perform the wet commissioning of the detector in cryogenic conditions, representing at the same time the first step towards Dark Matter detection. Differently from gas, in which the contribution of ^{39}Ar was small ($\sim$1 Hz) due to the low mass of Ar contained inside the detector vessel, ^{39}Ar becomes the dominant electron background in liquid ($\sim$1 kHz), thus we measured its contribution to the energy spectrum. The main goal of these first underground runs has been completely fulfilled, demonstrating the stability of the detector operation, which ran without any safety problems during the whole period, and the successful data analysis.

During the first run of underground operation, we carried out calibrations with gamma sources, obtaining a light yield of $\sim$1 p.e./keV$_{\mathrm{ee}}$. In particular, ^{83}Kr runs have been extremely useful to perform calibrations at low energy, in the region of interest important for Dark Matter detection. At the same time, the ^{57}Co source, being outside the detector vessel, allowed to carry out fast calibrations and to monitor the runs in order to assess the detector stability during cryogenic operations. In addition, the reconstruction of the interaction position has been crucial to understand the detector response, specially considering that the Ar-TPC was not operative during the first underground run, which means that there was no information on the interaction position. I developed an Artificial Neural Network algorithm based on the S1 signal detected by the two arrays of PMTs in order to have information on the xy position. Once the TPC will be in place and operative for ArDM Run II, this algorithm could be used through the S2 signal, measured in gas by the top PMT array, to have a much more straightforward reconstruction of the xy interaction position.

Although during Run I ArDM did not reach the status for a possible Dark Matter analysis because we did not have the TPC, we have developed all the required tools for the future ArDM Run II, including an extensive investigation of the background and of the detector performances. The analysis of the screening measurements allowed us to identify the most radioactive detector components, which will be replaced for Run II.

One of the main goals of the first liquid underground run, which has been successfully fulfilled, was to measure for the first time the statistical rejection power capability at ton-scale, thus allowing to assess the potential of the experiment. These results, obtained with ^{252}Cf data, are particularly important to evaluate the expected sensitivity for the ArDM experiment. I calculated the sensitivity with the tools developed in the present Thesis, showing the possibility for ArDM to set the most competitive Dark Matter limit in the world with an argon detector within a few weeks of data taking.

In addition, we investigated, in collaboration with the Nuclear Innovation Unit from CIEMAT, a possible way to measure the neutron flux in the energy range of interest for ArDM (1-10 MeV) to evaluate the contribution of environmental neutrons. In order to do that, a BC501A liquid scintillator detector, foreseen for fast neutron spectroscopy (few keV to 20 MeV), was installed underground in Hall A, near the ArDM detector, and has been taking data for more than one year. Due to the discrepancies found with previous measurements of the neutron flux, the setup was introduced inside a polyethylene shield in order to evaluate the internal radioactive contamination and the BC501A capsule was screened. The main goal of the future analysis is therefore to evaluate if the difference in the rate, spectrum and in the signals extracted in the neutron region inside and outside the shield is statistically significant. For this reason, the detector keeps taking data, since it is necessary to have comparable statistics inside and outside the shield.

Finally, I developed specific tools to study the dynamic of the positive charge in liquid argon. According to the results, the study has not a big impact for ArDM, since it operates underground, has a limited drift length and its current design does not include a dedicated charge amplification system. It could be relevant for a massive Dark Matter experiment only if it operates with high gains. At the same time, the study seems to be extremely important for a neutrino detector operating on surface, such as WA105, since a measurable recombination ($\sim$5-10%) is expected for a single phase detector placed on surface with maximum drift of some meters.

This Thesis has been financed by the Ministry of Economy and Competitiveness through the FPA2012-30811 support. Several papers including the main results from the analysis presented in this Thesis are under preparation [2]. In addition, results regarding the event position reconstruction have been accepted for publication in HAIS (LNAI 9648) 2016.

Appendix A

Raconv

```
// USAGE:
// raconv [number] [unit] [nuclide] [density]
// compile with g++ raconv2.C -o raconv

#include <stdio.h>
#include <stdlib.h>
#include <math.h>
#include <iostream>
#include <string>
#include <vector>

using namespace std;
///////////////////// CONSTANTS ///////////////////////////////
//const float ver=2.1;       // chain and new elements added
//const float ver=2.2;       // Ci option added
//const float ver=2.3;       // mBq/kg option added - df
                             // density factor added as
                             // hidden input argv[4]
const float ver=2.4;         // stdlib not inclided (fixed)
const int   MaxEl=45;        // Max nuclide number
const int   dbg=0;           // debugging (0,1)
///////////////////////////////////////////////////////////////

const double N=6.02214179e23; // Avogadro number
const float sy=31556926.;     // seconds in a y
const float dy=365.242;       // days in a year
const float g=9.80665;        // gravity acc
```

```
const float uci=0.000027027;  // Bq -> uCi conversion
///////////////////////////////////////////////////////////////


const double amhl[2*MaxEl]={
///////////////// DEFINITIONS //////////////////////
 39.9640       ,  1.277e9  ,  // atomic mass and  half life(y) for 40K
 59.9338       ,  5.2714   ,  // atomic mass and  half life(y) for 60Co
 56.9362       ,  271.79   ,  // atomic mass and  half life(y) for 57Co
 136.907       ,  30.07    ,  // atomic mass and  half life(y) for 137Cs
 241.0568      ,  432.2    ,  // atomic mass and  half life(y) for 241Am
/////////////////////////////////////////////////////////
 232.0380553   ,  1.405e10    , // atomic mass and  half life(y) for 232Th
 228.03107     ,  5.75        , // atomic mass and  half life(y) for 228Ra
 228.03102     ,  0.000702055 , // atomic mass and  half life(y) for 228Ac
 228.02874     ,  1.9116      , // atomic mass and  half life(y) for 228Th
 224.020      ,  0.010027397 , // atomic mass and  half life(y) for 224Ra
 220.011      ,0.000001763 , // atomic mass and  half life(y) for 220Rn
 216.001915    ,4.5979e-9   , // atomic mass and  half life(y) for 216Po
 211.991897    ,0.001214612 , // atomic mass and  half life(y) for 212Pb
 211.991285    ,0.000115205 , // atomic mass and  half life(y) for 212Bi
 207.982018    ,5.8086e-06  , // atomic mass and  half life(y) for 208Tl
 211.988867    ,  9.4812e-15  , // atomic mass and  half life(y) for 212Po
//////////////////////////////////////////////////////////
 238.050788    ,  4.468e9     , // atomic mass and  half life(y) for 238U
 234.048420    ,  0.06598361  , // atomic mass and  half life(y) for 234Th
 234.043601    ,  2.234058e-6 , // atomic mass and  half life(y) for 234Pa
 234.040952    ,  2.45e5      , // atomic mass and  half life(y) for 234U
 230.033133    ,  7.538e4     , // atomic mass and  half life(y) for 230Th
 226.025409    ,  1600.       , // atomic mass and  half life(y) for 226Ra
 222.017577    ,  0.0104683961, // atomic mass and  half life(y) for 222Rn
 218.008973    ,  5.79904e-6  , // atomic mass and  half life(y) for 218Po
 218.008694    ,  6.3378e-8   , // atomic mass and  half life(y) for 218At
 213.999805    ,  5.09555e-5  , // atomic mass and  half life(y) for 214Pb
 213.998711    ,  3.78364e-5  , // atomic mass and  half life(y) for 214Bi
 209.990073    ,  2.4717e-6   , // atomic mass and  half life(y) for 210Tl
 213.995201    ,  5.206464e-12, // atomic mass and  half life(y) for 214Po
 209.984188    ,  22.3        , // atomic mass and  half life(y) for 210Pb
 209.984120    ,  0.013725139 , // atomic mass and  half life(y) for 210Bi
 209.982873    ,  0.37892664  , // atomic mass and  half life(y) for 210Po
//////////////////////////////////////////////////////////////////////////
```

```
 235.0439299   ,  7.038e+8    , // atomic mass and  half life(y) for 235U
 231.0363043   ,  0.00291131  , // atomic mass and  half life(y) for 231Th
 231.0358840   ,  32760       , // atomic mass and  half life(y) for 231Pa
 227.0277521   ,  21.773      , // atomic mass and  half life(y) for 227Ac
 223.0197359   ,  5.28569e-5  , // atomic mass and  half life(y) for 223Fr
 227.0277041   ,  0.051253661 , // atomic mass and  half life(y) for 227Th
 223.0185022   ,  0.0313079924, // atomic mass and  half life(y) for 223Ra
 219.0094802   ,  1.254875e-7 , // atomic mass and  half life(y) for 219Rn
 214.9994200   ,  5.643768e-11, // atomic mass and  half life(y) for 215Po
 210.9887370   ,  6.86379e-5  , // atomic mass and  half life(y) for 211Pb
 210.987269    ,  4.06884e-6  , // atomic mass and  half life(y) for 211Bi
 210.9866532   ,  1.6351403e-8, // atomic mass and  half life(y) for 211Po
 206.977419    ,  9.06932e-6    // atomic mass and  half life(y) for 207Tl
};


int getnuclID (string snucl, int& chain){// get nuclide raconv id number from name
int nucl=100*MaxEl;
if(snucl=="40K")   nucl=0;
if(snucl=="60Co")  nucl=1;
if(snucl=="57Co")  nucl=2;
if(snucl=="137Cs") nucl=3;
if(snucl=="241Am") nucl=4;
if(snucl=="232Th") nucl=5;
if(snucl=="232Thc"){nucl=5;chain=15;}
if(snucl=="228Ra") nucl=6;
if(snucl=="228Ac") nucl=7;
if(snucl=="228Th") nucl=8;
if(snucl=="224Ra") nucl=9;
if(snucl=="220Rn") nucl=10;
if(snucl=="216Po") nucl=11;
if(snucl=="212Pb") nucl=12;
if(snucl=="212Bi") nucl=13;
if(snucl=="208Tl") nucl=14;
if(snucl=="212Po") nucl=15;
if(snucl=="238U")  nucl=16;
if(snucl=="238Uc") {nucl=16;chain=31;}
if(snucl=="234Th") nucl=17;
if(snucl=="234Pa") nucl=18;
if(snucl=="234U")  nucl=19;
if(snucl=="230Th") nucl=20;
```

```
if(snucl=="226Ra") nucl=21;
if(snucl=="222Rn") nucl=22;
if(snucl=="218Po") nucl=23;
if(snucl=="218At") nucl=24;
if(snucl=="214Pb") nucl=25;
if(snucl=="214Bi") nucl=26;
if(snucl=="210Tl") nucl=27;
if(snucl=="214Po") nucl=28;
if(snucl=="210Pb") nucl=29;
if(snucl=="210Bi") nucl=30;
if(snucl=="210Po") nucl=31;
if(snucl=="235U") nucl=32;
if(snucl=="235Uc") {nucl=32;chain=44;}
if(snucl=="231Th") nucl=33;
if(snucl=="231Pa") nucl=34;
if(snucl=="227Ac") nucl=35;
if(snucl=="223Fr") nucl=36;
if(snucl=="227Th") nucl=37;
if(snucl=="223Ra") nucl=38;
if(snucl=="219Rn") nucl=39;
if(snucl=="215Po") nucl=40;
if(snucl=="211Pb") nucl=41;
if(snucl=="211Bi") nucl=42;
if(snucl=="211Po") nucl=43;
if(snucl=="207Tl") nucl=44;

return nucl;
}

double getfrac (int nucl, double& frac){
// fraction for elemetns in U and Th chain
frac =1.;
double frapp=amhl[2*nucl+1]/amhl[2*(nucl-1)+1];
        //   208Tl
if(nucl==14){frac=0.3594;}
         //  212Po
if(nucl==15){frac=0.6406;frapp=amhl[2*nucl+1]/amhl[2*(nucl-2)+1];}
        //  218At
if(nucl==24){frac=0.00018;}
        //  214Pb
if(nucl==25){frac=0.99982;frapp=amhl[2*nucl+1]/amhl[2*(nucl-2)+1];}
```

```
        //  210Tl
if(nucl==27){frac=0.00021;}
        //  214Po
        if(nucl==28){frac=0.99979;frapp=amhl[2*nucl+1]/amhl[2*(nucl-2)+1];}
        //  223Fr
        if(nucl==36){frac=0.0138;}
        //  227Th
        if(nucl==37){frac=0.9862;frapp=amhl[2*nucl+1]/amhl[2*(nucl-2)+1];}
        //  211Po
        if(nucl==43){frac=0.0032;}
        //  207Tl
        if(nucl==44){frac=0.9968;frapp=amhl[2*nucl+1]/amhl[2*(nucl-2)+1];}

return frapp;
}

string getnucl (int nucl){                  // get nuclide name from ID
string snucl;
if(nucl==0)  snucl="40K"     ;
if(nucl==1)  snucl="60Co"    ;
if(nucl==2)  snucl="57Co"    ;
if(nucl==3)  snucl="137Cs"   ;
if(nucl==4)  snucl="241Am"   ;
if(nucl==5)  snucl="232Th"   ;     // 232Th chain
if(nucl==6)  snucl="228Ra"   ;
if(nucl==7)  snucl="228Ac"   ;
if(nucl==8)  snucl="228Th"   ;
if(nucl==9)  snucl="224Ra"   ;
if(nucl==10) snucl="220Rn"   ;
if(nucl==11) snucl="216Po"   ;
if(nucl==12) snucl="212Pb"   ;
if(nucl==13) snucl="212Bi"   ;
if(nucl==14) snucl="208Tl"   ;
if(nucl==15) snucl="212Po"   ;
if(nucl==16) snucl="238U"    ;     // 238U chain
if(nucl==17) snucl="234Th"   ;
if(nucl==18) snucl="234Pa"   ;
if(nucl==19) snucl="234U"    ;
if(nucl==20) snucl="230Th"   ;
if(nucl==21) snucl="226Ra"   ;
if(nucl==22) snucl="222Rn"   ;
```

```
if(nucl==23) snucl="218Po"   ;
if(nucl==24) snucl="218At"   ;
if(nucl==25) snucl="214Pb"   ;
if(nucl==26) snucl="214Bi"   ;
if(nucl==27) snucl="210Tl"   ;
if(nucl==28) snucl="214Po"   ;
if(nucl==29) snucl="210Pb"   ;
if(nucl==30) snucl="210Bi"   ;
if(nucl==31) snucl="210Po"   ;
if(nucl==32) snucl="235U"    ;      // 235U chain
if(nucl==33) snucl="231Th"   ;
if(nucl==34) snucl="231Pa"   ;
if(nucl==35) snucl="227Ac"   ;
if(nucl==36) snucl="223Fr"   ;
if(nucl==37) snucl="227Th"   ;
if(nucl==38) snucl="223Ra"   ;
if(nucl==39) snucl="219Rn"   ;
if(nucl==40) snucl="215Po"   ;
if(nucl==41) snucl="211Pb"   ;
if(nucl==42) snucl="211Bi"   ;
if(nucl==43) snucl="211Po"   ;
if(nucl==44) snucl="207Tl"   ;

return snucl;
}

int getalpha (int nucl){
   int alpha=0;
   if(nucl==5 || nucl==8 || nucl==9 || nucl==10 || nucl==11 || nucl==12
     || nucl==13 || nucl==15 || nucl==16 || nucl==19 || nucl==20
     || nucl==21 || nucl==22 || nucl==23 || nucl==24 || nucl==26
     || nucl==28 || nucl==31 || nucl==32 || nucl==34 || nucl==35
     || nucl==37 || nucl==38 || nucl==39 || nucl==40 || nucl==42
     || nucl==43) alpha=1;

   return alpha;
}


vector<double> getfrom_g(double vinp, double vnm, double vdt){
// get results from mass input
```

```
vector<double> vres(4,0);
double dcost=log(2)/vdt;   // decay constant;
  vres[0]=vinp;               // mass
vres[1]=vres[0]*N/vnm;       // number of Atoms
vres[2]=dcost*vres[1]/sy;    // activity in Bq
vres[3]=dcost;              // decay constant

return vres;
}

vector<double> getfrom_nb(double vinp, double vnm, double vdt){
// get results from number of atoms
vector<double> vres(4,0);
double dcost=log(2)/vdt;    // decay constant;
  vres[1]=vinp;                // number of Atoms
vres[2]=dcost*vres[1]/sy;     // activity in Bq
vres[0]=vres[1]*vnm/N;        // mass
vres[3]=dcost;               // decay constant

return vres;
}

vector<double> getfrom_Bq(double vinp, double vnm, double vdt){
// get results from absolute activity
vector<double> vres(4,0);
double dcost=log(2)/vdt;   // decay constant;
  vres[2]=vinp;               // activity in Bq
  vres[1]=vres[2]/dcost*sy;    // number of Atoms
  vres[0]=vres[1]*vnm/N;       // mass
  vres[3]=dcost;              // decay constant

return vres;
}

vector<double> getfrom_ppb(double vinp, double vnm, double vdt){
// get results from contamination
vector<double> vres(4,0);
double dcost=log(2)/vdt;   // decay constant;
  vres[0]=vinp*1e-9;          // mass of contaminants in 1 g of material
  vres[1]=vres[0]*N/vnm;       // number of Atoms
  vres[2]=dcost*vres[1]/sy;    // activity in Bq
```

```
  vres[3]=dcost;              // decay constant

return vres;
}

string blankrem (string sin){
// edge blank spaces removed from the input string
int l1,l2,len;
l1=sin.find_first_not_of(" ");
  l2=sin.find_last_not_of(" ");
  len=l2-l1;
  sin=sin.substr(l1,len+1);

  return sin;
}

double getact (string sin, int& dim){
// get input number & number of digit
int len;
char in1[20];
double nbinp=0;
  dim=sin.find_first_of(" ");
  len=sin.copy(in1,dim,0);
  in1[len]='\0';                  // activity (char)
  nbinp = atof ( in1 );           // input nb

  return nbinp;
}

string getinput (string sin){    // get activity unit or nuclide
int l3,len;
char in2[20];
string sinput;
l3=sin.find_first_of(" ");
  len=sin.copy(in2,l3,0);
  in2[len]='\0';                 //  (char)
  len=sin.length();
  sinput=sin.substr(0,l3);       //  (string)

return sinput;
}
```

```
//////////////////////////////////////////////////
////////////////   MAIN  /////////////////////////
//////////////////////////////////////////////////

int main(int argc, char *argv[])

{

int dim=0;
string srin,sin,sunit,snucl;             // string inputs
double nm,actnb,NAT[MaxEl],NAC[MaxEl],NMASS[MaxEl],dt,dcost;
double df=1.;      // density factor for SOURCES
for(int i=0;i<MaxEl;i++){NAT[i]=0;NAC[i]=0;NMASS[i]=0;}
int chain=100*MaxEl;
double frac=1,frapp=1;
double scmass=1.;
float n232thC[11],d232thC[11];
vector<double> vres(4,0);


cout << endl<< endl<<  "\e[1;33m---------------------------" << endl;
cout << " Welcome to RACONV the activity conversions programs V. " <<ver<<endl;
cout << "   (by RS & BM, CIEMAT 2010-2012)" << endl;
cout << "  -------------------------------" << endl;
cout << "  Write number, units and Nuclide  "<< endl;
cout << "  (m and k multiple allowed) " << endl;
cout << "    UNITS                    NUCLIDE "<< endl;
cout << "Ab. activity | Contamination  Primordial | Non primordial" << endl;
cout << "Bq, Ci, g ,   ppb, g/g     232Th,238U,40K  60Co,57Co,137Cs, "<< endl;
cout << " N             mBq/kg         Chain:232Thc,238Uc   241Am" << endl;
cout << "------------------------------------------------------\e[0m" << endl;
cout << "                          " << endl;
top:
cout<<"(Es: - ’200 mBq 232Th’ - or - ’100 g 238U’ - or ’1000 N 60Co’)"<<endl;
cout << ">" ;

if(dbg==1 && argc>0){
cout << argc;
for(int i=0;i<argc;i++) cout << " " << argv[i] ;
```

```
cout << endl;
}
if(argc<4 || sin.length()>0)    getline(cin,srin);
if(argc>=4 && sin.length()==0) {
srin.append(argv[1]);
srin.append(" ");
srin.append(argv[2]);
srin.append(" ");
srin.append(argv[3]);
cout << srin << endl;
}
sin = srin;

///////////////////////////////////////////
if(sin=="q" || sin=="Q") exit(0);
if(sin.length()<6){
    cout <<  "Error (0): input not valid!" << endl;
    goto top;
}
sin=blankrem(sin);
if(dbg==1)cout << "sin :"<< sin << endl;
///////////////////////////////////////////
actnb=getact(sin,dim);
if(actnb==0){cout <<  "Error (1): number not valid!" << endl;  goto top;}
sin=sin.substr(dim,sin.length());
sin=blankrem(sin);
if(dbg==1)cout<<"activity :"<<actnb<<"  dim :"<<dim<<"  sin :"<<sin<<endl;
///////////////////////////////////////////
sunit=getinput(sin);
if(sunit.length()==0){cout << "Error (2): write unit!" << endl; goto top;}
if(sunit!="Bq" && sunit!="mBq" && sunit!="kBq" &&
 sunit!="g"  && sunit!="mg" && sunit!="kg" &&
 sunit!="ppb" && sunit!="ppm" &&
 sunit!="g/g" && sunit!="N" && sunit!="Ci" &&
         sunit!="uCi" && sunit!="mCi" && sunit!="pCi" &&
         sunit!="mBq/kg") {
               cout <<  "Error (3): unit not valid!" << endl;
               goto top;
         }
sin=sin.substr(sunit.length(),sin.length());
sin=blankrem(sin);
```

```
if(dbg==1)cout << "sunit :" << sunit << "   sin :"<< sin << endl;
//////////////////////////////////////////
snucl=getinput(sin);
if(snucl.length()==0){cout <<  "Error (4): insert nuclide!" << endl;
                      goto top;}
int nucl=getnuclID(snucl,chain);
if(nucl>MaxEl){cout << "Error (5): nuclide not valid!" << endl;
               goto top;}
if(dbg==1)cout << "snucl :" << snucl << "   sin :"<< sin << endl;
//////////////////////////////////////////



cout << endl << "-------------------------------" << endl;
cout << " Your input : ’\e[1;33m" << srin << "\e[0m’"<<  endl;
cout << " Value : " <<  actnb << ""<<  endl;
cout << " Units : " <<  sunit << ""<< endl;
cout << " Nuclide : " <<  snucl << ""<< endl;
if(argc>4){df=atof(argv[4]);cout << " Density factor : " <<  df << endl;}
cout <<  "-------------------------------" << endl;

if(chain== 100*MaxEl)cout << " Chain calculation : No" << endl ;
if(chain<100*MaxEl)cout<<" Chain calculation : Yes -> Equilibrium assumed!"<<endl;
if(sunit=="ppb" || sunit=="ppm" || sunit=="g/g" || sunit=="mBq/kg"   ){
cout <<  " \033[4;36m->WARNING contamination introduced
                           (ppb, ppm, g/g or mBq/kg):" << endl;
cout <<  " ->Absolute activity are per g of screened
                           material!\e[0m" << endl; }

if(sunit=="mBq/kg"){actnb=actnb/1e6;sunit="Bq";scmass=1000.;}
if(sunit=="kg"){actnb=actnb*1000.;sunit="g";}
if(sunit=="mg"){actnb=actnb/1000.;sunit="g";}
if(sunit=="Ci"){actnb=actnb*1e6;sunit="uCi";}
if(sunit=="mCi"){actnb=actnb*1e3;sunit="uCi";}
if(sunit=="uCi"){actnb=actnb*1/uci;sunit="Bq";}
if(sunit=="pCi"){actnb=actnb*1e-3/uci;sunit="Bq";}
if(sunit=="kBq"){actnb=actnb*1000.;sunit="Bq";}
if(sunit=="mBq"){actnb=actnb/1000.;sunit="Bq";}
if(sunit=="g/g"){actnb=actnb*1e9;sunit="ppb";}
if(sunit=="ppm"){actnb=actnb*1000.;sunit="ppb";}
```

```
while(1){
  nm=amhl[2*nucl];
  dt=amhl[2*nucl+1];
  if(sunit=="g") vres=getfrom_g(actnb,nm,dt);
    if(sunit=="N") vres=getfrom_nb(actnb,nm,dt);
    if(sunit=="Bq") vres=getfrom_Bq(actnb,nm,dt);
    if(sunit=="ppb") vres=getfrom_ppb(actnb,nm,dt);
    NMASS[nucl]=vres[0]; NAT[nucl]=vres[1];
    NAC[nucl]=vres[2]; dcost=vres[3];

    cout << "  -------------------------------" << endl;
    cout << "  ---------- RESULTS ------------" << endl;
    cout << "  -------------------------------" << endl;
    cout << "  |  \e[1;31mNuclide : "  << snucl <<"\e[0m \t   |"<<endl;
    cout << "  |  Raconv ID : " << nucl << "             |" <<endl;
    cout << "  |  Fraction : " << fixed << frac*100 << " %\t   |"
         << scientific <<endl;
    cout << "-----------------------------------------" << endl;
    cout << " Nb. Atoms : " << NAT[nucl]*df << "" << endl;
    cout << " Mass number : " << fixed << nm << " "
         << scientific <<endl;
    cout << " Mass     : " <<  NMASS[nucl] << " g["
         << snucl<< "]" <<  endl;
    cout << " Nb. of moles: " << NAT[nucl]/N << endl;
    //cout << " Weight     : " <<  NMASS[nucl]*g << " g" <<  endl;
    cout << " Half life : " << dt << " y  (" << dt*dy << " days)" <<endl;
    cout << " Mean lifetime : " << dt/log(2) << " y" << endl;
    cout << " Decay constant : " << dcost << " 1/y "
         <<  "  (" << dcost/sy << " 1/s)" << endl;
    cout <<  scientific << " Specific activity : "
         <<  NAC[nucl]/NMASS[nucl] << " Bq/g[" << snucl<< "]"
         <<  "  (" << NAC[nucl]*uci/NMASS[nucl] << " uCu/g["
         << snucl<< "])" << endl;
    cout <<    "------------------------------------------------" << endl;
    cout <<  "  ABSOLUTE ACTIVITY:\e[0m" << endl;
    cout << " Activity : " <<  NAC[nucl]*1000. << " mBq" <<  "  ("
         << NAC[nucl]*uci*1e3 << " nCu)" << endl;
    cout << " Activity : " <<  NAC[nucl] << " Bq"<<  "  ("
         << NAC[nucl]*uci << " uCi)" << endl;
    cout << " Activity : " <<  NAC[nucl]/1000. << " kBq"
         <<  "  (" << NAC[nucl]*uci/1000. << " mCu)" << endl;
```

```
cout <<  "------------------------------------------------" << endl;
cout <<  "CONTAMINATION if activity is per g of the sample:\e[0m" << endl;
cout << " Contamination (/g)  : " <<  NMASS[nucl]
     << " g[" << snucl<< "]/g" <<  endl;
cout << " Contamination (/g)  : " <<  NMASS[nucl]*1e9
     << " ppb  (" <<  NMASS[nucl]*1e6 << " ppm)" <<endl;
cout << scientific << " Contamination (/g)  : "
     <<  NAC[nucl] << " Bq/g   (" << NAC[nucl]*uci
     << "  uCi/g)" <<  endl;
cout << scientific << " Contamination (/g)  : "
     <<  NAC[nucl]*1e6 << " mBq/kg   (" << NAC[nucl]*uci*1e9
     << "  pCi/kg)" <<  endl;
if(sunit!="ppb" && scmass==1 && chain==100*MaxEl) cout
   <<  "CONTAMINATION if activity is per kg of the sample:" << endl;

if(sunit!="ppb" && scmass==1 && chain==100*MaxEl)cout
    << " Contamination (/kg) : " <<  NMASS[nucl]*1e-3
    << " g[" << snucl<< "]/g" <<  endl;
if(sunit!="ppb" && scmass==1 && chain==100*MaxEl)cout
<< " Contamination (/kg) : " <<  NMASS[nucl]*1e-3*1e9
<< " ppb   (" <<  NMASS[nucl]*1e3 << " ppm)" <<endl;
if(sunit!="ppb" && scmass==1 && chain==100*MaxEl)cout
<< scientific << " Contamination (/kg) : " <<  NAC[nucl]/1000.
<< " Bq/g   (" << NAC[nucl]/1000.*uci << "  uCu/g)" <<  endl;
if(sunit!="ppb" && scmass==1 && chain==100*MaxEl)cout
<< scientific << " Contamination (/kg) : " <<  NAC[nucl]*1e3
<< " mBq/kg   (" << NAC[nucl]*1e6*uci << "  pCi/kg)" <<  endl;
cout <<"------------------------------------------------" << endl;
if(chain==100*MaxEl) break;
if(nucl==chain) break;
cout << "Ret (q to quit) : " ;
char c=getchar();
if(c=='q' || c=='Q') break;

nucl++;
snucl=getnucl(nucl);
if(sunit!="N")sunit="N" ;
frapp=getfrac(nucl,frac);
if(nucl!=15 && nucl!=25 && nucl!=28 && nucl!=37
   && nucl!=44)actnb=NAT[nucl-1]*frac*frapp;
else actnb=NAT[nucl-2]*frac*frapp;
```

```
    if(snucl=="214Bi" || snucl=="210Pb"
      || snucl=="223Ra" )  {
          actnb=actnb+NAT[nucl-2]*amhl[2*(nucl)+1]/amhl[2*(nucl-2)+1];
    }
}

cout << endl << "-------------- Summary -------------------" << endl;
cout <<         "-----------------------------------------" << endl;
cout <<         "            Your input : " << srin << " "<<  endl;
cout <<         "-----------------------------------------" << endl;
cout << "ID NUCL    Nb. Atoms     Ac[Bq]      Mass[g]  " << endl;
 for(int i=0;i<MaxEl;i++){
  int alpha=getalpha(i);
  if(alpha!=0)cout << "\e[1;36m";
if(NAT[i]!=0)cout << i << " " << getnucl(i)
                                  << "  " << NAT[i]*df << " "
                                  << NAC[i] << " " << NMASS[i]
                                  << "\e[0m " << endl;
}
cout << " -----------------------------------------" << endl;


return 0;




}
```

Bibliography

[1] R. Adam *et al.* [Planck Collaboration], "Planck 2015 results. I. Overview of products and scientific results," arXiv:1502.01582 [astro-ph.CO]. Accepted for publication by Astronomy & Astrophysics (A&A), 2016.

[2] J. Calvo *et al.* [ArDM Collaboration], "Status of ArDM-1t: First observations from operation with a full ton-scale liquid argon target," arXiv:1505.02443 [physics.ins-det].

[3] J. A. Peacock, "Cosmological Physics," Cambridge University Press (1999). ISBN: 9780521422703.

[4] K. C. Freeman, "On the disks of spiral and SO Galaxies," Astrophys. J. **160** (1970) 811.

[5] K. G. Begeman, A. H. Broeils and R. H. Sanders, "Extended rotation curves of spiral galaxies: Dark haloes and modified dynamics," Mon. Not. Roy. Astron. Soc. **249** (1991) 523.

[6] E. Corbelli and P. Salucci, "The Extended Rotation Curve and the Dark Matter Halo of M33," Mon. Not. Roy. Astron. Soc. **311** (2000) 441 [astro-ph/9909252].

[7] V. Sahni, "Dark Matter and Dark Energy," Lect. Notes Phys. **653** (2004) 141 [astro-ph/0403324].

[8] J. Bovy and S. Tremaine, "On the local Dark Matter density," Astrophys. J. **756** (2012) 89 [arXiv:1205.4033 [astro-ph.GA]].

[9] P. Coles and F. Lucchin, "Cosmology. The Origin and Evolution of Cosmic Structure," Wiley (2002). ISBN: 0471489093.

[10] P. A. R. Ade *et al.* [Planck Collaboration], "Planck 2015 results. XIII. Cosmological parameters," arXiv:1502.01589 [astro-ph.CO]. Submitted to Astronomy & Astrophysics (A&A), 2015.

[11] http://www.nasa.gov/mission_pages/hubble/science/strong-lensing.html

[12] http://www.nasa.gov/mission_pages/hubble/science/dark-matter-survey.html

[13] http://chandra.harvard.edu/photo/2006/1e0657/

[14] D. Harvey, R. Massey, T. Kitching, A. Taylor and E. Tittley, "The non-gravitational interactions of Dark Matter in colliding galaxy clusters," Science **347** (2015) 6229, 1462 [arXiv:1503.07675 [astro-ph.CO]].

[15] G. Gamow, "The Evolution of the Universe," Nature 162: 680-682 (1948).

[16] A. A. Penzias and R. W. Wilson, "A Measurement of excess antenna temperature at 4080-Mc/s," Astrophys. J. **142** (1965) 419.

[17] J. Tauber *et al.* [Planck Collaboration], "The Scientific programme of Planck," ESA-SCI(2005)1, astro-ph/0604069.

[18] G. Bertone, D. Hooper and J. Silk, "Particle Dark Matter: Evidence, candidates and constraints," Phys. Rept. **405** (2005) 279 [hep-ph/0404175].

[19] E. W. Kolb and M. S. Turner, "The Early Universe," Addison-Wesley, Redwood City, 1989. ISBN: 0201626748.

[20] D. Tytler, J. M. O'Meara, N. Suzuki and D. Lubin, "Review of Big Bang nucleosynthesis and primordial abundances," Phys. Scripta T **85** (2000) 12 [astro-ph/0001318].

[21] B. D. Fields, P. Molaro and S. Sarkar, "Big-Bang Nucleosynthesis," Chin. Phys. C **38** (2014) [arXiv:1412.1408 [astro-ph.CO]].

[22] K. Griest and M. Kamionkowski, "Supersymmetric Dark Matter," Phys. Rept. **333-334** (2000) 167-182.

[23] P. Gondolo, "Non-baryonic Dark Matter," NATO Sci. Ser. II **187** (2005) 279 [astro-ph/0403064].

[24] http://cosmicweb.uchicago.edu/index.html

[25] J. Hamann *et al.* "Sterile neutrino constraints from cosmology," Journal of Physics: Conference Series, 375, 3, 032003 (2012).

[26] L. Bergstrom, "Dark Matter Candidates," New J. Phys. **11** (2009) 105006 [arXiv:0903.4849 [hep-ph]].

[27] G. Rybka, A. Wagner, A. Brill, K. Ramos, R. Percival and K. Patel, Phys. Rev. D **91** (2015) 1, 011701 [arXiv:1403.3121 [physics.ins-det]].

[28] E. A. Baltz, “Dark Matter candidates,” eConf C **040802** (2004) L002 [astro-ph/0412170].

[29] S. P. Martin, “A Supersymmetry primer,” Adv. Ser. Direct. High Energy Phys. **21** (2010) 1 [hep-ph/9709356].

[30] J. Ellis and K. A. Olive, “Supersymmetric Dark Matter Candidates,” In *Bertone, G. (ed.): Particle Dark Matter* 142-163 [arXiv:1001.3651 [astro-ph.CO]].

[31] C. Muñoz, “Indirect Dark Matter Searches and Models,” Nucl. Instrum. Meth. A **692** (2012) 13 [arXiv:1203.0678 [hep-ph]].

[32] O. Adriani *et al.* [PAMELA Collaboration], “The PAMELA Mission: Heralding a new era in precision cosmic ray physics,” Phys. Rept. **544** (2014) 323.

[33] O. Adriani *et al.* [PAMELA Collaboration], “Cosmic-Ray Positron Identification with the PAMELA experiment,” Proc. 33rd International Cosmic Ray Conference, Rio de Janeiro (2013), arXiv:1306.2198 [astro-ph.HE].

[34] M. Ackermann *et al.* [Fermi-LAT Collaboration], “Measurement of separate cosmic-ray electron and positron spectra with the Fermi Large Area Telescope,” Phys. Rev. Lett. **108** (2012) 011103 [arXiv:1109.0521 [astro-ph.HE]].

[35] M. Ackermann *et al.* [Fermi-LAT Collaboration], “Limits on Dark Matter Annihilation Signals from the Fermi-LAT 4-year Measurement of the Isotropic Gamma-Ray Background,” JCAP **1509** (2015) 09, 008 doi:10.1088/1475-7516/2015/09/008 [arXiv:1501.05464 [astro-ph.CO]].

[36] M. Aguilar *et al.* [AMS Collaboration], “Electron and Positron Fluxes in Primary Cosmic Rays Measured with the Alpha Magnetic Spectrometer on the International Space Station,” Phys. Rev. Lett. **113** (2014) 121102.

[37] M. Aguilar *et al.* [AMS Collaboration], “Precision Measurement of the $(e^+ + e)$ Flux in Primary Cosmic Rays from 0.5 GeV to 1 TeV with the Alpha Magnetic Spectrometer on the International Space Station,” Phys. Rev. Lett. **113** (2014) 22, 221102.

[38] L. Accardo *et al.* [AMS Collaboration], “High Statistics Measurement of the Positron Fraction in Primary Cosmic Rays of 0.5-500 GeV with the Alpha Magnetic Spectrometer on the International Space Station,” Phys. Rev. Lett. **113** (2014) 12, 121101.

[39] J. Aleksi *et al.* [MAGIC Collaboration], "Optimized Dark Matter searches in deep observations of Segue 1 with MAGIC," JCAP **1402** (2014) 008 [arXiv:1312.1535 [hep-ph]].

[40] A. Abramowski *et al.* [H.E.S.S. Collaboration], "Search for Dark Matter annihilation signatures in H.E.S.S. observations of Dwarf Spheroidal Galaxies," Phys. Rev. D **90** (2014) 11, 112012 [arXiv:1410.2589 [astro-ph.HE]].

[41] K. Choi *et al.* [Super-Kamiokande Collaboration], "Search for neutrinos from annihilation of captured low-mass Dark Matter particles in the Sun by Super-Kamiokande," Phys. Rev. Lett. **114** (2015) 14, 141301 [arXiv:1503.04858 [hep-ex]].

[42] M. G. Aartsen *et al.* [IceCube Collaboration], "Multipole analysis of IceCube data to search for Dark Matter accumulated in the Galactic halo," Eur. Phys. J. C **75** (2015) 1, 20 [arXiv:1406.6868 [astro-ph.HE]].

[43] G. Aad *et al.* [ATLAS Collaboration], "Search for new phenomena in final states with an energetic jet and large missing transverse momentum in pp collisions at $\sqrt{s}$ =8 TeV with the ATLAS detector," Eur. Phys. J. C **75** (2015) 7, 299 [Eur. Phys. J. C **75** (2015) 9, 408] doi:10.1140/epjc/s10052-015-3517-3, 10.1140/epjc/s10052-015-3639-7 [arXiv:1502.01518 [hep-ex]].

[44] G. Aad *et al.* [ATLAS Collaboration], "The ATLAS Experiment at the CERN Large Hadron Collider," JINST **3** (2008) S08003.

[45] S. Chatrchyan *et al.* [CMS Collaboration], "The CMS experiment at the CERN LHC," JINST **3** (2008) S08004.

[46] V. Khachatryan *et al.* [CMS Collaboration], Phys. Lett. B **755** (2016) 102 doi:10.1016/j.physletb.2016.01.057 [arXiv:1410.8812 [hep-ex]].

[47] K. Freese, J. A. Frieman and A. Gould, "Signal Modulation in Cold Dark Matter Detection," Phys. Rev. D **37** (1988) 3388.

[48] C. J. Copi, J. Heo and L. M. Krauss, "Directional sensitivity, WIMP detection, and the galactic halo," Phys. Lett. B **461** (1999) 43 [hep-ph/9904499].

[49] R. Bernabei *et al.*, "Searching for WIMPs by the annual modulation signature," Phys. Lett. B **424** (1998) 195.

[50] G. Angloher *et al.*, "Commissioning Run of the CRESST-II Dark Matter Search," Astropart. Phys. 31, pp. 270-276 (2009), arXiv:0809.1829 [astro-ph].

[51] R. Agnese *et al.* [CDMS Collaboration], "Silicon detector results from the first five-tower run of CDMS II," Phys. Rev. D **88** (2013) 031104 [Phys. Rev. D **88** (2013) 5, 059901] [arXiv:1304.3706 [astro-ph.CO]].

[52] L. Baudis, "WIMP Dark Matter Direct Detection Searches in Noble Gases," Phys. Dark Univ. **4** (2014) 50 [arXiv:1408.4371 [astro-ph.IM]].

[53] K. Abe *et al.*, "XMASS detector," Nucl. Instrum. Meth. A **716** (2013) 78 [arXiv:1301.2815 [physics.ins-det]].

[54] P.-A. Amaudruz *et al.*, "DEAP-3600 Dark Matter Search," International Conference on High Energy Physics (ICHEP 2014), arXiv:1410.7673 [physics.ins-det].

[55] A. Badertscher *et al.* [ArDM and CERN, PH/DT group, 1211 Geneve 23, Switzerland Collaborations], "Status of the ArDM Experiment: First results from gaseous argon operation in deep underground environment," arXiv:1307.0117 [physics.ins-det].

[56] P. Agnes *et al.* [DarkSide Collaboration], "First Results from the DarkSide-50 Dark Matter Experiment at Laboratori Nazionali del Gran Sasso," Phys. Lett. B **743** (2015) 456 [arXiv:1410.0653 [astro-ph.CO]].

[57] E. Aprile *et al.* [XENON100 Collaboration], "The XENON100 Dark Matter Experiment," Astropart. Phys. **35** (2012) 573 [arXiv:1107.2155 [astro-ph.IM]].

[58] D. S. Akerib *et al.* [LUX Collaboration], "The Large Underground Xenon (LUX) Experiment," Nucl. Instrum. Meth. A **704** (2013) 111 [arXiv:1211.3788 [physics.ins-det]].

[59] M. Felizardo *et al.* [SIMPLE Collaboration], "The SIMPLE Phase II Dark Matter Search," Phys. Rev. D **89** (2014) 7, 072013 [arXiv:1404.4309 [hep-ph]].

[60] V. Zacek *et al.* [PICASSO Collaboration], "Dark Matter search with PICASSO," J. Phys. Conf. Ser. 375 012023 (2012).

[61] E. Behnke *et al.* [COUPP Collaboration], "First Dark Matter Search Results from a 4-kg CF_3I Bubble Chamber Operated in a Deep Underground Site," Phys. Rev. D **86** (2012) 5, 052001 [Phys. Rev. D **90** (2014) 7, 079902] [arXiv:1204.3094 [astro-ph.CO]].

[62] C. Amole *et al.* [PICO Collaboration], "Dark Matter Search Results from the PICO-2L C_3F_8 Bubble Chamber," Phys. Rev. Lett. **114** (2015) 23, 231302 [arXiv:1503.00008 [astro-ph.CO]].

[63] P. Cushman *et al.*, "Snowmass CF1 Summary Report: WIMP Dark Matter Direct Detection," Community Summer Study 2013 : Snowmass on the Mississippi (CSS2013), FERMILAB-CONF-13-688-AE, arXiv:1310.8327 [hep-ex].

[64] C. E. Aalseth *et al.* [DarksSide-20k Collaboration], "Collaborative Research: DarkSide-20k," INFN-NSF Proposal 2015.

[65] R. Bernabei *et al.* [DAMA Collaboration], "Search for WIMP annual modulation signature: Results from DAMA / NaI-3 and DAMA / NaI-4 and the global combined analysis," Phys. Lett. B **480** (2000) 23.

[66] R. Bernabei *et al.* [DAMA and LIBRA Collaborations], 'New results from DAMA/LIBRA," Eur. Phys. J. C **67** (2010) 39 [arXiv:1002.1028 [astro-ph.GA]].

[67] R. Bernabei, P. Belli, F. Cappella, V. Caracciolo, S. Castellano, R. Cerulli, C. J. Dai and A. dAngelo *et al.*, "Final model independent results of DAMA/LIBRA-phase1 and perspectives of phase2," Phys. Part. Nucl. **46** (2015) 2, 138.

[68] C. E. Aalseth, P. S. Barbeau, J. Colaresi, J. I. Collar, J. Diaz Leon, J. E. Fast, N. Fields and T. W. Hossbach *et al.*, "Search for an Annual Modulation in a P-type Point Contact Germanium Dark Matter Detector," Phys. Rev. Lett. **107** (2011) 141301 [arXiv:1106.0650 [astro-ph.CO]].

[69] C. E. Aalseth *et al.* [CoGeNT Collaboration], "Search for An Annual Modulation in Three Years of CoGeNT Dark Matter Detector Data," arXiv:1401.3295 [astro-ph.CO].

[70] P. S. Barbeau, J. I. Collar, Y. Efremenko and K. Scholberg, "Comment on Fitting the annual modulation in DAMA with neutrons from muons and neutrinos," Phys. Rev. Lett. **113** (2014) 22, 229001 [arXiv:1409.3185 [hep-ph]].

[71] G. Angloher, M. Bauer, I. Bavykina, A. Bento, C. Bucci, C. Ciemniak, G. Deuter and F. von Feilitzsch *et al.*, "Results from 730 kg days of the CRESST-II Dark Matter Search," Eur. Phys. J. C **72** (2012) 1971 [arXiv:1109.0702 [astro-ph.CO]].

[72] G. Angloher *et al.* [CRESST Collaboration], "Results on light Dark Matter particles with a low-threshold CRESST-II detector," Eur. Phys. J. C **76** (2016) 1, 25 doi:10.1140/epjc/s10052-016-3877-3 [arXiv:1509.01515 [astro-ph.CO]].

[73] Z. Ahmed *et al.* [CDMS-II Collaboration], "Results from a Low-Energy Analysis of the CDMS II Germanium Data," Phys. Rev. Lett. **106** (2011) 131302 [arXiv:1011.2482 [astro-ph.CO]].

[74] R. Agnese *et al.* [CDMS Collaboration], "Silicon Detector Dark Matter Results from the Final Exposure of CDMS II," Phys. Rev. Lett. **111** (2013) 25, 251301 [arXiv:1304.4279 [hep-ex]].

[75] E. Armengaud *et al.* [EDELWEISS Collaboration], "A search for low-mass WIMPs with EDELWEISS-II heat-and-ionization detectors," Phys. Rev. D **86** (2012) 051701 [arXiv:1207.1815 [astro-ph.CO]].

[76] E. Aprile *et al.* [XENON100 Collaboration], "Dark Matter Results from 225 Live Days of XENON100 Data," Phys. Rev. Lett. **109** (2012) 181301 [arXiv:1207.5988 [astro-ph.CO]].

[77] D. S. Akerib *et al.* [LUX Collaboration], "First results from the LUX Dark Matter experiment at the Sanford Underground Research Facility," Phys. Rev. Lett. **112** (2014) 091303 [arXiv:1310.8214 [astro-ph.CO]].

[78] D. S. Akerib *et al.* [LUX Collaboration], "Improved WIMP scattering limits from the LUX experiment," arXiv:1512.03506 [astro-ph.CO].

[79] L. Baudis, "Direct Dark Matter detection: the next decade," Phys. Dark Univ. **1** (2012) 94 [arXiv:1211.7222 [astro-ph.IM]].

[80] R. Agnese *et al.* [SuperCDMS Collaboration], "Search for Low-Mass Weakly Interacting Massive Particles with SuperCDMS," Phys. Rev. Lett. **112** (2014) 24, 241302 [arXiv:1402.7137 [hep-ex]].

[81] E. Aprile [XENON1T Collaboration], "The XENON1T Dark Matter Search Experiment," Springer Proc. Phys. **148** (2013) 93 [arXiv:1206.6288 [astro-ph.IM]].

[82] A. Ianni, "DarkSide-20k," International Conference on Particle Physics and Astrophysics (ICPPA-2015).

[83] D. S. Akerib *et al.*, "Radiogenic and Muon-Induced Backgrounds in the LUX Dark Matter Detector," Astropart. Phys. **62** (2015) 33 [arXiv:1403.1299 [astro-ph.IM]].

[84] V. A. Kudryavtsev [LZ Collaboration], "Expected Background in the LZ Experiment," AIP Conf. Proc. **1672** (2015) 060003, doi:10.1063/1.4927991.

[85] J. D. Lewin and P. F. Smith, "Review of mathematics, numerical factors, and corrections for Dark Matter experiments based on elastic nuclear recoil," Astropart. Phys. 6, 87-112 (1996).

[86] N. Mirabolfathi, "Direct and indirect searches for Dark Matter in the form of weakly interacting massive particles (WIMPs)," eConf C **0406271** (2004) TUET09 [astro-ph/0412103].

[87] R. W. Schnee, “Introduction to Dark Matter experiments,” In Physics of the Large and Small: Proceedings of the 2009 Theoretical Advanced Study Institute in Elementary Particle Physics, 629-681 (World Scientific, Singapore) Ed. Csaba Csaki and Scott Dodelson (2010) [arXiv:1101.5205 [astro-ph.CO]].

[88] http://pisrv0.pit.physik.uni-tuebingen.de/darkmatter/

[89] D. G. Cerdeño and A. M. Green, “Direct detection of WIMPs,” In *Bertone, G. (ed.): Particle Dark Matter* 347-369 [arXiv:1002.1912 [astro-ph.CO]].

[90] G. Jungman, M. Kamionkowski and K. Griest, “Supersymmetric Dark Matter,” Phys. Rept. **267** (1996) 195 [hep-ph/9506380].

[91] M. Schumann, “Dark Matter Search with liquid Noble Gases,” Proceedings of the 47th Rencontres de Moriond, 2012, Cosmology Session, arXiv:1206.2169 [astro-ph.IM].

[92] W. H. Lippincott *et al.* [MiniCLEAN Collaboration], “Scintillation yield and time dependence from electronic and nuclear recoils in liquid neon,” Phys. Rev. C **86** (2012) 015807 [arXiv:1111.3260 [nucl-ex]].

[93] K. Rielage *et al.* [MINICLEAN Collaboration], “Update on the MiniCLEAN Dark Matter Experiment,” Phys. Procedia **61** (2015) 144 [arXiv:1403.4842 [physics.ins-det]].

[94] Hamamatsu Photonics KK, “Photomultiplier Technical Handbook,” third edition, (2006).

[95] P. Benetti *et al.* [WARP Collaboration], “Measurement of the specific activity of ^{39}Ar in natural argon,” Nucl. Instrum. Meth. A **574** (2007) 83 [astro-ph/0603131].

[96] W. Jiang *et al.*, “^{39}Ar Detection at the 10^{-16} Isotopic Abundance Level with Atom Trap Trace Analysis,” Phys. Rev. Lett. **106** (2011) 103001 doi:10.1103/PhysRevLett.106.103001 [arXiv:1101.2933 [physics.atom-ph]].

[97] T. Heindl, T. Dandl, M. Hofmann, R. Krucken, L. Oberauer, W. Potzel, J. Wieser and A. Ulrich, “The scintillation of liquid argon,” Europhys. Lett. **91** (2010) 62002.

[98] V. Boccone [ArDM Collaboration], “Recent updates on the ArDM project: A Liquid Argon TPC for Dark Matter Detection,” J. Phys. Conf. Ser. **160** (2009) 012032 [arXiv:0810.4490 [physics.ins-det]].

[99] W. H. Lippincott, K. J. Coakley, D. Gastler, A. Hime, E. Kearns, D. N. McKinsey, J. A. Nikkel and L. C. Stonehill, “Scintillation time dependence and pulse shape discrimination in liquid argon,” Phys. Rev. C **78** (2008) 035801 [Phys. Rev. C **81** (2010) 039901] [arXiv:0801.1531 [nucl-ex]].

[100] C. Rubbia *et al.*, “Underground operation of the ICARUS T600 LAr-TPC: first results,” JINST **6** (2011) P07011 [arXiv:1106.0975 [hep-ex]].

[101] C. Adams *et al.* [LBNE Collaboration], “The Long-Baseline Neutrino Experiment: Exploring Fundamental Symmetries of the Universe,” FERMILAB-PUB-14-022, arXiv:1307.7335 [hep-ex].

[102] E. Aprile, A. E. Bolotnikov, A. I. Bolozdynya and T. Doke “Noble Gas Detectors,” Ed. WILEY-VCH (2006). ISBN: 9783527405978.

[103] S. Kubota, A. Nakamoto, T. Takahashi, S. Konno, T. Hamada, M. Miyajima, A. Hitachi, E. Shibamura and T. Doke, “Evidence of the existence of exciton states in liquid argon and exciton-enhanced ionization from xenon doping,” Phys. Rev. B **13** (1976), 1649.

[104] T. Doke *et al.*, “Absolute scintillation yields in liquid argon and xenon for various particles,” Jp. J. Appl. Phys. **41**, pp. 1538-1545 (2002).

[105] S. Kubota, A. Nakamoto, T. Takahashi, T. Hamada, E. Shibamura, M. Miyajima, K. Masuda and T. Doke, “Recombination luminescence in liquid argon and in liquid xenon,” Phys. Rev. B **17** (1978) 6, 2762.

[106] V. Chepel and H. Araujo, “Liquid noble gas detectors for low energy particle physics,” JINST **8** (2013) R04001 [arXiv:1207.2292 [physics.ins-det]].

[107] M. Schenk, “Studies with a Liquid Argon Time Projection Chamber: Addressing Technological Challenges of Large-Scale Detectors,” Ed. Springer (2015). ISBN: 9783658094300.

[108] R. Platzman, “Total ionization in gases by high-energy particles: an appraisal of our understanding,” The International Journal of Applied Radiation and Isotopes 10, 116 (1961).

[109] G. Jaffe, “Statistics of charge collection in liquid argon and liquid xenon,” Ann. der. Phys. **42**, 303 (1913).

[110] J. Thomas *et al.*, “Statistics of charge collection in liquid argon and liquid xenon,” Phys. Rev. A **38** (1998) 11.

[111] A. Marchionni *et al.* [ArDM Collaboration], "ArDM: a ton-scale LAr detector for direct Dark Matter searches," J. Phys. Conf. Ser. **308** (2011) 012006 [arXiv:1012.5967 [physics.ins-det]].

[112] J. Birks, "Theory and Practice of Scintillation Counting," Pergamon Press, New York, 1964.

[113] S. Amoruso *et al.* [ICARUS Collaboration], "Study of electron recombination in liquid argon with the ICARUS TPC," Nucl. Instrum. Meth. A **523** (2004) 275.

[114] D. W. Swan, "Electron Attachment Processes in Liquid Argon containing Oxygen or Nitrogen Impurity," Proc. Phys. Soc. **82** (1963) 74.

[115] E. Buckley *et al.*, "A study of ionization electrons drifting over large distances in liquid argon," Nuclear Instruments and Methods in Physics Research A 275, 364 (1989).

[116] W. Walkowiak, "Drift velocity of free electrons in liquid argon," Nucl. Instrum. Meth. A **449** (2000) 288.

[117] M. Suzuki and S. Kubota, "Mechanism of Proportional Scintillation in Argon, Krypton and Xenon," Nucl. Instrum. Meth. **164** (1979) 197.

[118] C. M. B. Monteiro, J. A. M. Lopes, J. F. C. A. Veloso and J. M. F. dos Santos, "Secondary scintillation yield in pure argon," Phys. Lett. B **668** (2008) 167.

[119] A. Rubbia, "ArDM: A ton-scale liquid Argon experiment for direct detection of Dark Matter in the universe," J. Phys. Conf. Ser. **39** (2006) 129 [hep-ph/0510320].

[120] V. Boccone *et al.* [ArDM Collaboration], "Development of wavelength shifter coated reflectors for the ArDM argon Dark Matter detector," JINST **4** (2009) P06001 [arXiv:0904.0246 [physics.ins-det]].

[121] C. Amsler *et al.* [ArDM Collaboration], "First results on light readout from the 1-ton ArDM liquid argon detector for Dark Matter searches," JINST **5** (2010) P11003 [arXiv:1009.3641 [physics.ins-det]].

[122] ArDM collaboration, "Specification and risk analysis document for the ArDM experiment," 2013.

[123] L. Kaufmann, "Detector Performance and Background Studies for the ArDM Experiment," PhD thesis, ETH Zurich, 2008.

[124] S. Agostinelli *et al.* [GEANT4 Collaboration], Nucl. Instrum. Meth. A **506** (2003) 250.

[125] A. Bettini, "The World underground scientific facilities: A Compendium," Proccedings of TAUP 2007, arXiv:0712.1051 [hep-ex].

[126] D. Ashitkov et al., "DBA. Search for double beta decay of ^{100}Mo with liquid argon ionization chamber," Nucl. Instr. Meth. A 416, 179 (1998)

[127] LBNL Isotopes Project Nuclear Data Dissemination Home Page (http://ie.lbl.gov/toi.html).

[128] L. Kaufmann and A. Rubbia, "Background studies for a ton-scale argon Dark Matter detector: ArDM," Invited talk at the 6th International Workshop on the Identification of Dark Matter, Greece (2006), hep-ph/0612056.

[129] A. Pocar, "Beyond DarkSide-50: Very Large Argon TPCs for Heavy WIMP Searches," Berkeley Workshop on Dark Matter Detection, June 2015.

[130] L. Reichhart *et al.*, "Measurement and simulation of the muon-induced neutron yield in lead," Astropart. Phys. **47** (2013) 67 [arXiv:1302.4275 [physics.ins-det]].

[131] E. Aprile, K. Arisaka, F. Arneodo, A. Askin, L. Baudis, A. Behrens, K. Bokeloh and E. Brown *et al.*, "Material screening and selection for XENON100," Astropart. Phys. **35** (2011) 43 [arXiv:1103.5831 [physics.ins-det]].

[132] Y. F. Wang, V. Balic, G. Gratta, A. Fasso, S. Roesler and A. Ferrari, "Predicting neutron production from cosmic ray muons," Phys. Rev. D **64** (2001) 013012 [hep-ex/0101049].

[133] C. F. Weizsäcker, Z. Phys. 88(1934)612; E.J. Williams, Kgl. Dan. Vidensk. Selsk. Mat Fys. Medd. XIII (1935)4.

[134] J. Delorme, M. Ericson, T. E. O. Ericson and P. Vogel, "Pion and neutron production by cosmic ray muons underground," Phys. Rev. C **52** (1995) 2222 [hep-ph/9504331].

[135] D. Jordan *et al.*, "Measurement of the neutron background at the Canfranc Underground Laboratory LSC," Astropart. Phys. **42** (2013) 1.

[136] U. Degunda, "Measurement of the Electronic Recoil Contamination and Development of the Control System for the ArDM Experiment," PhD thesis, No. 20966, ETH Zurich, 2013.

[137] ArDM collaboration, “ArDM (LSC EXP-08) status report. 14th Scientific Committee Meeting, May 2014”.

[138] http://www.lsc-canfranc.es/en/for-users/lsc-services/radiopurity.html

[139] Committee on Advanced Spectroscopic Portals, Nuclear and Radiation Studies Board Division on Earth and Life Studies. “Evaluating Testing, Costs, and Benefits of Advanced Spectroscopic Portals for Screening Cargo at Ports of Entry”. The National Academies Press. Washington, D.C (2009). ISBN: 0309140226.

[140] L. Baudis, A. D. Ferella, A. Askin, J. Angle, E. Aprile, T. Bruch, A. Kish and M. Laubenstein *et al.*, “Gator: a low-background counting facility at the Gran Sasso Underground Laboratory,” JINST **6** (2011) P08010 [arXiv:1103.2125 [astro-ph.IM]].

[141] C. Hurtgen, S. Jerome, and M. Woods, “Applied Radiation and Isotopes,” 53, 45 (2000), ISSN 0969-8043.

[142] W. B. Wilson et al., “SOURCES 4A: A Code for Calculating (α,n), Spontaneous Fission, and Delayed Neutron Sources and Spectra”. Edited by Maco Stewart, Group CIC-1. Los Alamos National Laboratory (1999).

[143] A. Badertscher *et al.*, “ArDM: first results from underground commissioning,” JINST **8** (2013) C09005 [arXiv:1309.3992 [physics.ins-det]].

[144] C. Lazzaro, “Reconstruction of the muon tracks in the OPERA experiment and first results on the light collection in the ArDM experiment,” PhD thesis, No. 20551, ETH Zurich, 2012.

[145] P. Arce *et al.*, “Gamos: A framework to do Geant4 simulations in different physics fields with an user-friendly interface,” Nucl. Instrum. Meth. A **735** (2014) 304.

[146] B. Montes, “Monte Carlo studies about the energy calibration for the Argon Dark Matter experiment,” Master thesis, e-prints Complutense, ID code: 16234, Facultad de Ciencias Físicas, UCM. Curso 2011-2012.

[147] A. Manalaysay *et al.*, “Spatially uniform calibration of a liquid xenon detector at low energies using $^{83\mathrm{m}}$Kr,” Rev. Sci. Instrum. **81** (2010) 073303 [arXiv:0908.0616 [astro-ph.IM]].

[148] V. Hannen *et al.*, “Limits on the release of Rb isotopes from a zeolite based $^{83\mathrm{m}}$Kr calibration source for the XENON project,” JINST **6** (2011) P10013 [arXiv:1109.4270 [astro-ph.IM]].

[149] L. W. Kastens, S. B. Cahn, A. Manzur and D. N. McKinsey, “Calibration of a Liquid Xenon Detector with $^{83\mathrm{m}}$Kr,” Phys. Rev. C **80** (2009) 045809 [arXiv:0905.1766 [physics.ins-det]].

[150] C. Peterson and T. Rognvaldsson, “An Introduction to artificial neural networks,” LU-TP-91-23.

[151] I. Fischer, F. Hennecke, C. Bannes andA. Zell, “Java Neural Network Simulator (JavaNNS) manual,” Universität Tübingen, 2001-2002.

[152] K. Nguyen, “Proof of concept for the direct WIMP search with ArDM and analysis of its first data,” PhD thesis, No. 23204, ETH Zurich, 2016.

[153] H. Daniel, “Shape of beta-ray spectra”, Reviews of modern physics, Vol. 40 No. 3 (1968).

[154] E. Sergre, “Nuclei and particles, an introduction to nuclear and subnuclear physics”, chapter 9, second edition 1977, ISBN: 0805386017.

[155] B. Cornell, B. R. Montes Núñez and A. D. Ferella, “Hands on XENON100 Dark Matter direct detection experiment: studying and modeling background and signal in a frequentist analysis framework,” PoS GSSI **14** (2015) 017.

[156] E. Aprile *et al.* [XENON100 Collaboration], “Likelihood Approach to the First Dark Matter Results from XENON100,” Phys. Rev. D **84** (2011) 052003 [arXiv:1103.0303 [hep-ex]].

[157] R. Trotta, F. Feroz, M. P. Hobson, L. Roszkowski and R. Ruiz de Austri, “The Impact of priors and observables on parameter inferences in the Constrained MSSM,” JHEP **0812** (2008) 024 [arXiv:0809.3792 [hep-ph]].

[158] Glenn F. Knoll, “Radiation Detection and Measurement”, Wiley, New York, (2000).

[159] C. Guerrero, D. Cano-Ott, M. Fernández-Ordóñez, E. González-Romero, T. Martínez, D. Villamarín, “Analysis of the BC501A neutron detector signals using the true pulse shape,” Nucl. Instrum. Meth. A **597** 212218 (2008).

[160] Saint-Gobain Crystals, “Material Safety Data Sheet: BC-501A,” January 17, 2003. Revised February 5, 2009.

[161] F. T. Kuchnir, “Time Dependence of Scintillators end the Effect on P.S.D.,” IEEE Trans. Nucl. Sci., NS-15, No.3, 107-113 (1968).

[162] P. A. Soderstrom, J. Nyberg and R. Wolters, "Digital pulse-shape discrimination of fast neutrons and gamma rays," Nucl. Instrum. Meth. A **594** (2008) 79 [arXiv:0805.0692 [nucl-ex]].

[163] Eckert & Ziegler, Isotope Products, "Nominal liquid source data sheet: Cf-252," March 6, 2003. Revised February 5, 2009.

[164] J. Quin *et al.*, "Characterizations of BC501A and BC537 liquid scintillator detectors," Applied Radiation and Isotopes 104 (2015)1524.

[165] H. J. Kim *et al.*, "Measurement of the neutron flux in the CPL underground laboratory and simulation studies of neutron shielding for WIMP searches," Astropart. Phys. **20** (2004) 549-557.

[166] T. Francke and V. Peskov,"Innovative applications and developments of micro-pattern gaseous detectors," ISBN: 1466660147, Advances in chemical and materials engineering (ACME) book series, Hershey: Engin. Sci. Ref. (2014), doi:10.4018/978-1-4666-6014-4.

[167] "Ion mobility and liquid motion in liquefied argon," J. Phys. D: Applied Physics, vol. 1, n 8, p 1019, (1968).

[168] A. Bueno, Z. Dai, Y. Ge, M. Laffranchi, A. J. Melgarejo, A. Meregaglia, S. Navas and A. Rubbia, "Nucleon decay searches with large liquid argon TPC detectors at shallow depths: Atmospheric neutrinos and cosmogenic backgrounds," JHEP **0704** (2007) 041 [hep-ph/0701101].

[169] M. Miyajima, *et al.*, "Average energy expended per ion pair in liquid argon", Phys. Rev. A 9 (1974) 1438.

[170] R.T. Scalettar *et al.*, "Critical test of geminate recombination in liquid argon", Phys. Rev. A 25 (1982) 2419.

[171] P. K. F. Grieder, "Cosmic rays at earth: Researcher's reference, manual and data book," Amsterdam: Elsevier (2001), ISBN: 9780444507105.

[172] A. Rubbia [WA105 Collaboration], "Technical Design Report for large-scale neutrino detectors prototyping and phased performance assessment in view of a long-baseline oscillation experiment," CERN-SPSC-2014-013.